SHM-NDT

Proceedings of the 3rd edition of the

International Symposium on Structural Health Monitoring and Nondestructive Testing, SHM-NDT 2020

and of the 9th **IWASPNDE WORKSHOP**

Nov. 25th - 26th, 2020, in a *distance digital format*

Conference officially hosted by

UNIVERSITÉ LAVAL

Symposium organized by:
Canada Research Chair on Multipolar Infrared Vision Infrarouge Mulipolaire (MIVIM)
of the *Electrical and Computer Engineering* Department

X.P.V. Maldague, Editor

É. du CAO

à la frontière des connaissances
at the cutting edge of knowledge

Table of contents

Page	Paper no.	Authors	Title
21	1	Qiang Fang, Farima Mamoudan, Clemente Ibarra Castanedo, Xavier Maldague	Defect depth estimation in infrared thermography with deep learning
32	5	Seyed Fouad Karimian, Ramin Moradi, Sergio Cofre-Martel, Katrina M. Groth and Mohammad Modarres	NEURAL NETWORK AND PARTICLE FILTERING: A HYBRID FRAMEWORK FOR CRACK PROPAGATION PREDICTION
44	7	Éric Guyot and Jean-Philippe Gagnon and Stephane Boubanga Tombet	ANALYSIS OF BALLISTIC IMPACTS ON COMPOSITE MATERIALS BY INFRARED ACTIVE THERMOGRAPHY
46	8	Simon Verspeek, Bart Ribbens, Michaël Hillen, Xavier Maldague and Gunther Steenackers	WOODEN FLOORING INSPECTION USING ACTIVE THERMOGRAPHY
48	9	Bardia Yousefi, Clemente Ibarra Castanedo and Xavier P.V. Maldague	INFRARED-BASED NON-INVASIVE COMPUTER-AIDED DIAGNOSIS FOR EARLY DETECTION OF BREAST CANCER USING DYNAMIC THERMOGRAPHY
54	10	Xiang Zhang, Jian-Ping Peng, Lingfan Feng Jie Bai, Xiaorong Gao	COMPARISON STUDY OF DIFFERENT ALGORITHM FOR MICROCRACK DETECTION USING EDDY CURRENT PULSED THERMOGRAPHY

61	11	Nidhal Bouslama, Nicolas Quaegebeur, Ahmed Maslouhi and Patrice Masson	COMPARISON OF NON-DESTRUCTIVE TECHNIQUES IN PLAIN WEAVE CARBON FIBER REINFORCED POLYMERS UNDER FATIGUE LOADING
63	13	Julien Fleuret , Samira Ebrahimi, Clemente Ibarra Castanedo, Xavier Maldague	INDEPENDENT COMPONENT THERMOGRAPHY APPLIED TO PULSED THERMOGRAPHIC DATA FOR CFRP INSPECTION
73	14	Davood Kalhor, Samira Ebrahimi, Roger Booto Tokime, Farima Abdollahi Mamoudan, Yohan Bélanger, Alexandra Mercier and Xavier Maldague	INFRARED THERMOGRAPHY FOR CULVERT INSPECTION
81	16	Kazushi Kimoto and Hiroto Shimada	ULTRASONIC IMAGING METHOD FOR THE DETECTION AND SIZING OF CRACKS IN A RIB-TO-DECK WELDED JOINT
83	17	Mohammad Ebrahim Bajgholi, Gilles Rousseau, Martin Viens, Denis Thibault	CAPABILITY OF ADVANCED ULTRASONIC INSPECTION TECHNOLOGIES FOR HYDRAULIC TURBINE RUNNERS
95	18	Fabian Krieg, Jan Kirchhof, Eduardo Pérez, Thomas Schwender, Florian Roemer and Ahmad Osman	LOCALLY OPTIMAL SUBSAMPLING STRATEGIES FOR FULL-MATRIX CAPTURE MEASUREMENTS IN PIPE INSPECTION
105	19	Shakeb Deane, Nicolas P. Avdelidis, Antonios Tsourdos, Xavier Maldague, Clemente Ibarra Castanedo, Alexander Williamson	UAV NDT OF AIRCRAFT STRUCTURES
106	20	Hossein Memarzadeh Sharifipour, Bardia Yousefi and Xavier P.V. Maldague	MATRIX CATEGORY ENRICHED OVER SEMIRINGS FOR MATHEMATICAL MORPHOLOGY
126	21	Henrique Fernandes, Jannik Summa, Julie Daudre, Ute Rabe, Stefano Sfarra, Gianfranco Gargiulo and Hans-Georg Herrmann	NON-DESTRUCTIVE INSPECTION OF DECORATIVE MARQUETRY SAMPLE
133	22	Faraz Masoumi, Afshin Sadri, Winnie Ying and Claudio Pasqualino	CONDITION ASSESSMENT OF PRESTRESSED CONCRETE GIRDERS OF A HIGHWAY BRIDGE IN CANADA
142	29	Valentin Serey, Huu Tinh Hoang, Tom Druet and Bastien Chapuis	PASSIVE GUIDED WAVES TOMOGRAPHY FOR STRUCTURAL HEALTH MONITORING OF PIPES
144	30	Farima Abdollahi Mamoudan, Sebastien Savard, Xavier Maldague, Abdel Hakim Bendada and Tobin Filleter	NUMERICAL SIMULATION AND EXPERIMENTAL STUDY OF CAPACITIVE IMAGING TECHNINQUE AS A NON-DESTRUCTIVE TESTING METHOD

155	33	Dominique Albert-Weiss, Egla Hadgini, Matthias Heinrich, Ahmad Osman	CNN FOR RIPENESS CLASSFICATION OF WATERMELON FRUITS BASED ON ACOUSTIC TESTING
160	34	Esmaeil Ghorbani, Dagmar Svecova, Evangeline Murison and Young-Jin Cha	OUTPUT-ONLY BRIDGE SCOUR MONITORING USING MEASURED VIBRATION
162	36	Konstantin Polyakov, Fernando Lopez and Martin Viens	ADVANCED SIGNAL PROCESSING TECHNIQUES TO IMPROVE THE DETECTION OF DEFECTS IN PRESSURE VESSELS BY ACOUSTIC EMISSION TESTING
164	37	Parham Nooralishahi, Fernando Lopez and Xavier Maldague	A NOVEL DRONE-ENABLED APPROACH FOR GAS LEAK DETECTION USING THERMAL IMAGE FLOW ANALYSIS
166	41	Rahimullah Habibzai	NONDESTRUCTIVE EVALUATION OF REPAIRED REINFORCED CONCRETE BEAM BY UNPRECEDENTED POLYMER CEMENT MORTAR MIXED WITH STEEL FIBER
175	44	Sandra Pozzer, Francisco Dalla Rosa, Zacarias Martin Chamberlain Pravia, Ehsan Rezazadeh Azar and Xavier Maldague	LONG-TERM NUMERICAL ANALYSIS OF SUBSURFACE DELAMINATION DETECTION IN CONCRETE SLABS VIA INFRARED THERMOGRAPHY
185	45	Jue Hu, Hai Zhang, Stefano Sfarra, Carlo Santulli, Guiyun Tian and Xavier Maldague	INFRARED-TERAHERTZ FUSION INSPECTION FOR JUTE/KENAF-GLASS HYBRID COMPOSITES

Preface

International Symposia on Structural Health Monitoring and Nondestructive Testing also known as SHM-NDT Symposia started in Lyon, France in 2013. In 2018, a second edition took place in Saarbrücken, Germany. The next Symposium, the Third one: the SHM-NDT 2020 is the symposium concerned by these proceedings. Originally the Symposium was intended to take place 14-15 May 2020 in Quebec City, Canada. However as the World started to be affected by a global pandemic of Coronavirus (Covid-19) in March 2020, it was no longer possible to hold the face-to-face event as we originally planned. It was hence decided to postpone the event which was finally hold in a digital form. Since the delivery mode of the Symposium was digital, the Symposium was more or less global! So despite the terrible sanitary situation we all experienced at that time and beyond, there are a few good things, fortunately!

We had the chance to have four keynote speakers who presented us with the latest information as live sessions with ZOOM:

• Prof. **P. Masson** from Canada talked about « Correlation-based Ultrasound Imaging in NDT and SHM».

• Prof. **A. Osman** from Germany discussed about «NDT in the context of the factory of the future».

• Prof. **V. Parfenov** from Russia presented his «Latest findings in cultural heritage».

• Prof. **G. Steenackers** from Belgium talked about «Multimodal NDE measurements coupled to modeling».

These proceedings contain the full-text and abstracts of all received papers, in electronic format. There was also a special agreement with *MDPI Applied Sciences* to publish a Special Issue. The SHM-NDT Special Issue regroups papers on the topic of SHM-NDT as well as selected papers presented at the Third Symposium. Important the selected papers from the Symposium that appears in the MDPI SHM-NDT 2020 Special Issue are different since they were updated following the peer-review process.

A big thank is due to our major sponsor: **TORNGATS**. It was also possible to organize a virtual exhibition with two exhibitors: **Telops** and **Visiooimage** both from Quebec City, Canada.

The usual Best Paper Award aimed to the under 35years old Presenters took place also with as winner: Seyed Fouad Karimian, Ramin Moradi, Sergio Cofre-Martel, Katrina M. Groth and Mohammad Modarres for their paper NEURAL NETWORK AND PARTICLE FILTERING: A HYBRID FRAMEWORK FOR CRACK PROPAGATION PREDICTION". Congratulations to the authors!

Additionally, it was also possible, at the closing ceremony, to announce the 4th edition of SHM-NDT, face-to-face this time: the 4th SHM-NDT will take place in 2022 at the

Southwest Jiaotong University in Chengdu, Sichuan, China. It will be organized by Prof. Xiaorong GAO.

I will finish this preface by thanking all the organizers and their staff, the exhibitors, the sponsors, the speakers, the attendees, the SHM-NDT Committee members: in the context of the pandemic, life is particularly difficult and makes the participation of all even more important! A special thank also to Mr. Patrick Deschênes-Labrie who helped so much as well as the Science & Engineering Faculty Staff and also the staff of our dept. of Electrical and Computing Engineering of University Laval.

A last important note, the website:
            `https://www.shm-ndt2020.gel.ulaval.ca/home/`
will be maintained for future references.

Xavier Maldague, professor
Chair, SHM-NDT 2020

Program Committee

General Chairman:

• Xavier Maldague
Faculty of Science and Engineering
Department of Electrical and Computer Engineering
Université Laval, Québec
maldagx@gel.ulaval.ca

Scientific Advisory Committee:

• Bernd Valeske,
htw saar University of Applied Sciences, Fraunhofer Institute for Nondestructive Testing IZFP

• Gao Xiaorong,
Southwest Jiaotong University, China

• Philipp Guy,
National Institute of Applied Sciences INSA-Lyon

• Hai Zhang,
Department of Mechanical and Industrial Engineering, University of Toronto

• Thomas Monnier,
National Institute of Applied Sciences INSA-Lyon

• Ulf Hassler,
Fraunhofer Development Center X-ray Technology EZRT

• Patrick Masson,
Université de Sherbrooke, Sherbrooke, Canada

• Nicolas P. Avdelidis,
National Technical University of Athens, Greece

• Bastien Chapuis,
Commissariat à l'énergie atomique et aux énergies alternatives (Imagerie et Simulation pour le Contrôle), France

• Yuxia Duan,
Central South University, Changsha, China

• Valerie Kaftandjian,
National Institute of Applied Sciences INSA-Lyon, France

• Junyan Liu,
Harbin Institute of Technology, Harbin, China

• G. Steenackers,
University of Antwerp, Antwerp, Belgium

• X. Maldague,
Université Laval, Quebec City, Canada

• Ahmad Osman,
htw saar University of Applied Sciences
Fraunhofer Institute for Nondestructive Testing IZFP, Germany

• Stefano Sfarra,
University of L'Aquila, Italy

• Vassilis Kappatos,
Hellenic Institute of Transport (HIT), Thessaloniki, Greece

• Henrique Coelho Fernandes
School of Computer Science,Federal University of Uberlandia (Brazil)

Organizing Committee

Xavier Maldague, chair
Université Laval, Quebec City, Canada

Abdelhakim Bendada
Université Laval, Quebec City, Canada

Marc Genest
Institute for Aerospace Research, National Research Council, Ottawa, Canada

Shashank Pant
Institute for Aerospace Research, National Research Council, Ottawa, Canada

Clemente Ibarra-Castanedo
Université Laval, Quebec City, Canada

Mohammad Ebrahim Bajgholi
University of Quebec, ETS, Montréal, Canada

Technical Secretariat - SHM-NDT 2020

• Mr. Patrick Deschênes Labrie
Department of Electrical and Computer Engineering
Université Laval, Québec, Canada, G1V 0A6
Phone : ++ 1 418 656-2962
Fax : ++ 1418 656-3159
Email : Quebec@gel.ulaval.ca

MAJOR SPONSOR

EXHIBITORS

PARTNERS

Third International Symposium on Structural Health Monitoring and Nondestructive Testing
3rd SHM-NDT 2020, 25-26 November 2020

- 12 -

Keynotes

OPTIMIZED NON-DESTRUCTIVE INSPECTION USING MULTI-MODAL MEASUREMENT SET-UP AND NUMERICAL MODELING

Gunther Steenackers[1*], Simon Verspeek[1], J. Peeters[1], Bart Ribbens[1]

[1] University of Antwerp, Op3Mech research group, Groenenborgerlaan 171, B-2020 Antwerp, Belgium

[*]Corresponding Author: gunther.steenackers@uantwerpen.com

ABSTRACT

In-line inspection of advanced components, remains a challenging task in industry. A methodology is discussed which uses numerical simulations to automatically determine the best set of experimental parameters to inspect the structure on defects using active thermography. The inspection is performed using an industrial conveyor belt or a robotic arm optimized using a numerical model of the defected test sample. The objective of this research is to develop a reliable damage detection and localization tool by combining NDT thermography data with FE modeling. As the amount of experimental data is very high and depending on the resolution of the IR camera, the goal is to use modeling in assistance of the NDT tests in order to gain accuracy and time-efficiency. Different experimental and numerical cases and measurement setups will be discussed.

KEYWORDS: Finite element modeling, infrared thermography, dynamic line scan, optimization, Composite Material, Defects

1. INTRODUCTION

Active thermography is internationally recognized as a fast and efficient way to detect defects in glued materials in a time span of a few minutes. Unfortunately, the correct implementation and interpretation of this methodology requires a great deal of experience, which is hardly present in Flanders to date. As a result, the implementation in the Flemish industry is considered to be very risky and too expensive. People excel in qualitative detection of deviations, but computers are more accurate to effectively measure them. But for experiments and computer simulations to work together, accurate correlation between model and experiment is the greatest concern. This project aims to make quantitative thermal measurements accessible to the industry and demonstrate the added value of linking them to numerical simulations. The questions come from a broad real target group ranging from bonding in the wood industry (+/- 31 companies in Belgium) to quality control of solar panels after damage (+/- 200 in Flanders), structural plastic composite producers in the aerospace sector (+/- 50 in Flanders), sterile blister packs (+/- 10) in the medical sector and sealing manufacturers (+/-5). All these sectors have the delamination problem as a common denominator in which an inspection solution is the primary objective of this project.

2. CONCRETE PROJECT GOALS

The SINT project aims to meet the demand for a fast, efficient and reliable inspection technique to detect delamination in complex materials during production.
1. Delivery of a validated, generic decision tree that allows an independent implementation of active thermography in product inspection. (KPI2: at least 5 validations in 5 different sectors in collaboration with students via master's theses).
2. Hands-on guide to perform accurate thermal-mechanical numerical simulations. (KPI2: 3 different validated simulation models for different sectors, in collaboration with students via projects)
3. Automatic detection of delamination by thermography based on an updated numerical model, how fast is this possible in a production process? Target 20m/min (KPI2+4)
5. Parameter determination for setup optimization of product inspection set-ups based on numerical model updating. (KPI4)

2.1 EXPECTED RESULTS AND IMPACT

The expected results are different for the different target groups. The target group is divided into different types of operation: 1) continuous inspection of production for delamination; 2) 100% piece inspection for high-risk products and 3) event-based batch inspection after e.g. hail damage or production error. For the three different groups, different implementation strategies and guidelines are developed, which are supported by validation measurements. The expected results:

1) Continuous inspection: Reduction of waste due to delamination from 5% to <1% total production (Ref Unilin) after implementation (possibly shortly after the end of the project).

2) 100% piece inspection: Scan time reduction of about 400% + automatic inspection 1 year after project completion (Ref. Sonaca: 40min Ultrasonic examination -> 10min active thermography for 1m2).

3) Event-based inspection: Solar panels inspection after hail damage (ref: Futech: now 2 man days inspection + complete disassembly and transport to the workshop of the site reduce to approximately 4 hours automatic in-situ inspection which is more weather independent). (2 years after the project expires on the market).
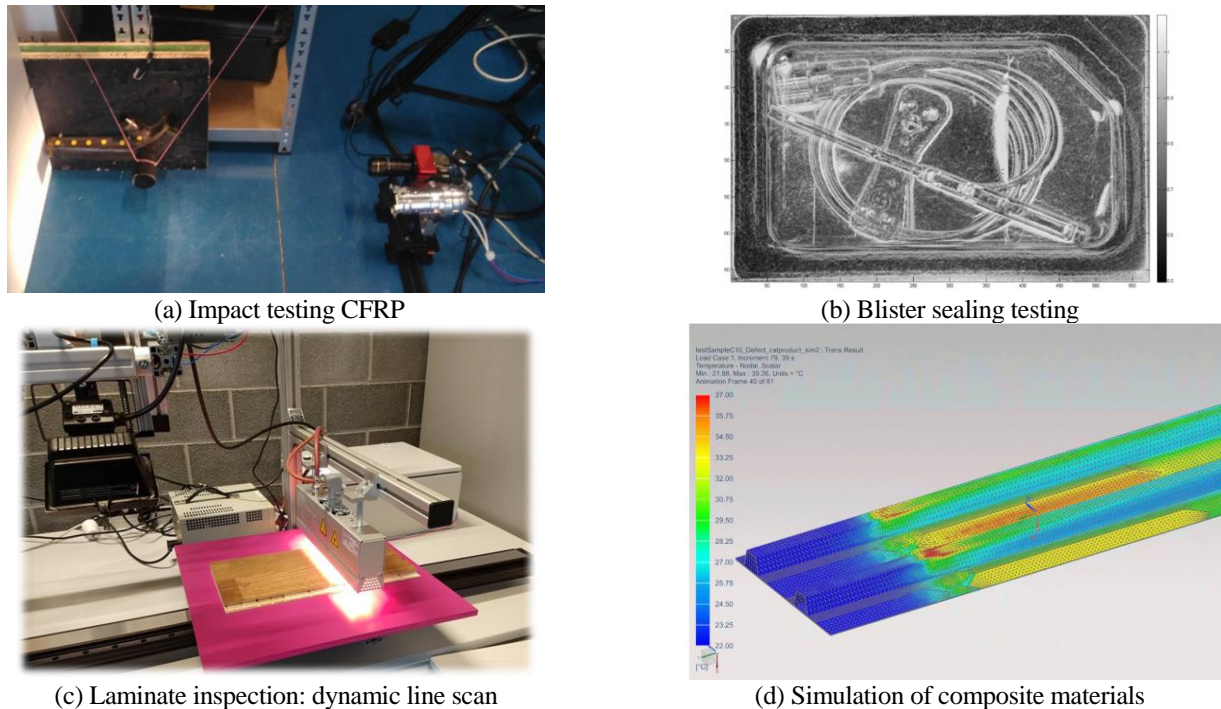

(a) Impact testing CFRP

(b) Blister sealing testing

(c) Laminate inspection: dynamic line scan

(d) Simulation of composite materials

Fig. 1 Different measurement setups and FE simulations developed during the project.

3. CONCLUSION

In this paper, the results of the SINT-project will be presented and discussed, ranging from active infrared thermography to mobile inspection assisted by numerical modeling for improved accuracy and decreasing measurement times. The listed applications are: visualizing damage during impact testing of composite CFRP frames, inspection of blister sealing, laminate inspection and inspection of welds. The different measurement parameters are optimized and automatic detection delamination by thermography based on updated numerical model is performed. Finally, a hands-on guide for thermal-mechanical numerical simulations is assembled by the authors.

ACKNOWLEDGMENT

REFERENCES

[1]   G. Steenackers, J. Peeters, B. Ribbens, and C. Vuye, "Development of an Equivalent Composite Honeycomb Model: A Finite Element Study," *Appl. Compos. Mater.*, vol. 23, no. 6, pp. 1177–1194, 2016.

[2]   G. Steenackers, J. Peeters, S. Verspeek, and B. Ribbens, "From Thermal Inspection to Updating a Numerical Model of a Race Bicycle: Comparison with Structural Dynamics Approach," *Appl. Sci.*, vol. 8, no. 2, p. 307, Feb. 2018.

[3]   J. Peeters, S. Verspeek, S. Sels, B. Bogaerts, and G. Steenackers, "Optimised dynamic line scanning thermography for aircraft structures," in *Quantitative infrared thermography*, 2018, pp. 1–9.

«Next Generation NDT - An Enabling Technology for the Factory of the Future»

Prof. Dr.-Ing. Ahmad Osman
Leader of the Group 3D-AutomaTiQ, IZFP
Topics coordinator algorithms and data processing
Department Component Inspections
Fraunhofer Institute for Nondestructive Testing - IZFP, Saarbruecken (Germany)

presented live on ZOOM at 10 am 25 Nov. 2020

MONITORING CULTURAL HERITAGE OBJECTS USING LASER AND OPTICAL 3D SCANNING

V. A. Parfenov
St.Petersburg Electrotechnical University,
Prof. Popova str., 5, Saint-Petersburg, 197376, Russia

The paper presents the results of experimental works devoted to the investigation of the possibility of applying 3D scanning technology for monitoring the state of preservation of historical and cultural monuments. Artifacts of history and culture, regardless of whether they are exhibited (in the open air or stored in museum collections), are gradually destroyed over time. This happens under the influence of adverse environmental factors, whose impact has increased significantly in recent decades due to a dramatic environmental deterioration. In this situation, regular monitoring of the state of conservation of artworks is becoming an increasingly urgent task in the field of preserving cultural heritage.

There were two objects of our study. Among are the marble sculpture of the mourner at the monument to A. Ya. Okhotnikov in the Necropolis of the XVIII century of the Alexander Nevsky Monastery in St. Petersburg and oil painting "Equestrian artillery company No. 13 barrages French columns during the retreat of the "great army" from Russia" (created by Russian artist P. Karyagin in 1912) with collection of the Military-Historical Museum of Artillery, Engineer and Signal Corps in St. Petersburg.

For scanning of the marble sculpture, laser triangular-type Konica Minolta Vi-9i scanner was used, which ensures the accuracy of measurements of the relief of the investigated surface at a level of 50-100 μm. The sculpture was scanned twice: before and after the completion of planned works for its restoration, which allowed modeling the change in the microrelief of its surface..

The painting was scanned using an optical 3D scanner Cronos 3D. The choice of this painting as an object of study was connected with that fact its surface has a complex relief. This artist is characterized by the "volumetric" style of painting technique, which is manifested in the application of the paint layer by separate textured strokes of different thickness and width. It allows one to easily capture the 3D relief of the painting's surface and track the changes of the paint layer's state as the relief changes during the reference time interval.

It should be noted that importance of monitoring the paintings is connected the fact that defects in the paint layer usually occur at the "micro level", and it is very difficult to detect them in a timely manner using photography (including high resolution one), which is traditionally used in museums to monitor the state of paintings. The scanning was carried out 2 times with time interval of 4.5 years. In

both cases we created computing 3D models of the same paintings, which then were matched and compared using specialized computing software that gave information about changes of the paintings.

Our studies have shown that both laser and optical 3D scanning can be recommended for practical museum work as a highly accurate and informative method of monitoring artworks. One of the most accurate criteria for changing the state of preservation of sculptural monuments as a result of this type of monitoring is the determination of the area of destruction of their surface. Another criterion by which it is also possible to assess the degree of destruction of the monument during the control interval of time is the length of cracks and chips on its surface. In case of painting this approach to monitoring the artworks allows one to control the state of the surface of the painted layer as well as the wooden frame with high accuracy (fractions of a millimeter). Such information can be useful for the conservators of paintings to decide on the need to change the conditions of storage and exposure of paintings.

CORRELATION-BASED ULTRASOUND IMAGING IN NDT AND SHM

Patrice Masson[1*], Nicolas Quaegebeur[1]

[1]GAUS, Dept Génie mécanique, Université de Sherbrooke, Sherbrooke (QC) J1K 2R1, Canada

[*]Corresponding Author: Patrice.Masson@USherbrooke.ca

ABSTRACT

Ultrasound imaging is implemented either with bulk waves using phased-array (PA) transducers in classical Non-Destructive Testing (NDT) techniques, or with guided waves using compact or distributed arrays of *in situ* bonded transducers in Structural Health Monitoring (SHM). However, due to limitations of ultrasound-based NDT or SHM methods in terms of contrast, resolution and penetration depth, the characterization of precursor damage in structures such as composites is still challenging. High-performance damage imaging techniques based on the Full Matrix Capture (FMC) technique, such as Total Focusing Method (TFM), can now be implemented in portable Graphics Processing Units (GPU). This work discusses advanced super-resolution signal processing algorithms such as multi-modal plane wave imaging, phase coherence imaging, and correlation-based imaging. The latter imaging approach implements the correlation of measured signals with theoretical propagated signals computed over a given grid of points. The technique considers transducer directivity and dynamics, and also the refraction and transmission at the interface between the wedge and the host structure, such that the number of required array elements for a given imaging performance can be greatly reduced. Simulation and experimental results in NDT demonstrate that the correlation-based imaging approach offers better separation between scatterers with the same number of transducers, or similar separation with a much lower number of transducers Simulation and experimental results in SHM demonstrate that the correlation-based imaging approach offers better resolution and increased robustness for damage localization in metallic and composite structures.

KEYWORDS: Ultrasound imaging, correlation-based imaging, phased-array transducers, damage localization.

1. INTRODUCTION

The Non-Destructive Testing (NDT) and Structural Health Monitoring (SHM) industries are still defining a framework for the use of high-performance damage imaging based on Full Matrix Capture (FMC) technique, such as Total Focusing Method (TFM). The advent of Graphics Processing Units (GPU) now enables the implementation of super-resolution signal processing algorithms such as multi-modal plane wave imaging [1] or phase coherence imaging [2]. The correlation-based algorithm *Excitelet* allows super-resolution imaging at much lower frequencies as compared to conventional NDT or SHM techniques. *Excitelet* inherently considers a detailed model of the full wave propagation path, with the transducer dynamics and the coupling interfaces.

2. CORRELATION-BASED IMAGING

The *Excitelet* imaging approach has been first derived in the case of guided wave inspection in SHM using compact or sparse transducer arrays [3], extended to bulk wave inspection of isotropic structures using contact probes [4] and to the case of inspection using an angle wedge. The approach is based on the correlation between measured signals extracted from FMC and theoretical predictions. For each point of a defined grid on the inspected structure, theoretical pitch-catch signals $\mathbf{T}_{AS}(x_o, y_o, t)$ are pre-computed using Spatial Impulse Response (SIR) method and stored in memory in order to be correlated with real-time acquired signals $\mathbf{M}_{AS}(t)$. Eq. 1 presents the correlation coefficient calculated for each pixel and used to plot the image.

$$\mathbf{C}_{AS}(x_o, y_o) = \int_0^{+\infty} \mathbf{M}_{AS}(t)\ \mathbf{T}_{AS}(x_o, y_o, t)dt \tag{1}$$

2.1 ASSESSMENT IN NDT

The *Excitelet* imaging approach has been validated experimentally for the imaging of holes with P waves, first in direct contact on an aluminum block of dimensions 200 x 100 x 50 mm, and then through a wedge on a carbon steel block of dimensions 210 x 150 x 30 mm. Imaging results obtained using *Excitelet* and presented in Fig. 1 illustrate the effect of varying the number N of transducer elements used, when compared with the standard TFM.
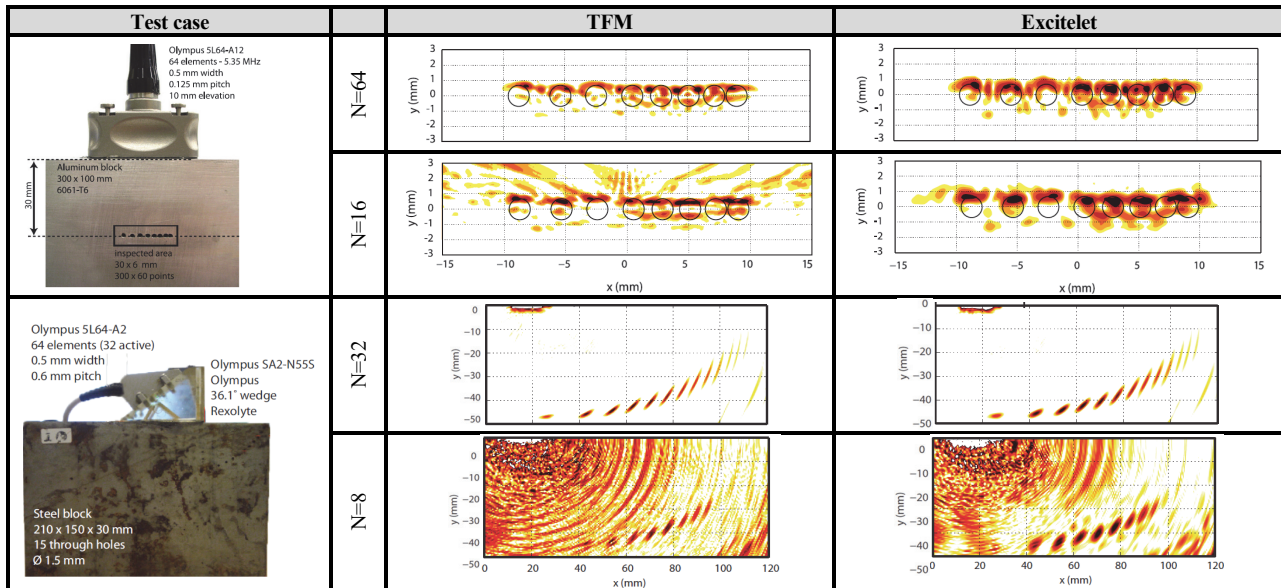
Fig. 1 Test cases for hole imaging in NDT, with TFM and *Excitelet*, and with varying number N of transducer elements.

2.2 ASSESSMENT IN SHM

The *Excitelet* imaging approach has also been validated for the imaging of defects on plates with guided waves. Imaging results presented in Fig. 2 illustrate the simulated defect localization performance of *Excitelet* on a unidirectional composite structure, when compared with a standard delay-and-sum (DAS) approach.
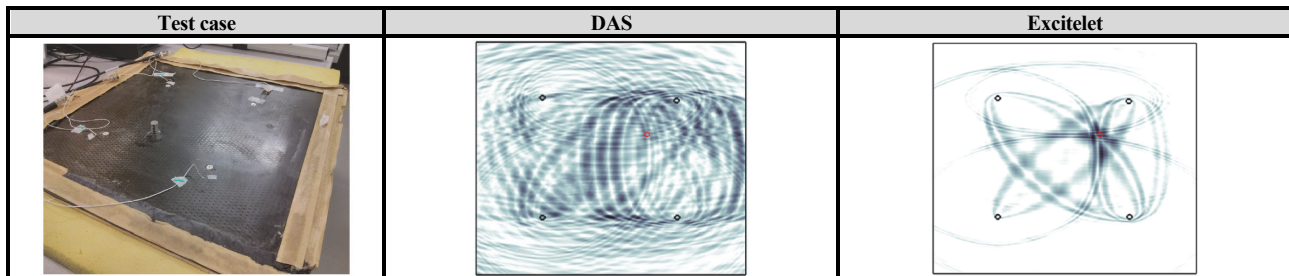

Fig. 2 Test case for simulated defect (red circle) localization on unidirectional composite in SHM, with DAS and *Excitelet*.

3. CONCLUSIONS

The correlation-based imaging approach *Excitelet* inherently considers transducer directivity and dynamics, and also allows for compensating diffraction, refraction and dispersion in the wave propagation path. The approach has been implemented in NDT and SHM applications and benchmarked against standard approaches. NDT assessment has shown that *Excitelet* allows to greatly reduce the number of required transducers without loss of imaging quality. SHM assessment has demonstrated that the approach can be tailored to the application, for example by considering non-isotropic propagation in plate structures.

ACKNOWLEDGMENT

REFERENCES

[1]   Le Jeune, L., Robert, S., Lopez Villaverde, E., Prada, C., "Plane wave imaging…", *Ultrasonics*, 64, 128-138, 2016.
[2]   Camacho, J., Parrilla, M., Fritsch, C., "Phase coherence imaging", *IEEE Trans. Ultrason. Ferroelectr. Freq. Control,* 56(5), 958-974, 2009.
[3]   Quaegebeur, N., Masson, P., Langlois-Demers, D., Micheau, P., "Dispersion-based imaging…", *Smart Mater. Struct.*, 20, 12p., 2011.
[4]   Quaegebeur, N., Masson, P., "Correlation-based imaging technique using ultrasonic…", *Ultrasonics*, 58(2), 1056-1064, 2012.

Papers

(in paper n° order)

DEFECT DEPTH ESTIMATION IN INFRARED THERMOGRAPHY WITH DEEP LEARNING

Qiang. Fang[* 1], Farima. Abdolahi. Mamoudan[1], Celment. Ibarra. Castanedo[1], Xavier. Maldague[1]

[1] Computer Vision and Systems Laboratory, Department of Electrical and Computer Engineering, Université Laval, 1065, av. de la Médecine, Québec (QC), Canada, G1V 0A6

[*]Corresponding Author: qiang.fang.1@ulaval.ca

ABSTRACT

Infrared thermography has already been proven to be a significant method in non-destructive evaluation since it gives information with immediacy, rapidity, and low cost. However, the thorniest issue for the wider application of IRT is quantification. In this work, we proposed a specific depth quantifying technique by employing the Gated Recurrent Units (GRUs) in composite material samples via pulsed thermography (PT). Finite Element Method (FEM) modeling provides the economic examination of the response pulsed thermography. In this work, Carbon Fiber Reinforced Polymer (CFRP) specimens embedded with flat bottom holes are stimulated by a FEM modeling (COMSOL) with precisely controlled depth and geometrics of the defects. The GRU model automatically quantified the depth of defects presented in the stimulated CFRP material. The proposed method evaluated the accuracy and performance of synthetic CFRP data from FEM for defect depth predictions.

KEYWORDS: NDT Methods; Defects depth estimation; Deep learning; Pulsed thermography; Gated Recurrent Units

1. INTRODUCTION

Non-destructive evaluation (NDE) has emerged as an important method for the evaluation of the properties of components or systems without damaging their structure. Several state of the arts methodologies such as Pulsed Phase Thermography (PPT) [1], Principal Component Thermography (PCT) [2], Differential of Absolute Contrast5 (DAC) [3], Thermographic Signal Reconstruction (TSR) [4], as well as Candid Covariance Free Incremental Principal Component Thermography [5], have been implemented to process thermographic sequences and improve the defect visibility. These techniques can be beneficial for qualitative analysis of composite materials. However, to introduce a method for conducting quantitative study (defect depth estimation) with deep learning is a novel topic to be explored.

Quantitative analysis is playing an important role in the modern industrial field of non-destructive testing (NDT). Defect characterization is one of the current topics of interest in quantitative data analysis of active thermography. In this topic, thermographic information involves extracting quantitative subsurface properties from defects such as defect depth, lateral size, thermal resistivity, from an experimental Thermal Non-destructive Testing (TNDT) dataset utilized to characterize defects. Several approaches have already been proposed to analyze the depth in the region of defects in pulsed thermography. In general, these approaches evaluate the defects depth by using the maximum thermal contrast C_max, the instant of maximum thermal contrast Tc_max or artificial neural networks to analyze the depth of defects based on mathematical equations. The Peak Temperature Contrast Method [6] estimated the depth based on the characteristic time from peak contrast. The peak contrast corresponding to the maximum contrast has a proportional correlation with the square of the defect depth. Daribi et al. [7] proposed neural networks for defect characterization of defect depth. The results demonstrated that the networks should be trained by representative and non-redundant data in order to obtain a high degree of classification accuracy.

In this work, there is an attempt to detect the depth of defects in Carbon Fiber Reinforced Polymer (CFRP) via Gated Recurrent Units (GRUs) [8]. GRU is an updated recurrent neural network (RNN) particularly designed for time series prediction. GRU can be considered as a variation of Long Short-Term Memory (LSTM) [9]. Compared with the LSTM and RNN temporal model, the

GRU has adapted a few learning parameters which could save computational expenses for training and obtained an excellent performance. According to our knowledge, this is the first time that the thermal temporal characteristic model (GRU; RNN; LSTM etc.) is used to qualify the depth of defects.

We modeled a 3D version of CFRP specimen stimulation from COMSOL. Then, it was further tested on the systemic data by the GRU model to validate its accuracy. The remainder of this paper is structured as follows: Section 2 provides the pulsed thermography theory and conception indication, as well as the detailed characteristics of FEM simulations. Section 3 proposed a GRU model-based defects depth estimation strategy and introduces the GRU deep learning model architectures. Section 4 provides the experimental results analysis. Section 5 concludes this paper.

2. THERMAL CONSIDERATION AND FEM SIMULATIONS

2.1 PULSE THERMOGRAPHY

In pulsed thermography (PT), a high-power exponential heating impulse is applied to the samples, and a thermal response is measured during a period of time. Due to the heat conduction, a surface region which has an internal defect underneath the surface perturbs the thermal waves propagation on the surface of specimens in comparison to the sound (non-defective) region. We can then see the changes of the temperature variation, since the internal defects possess different thermo-physical (conductivity, density and heat capacity) that have an impact on heat flow. These thermal differences can be observed as surface features and recorded with an infrared camera as indicated in Figure 1 [10].

Temporal evolutions can be observed from the defective regions and subsurface sound regions. A thermal contrast is acquired as a feature vector which is obtained distinctly via the thermal value from the defective region subtracted from the corresponding value from the surrounding sound region [11] as indicated in Equation (1), where Td(t) is the temperature value on the pixel point of the defect area. The temperature value on the reference point of the sound area is T_s(t). Then the ΔT(t) is the absolute thermal contrast extracted from the defect and sound region. The thermal contrast is an excellent technique to distinguish the temperature difference to learn the depth of the defects, as shown in Figure 1.
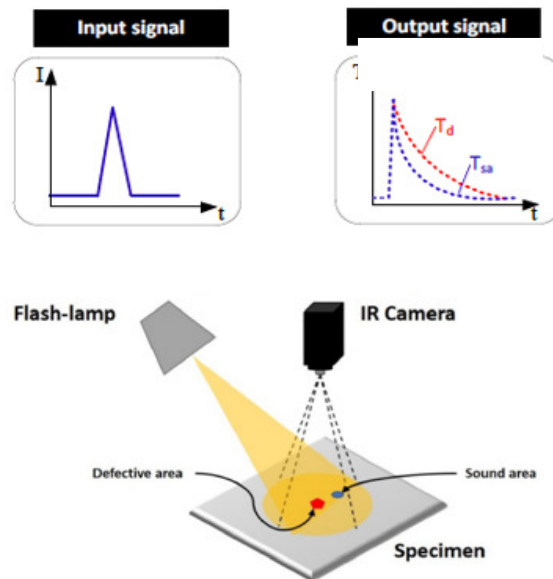
$$\Delta T(t) = T_d(t) - T_s(t) \qquad (1)$$

Figure 1. Pulsed thermographic testing using optical excitation.

2.2 FINITE ELEMENT MODELLING WITH TRANSIENT HEAT TRANSFER

Finite Element Modelling (FEM: COMSOL, etc.) [12] has become an important and economical platform to evaluate the thermal response of pulsed thermography, which builds up models for the platform of components that allow us to flexibly examine all specific physical aspects of thermal data such as geometries and properties of materials. Simulated thermograms matched well with experimental data.

In this work, COMSOL will be utilized as a 3D based simulation to build up models for the synthetic data to provide for depth estimation of artificial defects. A Carbon Fiber Reinforced Polymer (CFRP) structure-based specimen containing artificial defects of different shapes (flat-bottom holes) is modeled as shown in Figure 2. A high thermal pulse is projected on the surface of specimens. Due to the existence of the temperature gradients in the sample, a thermal front propagates from the high temperature region on the surface to the region underneath. A delamination or discontinuities create a lower thermal diffusion rate to the heat flow and then reflect the unnormal thermal patterns on the surface. The COMSOL software is utilized as the heat transfer simulation model for obtaining the temperature evaluations of the surface of each sample, as indicated below [13]:

$$\rho C_P \left(\frac{\partial T}{\partial t}\right) - \nabla \cdot (k \nabla T) = 0 \tag{2}$$

$$\frac{\partial}{\partial x}\left(w_x \frac{\partial T}{\partial x}\right) + \frac{\partial}{\partial y}\left(w_y \frac{\partial T}{\partial y}\right) + \frac{\partial}{\partial z}\left(w_z \frac{\partial T}{\partial z}\right) = \rho C_P \frac{\partial T}{\partial t} \tag{3}$$

$$n \cdot (w \cdot \nabla T) = h_{conv}(T_{amb} - T) + \sigma_{Tc}\varepsilon(T_{amb}^4 - T^4) \tag{4}$$

where in Equations (2)– (4), the density is $\rho(\frac{kg}{m^3})$, constant specific heat is $c_\rho(\frac{J}{kg.m})$, and the absolute temperature is T(K). Time variable is set as t(s). A rectangular coordinate system (x, y, z) as in Equation (3) in anisotropic media can lead to numerous possible solutions. w, w_x, w_y, w_z ($\frac{w}{m}.K$) are the main conductivity rates and conductivity rates which respectively for three coordinates (x, y, z) in 3D thermal modeling. The convection heat transfer is given by h_{conv} ($\frac{w}{m^2 k}$). In Equation (4), a boundary condition that regarding to the thermal heat transfer from radiation and convection between the all the specimen surfaces and the ambient temperature has been indicated, where T_{amb} is an initial environment temperature which consider all the external environment as the same temperature; $\sigma_{Tc}(\frac{w}{m^2 k^4})$ is the Stefan–Boltzmann physical constant which links the temperature with energy; ε represents surface emissivity.

Table 1 briefly illustrates the physical properties of CFRP specimens and pulsed thermography parameters involved in the COMSOL simulation in this experiment. All properties and parameters in Table 1 are cited from the literature [14]. Table 2 and Table 3 provide the description of defect characteristics. Each row in every CFRP samples has the same depth of defect, which included 22 different constant values from 0.5 to 2.2 to be set from the first row in training sample 1 to the last row in the training sample 6. We extracted 5 vectors from each defect region for GRU model training with depth estimation. The testing group has 4 CFRP samples (30×30). In order to differ from training samples, the testing group consists of samples A, B, C, D. The defects in the test samples range from [0.5, 2.2] but have a size differs from that of the training samples. The CFRP geometrics of the structure of training sample 1 is stimulated based on Figure 2.
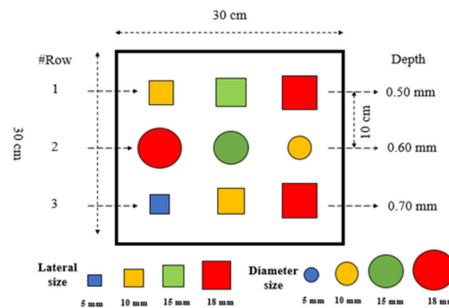

Figure 2. Representative CFRP training sample 1 configuration

Sign	Parameters in experimental simulation	Real value
ρ	Material density	$1500 \frac{kg}{m^3}$
ε	Emissivity	0.90
C_P	Constant specific heating	$1000 \frac{J}{kg.m}$
L	Specimen length	300mm
W	Specimen width	300mm
H	Specimen height	5mm
t_{end}	End time	9s
T_n	The temperature from initialization	293.15k
T_{amb}	The temperature from ambient	293.15k

Table 1 Physical properties and parameters of stimulation

Sample	Row	Depth(mm)	Shape	Defect Size (mm)
1	1	0.5 mm	Quadrangle	Size = 10; 15; 18
	2	0.6 mm	Round	Diameter = 18; 15; 5
	3	0.7 mm	Quadrangle	Size = 5; 10; 18
2	1	0.8 mm	Quadrangle	Size = 5; 10; 15
	2	0.9 mm	Round	Diameter = 18; 15; 10
	3	1.0 mm	Quadrangle	Size = 5; 15; 18
3	1	1.1 mm	Quadrangle	Size = 5; 10; 18
	2	1.2 mm	Round	Diameter = 15; 10; 5
	3	1.3 mm	Quadrangle	Size = 10; 15; 18
4	1	1.4 mm	Round	Size = 5; 15; 18
	2	1.5 mm	Quadrangle	Diameter = 18;10; 5
	3	1.6 mm	Round	Size = 5; 10; 15
5	1	1.7 mm	Round	Diameter = 10; 15; 18
	2	1.8 mm	Quadrangle	Size = 18; 15; 5
	3	1.9 mm	Round	Diameter = 5; 10; 18
6	1	2.0 mm	Round	Diameter = 5; 10 ;15
	2	2.1 mm	Quadrangle	Size = 18; 15;10
	3	2.2 mm	Round	Diameter = 5 ;15 ;18

Table 2 Defect characteristics of training samples

Sample	row#	Depth (Left; Middle; Right)	Shape	Defect Size (Left; Middle; Right) (mm)
A	1	Depth = 0.5; 0.8; 1.1	Quadrangle	Size = 3 ;16 ;13
	2	Depth = 0.6; 0.9; 1.2	Round	Diameter = 8; 3; 16
	3	Depth = 0.7; 1.0; 1.3	Quadrangle	Size = 13; 8; 16
B	1	Depth = 1.4; 1.7; 2.0	Quadrangle	Size = 8; 3; 16
	2	Depth = 1.5; 1.8; 2.1	Round	Diameter = 13; 8; 3
	3	Depth = 1.6; 1.9; 2.2	Quadrangle	Size = 16; 13; 8
C	1	Depth = 0.5; 0.8; 1.1	Round	Size = 4; 17; 14
	2	Depth = 0.6; 0.9; 1.2	Quadrangle	Diameter = 9; 4; 17
	3	Depth = 0.7; 1.0; 1.3	Round	Size = 14; 9; 4
D	1	Depth = 1.4; 1.7; 2.0	Round	Size = 9; 4; 17
	2	Depth = 1.5; 1.8; 2.1	Quadrangle	Diameter = 14;9;4
	3	Depth = 1.6; 1.9; 2.2	Round	Size = 17; 14; 9

Table 3 Defect characteristics of testing samples

2.3 TEMPERATURE AND THERMAL CONTRAST CURVES

In transient thermography, previous researchers [6] concluded that the time of maximum contrast ΔT that corresponds to the maximum contrast ΔT in the temperature contrast curves has an approximately proportional relationship with the square of the depth of the defect (d^2). Simultaneously, the proportionality coefficient of this relationship rested with the lateral size of the depth: the smaller the defects, the lower maximum contrast ΔT and earlier peak time. As indicated in Figure 3, an interesting case is highlighted. We observed the temperature evaluation of three defects of the same size (18 ×18) but different depth such as (0.5 mm,1.0 mm,1.5 mm). Although the three defects have the same shape, it can be demonstrated that the shallower the defect, the higher the peak temperature value which can be obtained.

In Figure 4, a corresponding synthetic thermogram frame for training sample 2 in t=15s generated from COMSOL is indicated at (a); Nine artificial flat bottom (b) flat-bottom-holes were embedded with different depths in the shapes of either circles or squares. In Figure 5, the data distribution of the thermal contrast curves is illustrated. Five contrast vectors have been extracted above each defect region on the surface from the different points in the defects (upper left; upper right; center; lower right; lower left; lower right) to reduce the inaccurate influences caused by the small temperature variation. Notice that, all the training sequences to be processed in this work are extracted from the first 1409 frames of a whole 2000 frames thermal sequence in total (including the information of peak thermal contrast $\Delta Tmax$ and corresponding t_max.) As a result, the last 581 frames of thermal curves were not extracted in this work which would show a dramatic decrease of the thermal contrasts in the graphs. This partial extraction in COMSOL saves the computational expense for the training in GRU to some extent.
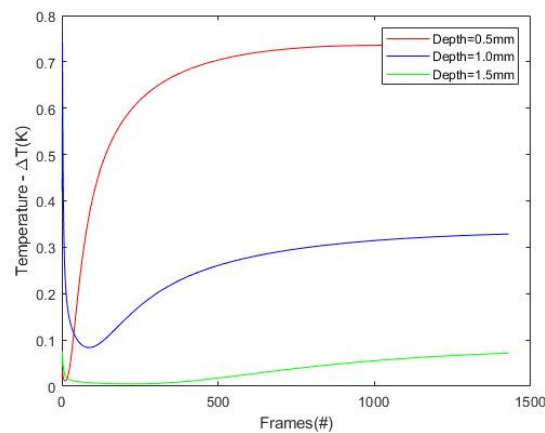

Figure 3. Temperature contrast evaluation for defects located at different depths with the same size (0.5mm; 1.0mm; 1.5mm) in training samples
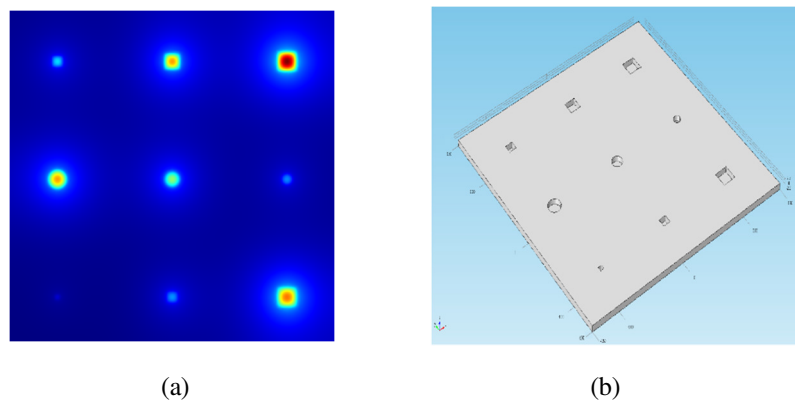

(a)   (b)

Figure 4. The corresponding synthetic colorful thermograms (a) in t=15s; (b) Geometrics distribution in training samples 1
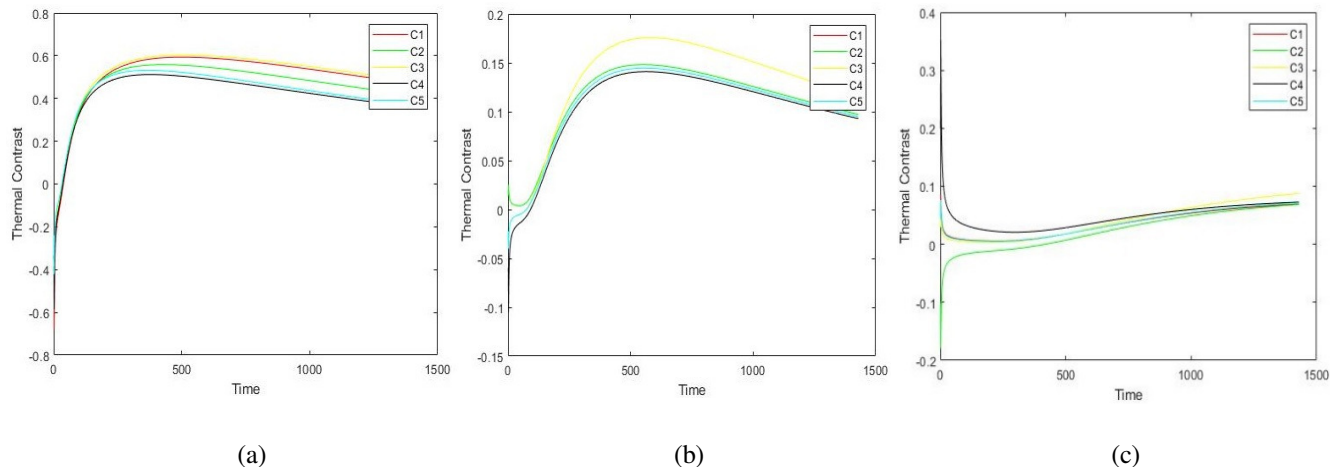
(a)   (b)   (c)

Figure 5. Data distribution of temperature contrast evaluation for different depths in training samples (a) 0.5mm; (b)1.0 mm; (c) 1.5mm
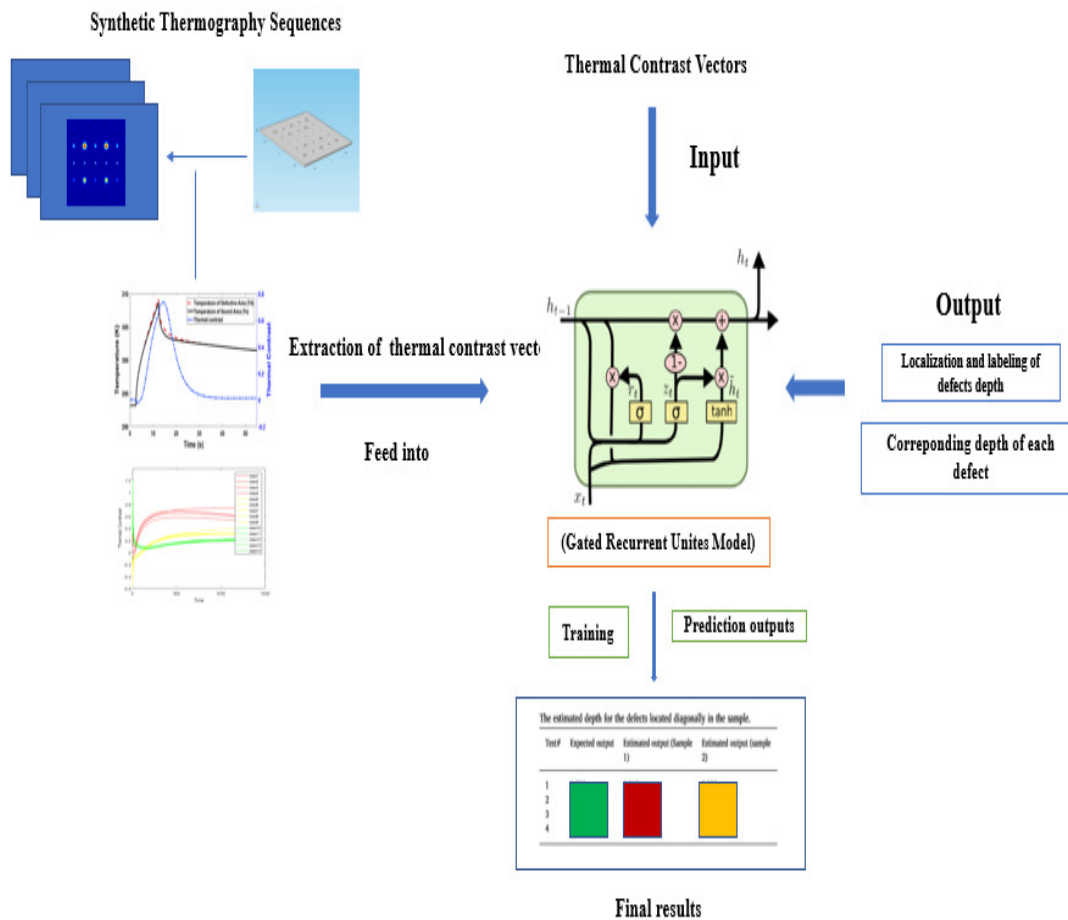

Figure 6. GRU model-based defects depth estimation strategy

3. PROPOSED STRATEGY FOR DEFECTS DEPTH ESTIMATION

In this section, a defect depth estimation strategy has been proposed to detect and identify the depth of each defect in thermal images as indicated in Figure 6. This design of detection system originated from the GRU neural network. The infrared thermal module and simulations are provided by COMSOL (FEM simulation) to examine the depth of defects in pulsed thermography (PT). First, the synthetic thermal sequences are acquired from FEM (COMSOL) based on the heat transfer modeling in FEM. Then, several thermal contrast feature vectors are extracted from each defect region to feed into the input of GRU. The output of GRU consists of a unique node which estimated the depth during the training. The mean absolute error is chosen as the loss function with the GRU model in the equation as below Equation (5). In the end, the predicted depth output from the GRU is based on the feature extraction of thermal contrast vectors.

$$L_{cost} = \frac{\sum_{i=1}^{m}(y-\hat{y})^2}{m} \tag{5}$$

The GRU takes each vector at a time point in the input. This learning model was trained for 2500 epochs of each process. The training loss converged to the optimistic value and then flattened. In addition, the number of training curves (batch size) is set m. $y, \hat{y}$ are the ground truth and estimated depth respectively.
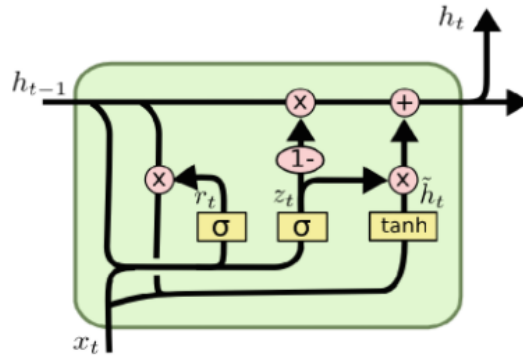

Figure 7. Gated Recurrent Unite

3.1 GATED RECUR1RENT UNITS MODEL WITH DEPTH ESTIMATOR

Due to the time continuity of the thermal sequence, each frame collected from the experiment is related to the recent historical frame; therefore, the time series memory deep learning model can be applied to the thermography data based on this feature. The GRU model is originally from RNN which is a time series model can handle the continuous information like thermal sequences [15]. During the cooling period of the thermal data, the temperature evaluation curves over time are acquired from the given infrared frames. The Learned GRU model is able to distinguish whether the pixel from a defective region or a sound region due to the training period. Therefore, the multiple units of GRU could be applied to extract the features of the temperature evaluations from the samples based on physical properties.

The GRU neural network in Figure 7 are structured as follows [16]. In equations (6)-(9), R_t, Z_t represent the update, reset gate units respectively. $S^{(z)}, S^{(r)}, S$ are the weight factors for each gate unit. x_t is the current input. h_{t-1} is the input from the previous time step in the hidden state. h'_t is the input of current memory from the hidden state. $U^{(z)}, U^{(r)}, U_o$ are the weight factors for previous time information h_{t-1}. $\delta(.)$ represents the sigmoid function. ° is denoted as the Hadamard product. [17]

$$Z_t = \delta\left(S^{(z)}(x_t) + U^{(z)}(h_{t-1})\right) \tag{6}$$

$$R_t = \delta\left(S^{(r)}(x_t) + U^{(r)}(h_{t-1})\right) \tag{7}$$

$$h'_t = tanh\left(S(z_t) + R_t°U_o(h_{t-1})\right) \tag{8}$$

$$h_t = Z_t°tanh + (1 - Z_t)° \, h'_t \tag{9}$$

As shown in Figure 8, in this work, the original thermal sequences were reshaped into vectors. The particular thermal contrast vectors are directly fed into the input of the GRU network structure. Each thermal contrast vector in the defect region is decoded with the depth value of corresponding defect at the output of GRU based on the thermal properties from the training sequences. In order to select the points for the simulated thermal sequences to extract temperature curves vectors, 5 different locations inside each defect surface in these defective areas were selected. Since the temperature of the defect region is not even, these selected points accounted for small temperature variations and change above each defect surface region. Each thermal contrast vector is vectorized with the same length in the time of the thermal sequence. Therefore, the input values of GRU are fed into the particular thermal contrast vectors. The output from the decode section (to be connected with the fully connected layer) are set with the corresponding defect depth of each vector. The estimated depth values in the defect region output from GRU are based on the thermal properties from the training sequences.
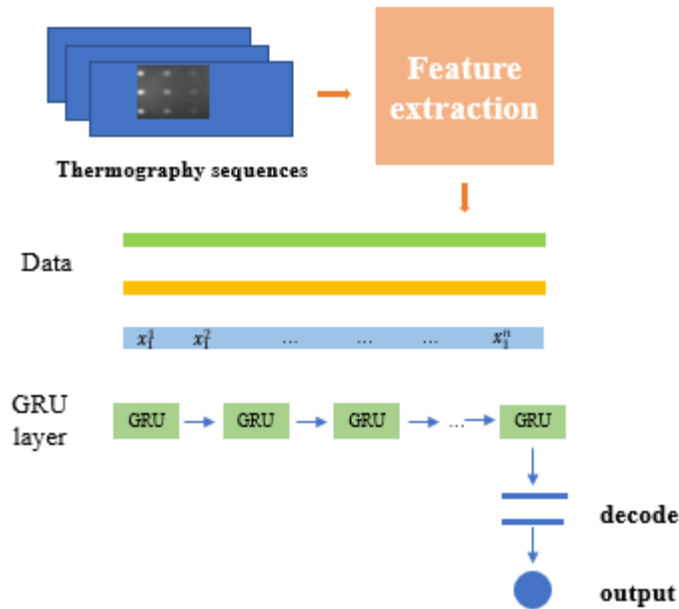

Figure 8. The process of GRU depth estimation

4 EXPERIMENTAL VALIDATION AND RESULTS

4.1 INFERENCE AND TRAINING

In this research, the training processing on GPU (NVIDIA GeForce GTX 1080Ti) took about 30 min. The operating system was set as: Ubuntu 14. 04. CPU: i7-5930k. Memory: 64 GB. Adam was introduced as optimizer.
The whole training process was also conducted using the Adam optimization. Some main hyper parameters and training parameters are set as below: weight decay 0.0001, the learning rate 0.001 and learning momentum 0.9. In this work, the temperature variety and contrast reflect on each vector. Therefore, the GRU time step was set to 1429 (1429 frames as a time step as input).

4.2. DATA PROCESSING

To reducing the overfitting issue, the cross-validation verification method is proposed in this study. First, we collected 270 thermal contrast curves from the simulation data (5 thermal contrast curves extracted from each defect averagely). Then, we shuffled all of the data and spilt 80% of the data to train with GRU model, while 20% was utilized to validate the performance of the GRU.

All obtained training data (the thermal contrast evaluation curves) is normalized and truncated as a fixed length of duration. Simultaneously, the input data is normalized by subtracting from the mean value of the thermal curves (μ_{T_c}) and dividing by the standard deviation of the thermal contrast (σ_{T_c}) using Eq. (10).

$$\widehat{T_{c,n}^i}(t) = \frac{\widehat{T_c}(t) - \mu_{T_c}}{\sigma_{T_c}} \tag{10}$$

4.3 DEPTH ESTIMAPTION RESULTS AND VALIDATION

Sample	Expected Output (mm)	Estimated Output 1 (mm)	MAE1 * (mm)	Estimated Output 2 (mm)	MAE2* (mm)
A C	0.5	0.522	0.022	0.507	0.007
A C	0.6	0.604	0.004	0.603	0.003
A C	0.7	0.708	0.008	0.706	0.006
A C	0.8	0.814	0.014	0.807	0.007
A C	0.9	0.912	0.012	0.913	0.013
A C	1.0	1.041	0.041	1.025	0.025
A C	1.1	1.109	0.009	1.011	0.011
A C	1.2	1.222	0.022	1.218	0.018
A C	1.3	1.318	0.018	1.314	0.014
B D	1.4	1.420	0.020	1.418	0.018
B D	1.5	1.514	0.014	1.509	0.009
B D	1.6	1.630	0.030	1.619	0.019
B D	1.7	1.718	0.018	1.715	0.015
B D	1.8	1.820	0.020	1.817	0.017
B D	1.9	1.918	0.018	1.920	0.020
B D	2.0	2.013	0.013	2.005	0.005
B D	2.1	2.112	0.012	2.010	0.010
B D	2.2	2.225	0.025	2.222	0.022

Table 4 The results of depth estimation of defects located in the designated specimen

* MAE means mean square error. An average over sample for absolute different between actual and predicted observation.

4.3.1 Results analysis - Mean Absolute Error (MAE)

In statistics, the mean absolute error (MAE) [18] is one of the metrics to evaluate how close the forecasts are to the eventual outcomes. In the machine learning field, it can indirectly reflect the accuracy and performance of the machine learning model (GRU). In this work, we adapted the MAE to assess the performance of the GRU for depth estimation with infrared thermography. As we can see from Figure 9 (a), we trained the GRU to estimate the data from testing before the data normalization. The obtained training loss is 0.055. The MAE converged to 0.0165. The error between the predictive value and actual value is within the range of $[-0.17mm, 0.17mm]$. After the standard deviation normalization for all the distributed data in Figure 9 (b), the predictive value trends to approach the actual depth for the defect. The MAE error shrinks to the range of $[-0.11mm, 0.11mm]$ and the training loss converged to 0.0295. This shows an acceptable performance with an improved estimate of the depth by the GRU model with standard deviation normalization.

In table 4, the estimated output 1 and the MAE 1 are obtained from raw data without normalization. The estimated output 2 and the MAE 2 result from raw data with normalization. Based on Table 4, the calculated accuracy in the GRU model for the depth estimation reached 90 % before data normalization (standard deviation). After normalization, the results provide an accuracy greater than 95 %. This performance demonstrated that the GRU enable a high performance for accurate depth estimation. This estimation is attributed to the ideal environment without experimental issues (noise; defective pixels). As shown in the Figure 10 below, the thermal data distribution from training (before; after) normalization has been indicated. In the data distribution(a), each

group of color data curves (yellow; red; green) represents a different specific depth from defects. The thermal data is normalized by Eq. (10) in Figure 10 (b). The distinguishable features of difference between the depths is recognized by the following principle: shallow defects have greater maximum thermal contrasts that occur earlier than deep defects. These results outperformed the previous works obtained from [7] for depth estimation in automated infrared thermography with regular neural networks.
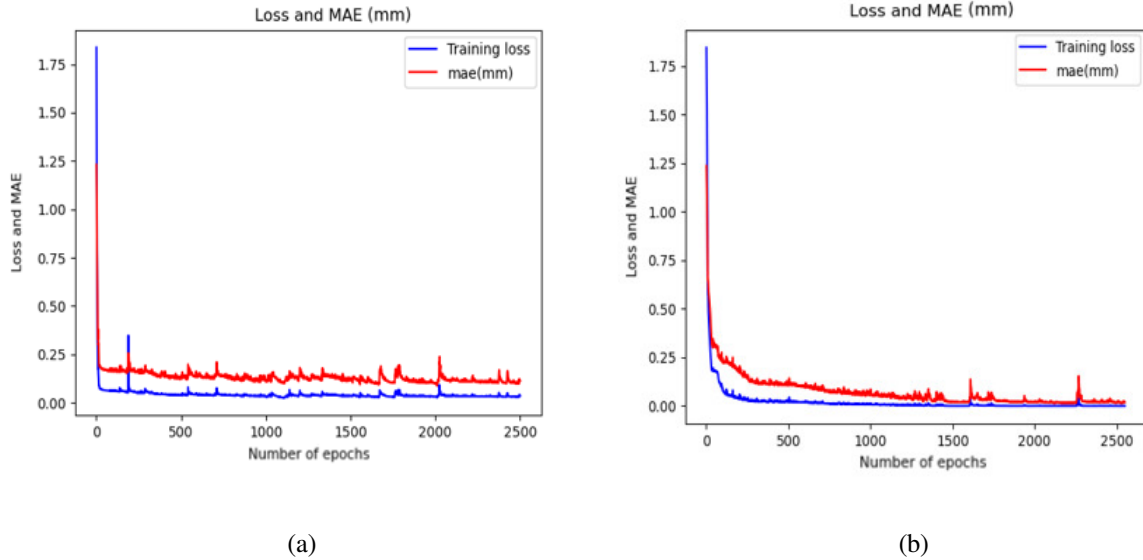

(a)   (b)

Figure 9. The mean absolute error and the training loss with GRU before (a) and after (b) standard deviation normalization

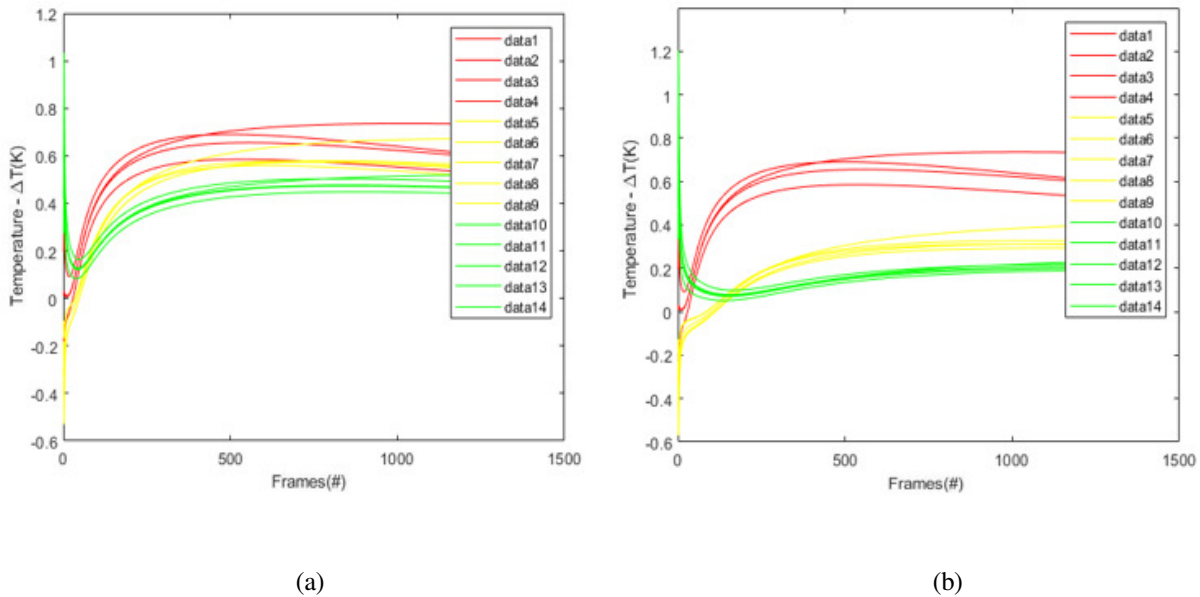(a)   (b)

Figure 10. The data distribution before (a) and after (b) standard deviation normalization from all the selected locations for training

5. CONCLUSION

This work elaborated the complicated and non-linear issues of evaluating defect depths in composite materials via infrared thermography with a GRU learning model. The methodology proposed here employed a GRU model combined with pulsed thermography to analyze the depth of defects. The simulated samples provide an economical platform for GRU training and depth estimation. Quantitative analysis of defect depth (subsurface features) has been evaluated by a GRU based statistical method through developed neural network modeling and cross validation experimental verification. It has been proven that the GRU modeling can produce an advanced depth detection. For future work, the experimental data have to be evaluated for the robustness of the GRU model. Further, other types of deep learning models and modified versions of the GRU model have to be applied to increase the depth estimation ability in this topic.

REFERENCES

[1]   Maldague X, Galmiche F, Ziadi A. Advances in pulsed phase thermography[J]. Infrared physics & technology, 2002, 43(3-5): 175-181.

[2]   Nikolas Rajic. Principal component thermography for flaw contrast enhancement and flaw depth characterisation in composite structures. Composite Structures, 58(4) :521– 528, 2002

[3]   Martin, R.E., Gyekenyesi, A.L., Shepard, S.M.: Interpreting the results of pulsed thermography data. Mater. Eval. 61(5), 611–616 (2003)

[4]   Shepard, S.M., Lhota, J.R., Rubadeux, B.A., Wang, D., Ahmed, T.: Reconstruction and enhancement of active thermographic image sequences. Opt. Eng. 42(5), 1337–1342 (2003)

[5]   Weng J, Zhang Y, Hwang W S. Candid covariance-free incremental principal component analysis[J]. IEEE Transactions on Pattern Analysis and Machine Intelligence, 2003, 25(8): 1034-1040.

[6]   Sun J G. Analysis of pulsed thermography methods for defect depth prediction[J]. 2006.

[7]   Darabi A, Maldague X. Neural network-based defect detection and depth estimation in TNDE[J]. Ndt & E International, 2002, 35(3): 165-175.

[8]   Chung J, Gulcehre C, Cho K H, et al. Empirical evaluation of gated recurrent neural networks on sequence modeling[J]. arXiv preprint arXiv:1412.3555, 2014.

[9]   Hochreiter S, Schmidhuber J. Long short-term memory[J]. Neural computation, 1997, 9(8): 1735-1780.

[10] Zissis, G.J. Infrared technology fundamentals. Opt. Eng. 1976, 15, 156484

[11] Saeed, N.; Abdulrahman, Y.; Amer, S.; Omar, M.A. Experimentally validated defect depth estimation using artificial neural network in pulsed thermography. Infrared Phys. Technol. 2019, 98, 192–200.

[12] Peeters, J.; Steenackers, G.; Ribbens, B.; Arroud, G.; Dirckx, J. Finite element optimization by pulsed thermography with adaptive response surfaces. In Proceedings of the 12th International Conference on Quantitative Infrared Thermography (QIRT), Bordeaux, France, 7–11 July 2014.

[13] Lopez, F.; de Paulo Nicolau, V.; Ibarra-Castanedo, C.; Maldague, X. Thermal–numerical model and computational simulation of pulsed thermography inspection of carbon fiber-reinforced composites. Int. J. Therm. Sci. 2014, 86, 325–340.

[14] Pilling, M.W.; Yates, B.; Black, M.A.; Tattersall, P. The thermal conductivity of carbon fibre-reinforced composites. J. Mater. Sci. 1979, 14, 1326–1338.

[15] Chung J, Gulcehre C, Cho K, et al. Gated feedback recurrent neural networks[C]//International conference on machine learning. 2015: 2067-2075.

[16] Gulcehre C, Cho K, Pascanu R, et al. Learned-norm pooling for deep feedforward and recurrent neural networks[C]//Joint European Conference on Machine Learning and Knowledge Discovery in Databases. Springer, Berlin, Heidelberg, 2014: 530-546.

[17] Horn R A. The hadamard product[C]//Proc. Symp. Appl. Math. 1990, 40: 87-169.

[18] Kassam, S. Quantization based on the mean-absolute-error criterion. IEEE Trans. Commun. 1978, 26, 267–270

Neural Network and Particle Filtering: A Hybrid Framework for Crack Propagation Prediction

Seyed Fouad Karimian[1], Ramin Moradi[1], Sergio Cofre-Martel[1], Katrina M. Groth[1], Mohammad Modarres[1]

[1]Center for Risk and Reliability, University of Maryland, MD, USA

Corresponding Author: `foadkrmn@umd.edu`

Abstract

Crack detection, length estimation, and Remaining Useful Life (RUL) prediction are among the most studied topics in reliability engineering. Several research efforts have studied physics of failure (PoF) of different materials, along with data-driven approaches as an alternative to the traditional PoF studies. To bridge the gap between these two techniques, we propose a novel hybrid framework for fatigue crack length estimation and prediction. Physics-based modeling is performed on the fracture mechanics degradation data by estimating parameters of the Paris Law, including the associated uncertainties. Crack length estimations are inferred by feeding manually extracted features from ultrasonic signals to a Neural Network (NN). The crack length prediction is then performed using the Particle Filter (PF) approach, which takes the Paris Law as a move function and uses the NN's output as observation to update the crack growth path. This hybrid framework combines machine learning, physics-based modeling, and Bayesian updating with promising results.

Keyword: Structural Health Monitoring, Fatigue, Ultrasonic Signal Processing, Particle Filter, Neural Network

1. Introduction

Although assumed to be identically manufactured, components always present some variability in their performance while in service. This variability can be seen in their degradation path and time to failure as they are tested under identical conditions. In engineering, fatigue is the most common degradation mechanism, and it has been under extensive study over the past century [1]. The fluctuating loads applied to components result in damage accumulation. The damage starts at the micro-scale constituent levels of materials and grows to a macro-scale level, eventually causing a catastrophic failure. In metals, accumulated damage causes a macro-crack to form and develop until final fracture. The fatigue damage modeling and life prediction in metals encompass a rich history of research studies, mainly focused on damage mechanisms and damage accumulation models [2]. Fatigue life prediction in metals is usually divided into two main regimes: crack initiation and crack propagation. Fracture mechanics focuses on crack length estimation based on the applied stress and other factors such as geometry. One of the most widely accepted models in fracture mechanics is the Paris' Law [3]. The flexibility to adapt to unseen situations and the available historical information on physics-based models make them a reliable tool for fatigue life prediction. However, due to the stochastic nature of fatigue and the need to decrease the uncertainty in degradation prediction of sensitive structures, several data-driven methods have been developed over the past years. The implementation of data-driven methods seeks to exploit the interpretation of high volumes of data collected by sensors during the operational life of a component. Hence, the assessment of the health state can constantly be updated based on the operational conditions, allowing to guide the maintenance decision-making towards a condition-based one.

One of the sensor measurements that have proven to be a good assessment tool for crack identification and propagation are ultrasonic signals, particularly Lamb waves. By studying anomalies in their behavior, such as dispersion characteristics and propagation speeds, Lamb waves can be used for damage identification [4] and quantification through Bayesian updating [5, 6]. Other applications of Lamb wave properties for crack damage identification can be found in structural health monitoring through a defect imaging system [7], an enhanced hierarchical probability damage-imaging [8], and on-line crack prognostics using particle filtering based method [9]. The compelling evidence of the strong relationship between ultrasonic waves and

damage identification led researchers to apply Machine Learning (ML) approaches of high hierarchical order, aiming to extract abstract features from the signals [10, 11, 12]. Among these, Artificial Neural Networks (ANN) stand out as the most popular approach. Indeed, De Fenza et al. [13] analyzed Lamb waves to determine the location and quantification of damage in metallic and composite plates, based on a damage index determined from the propagation of the waves. These indices were then used to train the ANN, which outputs the health state diagnostic of the plate. Sbarufatti et al. [12] addressed a similar problem scenario, training an ANN with synthetically generated data, which was then validated with experimental data from a plate. In [12], indices were extracted from Lamb waves to create a feature vector, which was later used as input for two regression networks, one for localization and the second for quantification. Further, application of NN for damage identification and quantification based on wave signals have been applied in [14, 15, 16].

Prediction accuracy in data-driven models heavily depends on the availability of reliable training data. Uncertainty in the remaining useful life (RUL) estimation of degradation processes increases when a limited amount of training data is available. Meanwhile, the adaptability of physics-based models to account for different conditions and availability of historical data can provide a reliable estimation of the degradation path specifically in the case of widely used materials. To incorporate the benefits of both data-driven and physics-based models, hybrid approaches are widely used to model the degradation behaviors [17, 18, 19]. Particle Filtering (PF) and its evolved versions (thoroughly discussed by Jouin et al. [20]) are among the most popular hybrid prognostic techniques. PF can be updated in real-time, captures nonlinearity's, accounts for uncertainty, and can to perform prognostic and prediction tasks, which are great assets to hybrid techniques.

In this paper, we propose a novel hybrid Neural Network-Particle Filtering (NN-PF) model as a powerful probabilistic tool for crack length estimation and prognostics. This model fuses the physics-based degradation model for crack growth (Paris' Law) with the output of the data-driven approach (NN). To the best of our knowledge, there is only one similar application of an assembled neural network-particle filtering framework by Baraldi et al. [21], in which the authors present a bagged ensemble artificial neural network to map the state of the particle to the measurement. Their main focus is to quantify the uncertainty over the RUL predictions. Our approach, however, focuses on the framework development, which assembles NN with PF to output a crack length estimation.

2. Proposed Framework

A hybrid physics-based and data-driven framework is proposed to describe the stochastic nature of crack growth and decrease the uncertainty of crack propagation estimation. In this framework, fracture mechanics is used to model the physics of crack growth. The uncertainty in the component degradation path is captured through the physics-based model. Parameters of the governing equation of fatigue crack growth, Paris' Law, are estimated based on the available training data, through a probability distribution fitting. As a result, instead of describing the behavior of an unseen component using deterministic parameters, a series of potential crack growth paths with their associated probabilities are used.

Neural network (NN) estimates the crack length based on features extracted from ultrasonic signals recorded at different crack lengths. One important advantage of using NN for crack length estimation is that it is independent of the cycle numbers and loading conditions and only dependent on the signals. The crack length estimates from NN is used to select the most likely path of crack growth in the series of potential crack growth paths. Then, particle filter performs as a hybrid model, taking the selected crack growth path as the move function, and NN estimates as observations to update the degradation path of the fatigue test. This approach, while based on the general physics of crack growth, is tailored to the test conditions using NN outputs and is expected to decrease the uncertainty of RUL estimation and provide an accurate crack propagation estimation. Figure 1 shows the proposed framework. Details of each step are explained in the following.

2.1. Physics-Based Modeling

The fatigue crack propagation prediction in this study is described by the linear elastic fracture mechanics (LEFM) introduced by Paris [3]. The Paris' Law equation explains the crack growth rate in a material as a function of its geometry and applied load, and it is defined as:

$$\frac{da}{dN} = C(\Delta K)^m \tag{1}$$

In which a is the crack length, N is the number of cycles, and da/dN is the crack growth rate with respect to the number of cycles. C and m are material dependent parameters, and ΔK is stress intensity factor defined as:

$$\Delta K = f(g)\Delta\sigma\sqrt{\pi a} \tag{2}$$

In Equation 2, $f(g)$ is correction factor that depends on specimen and crack geometry, $\Delta\sigma$ is the applied stress and a is the crack length. Equations 1 and 2 can be used to describe the crack growth behavior of a known geometry and material
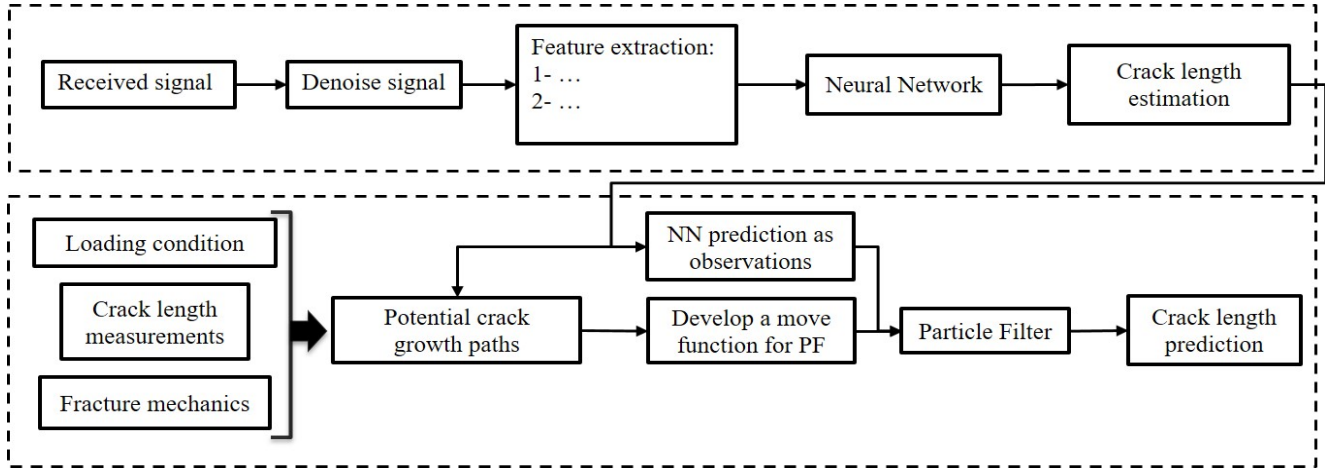
Figure 1. Flow diagram for the proposed framework.

component. Although the Paris' Law parameters for widely used materials are reported in many open-source databases, they are usually associated with high uncertainties. The material properties of a component can be measured by performing fatigue tests and crack length measurements and using:

$$N_2 - N_1 = \int_{a_1}^{a_2} \frac{da}{C(f(g)\Delta\sigma\sqrt{\pi a})^m} \tag{3}$$

To find the C and m parameters, crack growth data from the training database is fit to Equation 3. The parameters are material dependent and are expected to yield identical values if multiple fatigue results are used from components of identical material. However, due to the uncertainties associated with tests, measurements, geometry, etc., values show a scattered behavior. After finding the Paris' Law parameters for each training test, a distribution over life at each crack length is fitted. A Weibull distribution is then used to capture the scatter in crack growth paths of all training test data. This, results in a distribution of crack growth paths describing the Paris' Law for the training set with its confidence intervals. In the case that the loading condition is changed from a constant amplitude to a variable amplitude, the change in Paris Law parameter C is described using Newman's equation [22].

2.2. Deep Neural Network

Neural networks have popularly been used to address problems regarding classification and regression for the last decades [23]. Given their hierarchical nature, NN could extract abstract information from a given input data X_0 by stacking multiple layers of nonlinear functions. A layer (h_i) is mathematically described as:

$$h_i = \sigma(W_i^T \cdot X_{i-1} + b_i). \tag{4}$$

Where, W_i and b_i are the so-called weights and bias of layer i, respectively. X_{i-1} is the input data to the layer, and σ is known as the activation function, which is a nonlinear function such as the hyperbolic tangent (tanh), rectifier linear unit (ReLU), sigmoid, etc. Each of these nonlinear transformations are known as layers. The number of outputs in each layer (i.e., h_i's dimension) is equal to the number of neurons or hidden units, that the layer has. For a multi-layer neural network (i.e., Deep Neural Network), a layer's outputs h_i correspond to the input data X_{i+1} of the next layer. The output of the whole network (y) is then given by:

$$y = W_l^T \cdot h_l + b_l \tag{5}$$

where l corresponds to the number of hidden layers of the network.

The neural network used in this framework has two hidden layers of ten hidden units each, with ReLU as the activation function. The network takes as input different features extracted from the Lamb Waves signals, and it outputs the estimated crack length corresponding to those features. Note that the network does not take the number of cycles as an input. Thus, crack estimation is solely based on the abstract interpretation of the Lamb waves.

The training cost for the network is set as a combination of the prediction error and a penalization function T (Equation 7). This function was introduced as a penalization for the PHM Data Challenge 2019 [24]. This gives a greater penalization for prediction errors at greater crack lengths. The training cost function is then defined as:

$$\Delta = y_i - W^T \cdot X_i \tag{6}$$

$$T = 2.0 + 10.0 \cdot y_i \tag{7}$$

$$Cost = \frac{1}{N} \sum_{i=1}^{N} \Delta^T \cdot T \tag{8}$$

The network is trained using stochastic gradient descent through back-propagation with Adam optimizer [25]. The learning rate was set to be 0.001. Further, the training of the network does not depend on the particle filtering process, and we only train the network using a random sample set from the given dataset. Hence, the output corresponds to one output per input data, rather than a distribution as in [21]. The network was trained using Python 3.6 through Tensorflow 1.13 in Windows 10. An Intel i7 9700k CPU, a Titan RTX GPU of 24GB, and 32GB of RAM were used as the hardware.

2.3. Particle Filtering

Particle Filtering (PF) is a sequential Monte Carlo-based computational technique that is frequently used for Bayesian prognostics of nonlinear and/or non-Gaussian processes. Considering a system whose state at the discrete time step $t_k = k\Delta t$ is represented by a vector x_k. The state space model can describe the system's evolution as:

$$x_k = f_k(x_{k-1}, \omega_{k-1}) \tag{9}$$

Where f_k is the nonlinear state transition function (aka move function) and ω is the state noise vector. Noise is being introduced in the modeling to account for the stochasticity involved in fatigue crack growth that can vary from specimen to specimen. The objective in the particle filtering process is to recursively estimate x_k from measurements z_k which can be described by Equation 10.

$$z_k = h_k(x_k, \nu_k) \tag{10}$$

Where h_k is the measurement function and ν_k is the measurement noise. The Bayesian approach uses the following probability density function (PDF) $p(x_k|z_{1:k})$ to estimate the dynamic state x_k, given the measurements z_k up to time k. This PDF is calculated recursively from t_1 to t_k using Equation 11.

$$p(x_k|z_{1:k}) = \frac{p(z_k|x_k).p(x_k|z_{1:k-1})}{p(z_k|z_{1:k-1})} \tag{11}$$

To numerically perform PF, one should assume that a set of random samples, i.e., particles, $x_{k-1}^i, i = 1, ..., N$ of the system state at time $k - 1$ are available as a realization for the posterior $p(x_{k-1}|z_{1:k-1})$. Prediction step at time k is accomplished by:

- Sampling from the probability distribution of the system noise ω_{k-1}

- Simulating the system dynamics (application of the move function) to generate a new set of samples x_k^i which are realizations of the predicted probability distribution $p(x_k|z_{1:k-1})$.

- Updating each sampled particle's x_k^i assigned weight w_k^i based on the likelihoods of the observations z_k collected at time k. An approximation of the posterior distribution $p(x_k|z_{1:k})$ can then be obtained from the weighted samples $(x_k^i, w_k^i), i = 1, \ldots, N$.

In this framework the move function for PF is determined by the physics-based modeling. The initial particles distribution mean and standard deviation is determined according to the upper bound and lower bound (i.e., 5% and 95% confidence) of the crack growth path obtained by physics-based modeling at a reasonably low cycle number (in which we are confident that the component is healthy). The impact of the observations is determined by the standard deviation of the distribution, whose mean is placed on the observation point and the particles weights are updated by it. This standard deviation value, along with the noise of the move function, is optimized in a way to achieve maximum prediction accuracy on the training data. To do so, it is considered that NN predictions are only available for the first few cycles in training tests. Then, using PF, the crack lengths in higher cycle numbers are predicted.

3. Case Study

3.1. Data description

The dataset used for this study is publicly available at the PHM data challenge 2019 competition [24]. The dataset describes fatigue tests on lap-shear joints made of aluminum alloy, reporting ultrasonic signals and crack length measurements. The database includes six training tests and two validation tests. In the training tests, for each specimen, a set of cycle numbers and their corresponding crack lengths are provided. For each crack length, two sets of ultrasonic signals are given, which include an actuation and a received signal. The goal is to determine the crack lengths at given cycle numbers for two validation tests. In the validation data, ultrasonic signals are only provided for the first few cycles, and prognostics needs to be carried out for a determined number of cycles with no provided signals.

All training tests and one validation test are fatigued with a constant amplitude loading, while the second validation test is fatigued under variable amplitude loading. Constant amplitude loading is described with a maximum stress $\sigma_{max} = 100.21$ MPa and a minimum stress $\sigma_{min} = 4.77$ MPa, at a 5 Hz frequency. Variable amplitude spectrum is described as 500 cycles with $\sigma_{max} = 90$ MPa and $\sigma_{min} = 4.77$ MPa followed by 500 cycles with $\sigma_{max} = 100.21$ MPa and $\sigma_{min} = 4.77$ MPa, at the same 5 Hz frequency. The loading conditions are shown in Figure 2. The only information available about the geometry of the specimen is the distance between actuator and receiver sensors that is 161.0 mm.
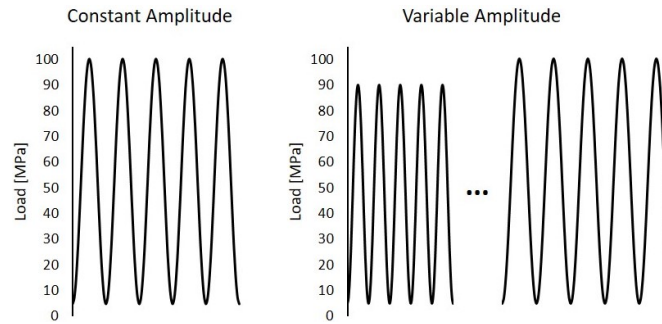

Figure 2. Tests loading conditions.

3.2. Crack growth path

The parameters of the Paris' Law are evaluated for each training test separately. The results of all training tests are used to find the mean and confidence intervals of the crack growth path for the specimen and material. Since the material type is not known, no prior distribution is used for the Paris' Law parameters. Furthermore, the geometry coefficient in Equation 2 cannot be directly selected due to the lack of knowledge about the geometry. Therefore, based on the description of the problem which states the crack is bracketed by the sensors, an equivalent center-cracked plate with tension loading is selected. The geometry coefficient, in this case, is defined as:

$$f(g) = \sqrt{sec\left(\frac{\pi a}{2b}\right)} \tag{12}$$

Where $2a$ is the crack length and $2b$ is the specimen width. The use of this $f(g)$ requires information about the specimen width. Hence, an optimization on the parameter b of Equation 12 and parameters C and m of Equation 1 is performed using Equation 3. The objective of the optimization is to minimize the error in crack length estimation using the known crack lengths. The optimization is done on all of the training tests individually. This results in a series of six values for the specimen width (parameter b). All the widths found are similar with an average of $39mm$ and a standard deviation of $3mm$. The optimization of Paris' Law parameters is then repeated for each training test using the average value for specimen width. Since the actual geometry of the specimen is different from the one assumed, the actual specimen width is also expected to be different from the equivalent specimen width found. The crack growth path of the training tests are used to find the mean and the confidence intervals for the crack growth path of the material and geometry. The mean, 5% and 95% confidence bounds of the crack growth path are found by fitting a Weibull distribution over the cycle numbers at different crack lengths. The results are shown in Figure 3, where we can see that the mean and the confidence interval capture all the variability in the crack growth paths for the different training tests.
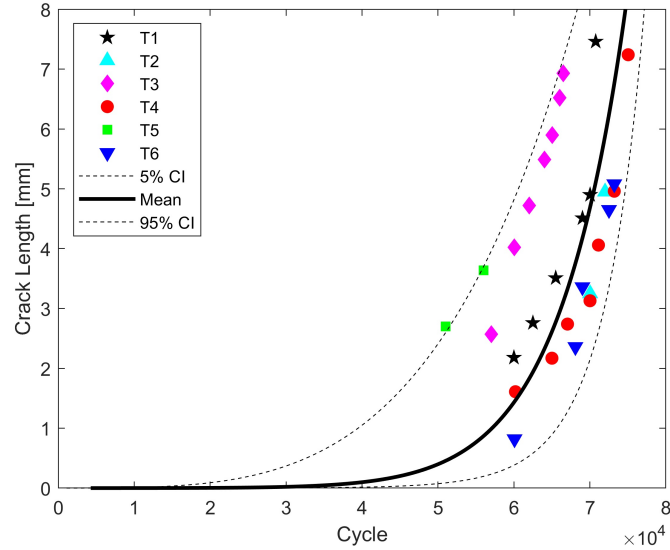
Figure 3. Crack growth path distribution based on the training data.

3.3. Data cleaning

The first step to use the ultrasonic signals is denoising. Since no information is provided regarding the actuation signals, we perform denoising aimed to increase the correlation coefficient for each set of two signals in the training tests. In order to increase the accuracy of signal denoising, only the signals that correspond to zero crack length are used. The correlation coefficient in each pair of signals is computed for both actuation and received signals.

Two methods of signal denoising are used in this study to achieve higher signal-to-noise ratios. The first one is wavelet analysis, where a 'db10' wavelet is used to denoise signals. The method is selected following the analysis presented in [8], which showed to be an effective denoising approach. The second method is based on the power spectrum of the signals. For each signal, the power spectrum shows a peak in the lower frequencies followed by an oscillation around lower power values for the rest of the frequency spectrum. Hence, the range of frequency showing the highest power spectrum is selected and used as a bandpass filter to denoise signals. It is assumed that the actual signal has the highest values in the power spectrum and therefore, the corresponding frequencies can be used to denoise signals. The average correlation coefficient for all the signals with zero crack length are summarized in Table 1. It can be seen that the bandpass filter has the highest value. Figure 4 shows a set of received signals before and after bandpass filtering. We observe that while the bandpass filtered signals have the same shape, raw signals include lots of noise, which significantly decreases the correlation coefficient.

Table 1. Comparison of two different signal denoising methods.

Mean Correlation Coefficient		
Signal	Actuation	Received
Raw	96.31%	81.01%
Wavelet filter	98.16%	83.48%
bandpass filter	**99.83**%	**97.29**%

3.4. Signal feature extraction

In the simplest approach, one can analyze the whole recorded signal and calculate commonly used features like phase change [5], correlation coefficient [8], information entropy [26], normalized amplitude [27], normalized energy [28], and time of flight [8]. Doing so would introduce a considerable amount of noise and uncertainty to the results, since the recorded signals are contaminated by boundary waves reflections and external sources of noise. In the literature, a specific portion of the signals is often considered for further analysis based on the expected time of receiving the actuation signal. This time window is determined by knowing the geometry and material of the test specimens and time of flight diffraction (ToFD) techniques [29, 30]. However, for our case study the exact geometry, material and piezoelectric sensors specifications are not known to perform a thorough ToFD.
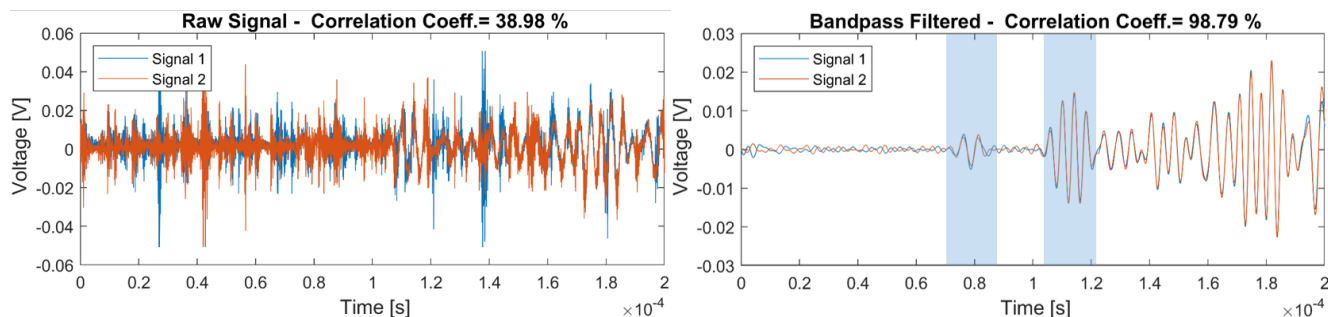
Figure 4. Raw signal vs. bandpass filtered signal and the time windows selected.

Considering the above, to select the most important portion of the signal, a time window with the length of the actuation signal is considered. This window is then moved along the received signals to find the most correlated portions of the received signals compared to the actuation signal. The two most correlated portions approximate time windows are shown in Figure 4.

This approach is justified since the actuation lamb wave frequency would remain constant when propagating through the material and only its energy (amplitude) gets dissipated. Further analysis of the extracted signals revealed that the features from signals corresponding to the second window (later in time) correlate better with the crack lengths. Therefore, only the second time window is used for further analysis. Figure 5 shows the signals extracted from the second window in test 4, where we can see a change in the trend of the signals corresponding to different cycle numbers (i.e., different crack lengths).
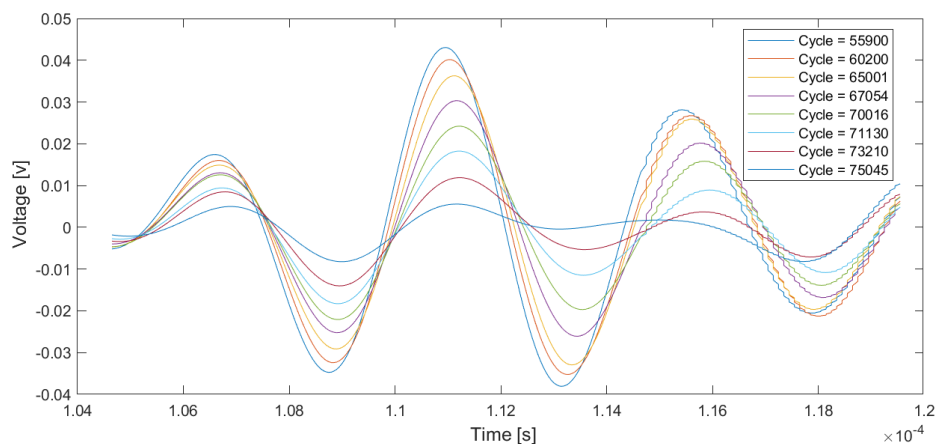

Figure 5. Signals at different cycles - Test 4.

Features investigated in this study are:

1. **Pearson Correlation Coefficient** which is a measure of the linear dependence between two random variables. If there are N observations for each signal, then the coefficient is calculated as:

$$\rho(A, B) = \frac{1}{N-1} \sum_{i=1}^{N} (\frac{\overline{A_i - \mu_B}}{\sigma_A})(\frac{B_i - \mu_B}{\sigma_B}) \tag{13}$$

Where μ and σ are the mean and standard deviation of random variables A and B, respectively. In this study, A and B are the received signals at different crack lengths for each test.

2. **Phase change** between different measurements of each test specimen [5]. Phase change between two signals can be calculated with different methods. In this study, we use the Discrete Fourier Transform (DFT) and Maximum Likelihood estimation (MLE) of the properties of the signals. The phase difference between harmonic components of lamb wave signals is found as the phase difference of the harmonics DFT phase spectrum values of Lamb wave signals. A detailed mathematical explanation for various phase change calculation methods is provided by Sedlacek

and Krumpholc [31]. The phase change relative to the received signal when there is no crack is considered as a feature in this paper.

3. **Energy** of the received signals. Cracks, damages, or any anomalies in the structure of the material would cause energy dissipation when the signal is traveling through the material. The energy of the actuation signal is considered as the total amount of energy released into the material. Thus, the energy of the received signals are calculated as a percentage of the actuation signal's energy. Energy of a signal calculated as follows.

$$E_s = \int_{-\infty}^{\infty} |x(t)|^2 dt \tag{14}$$

4. **Information Entropy**. This feature has recently received attention as a new parameter to quantify fatigue damage using recorded signals [26]. Information entropy relies on the information content of the distribution of received signals. It uses the signal distribution characteristics to measure the information content of the signal and consequently quantifies the damage. The information entropy defined by Shannon [32] is expressed as:

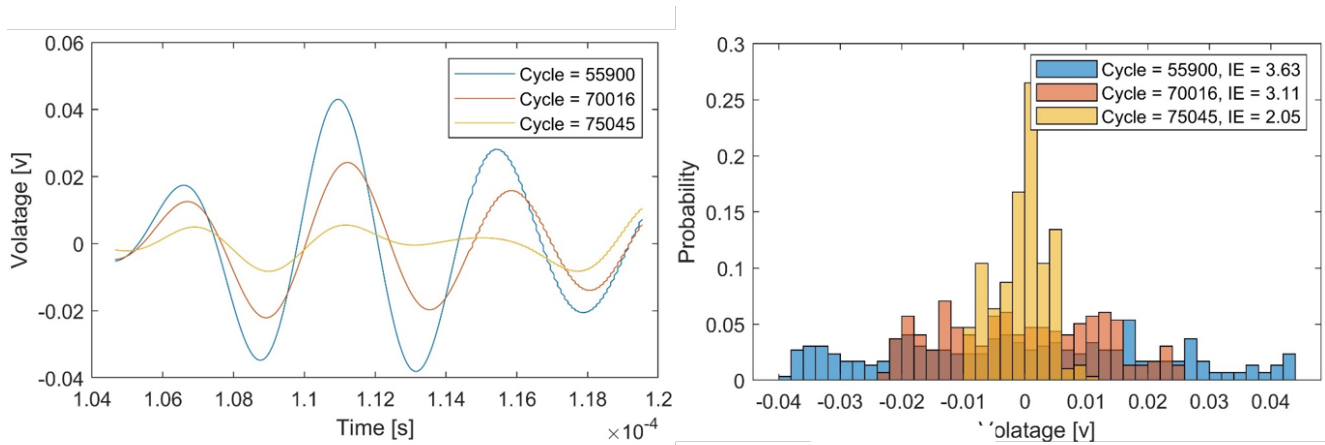$$I = -c \sum_{i=1}^{n} P(x_i) ln(1/P(x_i)) \tag{15}$$

Figure 6. Signals, their voltage histograms and their respective information entropy (IE) values.

Where I is the information entropy, c is a constant considered to be unity in this study and $P(x_i)$ is the probability distribution of the random variable. In the case of ultrasonic signals, voltage is the random variable and the histogram of signals is used as a non-parametric probability distribution. Figure 6 shows how the change in signal at different cycles results in a change of histogram and consequently its information entropy. Figure 7 shows the trend of information entropy change in all tests.

3.5. Results and discussion

The validation tests are referred to as Test 7 and Test 8. Both tests have similar geometries as the training tests. Test 7 is performed using constant amplitude loading. In this test, eight crack lengths are to be estimated for some given cycle numbers. Ultrasonic signals are only provided for the first four cycles. Test 8 is performed under variable amplitude loading. Ten crack lengths are to be estimated for the given cycle numbers with ultrasonic signals provided only for the first five cycles. For each signal, features are extracted and fed to the neural network, which outputs an estimation of the crack length for the corresponding signal. Then, based on the NN crack length estimations, the appropriate Paris' Law parameters from the crack growth path distribution (shown in Figure 3) are selected.

In Test 7, the mean value of the crack growth path shown in Figure 3 is considered as the move function. The NN crack estimations are used by the PF to predict the crack length values at cycle numbers with available signals. These estimations are then used to update the distribution of the crack growth path shown in Figure 8. To update the move function, the four
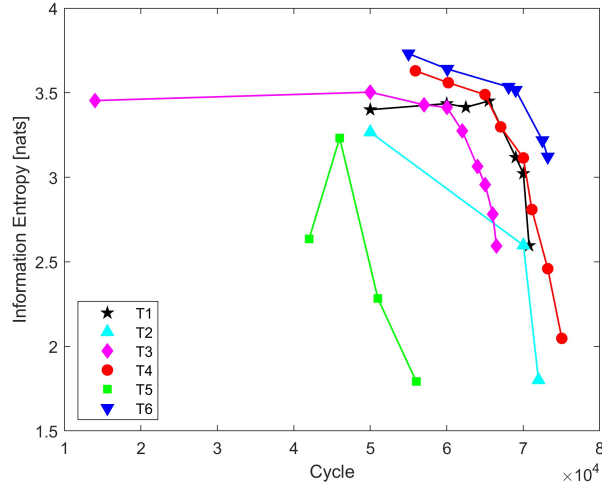
Figure 7. Trend of change in information entropy of training set.

crack lengths estimated by the PF are used to find Paris' Law parameters for Test 7. These parameters are then used to update the overall C and m and their confidence interval for the specimens. The updated moving function is then used for prognostics and crack length estimation of the remaining cycle numbers, starting from the last estimated crack length with observation (signal). Figure 8 shows all the PF estimations of crack length including the first four-cycle numbers (with signal) and crack length prognostics for the rest of the cycle numbers.

The NN's crack length estimations in Test 8 are closer to the upper end of the confidence interval(i.e., 5% confidence). Thus, the 5% curve's C and m are selected as the Paris' Law parameters for the PF's move function. NN estimations are then used as observations for PF to update the crack length values. Similar to Test 7, when no observation is available, PF is used to predict crack lengths without updates in its move function. In this case, we are not updating the move function based on a fit to Test 8 estimations due to the variable amplitude loading condition. Doing so would increase the overall uncertainty in estimated Paris Law parameters since there is no training sample with variable amplitude loading. The estimation for crack lengths for Test 8 are depicted in Figure 8.

The database in the case study has been previously used for fatigue crack estimation by He et al. [4] and Wang et al. [28]. In both studies, extracted features from ultrasonic signals are used to determine the parameters of proposed models. The models are based on multivariate equations by combining different features. Their approaches rely only on data-driven
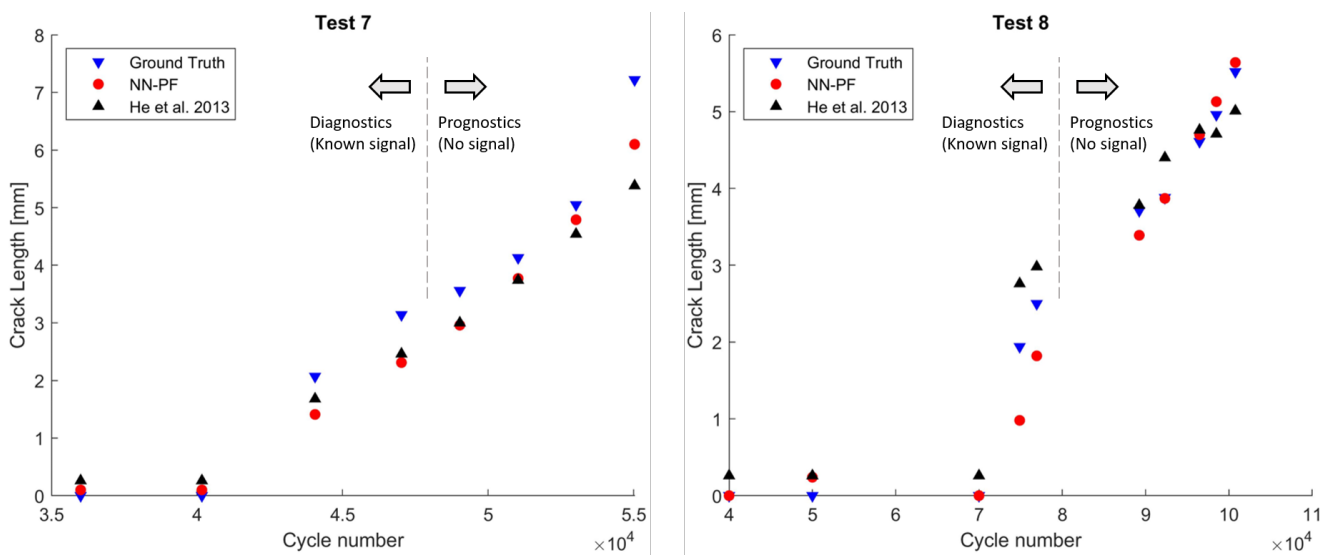

Figure 8. PF-NN framework results, ground truth, and He et al. [4] predictions.

methods with slightly different models proposed in each study. The probability of crack detection for each proposed model is also studied in the latter research. Wang et al. [28], used physics-based modeling (Paris' Law) to estimate fatigue life (as ground truth) and evaluated the models for RUL estimation. However, to determine the distribution for the Paris' Law parameters, fatigue crack growth results of the same material reported in a different study [33] are used.

In the present study, we have used all the available data, i.e., signals, crack lengths and their associated cycle numbers to derive a hybrid physics-based and data-based method to predict crack length despite the lack of information regarding exact geometry and material. Figure 8 shows how well our approach performs comparing to the He et al. [4] and Figure 9 shows the root meas square error (RMSE) in each study for both tests. It can be seen that although much less information was available regarding the test conditions, material and geometry of the specimen, crack length estimation results using the proposed framework yield if not better, as good results as the other study. An accurate comparison could not be made with Wang et al. [28] since they used a different validation test with slightly different training data.
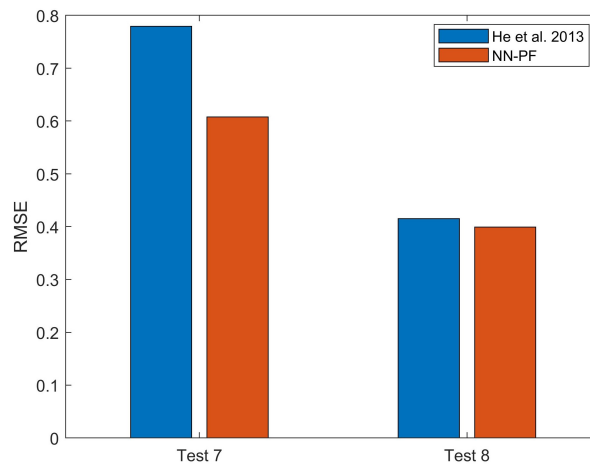

Figure 9. Root mean square error comparison of NN-PF and He et al. [4]

4. Conclusions

In this paper, we have developed a hybrid *Neural Network-Particle Filter* framework for crack lengths estimation based on Lamb Waves Signals and demonstrated its effectiveness in a case study. The signals in the case study were collected during multiple fatigue tests on lap-shear joint aluminum alloys. The denoising of the signals turned out to be a key factor in extracting representative features, which were then fed to a Neural Network for a first estimation of the crack length. Four features were selected and found to be sensitive to crack lengths, including the information entropy of signals which, to the best of the authors' knowledge, has not been used for the purpose of crack length estimation previously.

Two separate time windows in signals were found to be most correlated with the actuation signal and thus used to extract the features. The features from the second time window that appears with a time delay (i.e., Time of Flight) relative to the actuation signal, were identified as the most sensitive to damage quantification. A series of potential crack growth paths with their associated probability of happening are calculated based on the available training tests. The NN crack length estimations are then used to select the appropriate crack growth path (i.e., Paris' Law parameters).

The selected path is then considered as the move function for the particle filter. Crack length estimations from the NN were used as observation to update and adjust the PF model to decrease the uncertainty in crack length estimation further. This model allows crack propagation and RUL estimations under uncertainty, combining all the available data. Comparing to He et al. [4], this model decreased uncertainty in crack length prediction by 22% in test 7 and 4% in test 8. The proposed framework could be further improved by using the more general forms of the Paris' Law that can describe all the regions in crack growth. The comparison of the proposed framework with similar studies on the same dataset shows that fusing more of the available data, i.e., from a physics-based and data-driven approach, despite some lack in available information, can further decrease the uncertainties associated with crack length estimations and accurately predict RUL of components with minimal information on the geometry and material.

References

[1] Weicheng Cui. A state-of-the-art review on fatigue life prediction methods for metal structures. *Journal of marine science and technology*, 7(1):43–56, 2002. 1

[2] E Santecchia, AMS Hamouda, F Musharavati, E Zalnezhad, M Cabibbo, M El Mehtedi, and S Spigarelli. A review on fatigue life prediction methods for metals. *Advances in Materials Science and Engineering*, 2016, 2016. 1

[3] Pe Paris and Fazil Erdogan. A critical analysis of crack propagation laws. *Journal of basic engineering*, 85(4):528–533, 1963. 1, 2

[4] Jingjing He, Xuefei Guan, Tishun Peng, Yongming Liu, Abhinav Saxena, Jose Celaya, and Kai Goebel. A multi-feature integration method for fatigue crack detection and crack length estimation in riveted lap joints using Lamb waves. *Smart Materials and Structures*, 22(10):105007, 2013. 1, 9, 10

[5] Jinsong Yang, Jingjing He, Xuefei Guan, Dengjiang Wang, Huipeng Chen, Weifang Zhang, and Yongming Liu. A probabilistic crack size quantification method using in-situ Lamb wave test and Bayesian updating. *Mechanical Systems and Signal Processing*, 78:118–133, 2016. 1, 6, 7

[6] Jian Chen, Shenfang Yuan, Lei Qiu, Jian Cai, and Weibo Yang. Research on a Lamb wave and particle filter-based on-line crack propagation prognosis method. *Sensors*, 16(3):320, 2016. 1

[7] Aurelia Muller, Bradley Robertson-Welsh, Patrick Gaydecki, Matthieu Gresil, and Constantinos Soutis. Structural health monitoring using Lamb wave reflections and total focusing method for image reconstruction. *Applied Composite Materials*, 24(2):553–573, 2017. 1

[8] Ruihua Li, Hao Li, and Bo Hu. Damage identification of large generator stator insulation based on PZT sensor systems and hybrid features of Lamb waves. *Sensors*, 18(9):2745, 2018. 1, 6

[9] Shenfang Yuan, Jian Chen, Weibo Yang, and Lei Qiu. On-line crack prognosis in attachment lug using Lamb wave-deterministic resampling particle filter-based method. *Smart Materials and Structures*, 26(8):085016, 2017. 1

[10] Ye Lu, Lin Ye, Zhongqing Su, Limin Zhou, and Li Cheng. Artificial Neural Network (ANN)-based crack identification in aluminum plates with Lamb wave signals. *Journal of Intelligent Material Systems and Structures*, 20(1):39–49, 2009. 2

[11] Hossein Aminpour, Foad Nazari, and Sara Baghalian. Applying artificial neural network and wavelet analysis for multiple cracks identification in beams. *International Journal of Vehicle Noise and Vibration*, 8(1):51–59, 2012. 2

[12] Claudio Sbarufatti, G Manson, and K Worden. A numerically-enhanced machine learning approach to damage diagnosis using a Lamb wave sensing network. *Journal of Sound and Vibration*, 333(19):4499–4525, 2014. 2

[13] A De Fenza, A Sorrentino, and P Vitiello. Application of artificial neural networks and probability ellipse methods for damage detection using Lamb waves. *Composite Structures*, 133:390–403, 2015. 2

[14] Faisal Khan, Omer F Eker, Ian K Jennions, and Antonios Tsourdos. Prognostics of crack propagation in structures using time delay neural network. In *2015 IEEE Conference on Prognostics and Health Management (PHM)*, pages 1–6. IEEE, 2015. 2

[15] Piotr Nazarko and Leonard Ziemianski. Damage detection in aluminum and composite elements using neural networks for Lamb waves signal processing. *Engineering Failure Analysis*, 69:97–107, 2016. 2

[16] Sergio Cofre-Martel, Philip Kobrich, Enrique Lopez Droguett, and Viviana Meruane. Deep convolutional neural network-based structural damage localization and quantification using transmissibility data. *Shock and Vibration*, 2019, 2019. 2

[17] Rajesh Kumar Neerukatti, Kuang C Liu, Narayan Kovvali, and Aditi Chattopadhyay. Fatigue life prediction using hybrid prognosis for structural health monitoring. *Journal of Aerospace Information Systems*, 11(4):211–232, 2014. 2

[18] Theodoros Loutas, Nick Eleftheroglou, and Dimitrios Zarouchas. A data-driven probabilistic framework towards the in-situ prognostics of fatigue life of composites based on acoustic emission data. *Composite Structures*, 161:522–529, 2017. 2

[19] Ameneh Forouzandeh Shahraki, Om Parkash Yadav, and Haitao Liao. A review on degradation modelling and its engineering applications. *International Journal of Performability Engineering*, 13(3):299–314, 2017. 2

[20] Marine Jouin, Rafael Gouriveau, Daniel Hissel, Marie-Cécile Péra, and Noureddine Zerhouni. Particle filter-based prognostics: review, discussion and perspectives. *Mechanical Systems and Signal Processing*, 72:2–31, 2016. 2

[21] Piero Baraldi, Michele Compare, Sergio Sauco, and Enrico Zio. Ensemble neural network-based particle filtering for prognostics. *Mechanical Systems and Signal Processing*, 41(1-2):288–300, 2013. 2, 4

[22] Jr JC Newman. A crack opening stress equation for fatigue crack growth. *International Journal of Fracture*, 24(4):R131–R135, 1984. 3

[23] Sandhya Samarasinghe. *Neural networks for applied sciences and engineering: from fundamentals to complex pattern recognition*. Auerbach publications, 2016. 3

[24] PHMsociety. 2019 PHM conference data challenge – PHM society data repository. https://www.phmdata.org/2019datachallenge/, July 2019. (Accessed on 11/21/2019). 3, 5

[25] Diederik P Kingma and Jimmy Ba. Adam: A method for stochastic optimization. *arXiv preprint arXiv:1412.6980*, 2014. 4

[26] Seyed Fouad Karimian, Mohammad Modarres, and Hugh A. Bruck. A new method for detecting fatigue crack initiation in aluminum alloy using acoustic emission waveform information entropy. *Engineering Fracture Mechanics*, 223:106771, 2020. 6, 8

[27] Fuqiang Sun, Ning Wang, Jingjing He, Xuefei Guan, and Jinsong Yang. Lamb wave damage quantification using GA-based LS-SVM. *Materials*, 10(6):648, 2017. 6

[28] Dengjiang Wang, Jingjing He, Xuefei Guan, Jinsong Yang, and Weifang Zhang. A model assessment method for predicting structural fatigue life using Lamb waves. *Ultrasonics*, 84:319–328, 2018. 6, 9, 10

[29] AN Sinclair, J Fortin, B Shakibi, F Honarvar, M Jastrzebski, and MDC Moles. Enhancement of ultrasonic images for sizing of defects by time-of-flight diffraction. *NDT & e International*, 43(3):258–264, 2010. 6

[30] SK Nath, Krishnan Balasubramaniam, CV Krishnamurthy, and BH Narayana. Reliability assessment of manual ultrasonic time of flight diffraction (TOFD) inspection for complex geometry components. *NDT & E International*, 43(2):152–162, 2010. 6

[31] Milos Sedlacek and Michal Krumpholc. Digital measurement of phase difference-a comparative study of dsp algorithms. *Metrology and Measurement Systems*, 12(4):427–448, 2005. 8

[32] Claude Elwood Shannon. A mathematical theory of communication. *Bell system technical journal*, 27(3):379–423, 1948. 8

[33] Dennis Andrew Virkler, Brnm Hillberry, and PK Goel. The statistical nature of fatigue crack propagation. *Journal of Engineering materials and Technology*, 101(2):148–153, 1979. 10

ANALYSIS OF BALLISTIC IMPACTS ON COMPOSITE MATERIALS BY INFRARED ACTIVE THERMOGRAPHY

Eric Guyot, Jean-Philippe Gagnon and Stephane Boubanga Tombet[*]

Telops, 100-2600 St-Jean-Baptiste ave., G2E 6J5, Québec, Québec, Canada
[*]Corresponding Author: stephane.boubanga@telops.com

ABSTRACT

This work focused on the assessment of the damaged area on composites ballistic plates subjected to high velocity impact. Active pulsed thermography technique was used for performing post-mortem analysis of the impacted specimens. The post-mortem analysis was combined with inputs of the velocity of the projectile, the absorbed energy to evaluate how efficient the material is at spreading the absorbed energy to a large area.

KEYWORDS: Ballistic Impacts, NDT, Active Thermography, High speed Infrared Camera

1. INTRODUCTION

Since the beginning of the last century the ongoing advances in materials engineering have led to an unrestrained development of new technologies. Composite materials are the ones attracting most attention because they have many advantages over their homogeneous counterparts. These include high specific stiffness and high specific strength combined with a significant reduction in weight [1-2] making them attractive for many industrial applications. One of the most important fields of application is the defense industry were the composites properties such as low weight, rigidity, strength and durability are of key importance. Composite materials made from artificially obtained high strength fibers [3] are particularly interesting. These composites are characterized by many fiber-reinforced properties that make them ideal for ballistic protection applications. The ballistic protection equipment should protect the user from for instance arms fire. The proper analysis strategy of the area of internal damage caused by the impact of bullets is very important in the research and evaluation of protective composite ballistic equipment. Damage to the internal structure of the composite coating material can only be assessed using non-destructive testing methods. Such methods, such as infrared thermography test methods, are particularly effective in the case of composite materials. This work focused on the assessment of the damaged area on composites ballistic plates subjected to high velocity impact. Active pulsed thermography technique was used for performing post-mortem analysis of the impacted specimens. The post-mortem analysis was combined with inputs of the velocity of the projectile, the absorbed energy to evaluate how efficient the material is at spreading the absorbed energy to a large area.

2. EXPERIMENTAL INFORMATION

2.1 BALLISTIC IMPACT TESTING

In this study a M16 rifle using 5.56 mm caliber bullets was used to fire shots threw a wooden laminate located at a distance of 10 meters in front of the firearm. High speed visible cameras were used to measure the projectile velocity before and after the sample. The Telops high speed infrared camera was used pointing at the target with a small angle of incidence at a distance about 12 meters. Detailed test setup parameters are presented in table 1

Parameters	Unit	Value
Bullet diameter	mm	5.56
Bullet mass	g	4.1
Bullet entry speed	m/s	905
Infrared Camera frame rate	Hz	7000

Table 1. Experiment parameters.

2.2 ACTIVE THERMOGRAPHY TESTING

Active thermography experiments were conducted with Telops new non-destructive testing solutions called TESTD. Flash lamp source with pulse energy of 6 KJ was used to excite the wooden laminate sample after the ballistic testing. Telops high definition Infrared camera was used to capture the sample cooling after the pulse heating and Fourier transform analysis were conducted to obtained phase images.

3. RESULTS

The ballistic impact testing was conducted on 3 different materials (all composite type) with a total of about 80 shots. We analysed three different impact type: bouncing, perforation and partial perforation at different projectile speeds. The figure 1 a and 1b show phase images of the ballistic plate at 2 Hz and 0.03.Hz. Impact damage at the surface of the sample can be seen and quantified using the high frequency phase image, while the low frequency phase image is used to assess the subsurface damage. The impact radius was found to increase linearly with the projectile speed in the partial perforation case, while being independent of projectile speed in the total perforation scenario (see Fig 1.c)
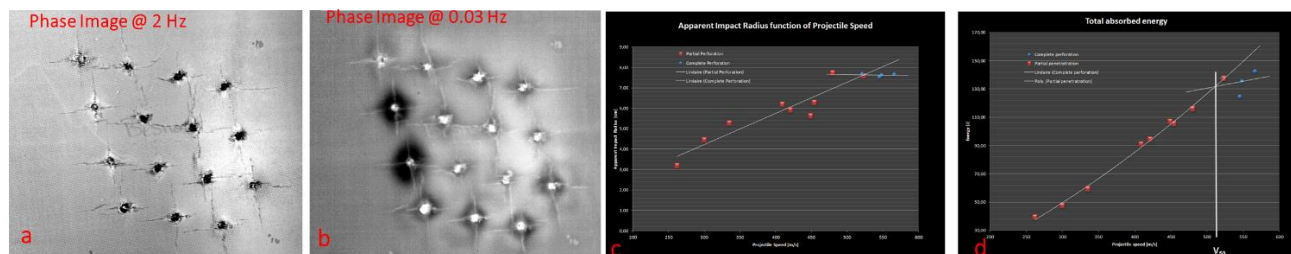

Fig. 1 Phase images (a,b) and radius (c) and total absorbed energy (d) as a function of projectile speed

We also analysed the total absorbed energy in the material (Fig.1d) for the different projectile speed and impact radius. This was used to assess the limit of V_{50} ballistic protection which is a determination of the arithmetic mean of the three highest values of projectile impact speed in the test sample resulting in partial penetration, and the three lowest values of impact velocity causing total penetration.

4. CONCLUSION

When sample is impacted by the projectile, at the moment of impact the projectile is slowed by a large number of individual fibers. As a result of the impact, fibers in the sample stretch and break to absorb the kinetic energy of the projectile casing. This creates a subsurface defect in the composite structure with a much greater area than the caliber of the projectile. We showed in this work that it is possible to assess the degree of destruction of the internal material as more damaged areas generate more heat, and over these areas, the surficial temperature signal has a higher value. We also demonstrated the benefits of using high speed infrared camera for energy measurement to the characterization of ballistic material are numerous. The most obvious of them is it's allowing the user to see beyond the visible deformation limit the real surface area affected by a ballistic impact. Heat is generated not only by the plastic mechanical deformation but also by the stress induced by the impact. These thermodynamic behaviours are easily captured by the high-speed infrared camera.

REFERENCES

[1] Hull D, Clyne TW (1996), An introduction to Composite Materials, Cambridge University Press, Cambridge.
[2] Jones RM (1975), Mechanics of Composite Materials, Hemisphere Publishing Corporation, New York.
[3] Reid SR, Zhou G. Impact behaviour of fibre-reinforced composite materials and structures. Woodhead Publishing; 2000.

WOODEN FLOORING INSPECTION USING ACTIVE THERMOGRAPHY

Simon Verspeek[1*], Bart Ribbens[1], Michaël Hillen[1], Xavier Maldague[2], Gunther Steenackers[1]

[1] Op3Mech Research Group, Faculty of Applied Engineering, University of Antwerp, 2020 Antwerp, Belgium
[2] Computer vision and systems laboratory, Department of Electrical and Computer Engineering, Université Laval, Quebec City, QC G1V 0A6, Canada

[*]Corresponding Author: Simon.Verspeek@uantwerpen.be

ABSTRACT

Wooden floorings have changed enormously in recent decades. Besides full wooden beams, different types of wooden composite materials are being used as flooring materials. These wooden composites mostly consist of different types of wood glued together. The technique of gluing several layers and pressing them together under high temperature makes it necessary to inspect the produced composites. Too little glue between two layers will result in air voids in the flooring while too much glue increases the production costs. These air voids can grow into delaminations. In order to produce wooden composites that look like full wooden beams, decals are being pressed into the top surface. These 3D decorations make it difficult to inspect the samples using visual inspections. Active thermography can offer a solution in detecting subsurface air voids and delaminations.

KEYWORDS: IR Thermography, Active Thermography, Wooden Flooring, NDT inspections, Wooden composites

1. INTRODUCTION

Active thermography is a widely known technique to detect subsurface defects and delaminations in composites. Frequently this technique is being used for carbon fiber reinforced parts. The technique however can be used to inspect different materials as well. Infrared thermography inspections use the differences in cooling down between the wooden sample and the air voids inside it. By performing a thermographic inspection in the beginning of the production line, it is possible to discard erroneous parts preventing unnecessary sawing and carving. Performing in-situ inspections will have to use the technique of dynamic line scan thermography since there is no place where the wooden plates rest for a time period during the production process.

2. METHODOLOGY

In order to inspect the wooden flooring in-situ, we have performed preliminary measurements in the lab. Since the characteristics of the wooden samples are unknown to us, we inspected the samples using pulse thermography first. During these tests we tried to discover the needed heating power and cooling time in order to detect the air voids in the wooden flooring. Secondly we performed dynamic line scan inspections on low speed (15 mm/s) to improve the set-up parameters for the inspection. As third step in the process we inspected the samples on higher velocities (2 m/s) and in the coming months we will perform in-situ measurements at 5 m/s.

2.1 PULSE THERMOGRAPHY

Performing inspections can be very challenging when the properties of the sample are unknown. Performing a basic pulse thermography inspection offers the possibility to easily find suitable set-up parameters for the measurements. The measurement set-up for the pulse thermography measurements is shown in **Fig. *1***.

Fig. 1: Measurement set-up for pulse thermography inspections. The set-up consists of a cooled FLIR X6540sc camera, the wooden sample and a halogen tube lamp.

2.2 DYNAMIC LINE SCAN THERMOGRAPHY

Performing inspections on the wooden flooring in-situ requires the use of dynamic line scan thermography (DLST) since the wooden plates move on conveyor belt without resting in the same place for a certain time . In order to reach the final speeds required for the real production process, dynamic inspections are performed first on lower speeds in our lab. This way we can optimise the measurement parameters. Once the measurements on low speed are adequate, we can increase the movement speed to the velocity used in the production process.

Fig. 2: Measurement set-up for dynamic line scan thermography on low speeds. The wooden samples translate beneath a heating source of 1 kW and are inspected using a thermal camera afterwards.

3. CONCLUSION

Inspecting wooden flooring is needed since the use of full wooden beams is more and more replaced by glued wood. Using too little glue will result in air voids trapped inside the panels, resulting in unwanted delaminations. Inspecting these samples using visible inspections is challenging regarding the decals that are pressed on the surface of the wooden flooring. Active thermography can offer a solution to inspect the wooden plates since the air voids are subsurface defects and the difference in cooling down between the wood and the air after the pressing under high temperatures. Since the flooring does not rest for a certain time period during the production process, dynamic line scan thermography is needed. Therefore we have optimized the measurement set-up to inspect wooden samples using dynamic line scan thermography on low speeds, before increasing the speed to match the production speed.

ACKNOWLEDGMENT

REFERENCES

[1]   Maldague X. Nondestructive evaluation of materials by infrared thermography. London: Springer; 1993.
[2]   J. Peeters, S. Verspeek, S. Sels, B. Bogaerts, and G. Steenackers, "Optimised dynamic line scanning thermography for aircraft structures," in *Quantitative infrared thermography*, 2018, pp. 1–9.
[3]   R. Pitarma, J. Crisóstomo, and L. Pereira, "Detection of wood damages using infrared thermography," in Procedia Computer Science, 2019, vol. 155, pp. 480–486.
[4]   G. López, L. A. Basterra, G. Ramón-Cueto, and A. De Diego, "Detection of singularities and subsurface defects in wood by infrared thermography," Int. J. Archit. Herit., vol. 8, no. 4, pp. 517–536, Jul. 2014.

Infrared-Based Non-Invasive Computer-Aided Diagnosis for Early Detection of Breast Cancer using Dynamic Thermography

Bardia Yousefi[*], Clemente Ibarra Castanedo, Xavier P.V. Maldague

Department of Electrical and Computer Engineering, Laval University, Québec City (Québec) G1V 0A6, Canada
Email : Bardia.Yousefi.1@ulaval.ca, {IbarraC, Xavier.Maldague}@gel.ulaval.ca
[*]Corresponding Author

ABSTRACT

Mammography is still a gold standard for breast cancer screening, which is an ionized imaging modality (X-ray). Magnetic resonance imaging (MRI) is also another common imaging system used for screening, but it is relatively expensive. With the current developments in infrared thermography, breast screening using dynamic thermography seems a great alternative system for early diagnosis of breast abnormality. Here, we use the frontal pose of 55 breast cancer screening participants for preliminary assessment of potential breast cancer symptoms. Sparse non-negative matrix factorization (Sparse NMF), and Semi NMF are used to extract the low-rank representation of the thermal image and generate thermal imaging features, called *thermomics*. Then we train a logistic regression to classify between healthy and symptomatic patients. The practicality and efficiency of these methods are demonstrated by the experimental results for preserving thermal heterogeneity led to detection of malignancy in breast cancer screening data with the accuracy of 74.1%, and 77.8% for Semi-NMF, and Sparse- NMF, respectively.

KEYWORDS: Breast cancer, infrared imaging modality, computer-aided diagnosis, sparse- and semi- non-negative matrix factorization.

1. Introduction

According to the world health organization (WHO), cancer is a foremost cause of death worldwide, accounting for an overall estimation of 9.6 million deaths in 2018, where breast cancer considers being the most common cancer with lung cancer having 2.09 million cases, which leads to 627,000 deaths [1,2]. Despite a far better survival rate versus lung cancer, early detection of breast abnormality creates a tremendous effect on prognosis and course of treatment. This paper presents an infrared-based breast cancer screening using thermal radiomics, called thermomics, and the application of sparse- and semi- non-negative matrix factorization (NMF) for low-rank matrix approximation of thermal sequence.

Matrix factorization methods can efficiently expose defects in the sequence of thermal images [3-11]. Several recognized matrix factorization techniques, for instance, principal component analysis/thermography (PCA/PCT) [3, 4, 6] and NMF [7,8-10], have been utilized for the past some years in various fields. The main challenge of dealing with high-dimensional infrared imaging sequences in various applications continues. In this paper, we propose an application of low-rank matrix approximation using semi- and sparse-NMF for thermal breast cancer screening passive thermographic imaging.

2. Methodology

NMF performs matrix factorization similar to PCA with non-negative constraints for basis and coefficient matrices. While keeping the constraint for the coefficient matrix and let the basis matrix to be negative, NMF converts to semi- NMF. Let I signify a sequence with τ thermal images where every image has a spatial dimension of $N \times M$. The X is the input data built by attaching the vectorized thermal images, $X = \{x_1, x_2, ..., x_\tau\}$ and $x_1 = vectorized\{I_1\}$. The PCT [3] decomposes the input data, X, to $U\Sigma V^T$, where U and Σ are the eigenvector (basis) and eigenvalue (coefficient) matrices. The bases corresponding to 80% maximum
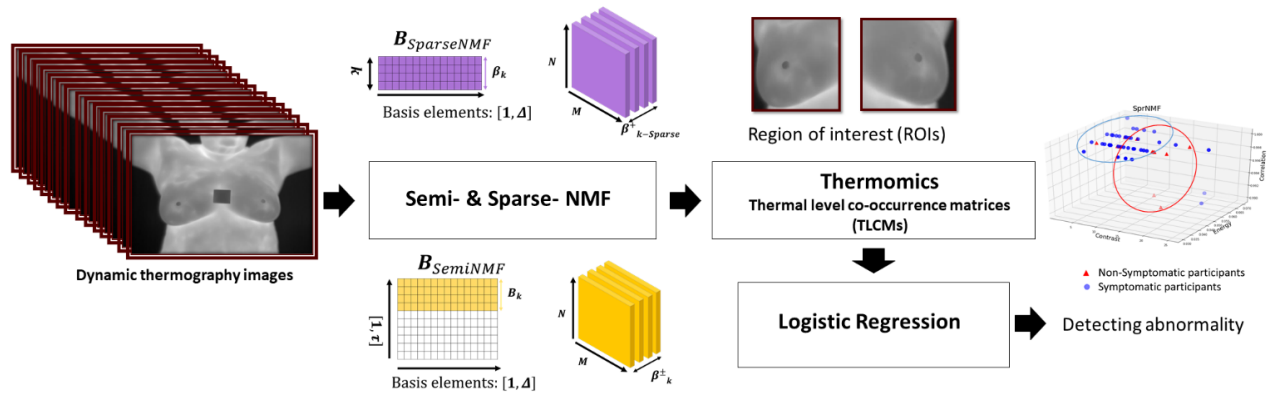
Figure 1. Workflow of the proposed method using low-rank matrix approximation using semi- and sparse- NMF and thermomic analyses to train a logistic regression presents.

variance catch the highest changes in thermal patterns (maximum thermal heterogeneity) amongst the bases, known as low-rank matrix approximation. But there is no guarantee of independency and non-overlapping property in the decomposed bases, which rises collinearity among the bases.

This directs to create many alike components and challenging selection of a representative basis. This is known to be a downside of PCT in low-rank approximation. Sparse-PCT [5,6,11] strives to alleviate this by inserting penalty terms, that expands the sparsity in the bases (from the basis matrix B - Figure 1) and controls the collinearity by limiting the domain of solution. Thermal patterns calculated by low-rank matrix approximation Sparse-PCT demonstrate more distinct bases than PCT [5,6,11].

NMF works similar PCA (PCT) and presents by a linear combination of k basis vectors to rebuild the data, X, whereas constrained the overlapping bases by having additive non-negative constraints for coefficient and basis matrices. NMF is similar to the PCA decomposition but the PCA's basis vectors can be negative. X is the input data and can be demonstrated by a linear combination of τ bases, $B = [\beta_1, \beta_2, \dots, \beta_\tau]$ and A coefficient. This is presented as follows:

$$X = BA \qquad s.t. \qquad A \geq 0, \qquad B \geq 0$$

where $X \in R^+_{\Delta \times \tau}, \Delta = MN, A \in R^+_{\tau \times \tau}$ [12].

The non-negative property substantially enhances the chance for having bases with a distinctive feature of thermal patterns as every basis relates to particular thermal patterns caught by maximizing the thermal variance. Consequently, the NMF associates with clustering because of nonnegative constraints for bases [12]. NMF employed in thermography and k first bases could be thermal patterns utilizing some numerical calculations such as non-negative least square error algorithms and gradient descent. Similar to sparse PCT, adding ℓ_1 norm term as penalty term increases the sparsity of bases [13], which can be presented by the following equation:

$$C_{sparse-NMF} = \frac{1}{2} \|X - BA\|_F^2 + \lambda \|\lambda\|_1$$

Let $\|B\|_p$ is the 'p-norm of B given by $\left(\sum_{d,m} \|B_{d,m}\|^p\right)^{\frac{1}{p}}$ [14] to calculate B for convex A. It also refers to as least absolute shrinkage and selection operator (LASSO) [15]. Sparse NMF is similar to sparse-PCT but with non-negative constraints, low-rank sparse-NMF obtains by selecting k bases correspond to the highest coefficients (as shown in Figure 1). Furthermore, sparsity in the bases decreases noise impact in the measurement of low-rank representation of the thermal matrix.

Having a low-rank approximated image, we select a region of interest (ROI) by selecting the breasts area and extracting thermal level co-occurrence matrices (TLCMs) features for the ROI. With that, we train a logistic regression model to be able to classify between healthy and non-healthy patients.

3. Study population

Fifty-five healthy participants (with/without symptoms) or sick (diagnosed by mammographic imaging) were employed for breast screening. The median age in our study sample was 61 years, and the participants comprised 28 Caucasian (51%), 15 African (27.3%), 11 Pardo (20%), and 1 Mulatto (1.8%) women. Among the participants, 18 had a history of diabetes in their families (32.7%), and 9 were undergoing hormone replacement (16.4%). All patients had IR images obtained by the following acquisition protocol: images have a spatial resolution of 640×480 pixels and were captured by a FLIR thermal camera (model SC620) with a sensitivity of less than $0.04°C$ range and capture standard of $40°C$ to $500°C$ [16,17]. Table 1 shows the clinical information and demography of the cohort.

Table 1. The clinical information and demographics of the database for mastology research are presented.

DMR - Database for Mastology Research		
Age	Median (±IQR)	61 (27,87)
Race	Caucasian	28 (51%)
	African	15 (27.3%)
	Pardo	11 (20%)
	Mulatto	1 (1.8%)
	Healthy[2]	24 (43.6%)
Diagnosis[1]	With symptoms	9 (16.4%)
	Without symptoms	15 (27.3%)
	Sick[3]	28 (51%)
	Unknown	3 (5.4%)
	Diabetes	18 (32.7%)
Family history	Leukemia	1 (1.8%)
	None	36 (65.5%)
Hormone therapy (HT)	Hormone replacement	9 (16.4%)
	None	46 (83.6%)

[1] *This diagnosis was performed with mammography as ground truth in this Dataset.*

[2] *Healthy term is used as non-cancerous patients but might have symptoms (symptomatic).*

[3] *We use the term "sick", which includes different types of breast cancer patients diagnosed by mammographic imaging.*

4. Results

For every participant, seven low-rank matrices were extracted using low-rank matrix approximation methods, where every case had 23 thermal images. Out of 7 low-rank matrices, we selected one matrix manually based on having comparatively the best contrast property. The selected representative images, called an *avatar*, are presented in Figure 2 for some example participants with normal and abnormal conditions. Heterogeneous thermal patterns were found for 31 participants in breast cancer screening indicating abnormality (healthy participants but with symptoms) or cancerous lesions in the breast area (Figure 2.a-c). More homogeneous thermal patterns were detected among the healthy participants (healthy with no symptoms, Figure 2.d-f).
Four properties of the TLCM matrices were determined to measure the level of contrast, dissimilarity, correlation, energy and homogeneity among the pixels in the ROI.
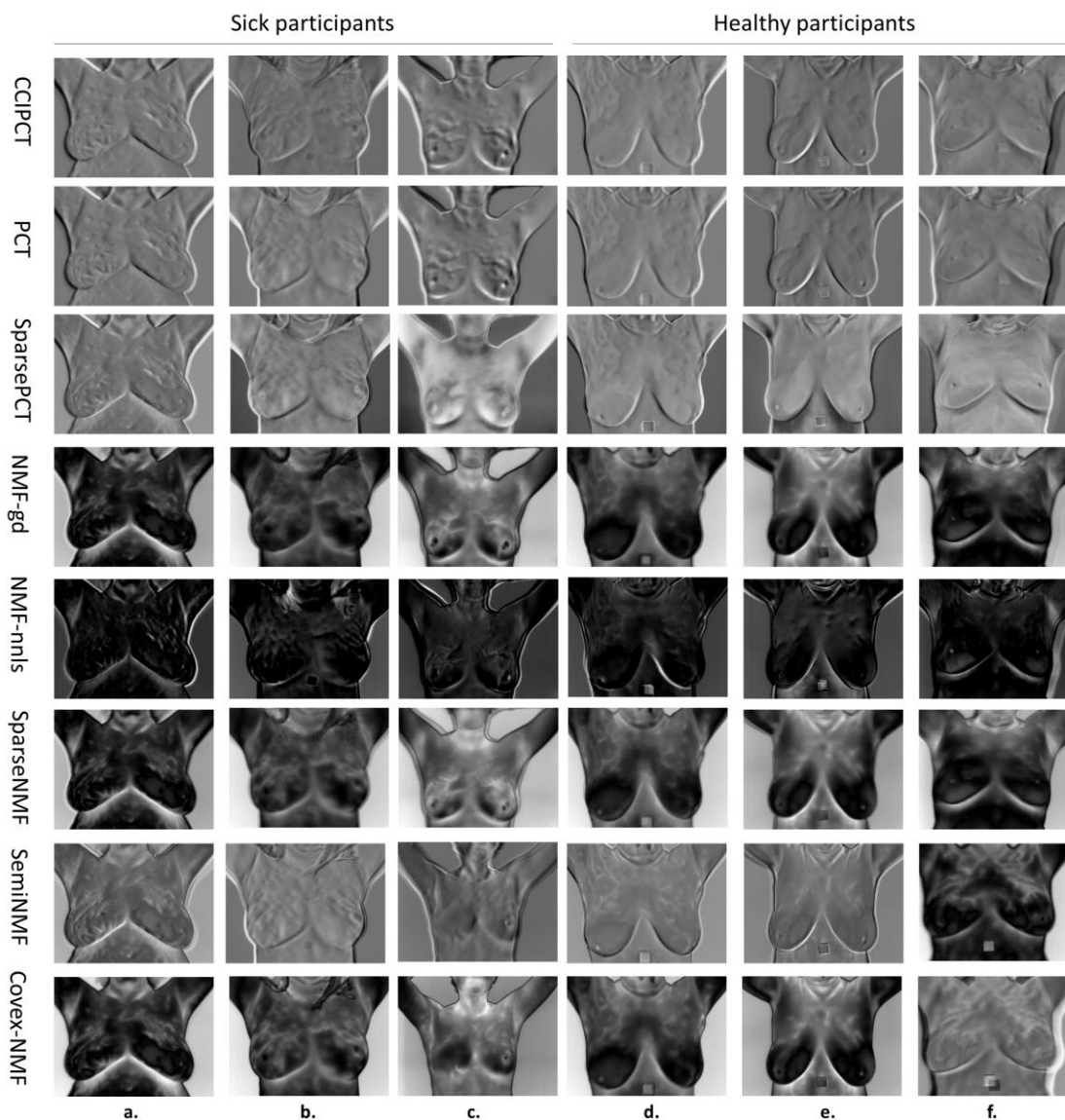
Figure 2. The results of low-rank approximation of thermal sequence are presented using different matrix factorization techniques. Columns (*a-c*) show symptomatic patients (diagnosed by mammography as cancer patients or healthy with symptoms), where columns (*d-f*) show the result of methods for healthy participants.

We classified the participants into two groups of symptomatic (non-healthy) and non-symptomatic (healthy) using thermomic properties based on the binary GT data obtained from mammography information. Semi- and sparse- NMF showed statistically significant separation of the two groups of participants when split on contrast-based TLCM. A logistic regression model fitted for multivariate thermal covariates (contrast, dissimilarity, correlation, homogeneity, and energy) was used to assess the hypothesis that the thermal heterogeneity can be utilized as a biomarker to stratify among participants (to determine symptomaticity). The accuracy levels were 74.1%, and 77.8% for Semi-, and Sparse- NMF, respectively. The two highest accuracies were found to belong to NMF-gd and sparse- PCT, with values of 81.5% and 79.6%, respectively. CCIPCT and PCT were commonly showed 75.9% accuracy. Figure 3 shows the receiver operating characteristic (ROC) curve for this comparative analysis of classifying potential breast cancer patients. Also, the separation of healthy and symptomatic patients using sparse NMF for contrast, correlation, and energy properties of thermomics are shown (left image).
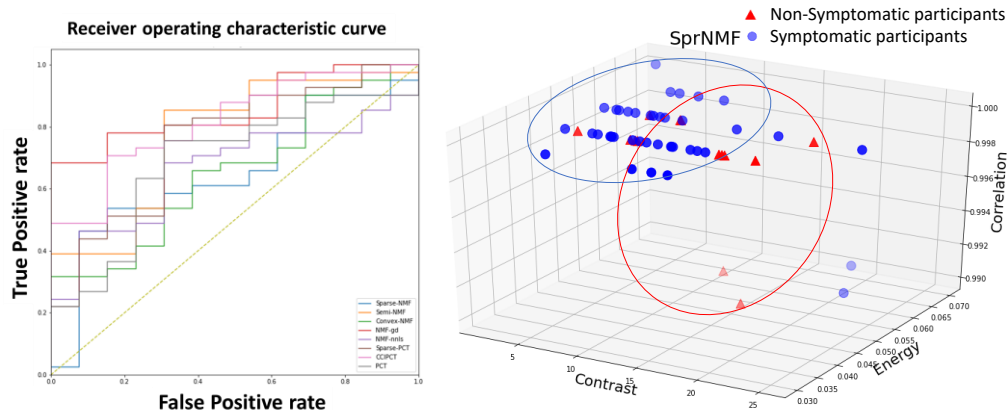
Figure 3. The ROC graph (right image) for different matrix factorization approaches are presented for multivariate covariates logistic regression binary classification (abnormal or healthy participants). Separation of healthy and symptomatic patients using sparse NMF for contrast, correlation, and energy properties of thermomics are shown (left image).

5. Conclusions

This study proposed comparative analyses and an application of the semi- and sparse- NMF algorithms in infrared diagnostic systems. We measured thermal heterogeneity in 55 cases of the breast cancer screening from DMR dataset. We compared the appropriateness of these approaches versus the state-of-the-art thermographic methods, such as PCT, CCIPCT, Sparse-PCT, NMF-gd, and NMF-nnls. The results indicated the significant performance of semi-, and sparse- NMF in preserving thermal heterogeneity to discriminate between symptomatic and healthy participants (accuracy of 74.1%, and 77.8%, respectively). Future works should substitute the manual selection of the basis from the low-rank matrix approximation with an automatic selection. Besides, an expansion of the validation set to a larger infrared imaging cohort can further confirm the strength and limitations of these approaches.

REFERENCES

[1] Siegel, R. L., Miller, K. D., & Jemal, A. Cancer statistics, 2019. CA: A Cancer Journal for Clinicians 69(1) 7-34 (2019).

[2] World Health Organization report on cancer, September 2018, URL: https://www.who.int/news-room/fact-sheets/detail/cancer .

[3] Rajic, N. (2002). Principal component thermography for flaw contrast enhancement and flaw depth characterisation in composite structures. Composite structures, 58(4), 521-528.

[4] Yousefi, B., Sfarra, S., Castanedo, C. I., & Maldague, X. P. (2017). Comparative analysis on thermal non-destructive testing imagery applying Candid Covariance-Free Incremental Principal Component Thermography (CCIPCT). Infrared Physics & Technology, 85, 163-169.

[5] Yousefi, B., Sfarra, S., Sarasini, F., Castanedo, C. I., & Maldague, X. P. (2019). Low-rank sparse principal component thermography (sparse-pct): Comparative assessment on detection of subsurface defects. Infrared Physics & Technology, 98, 278-284.

[6] Wu, J. Y., Sfarra, S., & Yao, Y. (2018). Sparse principal component thermography for subsurface defect detection in composite products. IEEE Transactions on Industrial Informatics, 14(12), 5594-5600.

[7] Marinetti, S., Finesso, L., & Marsilio, E. (2006). Matrix factorization methods: Application to thermal NDT/E. NDT & E International, 39(8), 611-616.

[8] Yousefi, B., Sfarra, S., Ibarra-Castanedo, C., Avdelidis, N. P., & Maldague, X. P. (2019). Thermography data fusion and nonnegative matrix factorization for the evaluation of cultural heritage objects and buildings. Journal of Thermal Analysis and Calorimetry, 136(2), 943-955.

[9] Yousefi, B., Ibarra-Castanedo, C., & Maldague, X. P. (2019). Infrared Non-Destructive Testing via Semi-Nonnegative Matrix Factorization. In Multidisciplinary Digital Publishing Institute Proceedings (Vol. 27, No. 1, p. 13).

[10] Yousefi, B., Castanedo, C. I., & Maldague, X. P. (2020). Measuring heterogeneous thermal patterns in infrared-based diagnostic systems using sparse low-rank matrix approximation: comparative study. IEEE Transactions on Instrumentation and Measurement. , doi: 10.1109/TIM.2020.3031129.

[11] Gao, B., Woo, W. L., He, Y., & Tian, G. Y. (2015). Unsupervised sparse pattern diagnostic of defects with inductive thermography imaging system. IEEE Transactions on Industrial Informatics, 12(1), 371-383.

[12] Lee, D. D., & Seung, H. S. (1999). Learning the parts of objects by non-negative matrix factorization. Nature, 401(6755), 788-791.

[13] Kim, H., & Park, H. (2008). Nonnegative matrix factorization based on alternating nonnegativity constrained least squares and active set

method. SIAM journal on matrix analysis and applications, 30(2), 713-730.

[14] Donoho, D. L. (2006). For most large underdetermined systems of linear equations the minimal ℓ1-norm solution is also the sparsest solution. Communications on Pure and Applied Mathematics: A Journal Issued by the Courant Institute of Mathematical Sciences, 59(6), 797-829.

[15] Tibshirani, R. (1996). Regression shrinkage and selection via the lasso. Journal of the Royal Statistical Society: Series B (Methodological), 58(1), 267-288.

[16] Sequeiros, G. O. Desenvolvimento de um Banco de Dados Acessiveis Via Web com Recuperação Baseado no Conteúdo. M. Sc. thesis, IC-UFF, 2013.

[17] Silva, L. F.; Saade, D. C. M.; Sequeiros, G. O.; Silva, A. C.; Paiva, A. C.; Bravo, R. S.; Conci, A., A New Database for Breast Research with Infrared Image, Journal of Medical Imaging and Health Informatics, Volume 4, Number 1, March 2014 , pp. 92-100(9).

COMPARISON STUDY OF DIFFERENT ALGORITHM FOR MICROCRACK DETECTION USING EDDY CURRENT PULSED THERMOGRAPHY

Xiang ZHANG, Jianping PENG[*], Lingfan FENG, Jie BAI, Xiaorong GAO

School of Physical Science and Technology, Southwest Jiaotong University,610031 Chengdu, China

[*]Corresponding Author: adams.peng@swjtu.edu.cn

ABSTRACT

In this paper, sample with a 2mm fatigue microcrack was detected by eddy current pulsed thermography (ECPT). Principal component analysis (PCA) and Tucker decomposition were used in the heating stage to enhance the detectability and sensitivity, the signal-to-noise ratios (SNR) of the two algorithms were obtained after processing. In addition, thermal quotient was used to assess the temperature variation trend. The potential correspondence between crack closure and temperature change is investigated.

KEYWORDS: Microcrack, Principal component analysis, Tucker decomposition, crack closure

1. INTRODUCTION

In recent years, infrared (IR) technology has been successfully applied to power, rail and other fields because its advantages for non-contact, high sensitivity, and visualization [1-3]. Eddy Current Pulsed Thermography (ECPT) belongs to active infrared thermography, uses external high frequency alternating current to excite the detection coil to generate heat on the surface or inside of the measured specimen [4].

In-service equipment may exist complex natural defects due to stress and impact loads [5]. There are several outstanding results based on ECPT in the fields of crack detection have been reported. Specifically, Vrana *et. al.* proposed the simplified models for crack detection with induction thermography [6]. Gao *et. al.* focus on the quantitative assessment for the surface defects [7]. Netzelmann *et. al.* introduces the applications for induction thermography [8]. Liu *et. al.* proposes a ferrite magnetic structure for fatigue crack inspection on metallic materials [9].

The rich transient information in the ECPT has become the grounding for further analysis [10]. For enhance resolution, Maldague *et al.* [11] proposed Pulse phase thermography, which has advantage in quantitative inversion. Wang *et. al* [12] used PCA to process the artificial crack in a steel sample and natural fatigue cracks in aircraft brake components, while Gao *et. al* [13] developed a spatial transient phase tensor model to extract and separate patterns. Ahmed *et al.* [14] proposed a low rank sparse algorithm to mine the weaker information for feature enhancement. Genest *et. al* [15] used both experimental and numerical assessments of the induction thermography technique detecting the microcrack in the notched steel coupons.

However, previous research rarely discusses the diagnosis of crack closure effect, which is commonly exist in industry. It remains a challenge to distinguish the weak thermal features of closed cracks. In this study, we aim to applications of ECPT in fatigue microcrack a more comprehensive way. Experimental tests on fatigue precrack by three-point bending have been conducted, which is an important step towards artificial crack to natural fatigue crack. Comparing with PCA, tensor decomposition could preserve more defect information. The performance to detect fatigue crack is discussed through SNR and thermal quotient. The remaining part of this paper has been organized as follows: The methodology used in this work is described in Section 2. The experimental setup and result for specimens with different shape are given in Section 3. Finally, Conclusion is outlined in Section 4.

2. METHODOLOGY

2.1 INDECTION HEATING THEORY OF ECPT

The main physical process of ECPT involves induced eddy currents heating and thermal diffusion. These eddy currents are governed by a subsurface penetration depth, based on an exponentially damped skin effect. According to Joule's law, the thermal power generated by the internal resistance of the material is:

$$P_w = \frac{1}{\sigma}\left|J_e\right|^2 = \frac{1}{\sigma}\left|\sigma E\right|^2 \tag{1}$$

Where J_e is the eddy current density and E is the electric field strength, equation (1) determines the resulting temperature field. In general, the environmental temperature or reference temperature is taken as a constant T_0. Thus, the heat conduction equation of a specimen in the company of a defect can be expressed as:

$$\frac{\partial^2 T}{\partial x^2} + \frac{\partial^2 T}{\partial y^2} + \frac{\partial^2 T}{\partial z^2} + \frac{1}{\lambda}q(x, y, z, t) = \frac{\rho C_p}{\lambda}\frac{\partial T}{\partial t} \tag{2}$$

where $T=T(x, y, z, t)$ denote the temperature distribution, λ is the thermal conductivity of the material, ρ is the density, and C_p is the specific heat, and $q(x, y, z, t)$ is the internal heat generation function per unit volume and unit time.

2.2 PRINCIPAL COMPONENT ANALYSIS

For raw data, PCA is an unsupervised classification method and has strength for reduces the dimensionality of the data, while keeping most of the variation in the data set. Each PC could be consider as a linear combination of the original thermal sequences and ranked in decreasing order. Singular value decomposition and covariance matrix decomposition methods were used to decompose the 2-D thermal matrix by:

$$T = URV^T \tag{3}$$

where U is a matrix, contains a series of empirical orthogonal functions (EOFs). R is a diagonal matrix with the singular values of T, V is an orthogonal matrix.

2.3 TENSOR DECOMPOSITION

A tensor is a multi-dimensional array. The infrared sequences recorded by IR camera can be represented by a third-order tensor $X \in R^{I_1 \times I_2 \times I_3}$, with two modes representing spatial position, and the third mode for the transient information. We decompose the higher-order tensor into a core tensor multiplied by a matrix along each mode. In the three-way case, the discretized tensor $X \in R^{I_1 \times I_2 \times I_3}$ can be calculated by Tucker decomposition [16] as:

$$X \approx G \times_1 A \times_2 B \times_3 C = \sum_{p=1}^{P}\sum_{q=1}^{Q}\sum_{r=1}^{R} g_{pqr} a_p \circ b_q \circ c_r \tag{4}$$

where $G \in R^{P \times Q \times R}$ is the core tensor, $A \in R^{I_1 \times P}$, $B \in R^{I_2 \times Q}$ and $C \in R^{I_3 \times R}$ are the factor matrices considered as the principal components in each mode. P, Q, and R are the number of components in the factor matrices. The operator '$\circ$' denotes the vector outer product. The tensor decomposition method does not perform dimensionality reduction on the thermal imaging high-dimensional image. Therefore, the tensor algorithm can maintain the structural stability of the original data and extract more crack features. This decomposition is illustrated in Fig. 1
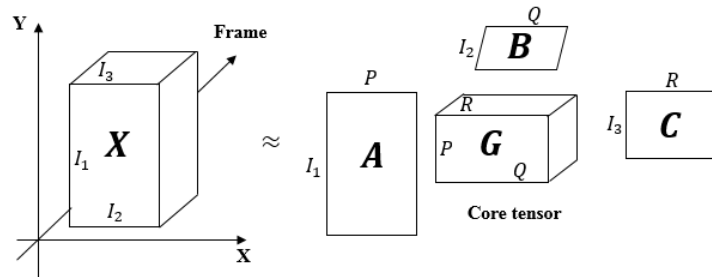

Fig. 1 Decomposition of 3rd-order tensor into one core tensor and three mode matrices.

2.4 FRAMEWORK FOR THIS WORK

Based on the theory introduction in this section, a research approach diagram for ECPT of defect characterization in two specimens with different shapes was proposed, as shown in Fig. 2. It is initiated by using ECPT platform to acquire the raw data. Then, the thermal sequences are preprocessed by PCA and tensor decomposition respectively in the region of interest (ROI) to enhancing the thermal contrast. After that, max thermal response and temperature linescan were used to extracted the thermal features. Finally, the SNR and thermal quotient are used to evaluate the performance.
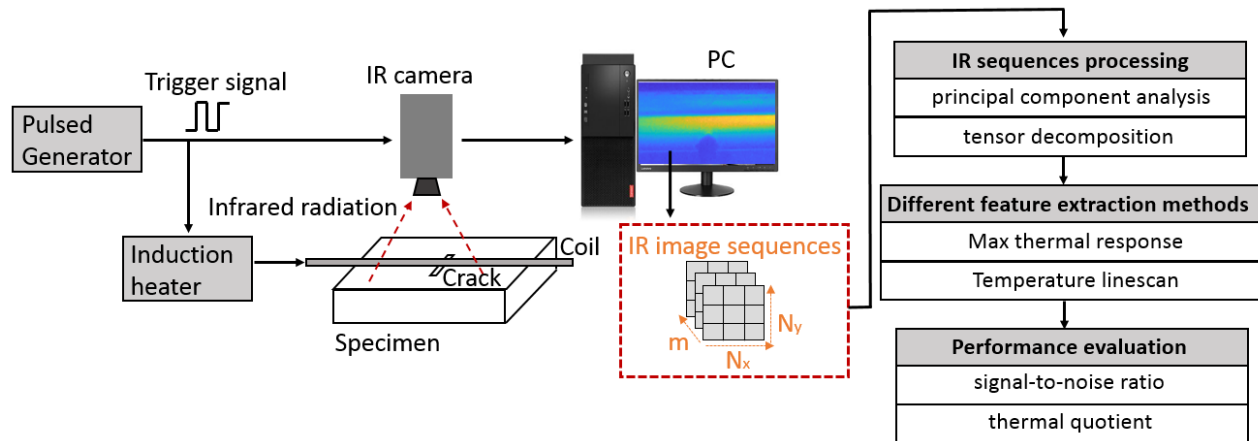
Fig. 2 Inductive thermography and research approach diagram.

3. EXPERIMENT AND RESULTS

3.1 SPECIMEN AND EXPERIMENTAL SETUP

The rail specimen with machined notch (type V) is described in Fig. 3. Table I gives its material properties. In this work, a straight-through notch with 1 mm in depth was introduced using spark discharge. The straight-through notch was placed at the to the machined notch's tip. Using this method, we were able to generate a well-defined and straight fatigue precrack by three-point bending. The setup of the three-point bending test is shown in Fig. 3. Prior to produce precrack, the specimen surfaces were polished by SiC paper up to #1000. After that, a straight fatigue crack was generated by using a fatigue testing machine (MTS809, USA) with a sinusoidal 20 Hz waveform.
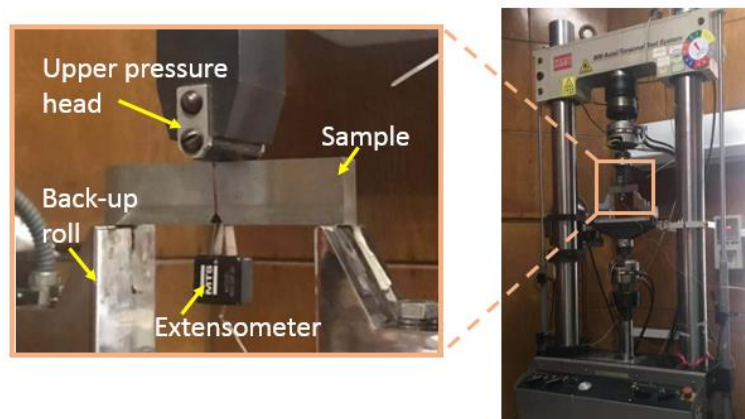

Fig. 3 Three-point bending test setup

The specimen with precrack then tested by ECPT method in two conditions each, with conditions before and after resection along the red dashed line in Fig. 4. That is, specimen were machined into two types (after three-point bending tests) as illustrated in Fig.

4, where a is the fatigue precrack length (2 mm), c is the length of machined notch (type v), b and d are the thickness and width, respectively.
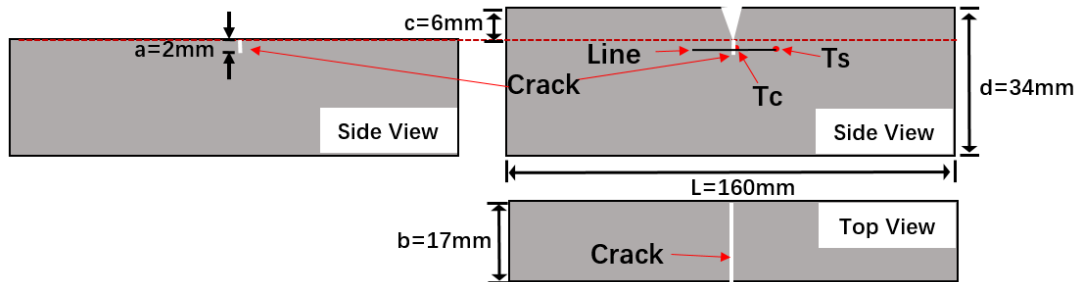
Fig. 4 Diagram of specimen

Table 1 Material parameters.

Parameters	Values
Relative permittivity	100
Conductivity (S/m)	5×10^6
Heat capacity ($J/(kg\ K)$)	490
Thermal conductivity ($W/(m\ K)$)	50
Thermal diffusivity (m^2/s)	1.172×10^{-5}
Temperature coefficient, α ($1/°C$)	5.0×10^{-3}
Density (kg/m^3)	7.7×10^3
Poisson's ratio	0.3
Elastic modulus (GPa)	200

The experimental platform for ECPT is shown in Fig. 5. Including an infrared camera, an excitation coil, a heating module and a PC. In the following experiments, the excitation current and frequency were set as 300 A and 286 kHz, respectively. The heating time was set as 200ms, and the total recording time was 2s. The FLIR SC650sc IR camera captures thermal images with a spatial resolution of 640*120 pixels at a frequency of 200 Hz, then, transmits the information of thermal sequences to computer for later analysis and data post-processing.
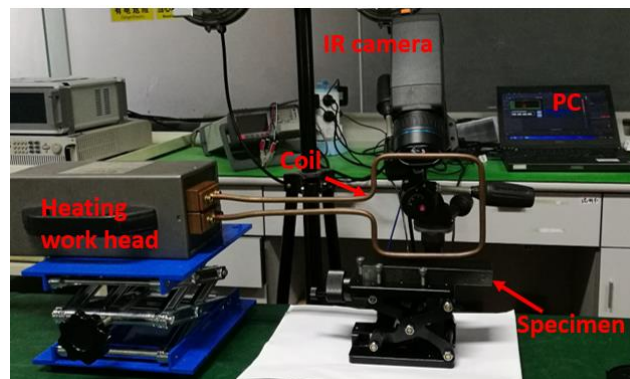
Fig. 5 Experimental platform for ECPT

A typical heating stage experimental results (at 0.2 s) for a specimen with machined V shape notch is shown in Fig. 6. The region of interest (ROI) including fatigue crack is presented for reduce of redundant background. A more detailed account of defect enhancement method is given in the following section.
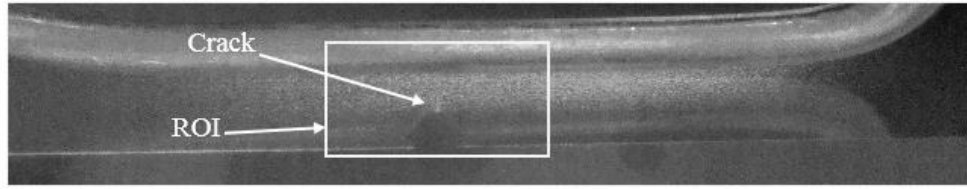
Fig. 6 Original thermal data and area of interest.

Fig. 7 and Fig. 8 show reconstructed data from 0 to 2 s by PCA algorithm. Setting same principal components for two different specimens, the difference between two blocks was whether they have v shape notch. In detail, the first two primary components contained mostly the information of coil and heat diffuses, means the contribution of these two parts plays an important role throughout the whole experiment. At the same time, component three represents the crack and the last component denotes the background noise. Clearly, PCA algorithm enhances defect characteristics, fatigue crack could be detected easier due to the less redundant information in the third principal component image.
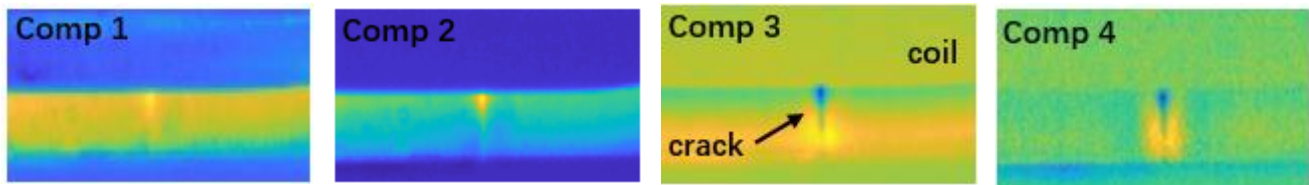
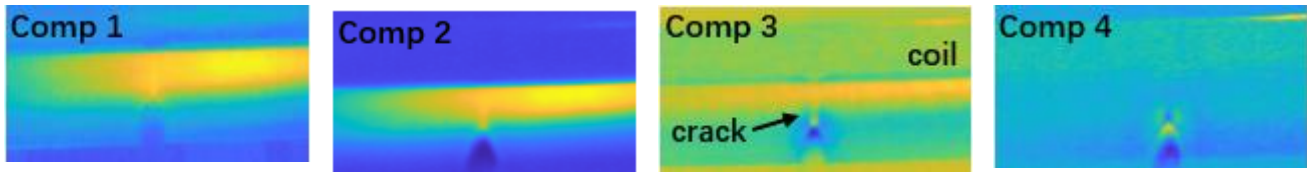**Fig. 7** PCA results for specimen without V shape machined notch

Fig. 8 PCA results for notched sample

Fig. 9 shows the results processing by tensor decomposition algorithm at heating stage, where two specimens both containing the low rank (background) part and the sparse (defect) part. From the results it can be seen that the precrack and background are well distinguished. As we mentioned before, background and thermal diffusion occupy the main part of the contribution rate. Therefore, after subtracted background in Low rank section, defect morphology is more clearly.
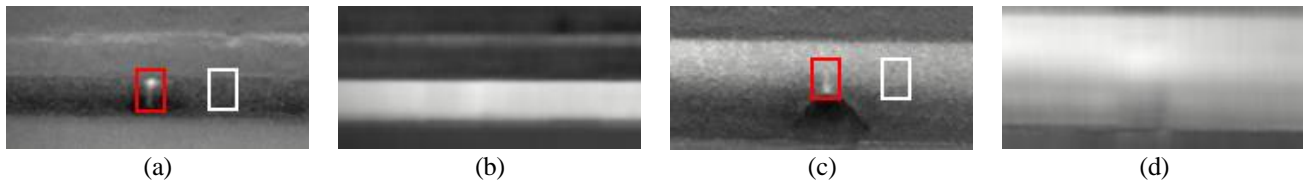

| (a) | (b) | (c) | (d) |

Fig. 9 Tensor decomposition results. (a) Sparse rank of sample without notch. (b) Low rank of sample without notch. (c) Sparse rank of sample with V shaped notch. (d) Low rank of sample with V shaped notch.

3.2 PERFORMANCE EVALUATION AND COMPARISON

Within our work, the signal-to-noise ratio (SNR) [17] is used to evaluates the performance for PCA and tensor decomposition. SNR describes the thermal contrast between the defective and non-defective region, prefabricated Crack region is selected as "signal" and defect-free region is selected as "noise". The calculation of SNR (dB) can be defined in the equation below:

$$SNR = 20\log_{10}\left(\frac{\sum_{i=1}^{m}\sum_{j=1}^{n}T_{d(i,j)}}{\sum_{i=1}^{m}\sum_{j=1}^{n}T_{n(i,j)}}\right) \tag{5}$$

Where $\sum_{i=1}^{m}\sum_{j=1}^{n}T_{d(i,j)}$ and $\sum_{i=1}^{m}\sum_{j=1}^{n}T_{n(i,j)}$ are sum temperature of crack region and non-defect area, respectively. Original image shows the raw data at 200 ms. The detection performance of various signal processing methods is listed in Table 2; high SNR value indicates better crack detection rate. The results show that the Tucker algorithm exhibits a higher crack identification ability than that of PCA algorithm in both specimens. Specifically, the result for original image showed that specimen with V shape notch is more efficient than un-notched sample. This could be due to the boundary effect, generated more heat than specimen without machined notch. This tendency was also present in the PCA results.

Table 2. Defect detection comparison for different algorithms with SNR in dB.

	Original	PCA	Tucker
SNR (un-notched)	0.984	0.823	1.233
SNR (with machined notch)	1.032	0.964	1.075

3.3 TEMPERATURE DISTRIBUTION COMPARISON

The heat distribution on the specimen is uneven due to the defect. In order to investigate the temperature profiles of different types of specimen, a line is created on the surface (see Fig. 4, specimen after resection should extract data with same position) and the temperature data on it are extracted (Fig. 10). This feature was extracted at pixel level. From the linescans, Fig. 10 have shown that 1) temperature present different distribution between the defective and defect-free areas; and 2) the width of heating up stage become narrower when the specimen without V shape notch; and 3) compare the results of different blocks, the temperature of defect-free region presents noticeably different. In detail, these phenomena may be explained that 1) crack closure effect may influenced by notch; and 2) Weak conductivity of closed cracks caused a different temperature response in the medial region, because the eddy current distribution has an inconsistency between specimens; and 3) The two tests were apart from each other by 120 days, they have different temperature in defect-free areas because the ambient temperature to vary.

Fig. 11 shows the result of maximum thermal response in defect region along heating periodicities, the effect of the specimen shape has been investigated. The ratio called thermal quotient were used to assess the temperature variation trend. It could be expressed by [18]:

$$T_q = \frac{\Delta T_{crack}}{\Delta T_{surface}}$$

(6)

Based on the result from Fig.11, it can be seen that both relations are monotonic. Then calculated the R-squared to evaluate the fitted linear relation. Specimen with V shape notch has a linear relation with high R-squared values (92.2%). The fluctuations in the unnotched data may related to crack closure.
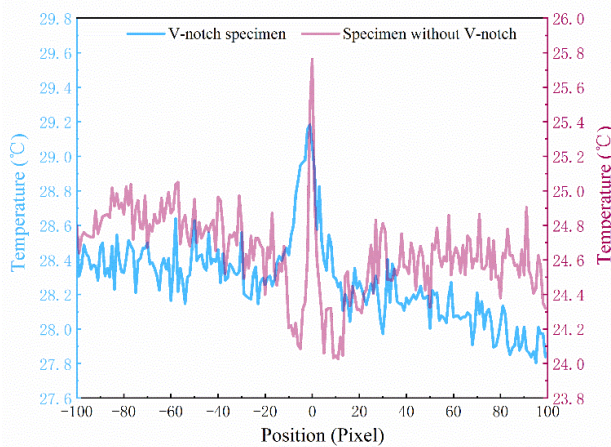

Fig. 10 Temperature line-scan of different specimen under 200-ms heating pulse.
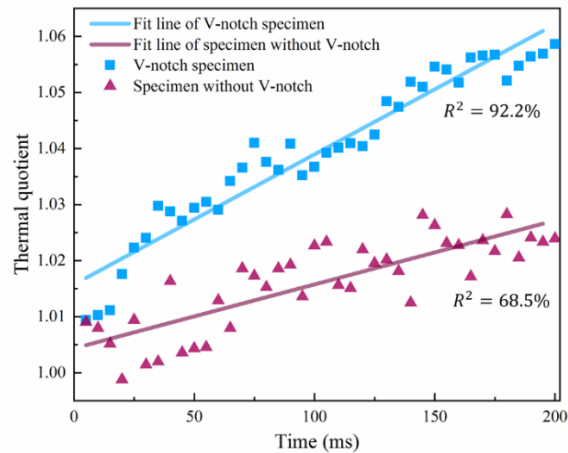

Fig. 11 Maximum Thermal Response versus time with linear fittings.

4. CONCLUSION

The microcrack is hard to detect with raw experimental data. Consequently, extract the feature of defect is useful to enhance the detection sensitivity. Compared with PCA, Tucker decomposition can maintain the structural stability of the original data and extract more crack features that denote a higher SNR. However, it should be noted that the shape of the sample will influence the detection results. Weak conductivity of closed cracks may change the temperature response in local areas.

ACKNOWLEDGMENT

REFERENCES

[1] Wilson John *et al.,* "PEC thermography for imaging multiple cracks from rolling contact fatigue." NDT & E International 44.6(2011):505-512.

[2] Ruizhen Yang *et al.,* "Induction infrared thermography and thermal-wave-radar analysis for imaging inspection and diagnosis of blade composites." IEEE Transactions on Industrial Informatics 14.12 (2018): 5637-5647.

[3] J. Peng *et al.,* Investigation into eddy current pulsed thermography for rolling contact fatigue detection and characterization, NDT&E Int. 74 (2015) 72–80.

[4] H Zhang *et al.,* "Eddy current pulsed thermography for ballistic impact evaluation in basalt-carbon hybrid composite panels." *Applied optics* 57.18 (2018): D74-D81.

[5] H Zhang *et al.,* "Optical and Mechanical Excitation Thermography for Impact Response in Basalt-Carbon Hybrid Fiber-Reinforced Composite Laminates." *IEEE Transactions on Industrial Informatics* (2017):1-1.

[6] Vrana J *et al.,* "MECHANISMS AND MODELS FOR CRACK DETECTION WITH INDUCTION THERMOGRAPHY." *AIP Conference Proceedings* (2008).

[7] B Gao *et al.,* Quantitative validation of Eddy current stimulated thermal features on surface crack[J]. Ndt & E International, 2017, 85:1-12.

[8] Netzelmann Udo *et al.,* "Induction thermography: principle, applications and first steps towards standardisation." *Quantitative InfraRed Thermography Journal* 13.2 (2016): 170-181.

[9] Zewei Liu *et al.,* "Natural cracks diagnosis system based on novel L-shaped electromagnetic sensing thermography." *IEEE Transactions on Industrial Electronics* (2019).

[10] B Gao *et al.,* "Electromagnetic Thermography Nondestructive Evaluation: Physics-based Modeling and Pattern Mining." *Rep* 6(2016):25480.

[11] Maldague Xavier, François Galmiche, and Adel Ziadi. "Advances in pulsed phase thermography." *Infrared physics & technology* 43.3-5 (2002): 175-181.

[12] Yizhe Wang *et al.,* "Thermal Pattern Contrast Diagnostic of Microcracks With Induction Thermography for Aircraft Braking Components." IEEE Transactions on Industrial Informatics 14.12 (2018): 5563-5574.

[13] B Gao *et al.,* "Multidimensional tensor-based inductive thermography with multiple physical fields for offshore wind turbine gear inspection." IEEE Transactions on Industrial Electronics 63.10 (2016): 6305-6315.

[14] Ahmedtl, Junaid, et al. "Ensemble Joint Sparse Low Rank Matrix Decomposition for Thermography Diagnosis System." *IEEE Transactions on Industrial Electronics* (2020).

[15] Genest Marc *et al.,* "Induction thermography of steel coupons with cracks." Applied optics 57.18 (2018): D40-D48.

[16] Junru Song *et al.,* "Ensemble tensor decomposition for infrared thermography cracks detection system." *Infrared Physics & Technology* 105 (2020): 103203.

[17] Lopez, Fernando *et al.,* "Optimization of pulsed thermography inspection by partial least-squares regression." NDT & E International 66. sep. (2014):128-138.

[18] Oswald-Tranta *et al.,* "Thermo-inductive crack detection." Nondestructive Testing & Evaluation 22.2-3(2007):137-153.

COMPARISON OF NON-DESTRUCTIVE TECHNIQUES IN PLAIN WEAVE CARBON FIBER REINFORCED POLYMERS UNDER FATIGUE LOADING

Nidhal Bouslama [1], Nicolas Quaegebeur [1*], Ahmed Maslouhi [1], Patrice Masson [1]

[1]GAUS, Dept Génie mécanique, Université de Sherbrooke, Sherbrooke (QC) J1K 2R1, Canada
*Corresponding Author: Nicolas.Quaegebeur@USherbrooke.ca

ABSTRACT

Damage initiation and development in a plain weave Carbon Fiber Reinforced Polymer (CFRP) composites is a complex and multiscale process, which requires a substantial investigation to understand their behavior under dynamic loading conditions. In this context, the present study proposes an in-situ approach based on three complementary Non-Destructive Testing (NDT) techniques. The experimental part consists of cycling two composite laminate configurations (with and without an embedded flaw, respectively noted WFS and NFS) under fatigue loading with continuous real-time measurement of the ultrasonic wave activity and surface strain evolution. For all specimens, monitoring was performed using acoustic emission (AE), digital image correlation (DIC) and air coupled ultrasonic (ACU) techniques. Damage indicators related to the fundamental antisymmetric A_0-mode velocity were established using ACU to quantify the damage state and remaining lifetime of the composite. A close correlation was found between the guided wave velocity and mechanical stiffness degradation.

KEYWORDS: NDT, ultrasound, DIC, composite fatigue testing, air-coupled, automated inspection

1. INTRODUCTION

Woven composites are constructed by interlacing two sets of threads, the warp and the fill, which offer balanced properties in the plane of the fabric and improve formability. The numerous advantages have promoted the integration of woven composites into the design of principal structure elements (PSE), even if there are still some hurdles to overcome issues related to damage initiation and their impact on structural integrity under fatigue loading.

Indeed, composite fatigue life and structural damage tolerance are much more complicated and less well understood than that of conventional metallic materials. Generally, fatigue damage in a composite is accompanied by extensive damage accumulation throughout the specimen volume, which is attributed to matrix cracks, fiber breakage, fiber-matrix shear damage and delamination. The complexity and the interaction between the different damage modes makes the development of a commonly accepted method for evaluating structural integrity difficult. In this context, Non-Destructive Testing (NDT) techniques have demonstrated valuable contributions for both understanding the mechanical behavior and identifying the damage process. In the current study, a robust monitoring approach was developed by cross-validation of results from three complimentary NDT techniques with multiscale capabilities. The proposed method is based on simultaneous and continuous in-situ measurements using acoustic emission (AE), digital image correlation (DIC) and air coupled ultrasonic (ACU) techniques. These methods have complimentary capabilities by monitoring both macro-scale features such as the global stiffness and strain fields as well as microstructural damages like matrix cracks and fibre-resin interfaces decohesion.

2. TEST MATERIAL AND EXPERIMENTAL SETUP

2.1 EXPERIMENTAL SETUP

The tested specimens are composed of a woven fabric composite with a plain weave configuration made of eight plies with the following staking: $[45,0,-45,90]_S$. The plate has an average thickness of 11.9 mm and dimensions of $304 \, x \, 76$ mm, as shown in Fig. 1. An artificial flaw was introduced by inserting a Teflon tape between the third and fourth plies, centered in the middle of the coupon. The artificial defect has a square shape with dimensions of 12.5 x 12.5 mm representing the typical inspectable damage size of a delamination in service condition.

In this study, all the tests were carried out on an MTS 320 hydraulic testing machine. The specimens were tested under the same constant loading amplitude, which was fixed at 60 % of the Ultimate Tensile Strength (UTS) with a stress ratio (R) of 0.1 and a cycling frequency of 7 Hz. To ensure the repeatability and appropriate statistical interpretation of the results, three specimens of each configuration were tested until final failure. Continuous in-situ measurement between AE, ACU and DIC systems was achieved by synchronizing the acquisition with the applied force signal such that all the measurements were performed simultaneously at the same load.
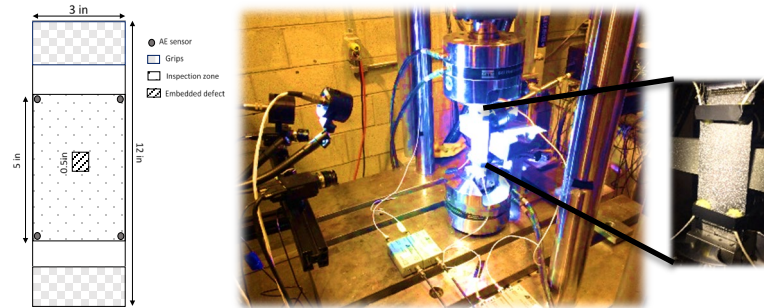
Fig. 1 Experimental testing configuration (left) and monitoring setup including AE – DIC and ACU (right)

2.2 EXPERIMENTAL RESULTS

The normalized evolution of the cumulative counts for the specimens over the normalized fatigue life are depicted in Fig. 2 (left) using the AE system. The cumulative count evolution exhibits a stepwise evolution in which three phases can be identified. The first phase is related to the damage originating at the specimen edges, followed by a flat zone with relatively low acoustic activity. An important rise is then observed between [40%-60%] of the fatigue life, during which local cracks increased from the mid-zone of the inspected area. The major part of this activity is attributed to the initiation of delaminations around the embedded flaw. The third phase is characterized by a much less pronounced increase where links between outside and around flaw take place leading to the final collapse of the specimen. The stiffness degradation caused by fatigue loading was determined using the DIC system based on the average strain field measured over the area of interest. Fig. 2 (middle) shows the normalized stiffness modulus (E/E_0) for the WFS configuration. The total stiffness decay for the three specimens varies between [10 to 18%] compared to [16 to 23%] for NFS. These values are in accordance with the level of damage observed in the failed coupons.

The changes of group velocity measured using the ACU system are presented in Fig. 2 (right). At the end of tests, the registered wave velocity has been decreased by [3.8%~4.2%], representing a decrease of [12%~16%] for the stiffness. Despite the observed different trends, the final decay interval obtained for the three specimens keep respects the stiffness-velocity relationship.
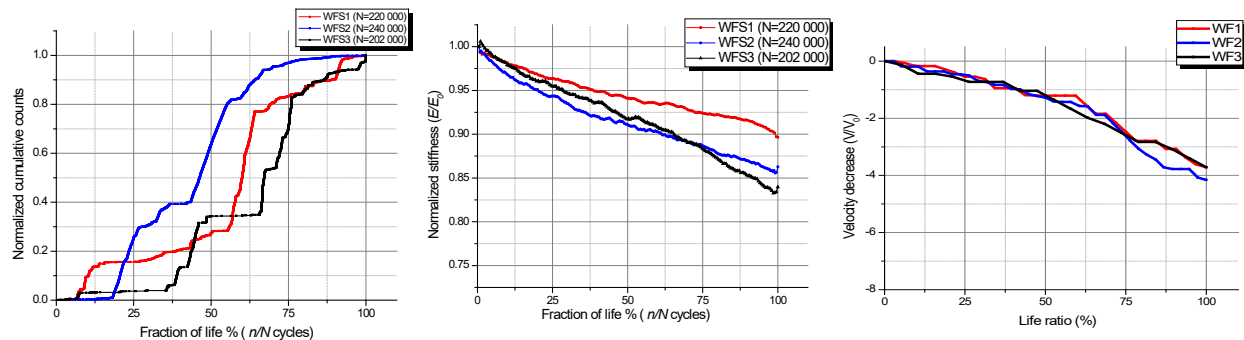

Fig. 2 Comparison of the metrics extracted form AE (left) – DIC (middle) and ACU (right) with respect to the life ratio (in %)

3. CONCLUSION

The proposed experimental method, based on synchronized acquisition of the different monitoring techniques with the applied load signal, has allowed to perform continuous measurements until the final failure, providing more effective interpretation of the damage mechanisms. Therefore, AE monitoring has emphasized the damage onset and reports its accumulation. The use of localization algorithm provided valuable information, as it was possible to evaluate the degradation rate, and rebuild the sequence of damage development from the inspection area over different fatigue phases. Simultaneously, the fundamental antisymmetric A_0 mode velocity was evaluated as an indirect measurement of the stiffness degradation and then compared with the surface stiffness obtained by DIC.

Independent Component Analyses Applied On Pulsed Thermographic Data For CFRP Inspection A Review

J. FLEURET[1,2], S. EBRAHIMI[1,2], C. IBARRA-CASTANEDO[1,2], X. MALDAGUE[1,2]

[1]Faculty of Sciences and Engineering, University Laval, Quebec City, Quebec, Canada,
julien.fleuret.1@univ.laval.ca
[2]Laboratory of Computer Vision and Numerical Systems, Multipolar Infrared Vision team, Quebec City, Quebec, Canada

Abstract

In this study, we investigated the application of several ICA implementations for material inspection using pulsed thermography. We compared our results with state-of-the-art methods, PCT and PPT. We conducted our experiments on a reference CFRP sample. We evaluated the different algorithms for all the defects surfaces at a given depth and all the depth for a given defect surface. Our results show that ICA does not outperform PCT or PPT but provides similar results and follows the same trends, making it an approach of interest for further analysis on other materials. We also found that the different implementations of the ICA provide similar results, and no implementation significantly outperforms the other. Further investigations on noisy data and different materials are still needed to assess the interest of the ICA for material inspection. With that in mind, we also only investigated the unsupervised implementation of the ICA; therefore, some investigation of the supervised version of the ICA might still outperform the state-of-the-art approaches.

1 Introduction

Non Destructive Testing (NDT) is a very popular field in many fields of industry. Among the many different NDT fields, InfraRed Thermography (IRT) is a famous field for evaluating materials. IRT's approaches consist of a set of tomographic approaches that are helpful to assess a wide range of features, from material homogeneity to the presence of void or foreign materials within another material. Within the field of IR-NDT, Pulsed Thermography (PT) is a very famous method. Among its fame are its simplicity and ability to provide valuable results on a wide range of materials. PT consists of submitting a sample of interest to a pulse of energy. Once the pulse reachs the material, it becomes a thermal wave that propagates by conduction through the material. The propagation will be affected by many features such as non-homogeneity in the density of the material, crack, void, foreign material, to cite a few. A thermal camera then records the decay of temperature. Thermal cameras are well known for being sensitive to a wide range of phenomenon and noises, including some created by the device itself, resulting in a wide range of distortions during the creation of the data [1–5]. The literature offers many methods proposed to enhance and improve the data returned by the thermal camera during PT experiments. Among the most famous are the Pulsed Phase Thermography (PPT) [6] and the Principal Component Thermography (PCT) [7]. The former consists of transforming the sequence into the Fourier domain and analyze the phase. The latter consists of applying a PCA to the sequence to extract the most meaningful frames. PCA projects the sequence into an orthogonal domain while maximizing the variance of the projected data. Nonetheless, the PCA is well-known to be sensitive to the noise present in the data. Several improvements of the PCA have been proposed in the literature and successfully applied to PT data. Yousefi et al. [8] proposed to use an improved version of the Candid Covariance-free Incremental Principal Component Analysis (CCIPCA) [9] under the name CCIPCT (Candid Covariance-free Incremental Principal Component Thermography). In their work, Yousefi et al. also update the cost function using the one proposed by Kompella et al. [10]. Later Yousefi et al. have proposed to apply the Sparse Principal Component Analysis (SPCA) [11] due to its increased robustness, under the name SPCT (Sparse Principal Component Thermography) [12]. SPCA robustness is mainly due to a penalization model called Least Absolute Shrinkage and Selection Operator or LASSO [13].

Another approach exists regarding the components analysis, among them the Independent Component Analysis (ICA) [14]. ICA, like PCA, tries to identify the most meaningful basis to project a multivariate dataset from a mathematical space to another. PCA uses an orthogonal transformation to convert a set of observations that may be correlated into a set of linearly uncorrelated variables. This set of uncorrelated variables is called the principal components. The ICA attempts to decompose the dataset as a set of independent signals. It is often

used for blind signal separation. From a more formal point of view, the ICA assumes that the thermal camera data are a mixture of different signals.

$$\mathbf{x} = \mathbf{A}\mathbf{s} \tag{1}$$

From the PT point of view, we assume that each defect within a sample is an independent signal $\mathbf{s}$ mixed with another non-defective part of the sample. The matrix $\mathbf{A}$ is a square invertible matrix. The goal of the ICA algorithm is to find an estimation of $\mathbf{s}$ from the data $\mathbf{x}$ by computing $\mathbf{W} = \mathbf{A}^{-1}$.

$$\hat{\mathbf{s}} = \mathbf{W}\mathbf{x} \tag{2}$$

The matrix $\mathbf{W}$ is known in the literature as an unmixing matrix. As one can note in equation 1, ICA is an under-constrained problem. This problem is known as blind source separation. A main concept regarding the ICA is the measurement of the independence of the components, which is similar to measure the non-gaussianity of two samples. Several methods have been proposed in the literature over time [15, 16]. Among the most famous is the work of Bell et al. [17], which was later extended by Lee et al. [18]. These works use the maximization of the output entropy of a neural network with non-linear outputs. Hyvärinen et al. [19] proposed a maximum likelihood approach, which at that time outperforms in terms of computation time the existing approaches. Recently Ablin et al. [20, 21] proposed several approaches regarding the computation of the Hessian matrix within optimization algorithms. ICA approaches have been used in different approaches regarding IRNDT. Morabito et al. [22, 23] were among the first to use ICA with Eddy-Current Testing (ECT) initially to analyze their features and later to detect and segment defects. Shin et al. [24] also used ICA to identify defects from an ECT distorted signal. Yang et al. [25] investigated the ICA application for defect detection in Pulsed Eddy-Current (PEC), which was later improved by Cheng et al. [26]. Wang et al. [27] used the method proposed by Hyvärinen et al. on Pulsed Thermographic data for the inspection of high silicon-oxygen phenolic resin. Javier-Rengifo et al. [28] already made a study regarding the application of both PCA and ICA in order to find a defect in Carbon Fiber Reinforced Polymer (CFRP) material. In their work, Javier-Renfigo et al. also proposed a new approach to select the best components for the ICA for applications regarding CFRP material inspection. However regarding the ICA method used in this study only investigated the method proposed by Hyvärinen et al. [19]. This paper investigates the usage of several state-of-the-art ICA methods on PT data for Carbon Fiber Reinforced Plastic (CFRP) inspection.

The rest of this paper is structured as follows. In the next section, the Independent Component Analysis is briefly introduced. Section 2, describes the different aspects of the experiments we conducted. Section 3 introduces the different results we generated from our experiments. Section 4 discuss and analyze the results. Finally, Section 5 concludes this work.

2 Materials and Methods

Our study aims to evaluate the accuracy of different formulations of the ICA on PT data and compare their results with state-of-the-art approaches. In this section, we introduce the different aspects of the experiments we conducted.

2.1 Data

In order to evaluate the potential interest of ICA in IRNDT, we analyzed a reference Carbon Fiber Reinforced Plastic (CFRP) sample. This sample contains twenty-five Teflon inserts which are divided into five batches of five defects. Each batch has five inserts having the same depth but different sizes (from 3x3 mm^2 to 15x15 mm^2). As illustrated in figure 1, each batch has been positioned at a specific depth (from 0.2 to 1 mm). The materials have been evaluated under a classic pulse thermographic procedure. Each material has been stimulated from the front side by a pulse generated by two photographic flashes (Balcar FX 60, $5\ ms$ thermal pulse, $6.4\ kJ/flash$). A mid-wave infrared (MWIR) camera FLIR x6900sc ($1.5\ \mu m$ to $5.0\ \mu m$, 14 bit per pixel, 640×512) was used for data acquisition. We conducted two acquisitions at different frequencies of acquisition. We acquired some data at a frequency of 145 Hz (145 images per second) and 120 Hz. For each experiment, a sequence between 2000 frames and 2200 frames was acquired during a period of 30 seconds. That duration ensured that the sensor had acquired both the warm-up and the cool-down.
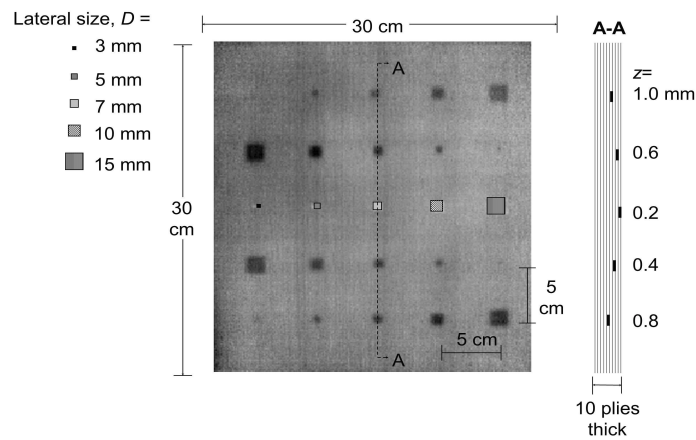
Figure 1: CFRP sample used for the experiments.

2.2 Analysis

To evaluate the different implementations of the ICA, we chose two state-of-the-art methods, the Pulsed Phase Thermography [6] and the Principal Component Thermography [7]. Among the different formulation of the ICA, we investigated the ICA using Infor-Max [17], The ICA using Info-Max extended [18], the Fast-ICA [19], simple quasi newton ICA, and trusted region ICA, which were introduced by Albin et al. [20, 21]. We also evaluated more recent approaches such as the uwedgeICA introduce [29] and the BIO-NICA [30]. For each frequency, we acquired a sequence of T images of dimensions $M \times N$ pixels. The first step consists of creating an overlay matrix of dimension $T \times P$ where $P = M.N$. T is the number of frames acquired in each sequence, P is the total number of pixels. Before applying the different algorithms we selected on the data overlay matrix
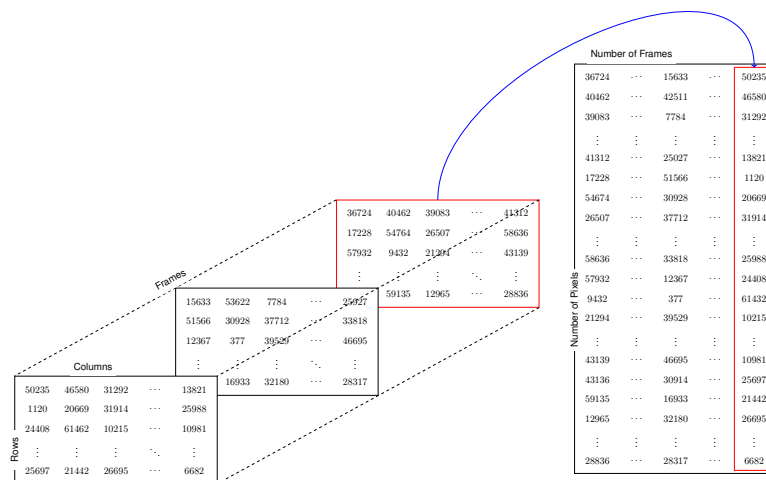

Figure 2: Generation of an overlay matrix from a sequence of images.

we first standardize the content of it by centering to 0 and normalizing the standard deviation to 1. Once the ICA models are applied, we only keep the seven first components before reconstructing an output sequence. Because we choose only to keep the seven first components when we apply the ICA on any data after the fitting step, it returns a matrix of size $7 \times P$. Before computing the metrics, we reshape the output to an array of dimensions $7 \times M \times N$. Note that the position order of the number of components in the dimensions is

arbitrary. Then we compute the metrics for each defect and each frame of the output sequence before applying a max-pooling over the frames. Using a mask in which we define both the defect region as well as the sound area for each defect, we computed the scores.
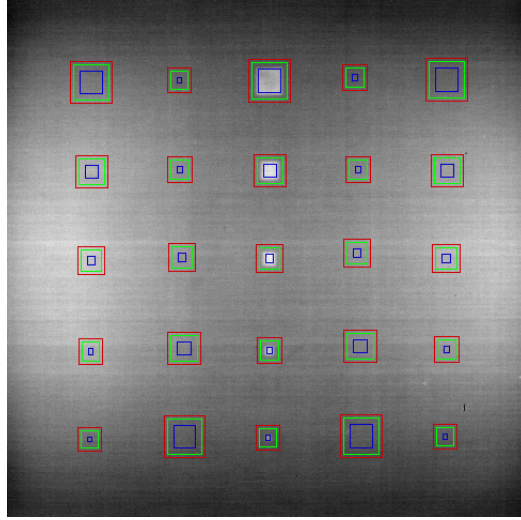

Figure 3: The blue contour represents the defect region, while the region between the green an red contours is our sound area.

Thus we only keep for each defect the best scores. Also note that each algorithm we used has a different set of hyper-parameters. We the prior values of these algorithm allows a computation in a reasonable time, i.e. within 20 minutes we try to tune them. In the next section, we introduce the metric we use for assessing the quality of the different methods we investigated.

2.3 Metrics

To evaluate the proposed works, we choose several metrics to highlight their robustness to different features. The first metric is quite well-known in Infrared Non-Destructive Testing (IRNDT): it is the Signal to Noise Ratio (SNR). This metric is prevalent in IRNDT due to its ability to provide information about the contrast in the image. Often, thermal or component images are noisy, which can significantly influence this metric. Many formulations of the SNR have been proposed; in this study, we used the formulation proposed by Usamentiaga [31].

$$SNR(roi_s, roi_n) = \frac{|\mu_s - \mu_n|}{\sqrt{\frac{(\sigma_s^2 + \sigma_n^2)}{2}}} \tag{3}$$

The next section introduces the different results we computed for this study.

3 Results

For each experiment we made, we reported the SNR scores obtained by each method for each defect in tables 1 and 2. In figures 4 and 6, we can see for each defect size the SNR scores obtained by each method in the function of the depth. Figures 5 and 7 show for the different depths the SNR score obtained by the different methods in function of the surface of the defects.

Table 1: Maximum SNR values for the different defects,
for each method at the frequency of 120 Hz.

Method	Depth (mm) \Lateral size (mm)	3	5	7	10	15
PCT	0.2	3.76	10.53	12.13	15.56	8.55
	0.4	1.63	9.66	3.56	8.41	10.33
	0.6	2.68	6.93	7.44	7.99	8.63
	0.8	2.20	4.39	6.04	8.38	6.25
	1	0.51	3.00	4.10	6.02	6.09
PPT	0.2	3.42	8.33	11.39	11.97	7.92
	0.4	1.50	7.15	3.76	7.79	7.74
	0.6	2.37	6.52	6.38	7.21	6.82
	0.8	1.92	3.77	5.32	7.63	5.71
	1	1.18	2.19	2.95	5.10	5.53
Fast-ICA	0.2	3.45	12.94	10.18	13.32	10.11
	0.4	1.71	7.96	3.05	9.04	9.63
	0.6	2.27	4.92	5.28	5.07	5
	0.8	1.01	3.02	4.94	6.02	4.83
	1	0.47	2.57	3.83	5.52	5.53
Infomax-ICA	0.2	3.56	10.50	11.20	14.18	9.13
	0.4	1.57	9.37	3.57	8.14	10.23
	0.6	2.52	6.77	6.90	8.00	6.73
	0.8	1.76	4.00	5.01	6.97	5.42
	1	0.52	2.24	3.29	4.61	4.73
trust-region-ICA	0.2	3.55	10.23	11.00	15.62	8.63
	0.4	1.64	8.16	3.55	8.10	8.02
	0.6	2.46	6.64	7.04	7.84	6.38
	0.8	1.94	3.83	5.65	7.30	5.99
	1	0.55	2.41	3.45	5.35	5.34
Quasi-newton-ICA	0.2	3.56	10.50	11.20	14.18	9.13
	0.4	1.57	9.37	3.57	8.14	10.23
	0.6	2.52	6.77	6.90	8.00	6.73
	0.8	1.76	4.00	5.01	6.97	5.42
	1	0.52	2.24	3.29	4.61	4.73

Table 2: Maximum SNR values for the different defects,
for each method, at frequency of 145 Hz.

| Method	Depth (mm) \Lateral size (mm)	3	5	7	10	15
PCT	0.2	2.84	6.4	11.97	15.99	11.33
	0.4	3.39	6.33	9.24	10.54	15.55
	0.6	2.37	7.32	7.45	7.15	12.04
	0.8	1.63	4.52	3.47	8.73	10.16
	1	2.14	3.47	3.88	7.82	5.95
PPT	0.2	3.4	6.64	13.07	15.95	9.32
	0.4	3.16	7.16	11.21	10.74	12.79
	0.6	2.12	7.29	7.38	7.69	10.56
	0.8	1.15	4.73	3.08	7.24	8.26
	1	0.87	3.08	3.55	5.89	6.57
Fast-ICA	0.2	2.78	7.28	12.13	16.63	11.46
	0.4	2.96	5.89	11.2	10.06	12.03
	0.6	2.12	7.58	7.71	7.64	10.31
	0.8	1.47	4.65	3.68	9.36	10.84
	1	1.02	2.70	2.78	4.72	4.05
Infomax-ICA	0.2	0.39	0.18	0.40	0.30	0.50
	0.4	0.12	0.25	0.17	0.34	0.40
	0.6	0.16	0.20	0.39	0.20	0.26
	0.8	0.40	0.25	0.28	0.18	0.14
	1	0.22	0.28	0.35	0.10	0.11
trust-region-ICA	0.2	2.84	6.34	11.85	15.82	11.15
	0.4	3.37	6.29	9.27	10.48	15.57
	0.6	2.36	7.31	7.57	7.14	12.05
	0.8	1.61	4.55	3.46	8.75	10.12
	1	2.14	3.46	3.86	7.76	5.95
Quasi-newton-ICA	0.2	0.39	0.18	0.40	0.30	0.50
	0.4	0.12	0.25	0.17	0.34	0.40
	0.6	0.16	0.20	0.39	0.20	0.26
	0.8	0.40	0.25	0.28	0.18	0.14
	1	0.22	0.28	0.35	0.10	0.11
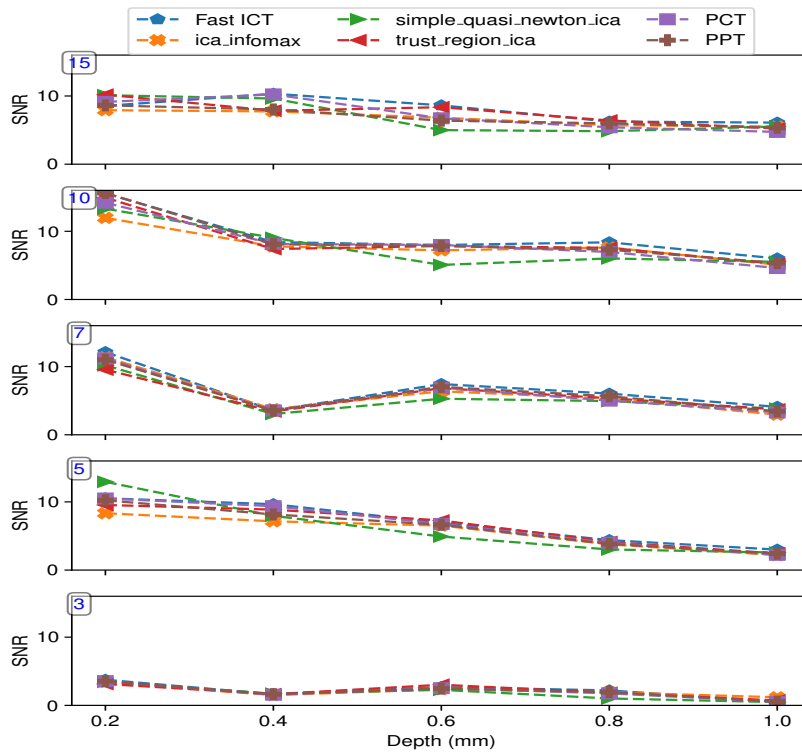
Figure 4: Maximum SNR by defect type as a function of the defect surface for all methods we investigated, which data is acquired at 120 fps.
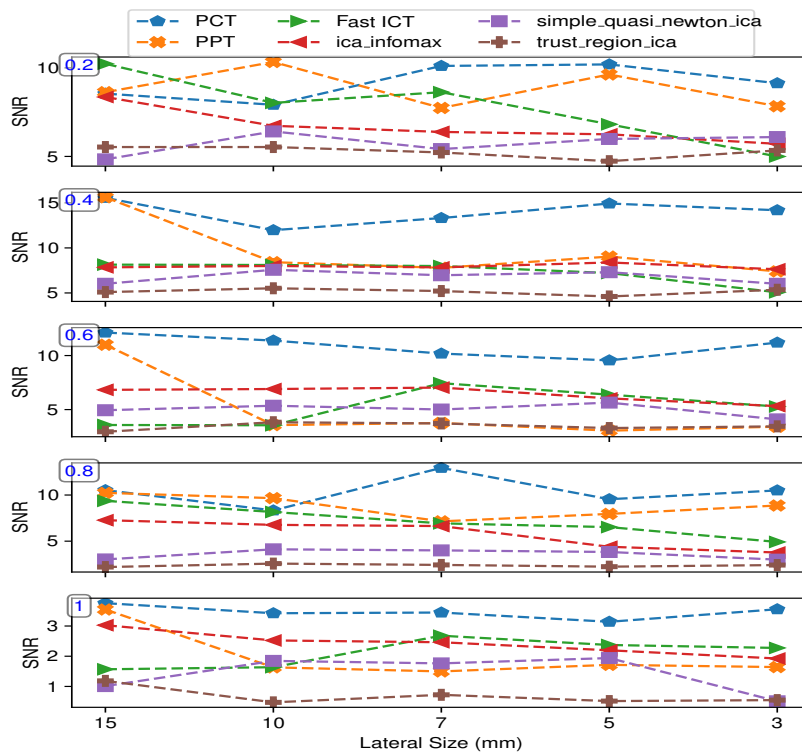

Figure 5: Maximum SNR by defect type as a function of the defect depth for all applied methods , which data is acquired at 120 fps.
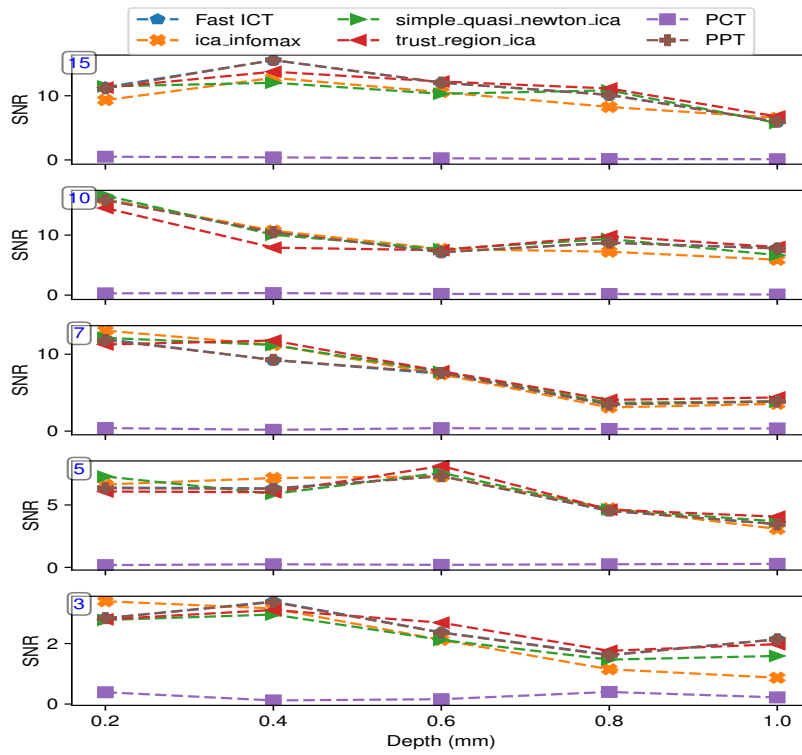
Figure 6: Maximum SNR by defect depth as a function of the defect surface for all applied methods, which data is acquired at 145 fps.
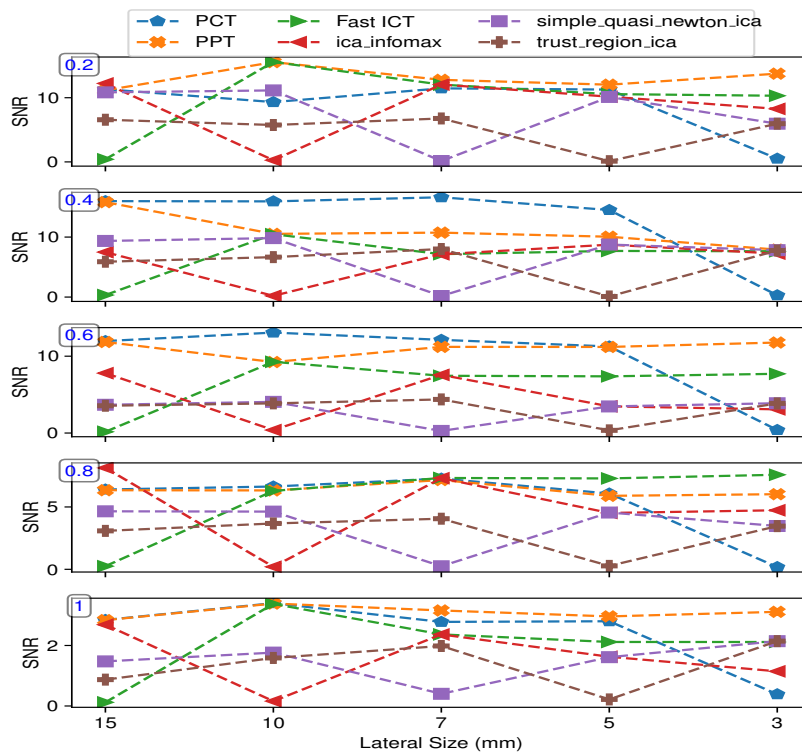

Figure 7: Maximum SNR by defect depth as a function of the defect depth for all applied methods, which data is acquired at 145 fps.

In the next section, we discuss the results we obtained.

4 Discussion

The goal of this study is to evaluate different ICA methods comparatively with state-of-the-art algorithms in order to assess their performance. As one can note in figure 5, the results obtained for the defects with a surface of 15 mm^2 seems unclear. Looking carefully, we can see that depend on the method used; we can categorize three trends. The first trend is followed by the PPT, the quasi-newton ICA, and the Infomax-ICA show a decrease of the SNR score function of the depth. Another trend is followed by the PCT and the Fast-ICA, for which the SNR score increases between the depth of 0.2 mm and 0.4 mm before decreasing for all the other depths. The last trend is only followed by the trust-region ICA, for which we can see a decrease of the SNR score between the depth of 0.2 mm and 0.4 mm, followed by an increase of the score between the depth of 0.4 and 0.6 mm. After 0.6 mm, all the SNR scores decrease with the increase of the depth. Despite the different trends, one can observe that for all the methods, the general trend decrease with depth. For the defects with a surface of 10 mm^2, one can note that the score obtained for the defects located at 0.2 mm from the surface obtained was significantly higher than in the previous plot. We can also see that, like previously observed, the general trend for all the methods is that the SNR score decreases when the depth increase. One can also note that for deeper defects, the Fast-ICA algorithm obtained the best scores. We can also observe that the simple quasi newton ICA is the method that appears to be the most contrasted. From the defects with a surface of 7 mm^2 and lower, we can observe that the smaller is the surface of the defects more similar is the trend regarding the scores obtained for the different methods. In the figure, we can also see that the Fast-ICA outperforms most of the other methods. Another observation is that the smaller is the surface of the defect, the lower is the SNR score, which is expected. Figure 5 shows the scores obtained by the different methods we investigated the function of the defect size for a given depth. At first look, two observations can be made. On the one hand, the deeper is the defect, the lower are the scores, which is expected. On the other hand, the PCT outperforms all the other methods. One can also note that the infomax-ICA, the simple quasi-newton-ICA, and the region-ICA does not show noticeable variation when the surface of the defect decrease significantly. It is also to note that it does not show a decreasing trend when the surface of the defect decrease. In figure 6, we can see the all the methods outperform the PCT. We can also see that all the methods decrease with the increase of depth. The score related to all the ICA methods close to the scores obtained by the PPT. One can also note that the amplitude of the scores obtained by the different metrics decreases with the size. In 7, one can note that PCT does not perform well on defects the smaller defects. However, PPT performs very well in most situations providing at least similar performances as PCT when not outperforming it. Among the ICA approaches, the Fast-ICA method outperforms all the other methods.
From all these results, we can see that the ICA approaches can provide similar results as state-of-the-art approaches when using to analyze the scores obtained for a surface function of the depth. State-of-the-art approaches outperform ICA's approaches for the analysis of the scores obtained for different sizes at a given depth. Nevertheless, ICA's show a similar trend. As a result, we can conclude that ICA can be used as a replacement for other state-of-the-art methods. In order to provide an extended conclusion regarding the performance of the ICA, we would need further investigation on both noisy data as well as applications data. Among the different methods to compute the ICA, we investigated none of them provided noticeably better results than another on the overall. Comparison with other works such as the work of Rengifo et al. [28] would also provide a clue regarding the performance of the ICA and can possibly also be used with a supervised implementation of the ICA.

5 Conclusions

We studied different implementation of the ICA in order to evaluate their interest for material inspection compaired with state of the art methods sucha as PCT and PPT. We found that if the oftenly ICA underperform state of the art approaches it follows the same trend in every analysis we conducted and therefore more investigations are needed in order to provide an overview of the interest of this method. Among the different implementation of the ICA we use none of them was significantly better than another.

Acknowledgement

References

[1] James S Houchin and Kenneth A Parulski. Method and apparatus for pixel non-uniformity correction, September 10 1991. US Patent 5,047,861.

[2] John G Harris and Yu-Ming Chiang. Nonuniformity correction of infrared image sequences using the constant-statistics constraint. *IEEE Transactions on image processing*, 8(8):1148–1151, 1999.

[3] Bradley M Ratliff, Majeed M Hayat, and J Scott Tyo. Radiometrically accurate scene-based nonuniformity correction for array sensors. *JOSA A*, 20(10):1890–1899, 2003.

[4] Matteo Perenzoni, Daniel Mosconi, and David Stoppa. A $160\times$ 120-pixel uncooled ir-fpa readout integrated circuit with on-chip non-uniformity compensation. In *2010 Proceedings of ESSCIRC*, pages 122–125. IEEE, 2010.

[5] Yanpeng Cao and Christel-Loic Tisse. Single-image-based solution for optics temperature-dependent nonuniformity correction in an uncooled long-wave infrared camera. *Optics letters*, 39(3):646–648, 2014.

[6] Xavier Maldague and Sergio Marinetti. Pulse phase infrared thermography. *Journal of applied physics*, 79(5):2694–2698, 1996. 1, 3

[7] Nikolas Rajic. Principal component thermography. Technical report, Defence Science and Technology Organisation Victoria (Australia), 2002. 1, 3

[8] Bardia Yousefi, Stefano Sfarra, Clemente Ibarra Castanedo, and Xavier PV Maldague. Comparative Analysis on Thermal Non-Destructive Testing Imagery Applying Candid Covariance-Free Incremental Principal Component Thermography (CCIPCT). *Infrared Physics & Technology*, 85:163–169, 2017. 1

[9] Juyang Weng, Yilu Zhang, and Wey-Shiuan Hwang. Candid Covariance-Free Incremental Principal Component Analysis. *IEEE Transactions on Pattern Analysis and Machine Intelligence*, 25(8):1034–1040, 2003. 1

[10] Varun Raj Kompella, Matthew Luciw, and Jürgen Schmidhuber. Incremental slow feature analysis. In *Twenty-Second International Joint Conference on Artificial Intelligence*. Citeseer, 2011.

[11] Hui Zou, Trevor Hastie, and Robert Tibshirani. Sparse principal component analysis. *Journal of computational and graphical statistics*, 15(2):265–286, 2006.

[12] Bardia Yousefi, Stefano Sfarra, Fabrizio Sarasini, Clemente Ibarra Castanedo, and Xavier PV Maldague. Low-Rank Sparse Principal Component Thermography (Sparse-PCT): Comparative Assessment on Detection of Subsurface Defects. *Infrared Physics & Technology*, 98:278–284, 2019. 1

[13] Fadil Santosa and William W Symes. Linear inversion of band-limited reflection seismograms. *SIAM Journal on Scientific and Statistical Computing*, 7(4):1307–1330, 1986.

[14] Pierre Comon. Independent component analysis, a new concept? *Signal processing*, 36(3):287–314, 1994.

[15] Aapo Hyvärinen and Erkki Oja. Independent Component Analysis: Algorithms and Applications. *Neural networks*, 13(4-5):411–430, 2000. 2

[16] Jianying Wang, Cheng Wang, Tianshu Zhang, and Bineng Zhong. Comparison of different independent component analysis algorithms for output-only modal analysis. *Shock and Vibration*, 2016, 2016.

[17] Anthony J Bell and Terrence J Sejnowski. An information-maximization approach to blind separation and blind deconvolution. *Neural computation*, 7(6):1129–1159, 1995.

[18] Te-Won Lee, Mark Girolami, and Terrence J Sejnowski. Independent component analysis using an extended infomax algorithm for mixed subgaussian and supergaussian sources. *Neural computation*, 11(2):417–441, 1999.

[19] Aapo Hyvarinen. Fast and robust fixed-point algorithms for independent component analysis. *IEEE transactions on Neural Networks*, 10(3):626–634, 1999.

[20] Pierre Ablin, Jean-François Cardoso, and Alexandre Gramfort. Faster independent component analysis by preconditioning with hessian approximations. *IEEE Transactions on Signal Processing*, 66(15):4040–4049, 2018.

[21] Pierre Ablin, Jean-François Cardoso, and Alexandre Gramfort. Faster ica under orthogonal constraint. In *2018 IEEE International Conference on Acoustics, Speech and Signal Processing (ICASSP)*, pages 4464–4468. IEEE, 2018.

[22] Carlo Francesco Morabito. Independent Component Analysis and Feature Extraction Techniques for NDT Data. *Materials Evaluation(USA)*, 58(1):85–92, 2000. 2

[23] FC Morabito and G Simone. Defect Signal Restoration and Eddy Current Measurments by Independent Component Analysis. *Modelling Measurement and Control a General Physics Electronics and Electrical Engineering*, 74(1/2):17–36, 2001. 2

[24] Byung Hyuk Shin. *Independent Component Analysis for Enhanced Feature Extraction From Non-Destructive Evaluation*. Michigan State University. Department of Electrical and Computer Engineering, 2004. 2

[25] Guang Yang, Gui Yun Tian, Pei Wen Que, and Tian Lu Chen. Independent Component Analysis–Based Feature Extraction Technique for Defect Classification Applied for Pulsed Eddy Current nde. *Research in Nondestructive Evaluation*, 20(4):230–245, 2009. 2

[26] Liang Cheng, Bin Gao, Gui Yun Tian, Wai Lok Woo, and Gerard Berthiau. Impact Damage Detection and Identification Using Eddy Current Pulsed Thermography Through Integration of PCA and ICA. *IEEE Sensors Journal*, 14(5):1655–1663, 2014. 2

[27] Fei Wang, Yong-hui Wang, Wei Peng, Jia-qi Ji, Jun-yan Liu, Peng Xiao, and Yang Wang. Independent component analysis enhanced pulse thermography for high silicon oxygen phenolic resin (hsopr) sheet with subsurface defects. *Infrared Physics & Technology*, 92:345–349, 2018.

[28] Carlos Javier Rengifo, Andrés David Restrepo, and Sandra Esperanza Nope. Method of selecting independent components for defect detection in carbon fiber-reinforced polymer sheets via pulsed thermography. *Applied optics*, 57(33):9746–9754, 2018.

[29] Niklas Pfister, Sebastian Weichwald, Peter Bühlmann, and Bernhard Schölkopf. Robustifying independent component analysis by adjusting for group-wise stationary noise. *Journal of Machine Learning Research*, 20(147):1–50, 2019.

[30] David Lipshutz and Dmitri B Chklovskii. Bio-nica: A biologically inspired single-layer network for nonnegative independent component analysis. *arXiv preprint arXiv:2010.12632*, 2020.

[31] R Usamentiaga, Clemente Ibarra-Castanedo, and X Maldague. More than fifty shades of grey: Quantitative characterization of defects and interpretation using SNR and CNR. *Journal of Nondestructive Evaluation*, 37(2):25, 2018. 4

INFRARED THERMOGRAPHY FOR CULVERT INSPECTION

Davood Kalhor[1*], Samira Ebrahimi[1], Roger Booto Tokime[1], Farima Abdollahi Mamoudan[1], Yohan Bélanger[1], Alexandra Mercier[1], Xavier Maldague[1]

[1]Department of Electrical and Computer Engineering, Laval University, 1065, av. Medecine, Quebec (QC), G1V 0A6, Canada

[*]Corresponding Author: davood.kalhor.1@ulaval.ca

ABSTRACT

Finding an efficient and less expensive technique for culvert inspection is very much needed. This study assesses the potential of infrared (IR) thermography as an alternative approach to find the presence of cavities in a culvert structure. This work focusses on detecting cavities adjacent to pipes for culverts made from metallic pipes. For analysis of the cavities, pulsed thermography (PT) with absolute thermal contrast (ATC) and principal components thermography (PCT) are utilized. Using a large number of experiments, we explored the advantages of IR thermography for examining a culvert. Empirical results showed a promising future for application of this approach in culvert inspection. The size and location of cavity are among information that can be extracted from analyzing thermograms. The key finding of this research is that the proposed approach can provide useful information about different problems around culvert pipes which can be a sign of forming cavities. Therefore, it provides some clues to detect cavity creation in earlier stages which will certainly help to prevent any costly incidents later.

KEYWORDS: Culvert Inspection, NDT, PCT, PT

1. INTRODUCTION

Culverts are a type of structure mostly located under roadways, embankments, and service areas. For example, larger culverts may be used to cross the road by pedestrians and cyclists, whereas smaller ones may allow fish and small wildlife [1] to pass through. The length of a culvert varies from a few meters to several hundred meters with a diameter between 30 cm and 10 meters. Cavities may appear around culverts due to different reasons, including direct contact with water and its flow, soil acidity problems, and vibration. The air pockets can form at any areas around the culvert. The presence of cavities weakens the culvert's structure, and thus increases the risk of collapse and relevant incidents which can be costly and fatal. Therefore detecting cavities at early stages can play a crucial role in any incident prevention plan.

There exit several NDT methods to inspect culverts. Visual inspection, electromagnetic, acoustic, ultrasound, and radiographic testing are examples of well-known techniques for this purpose [2-3]. Culvert analysis for detecting cavities can be complex, very costly, and time consuming. For this reason, less expensive approaches with sufficient accuracy and efficiency are in high demand, but also challenging to devise. This paper assesses the potential of infrared thermography [4] as an alternative approach.

2. THEORETICAL BASIS

The heat conduction is described by the following heat equation:

$$\frac{\partial u}{\partial t} - \alpha \nabla^2 u = 0 \tag{1}$$

where u is the temperature, α is the thermal diffusivity (showing the heat transfer rate in $\mathrm{m^2.s^{-1}}$), and ∇^2 is the Laplace operator. This equation can be solved using the Fourier analysis. For 1D (z coordinate) and semi-infinite isotropic solids with initial temperature $\mathrm{u_0}$ (in K), the temperature at the surface ($z = 0$) can be expressed by

$$u(z = 0, t) = \mathrm{u_0} + \frac{Q}{e\sqrt{\pi}} t^{-\frac{1}{2}} \tag{2}$$

where Q (in J. m^{-2}) is the energy absorbed by the surface, and e is the thermal effusivity defined as

$$e = \sqrt{k\rho c_p} \tag{3}$$

where k (in W. m^{-1}. K^{-1}) denotes the thermal conductivity, c_p (in J. kg^{-1}. K^{-1}) is the specific heat capacity, and ρ (in kg. m^{-3}) represents the mass density of the material. The existence of the cavities in adjacent areas of the specimen leads to changes in the thermal effusivity of those regions and hence the temperature curve. We exploit this variation to detect the cavities.

3. METHODOLOGY

3.1 EXPERIMENT SETUP AND DATA ACQUISITION

Conducting experiment with real culverts involves several challenges such as logistic issues (difficulties of accessing to culverts for most part of year due to flooding and icing condition) and getting authorization to access culverts and test them. More importantly, accurate information such as the location and size of cavities for selected culverts should be known to verify the result. Replicating a real scenario in the laboratory is also extremely difficult if not impossible, therefore we tried to setup a laboratory experiment as close as possible to the reality. An overview of the setup is depicted in Fig. 1. A specimen is located on the top of a box filled with sand. The specimen lies totally on the sand except on a small area under which the air cavity is created. Halogen lamps were used as the source of thermal excitation. Thermal images were recorded using IR cameras during both heat up and cool down process and acquired thermograms were recorded by a PC.
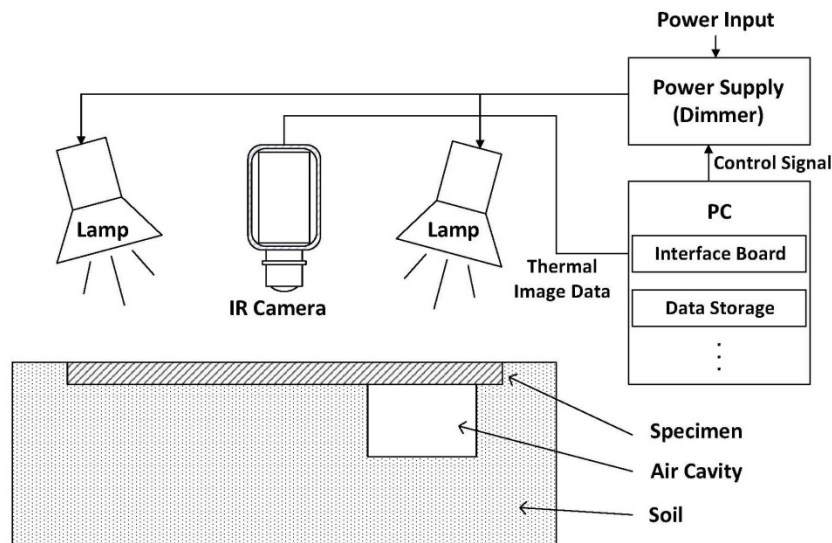

Fig. 1 The experiment setup overview.

Camera– Thermal images were produced using a FLIR Phoenix mid-wave infrared (MWIR) and a hand held Jenoptik VarioCAM long-wave infrared (LWIR) thermal cameras. Considering the higher thermal accuracy FLIR Phoenix, the analysis was mainly made based on thermal images from this camera. Technical specifications of these two cameras are summarized in Table 1.

Thermal stimuli– Four 1000 W halogen Lamps were used as the source of thermal excitation. The power of lamps was controlled through an eight channel dimmer pack and an electronic interface circuit. With the help of this controller and appropriate location of the lamps, it was tried to reduce the nonuniformity of thermal stimuli.

Box– A box of size 78×33×60 cm was used to represent the soil around the culvert pipe. It was filled with a mixture of sands and small stones.

Specimen– The experiments were conducted with a few specimens, including a 2 mm flat steel plate with dimensions 70×30 cm, referred to as specimen 1 (Fig. 2a). It was painted black flat to solve the low emissivity and reflection issues. Since the laboratory test with this specimen could not represent a real scenario, we continued experiments using specimen 2 (Fig. 2b) which is a horizontal cut of a typical culvert pipe with diameter 65 cm.

Cavities– The first air cavity (Fig. 2c) was created using a 10×10×6 cm cube of foam with a carved area with dimensions 6×6×3 cm so that 6×6 cm surface of the plate could be in touch with air rather than sands. The second configuration (Fig. 2d) was made using a cylindrical ceramic ashtray with the interior radius 5.5 cm and height 2.5 cm.

Feature	FLIR Phoenix	Jenoptik VarioCAM
IR detector	Cooled Indium Antimonide (InSb)	Uncooled microbolometer array
Image resolution	640×512	640×480
Spectral range	3-5 μm	7.5-14 μm
Thermal sensitivity	< 25 mK	< 70 mK
		< 30 mK (at 30°C object)
Frame rate	50 Hz	50 Hz (PAL), 60 Hz (NTSC)

Table 1 Thermal camera specifications.

(a)

(b)

(c)

(d)
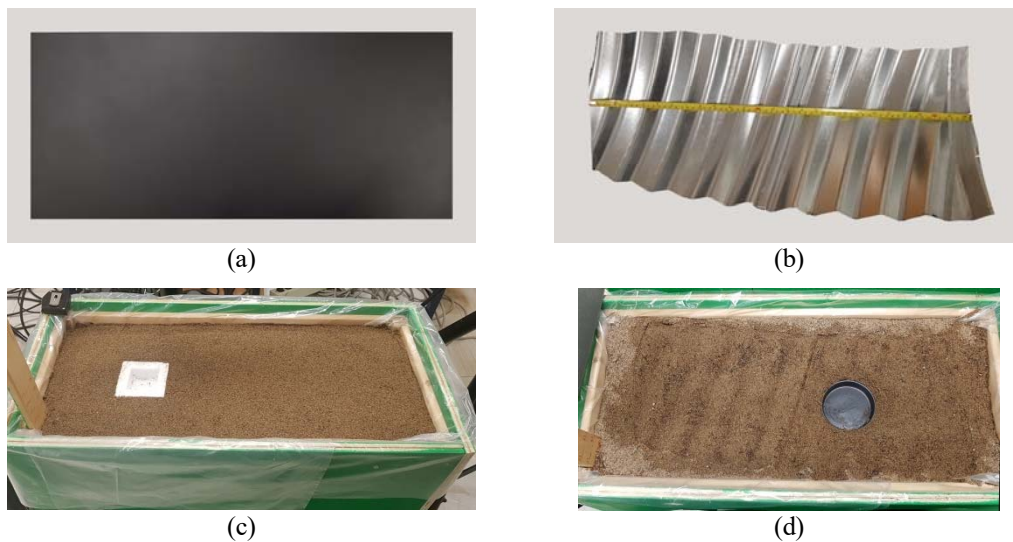
Fig. 2 Specimens and cavity configurations used in the tests. (a) Specimen 1. (b) Specimen 2. (c) Cavity configuration 1. (d) Cavity configuration 2.

3.2 IMAGE PROCESSING ALGORITHM

The image sequences (thermograms), representing the specimen surface temperature, were taken at 50 Hz and stored by a computer for offline inspection. The thermal camera used for thermogram acquisition records the image sequence as '*.sfmov' which is based on the file format known as the Standard Archive Format (SAF). This format is not readable in Matlab and therefore, a code snippet was developed to convert '*.sfmov' files into 3D arrays (x, y, t) such that x and y represent the horizontal and vertical pixels of the thermograms and t refers to the time slice of the recorded images. The arrays were then saved as Matlab data ('*.mat') files.

Before cavity detection analysis, three more preprocessing steps were applied to the data. The raw thermal images included the box and surrounding area in addition to the specimen. By removing these areas, we could reduce the computational cost. The image height and width after cropping were 405×165 pixels. To remove noise from the thermal images, we took advantages of temporal and spatial filtering. First, a median filter along t-axis was applied to each image sequence. Then a two-step filtering in spatial domain were used: a 3×3 median filter followed by a Gaussian filter with the standard deviation $\sigma = 1$. Median filter was effective in eliminating sharp, sudden

disruptive changes in the image intensity (aka salt-and-pepper noise). However, it failed in removal of other major noises in the image, including fixed pattern noise and shot thermal noise.

In this paper, we hypothesize that if the size of cavity is large enough and adjacent to the culvert pipe, it causes a noticeable change in the thermal effusivity and thereby the temperature deviations of regions close to the cavity from other areas of the pipe. For detecting the cavities, we utilized two known methods of IR thermography for NDT: PT [5] with ATC and PCT [6]. PCT is based on Singular Value Decomposition (SVD). The image processing algorithms were implemented in Matlab R2018a and Python.

4. EXPERIMENTAL RESULTS AND DISCUSSION

A large number of experiments were done but only two scenarios are discussed here.

4.1 SPECIMEN 1 WITH CAVITY CONFIGURATION 1

Raw images are corrupted with noise and cannot provide users with any clear clue about the cavity. To show the impact of the preprocessing algorithms, a frame of the thermal images before and after processing is shown in Fig. 3. This image can be used as input to a segmentation algorithm. Fig. 3c illustrates how segmenting image pixels into bins of a color space can contribute to a better understanding and easier analysis of thermograms. Segmentation can be done at different levels of granularity to achieve a desirable output.
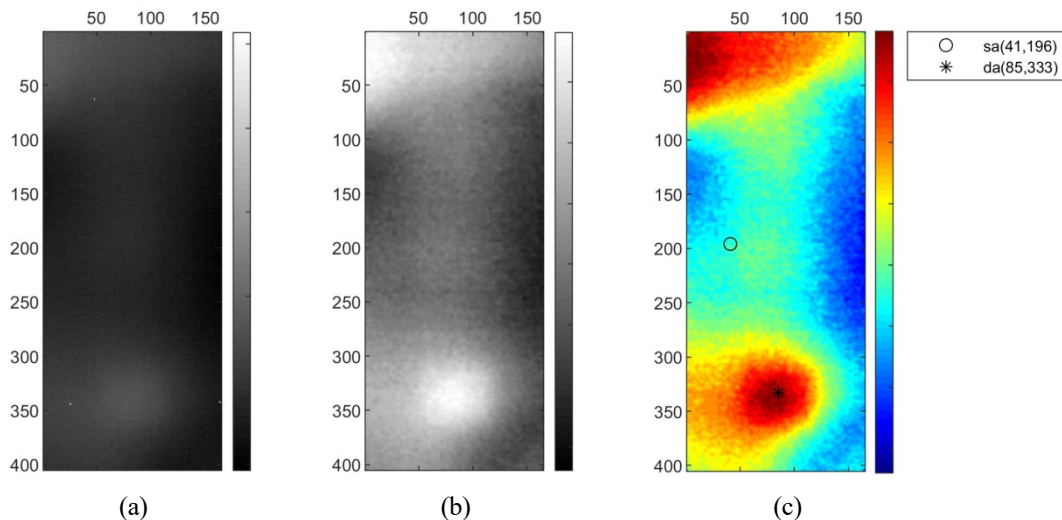

(a)   (b)   (c)

Fig. 3 Image processing; specimen 1 with cavity configuration 1. (a) An example of the cropped raw thermal image. (b) The processed image. (c) The segmented image. The circle and star indicate the selected points (one from sounding areas and the other from defective regions) for temperature-time curve analysis.

As earlier mentioned, we hypothesized that existence of cavity behind the specimen leads to variation in thermal radiation from the surface of the specimen. Therefore, the most straightforward approach would be to compare the thermal pattern of thermograms at different points. For this purpose, a point from the sounding areas (without any cavity) and the other from the defective areas were randomly selected (Fig. 3c). The temperature-time curves for these points are drawn in Fig. 4. The red curve represents the temperature of defective regions and the black curve is related to nondefective areas. The blue curve, which is the thermal difference, illustrates a bold contrast between the temperature of the specimen at regions close to cavity and the surrounding areas. The thermal contrast indicates disintegrity of materials behind the pipe and a sign of the cavity.

Thermograms were also analyzed using PCT. Fig. 5 shows Empirical Orthogonal Functions (EOF) 3 for cavity configuration 1. The power of this technique is evident in the details (the shape, size and location of the cavity) revealed by this method. It is important to bear in mind the depicted result was the best one, achieved following several experiments to find an optimal set of parameters.
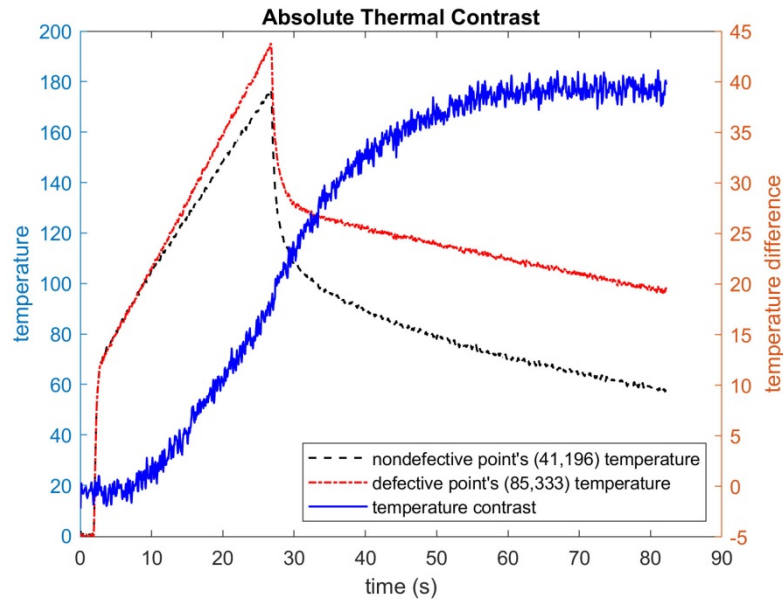
Fig. 4 Temperature-time curve and absolute thermal contrast; specimen 1 with cavity configuration 1.
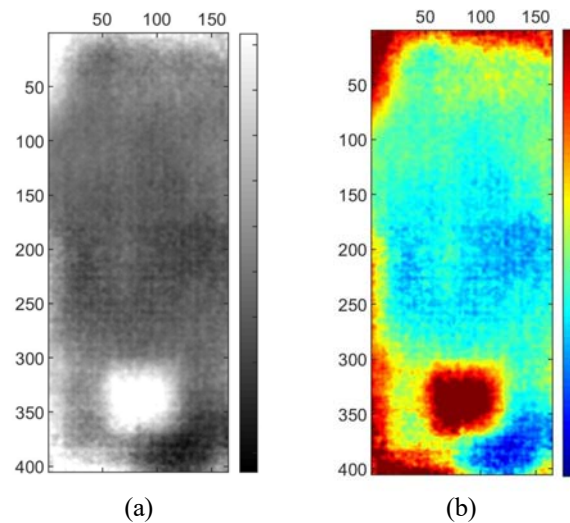

(a)   (b)

Fig. 5 PCT analysis for specimen 1 with cavity configuration 1. a-b) EOF 3.

4.2 SPECIMEN 2 WITH CAVITY CONFIGURATION 2

This group of experiment aimed to check the possibility of detecting air pockets behind the real specimen using PCT and ATC. Analyzing the real specimen introduced two serious issues. First, it has a low thermal emissivity and therefore a very low level of infrared light radiates from its surface. Second, its thermal wave reflection coefficient is very high. To handle these issues, the internal layer (toward the camera) of the specimen was painted black matte.
The result of PCT analysis as shown in Fig. 6 is encouraging. In addition to the size, location and shape of the cavity, EOF 4 also carries other information which is a reflection of the complex shape of the second specimen in comparison to the flat surface of specimen 1.

Thermograms were also analyzed using thermal contrast. Fig. 7a-b shows the thermogram for a frame during the cooling down phase. To demonstrate the power of the technique and comparison, the thermogram of the soil surface without the specimen (while other conditions are kept the same) is shown in Fig. 7c. This shows how closely the size and shape of the cavity can be detected with the help of IR thermography. The temperature graphs of sample points (one from sounding areas and the other from the defective region) illustrate that there is a clear thermal dissimilarity between defective and nondefective areas. Although the thermal dissimilarity is not as significant as for specimen 1, it still provides us with very useful information about the cavity.
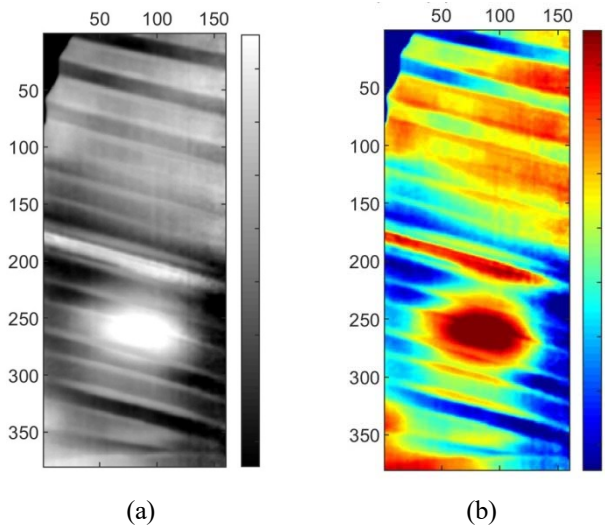
(a)   (b)

Fig. 6 PCT analysis for specimen 2 with cavity configuration 2. a-b) EOF 4.

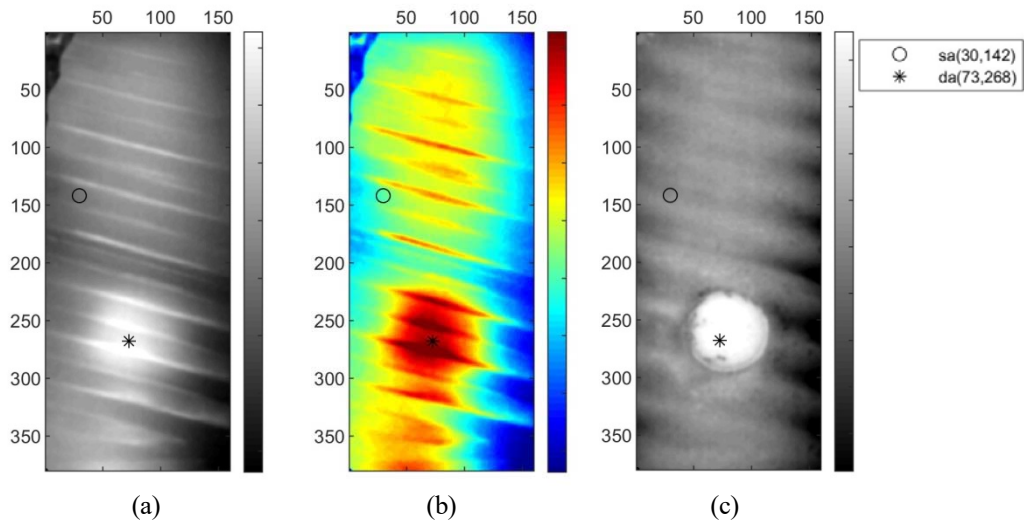(a)   (b)   (c)

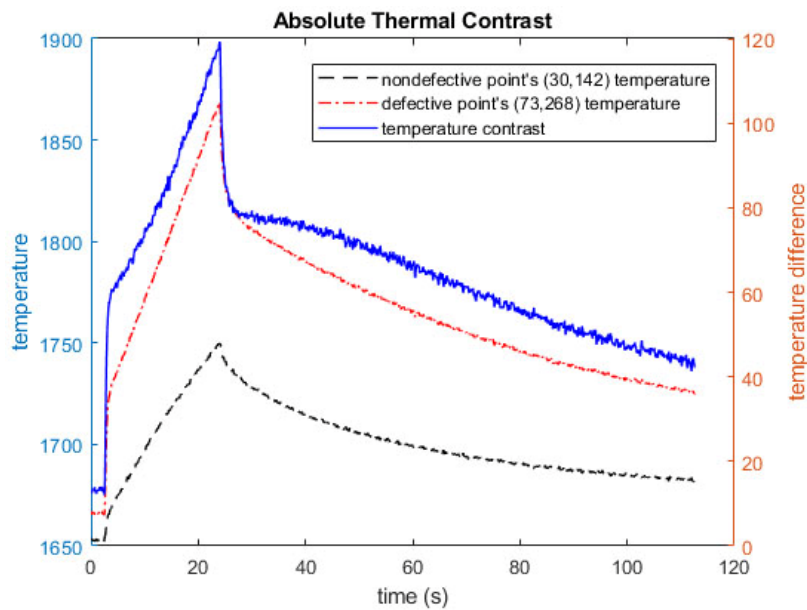**Fig. 7** PT analysis for specimen 2. a-b) PT with specimen. c) PT without specimen.

Fig. 8 Temperature-time curve for specimen 2. The corresponding sounding and defective points shown in Fig. 7c.

4.3 FINDING AND DISCUSSION

Our tests showed that the thermal behavior of the real specimen was very different from the other one (specimen 1) because of the dissimilarity in the material and the surface appearance. Moreover, the thermal behavior of the whole system depends on several other factors such the soil components, size and type of the pipe, the depth in which the pipe has been buried, the pipe distance from the ground surface, and ambient temperature. Preparing an experimental setup taking into account for all these factors, even if possible, it would be too costly and time consuming. Therefore, to verify the performance of this technique, it is required to carry out further test in real setups.

Since the passive thermography approach could not provide enough information about cavities in our experiment, the active approach was used. However, in real scenarios the thermal behavior of the whole system will be largely different and therefore we think that the passive thermography might be able to provide sufficient information for cavity detection. Since the passive approach is easier and less expensive to implement, this possibility should be investigated in a real setup.

In the experiments, some unexpected thermal patterns were observed in thermograms. For example, in Fig 5b there are some other regions. Further investigation revealed that the red areas, apart from the cavity, were often boundary or locations where the specimen was not in contact with the sands (i.e., a thin layer of air). Consequently, the temperature of these areas increased more rapidly in comparison with the areas in contact with the soil. On the contrary, blue regions represented good contact and thereby a good thermal conduction between the specimen and the sand which in turn led to a faster cooling down step. In other words, thin air layers adjacent to the specimen surface can cause a noticeable variation in the thermal radiation from the specimen surface. Nevertheless, we later figured out that this feature of thermograms can be very helpful in detecting other problems in a culvert. Formation of thin air layers adjacent to the specimen can be a sign of cavity creation in earlier stages and our experiments showed that this stage can be identified by IR thermography.

Before achieving the reported results, we had to find a set of parameters. For example, the duration of thermal stimuli has a crucial role on the quality of thermal images and may dictate the level of information that can be extracted from thermograms. Very short and weak thermal excitation may not be enough for detecting the required information while long and strong thermal stimuli may yield more fruitful thermograms, but they extend the test period and usually are more costly. In addition to the thermal stimuli, it is necessary to adjust a few other parameters such as the distance between the camera and specimen, distance between the thermal sources and the specimen, locations and directions of thermal sources (to minimize nonuniform excitation on the specimen surface). We think the results can be improved by further tuning of these parameters.

5. CONCLUSION AND FUTURE WORK

This study aimed to assess the potential of IR thermography as an alternative approach to find the presence of cavities in a certain type of culvert. Empirical studies in a laboratory setup showed that IR thermography can be utilized for cavity detection. The size and location of cavity are among information that can be extracted from analyzing thermograms. In examining the real specimen, we faced with some difficulties including emissivity issue, which we could effectively deal with by coating its internal layer.

Although this preliminary study showed a promising future for application of IR thermography in culvert inspection, further research is necessary. In particular, it is essential to verify the power of the technique in real setups despite logistic and technical difficulties of the on-site evaluation. Another direction that future researches should pay attention to is the fine tuning of the experimental setup and parameters as discussed in Section 4.3.

ACKNOWLEDGMENT

REFERENCES

[1] J. Cabonce, R. Fernando, H. Wang, and H. Chanson. Using small triangular baffles to facilitate upstream fish passage in standard box culverts. Environmental Fluid Mechanics, vol. 19, no. 1, pp. 157–179, 2019. doi: 10.1007/s10652-018-9604-x.

[2] K. R. Piratla, W. Pang, H. Jin, M. Stoner, et al. Best practices for assessing culvert health and determining appropriate rehabilitation methods: A research project in support of operational requirements for the south Carolina department of transportation. South Carolina. Dept. of Transportation. Office of Materials and Research, Tech. Rep., 2016.

[3] M. Karray, G. Lefebvre, et al. Detection of cavities under pavements by the model analysis of Rayleigh waves (MASW). Canadian Geotechnical Journal, vol. 46, no. 4, pp. 424–437, 2009.

[4] X. P. Maldague. Theory and Practice of Infrared Technology for Nondestructive Testing. John Wiley & Sons, New York. 2001

[5] C. Ibarra-Castanedo and X. Maldague. Pulsed phase thermography reviewed. Quantitative InfraRed Thermography Journal, vol. 1, no. 1, pp. 47–70, 2004. doi: 10.3166/qirt.1.47-70. eprint: https://doi.org/10.3166/ qirt.1.47-70. [Online]. Available: https://doi.org/10.3166/qirt.1.47-70.

[6] N. Rajic. Principal component thermography for flaw contrast enhancement and flaw depth characterisation in composite structures. Composite Structures, vol. 58, no. 4, pp. 521–528, 2002.

[3] M. Karray, G. Lefebvre, et al. Detection of cavities under pavements by the model analysis of Rayleigh waves (MASW).

ULTRASONIC IMAGING METHOD FOR THE DETECTION AND SIZING OF CRACKS IN A RIB-TO-DECK WELDED JOINT

Kazushi KIMOTO[1*], Hiroto SHIMADA[1]

[1]Okayama University, 3-1-1, Tsushima-naka, Kita-ku Okayama-shi, 700-8530, Okayama, Japan
[*]Corresponding Author: kimoto@okayama-u.ac.jp

ABSTRACT

This study develops a laser-based ultrasonic imaging method for the detection and sizing of a crack in a rib-to-deck welded joint. To this end, ultrasonic echo signals are measured using an aluminum specimen that mimics the geometry of a welded joint. In the measurements, a laser Doppler vibrometer is used as a receiver to resolve a spatially traveling ultrasonic wave field finely. A conventional, 5MHz angle-beam shear wave transducer is used to transmit well-directed incident waves to the inspection area. For a set of waveforms thus measured, major flaw echoes and their travel paths are identified by a theoretical travel time analysis. Based on the travel paths that have been identified, a synthetic aperture focusing image is created to estimate the crack tip location. It is found as the result, the tip of a 4mm-depth-crack can be estimated with an approximate error of 0.2mm.

KEYWORDS: Crack, Ultrasonic Imaging, Laser Doppler Vibrometer, Synthetic Aperture Focusing, Welded Joint

1. INTRODUCTION

A steel plate with stiffening U-ribs is a structural detail used in many welded structures. It has been reported, however, that fatigue damage often occurs at the welded joint of the deck plate and the U-rib initiating a crack from the toe of the welding root. Since the welding root is not exposed to the side that inspectors get an access, crack initiation and growth cannot be monitored by visual inspection. Ultrasonic flaw detection methods have therefore been studied as an alternative inspection method. When inspecting a plate like structure ultrasonically, numerous echoes could appear in the measured waveform due to multiple reflections. In such situations, correctly identifying flaw echoes and back tracing them to their origin for a flaw characterization is not straightforward. To address this issue and to provide a possible solution, this study develops a laser-based ultrasonic measurement technique in conjunction with a synthetic aperture imaging method for the detection and sizing of crack in a plate-to-rib joint. In what follows, the experimental and imaging methods are outlined, and the accuracy of the proposed crack sizing approach is discussed.

2. EXPERIMENT

A specimen for ultrasonic echo measurements is made by machining an aluminum block into a shape shown in Fig.1-(a). The specimen has a uniform cross section that mimics a geometry of the rib-to-plate welded joint. In the specimen, two through thickness slits are introduced as a simulated root gap and a crack growing from the root into the plate, respectively. The details of the slits are shown in Fig.1-(b) and (c).
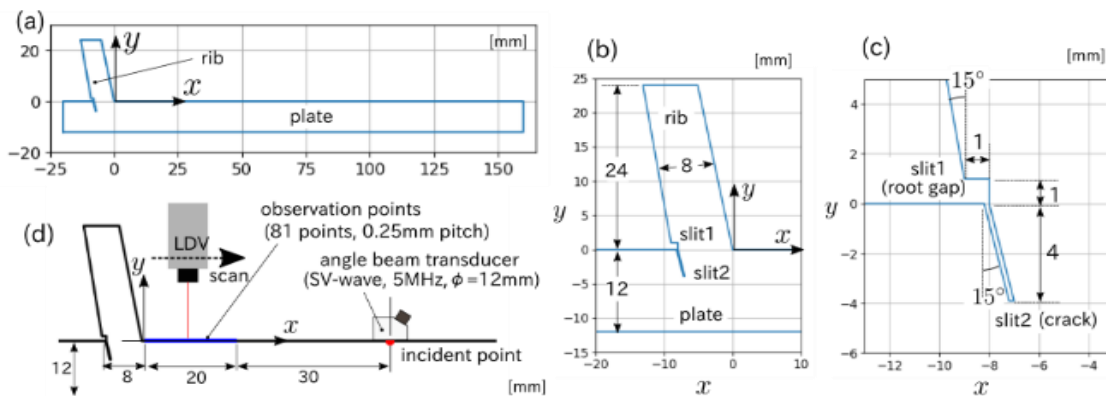

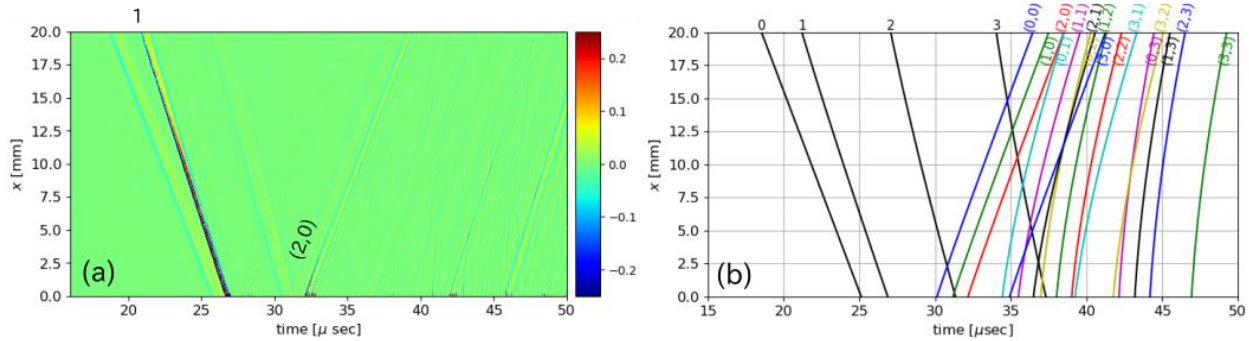**Fig. 1** (a)-(c) The geometry of the specimen. (d) the transmitter-receiver configuration for the ultrasonic measurement.

Fig. 2 (a) A B-scan presentation of the measured waveforms. (b) Theoretical travel time curves.
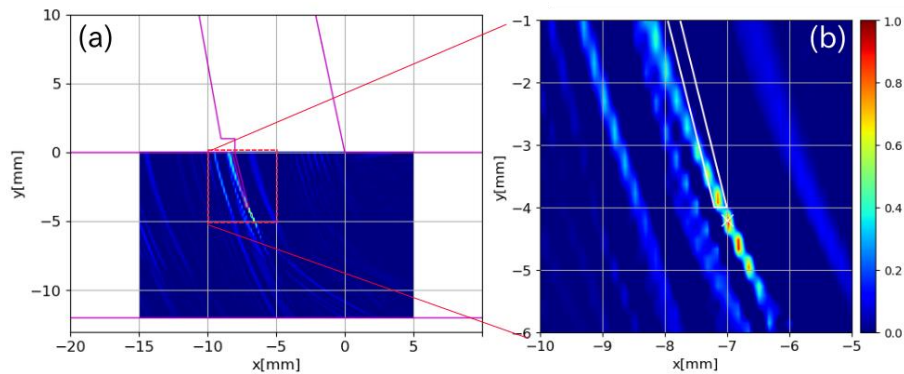

Fig. 3 (a) An ultrasonic image synthesized from the measured waveforms, and (b) a close-up around the crack tip.

The source and receiver configuration as shown in Fig.1-(d). As depicted, a conventional angle-beam transducer is used as a transmitter, while a laser Doppler vibrometer (LDV) is used to observe wave fields with sufficient spatial resolution along the measurement line shown in Fig.1-(d). The measured set of waveforms are shown in Fig.2-(a) as a B-scan image To identify echoes from the simulated crack (slit 2) in the B-scan, the flight times for the SV-waves reverberating in the plate are computed theoretically. The results are shown in Fig.2-(b) as a sequence of travel time curves. In this plot, the flight times of the incident waves are shown by black lines with the number of reflections each incident wave undergoes on the way to the observation points. The remaining curves of various colors are scattered waves from the crack tip. The tuples (i, j) attached show the number of reflections that occurs on the way to (i) and from (j) the crack tip, respectively. Note that mode conversions upon reflection are not considered assuming that dominant SV-wave components travel along mode-preserving paths. Comparison between the B-scan and the travel time plot reveals that the scattered wave of type (2,0) is observed most clearly in the present setup.

3. SYNTHETIC APERTURE IMAGING

The synthetic aperture imaging is a delay-and-sum operation on the waveforms followed by a sampling according to the flight time of the underlying wave paths. In this study, the delayed sum is taken for the path of (2,0) scattered wave, while the sampling is implemented as a correlation between the summed waveforms and a reference signal for which the wave arrival time is accurately known. Figure 3-(a) shows a synthesized ultrasonic image. To get a better view, a close-up around the crack tip is shown in Fig.3-(b). Note that the image intensity is normalized with respect to the maximum value, and negative image intensity is zeroed since the indication of the scattering object should come as a positive intensity. Some arc shaped artefacts are present in the image, however, the pixels having the intensity greater than 0.5 is localized to a close vicinity of the crack tip. In the close-up image (b), the location of the pixel with maximum intensity is indicated by a white cross symbol, which is an ultrasonically located crack tip. Although the synthesized image overestimates the crack depth by about 0.2mm, the accuracy is satisfactory for the interrogating wave length of 0.6mm.

3. CONCLUSION

An ultrasonic imaging method developed in this study has performed well with the LDV measured signals, locating the crack tip with an accuracy of about 0.2mm. The image-based sizing method will be further validated in the future researches for cracks of greater variety in terms of depths and angles.

CAPABILITY OF ADVANCED ULTRASONIC INSPECTION TECHNOLOGIES FOR HYDRAULIC TURBINE RUNNERS

Mohammad Ebrahim Bajgholi [1], Gilles Rousseau [2], Martin Viens [1], Denis Thibault [2]

[1] École de Technologie Superieure, Montreal; QC; H3C 1K3, Canada
[2] Institut de recherche d'Hydro-Québec (IREQ), Varennes, QC, J3X 1S1, Canada

[*]Corresponding Author: mohammadebrahim.bajgholi.1@ens.etsmtl.ca

ABSTRACT

This paper presents the results of a project aimed at evaluating the performance of ultrasonic techniques for detecting flaws in Francis turbine runners. This work is the first phase of a more ambitious program aimed at improving the reliability of inspection of critical areas in turbine runners. Francis runners may be utilized to supply power during peak periods, which means that they experience additional load stress associated with start and stop sequences. Inspection during manufacturing is then of paramount importance to remove as much as feasible all flaw initiation sites before the heat treatment. This phase one objective is to collect initial data on a simplified mock-up and then to compare the experimental ultrasonic data with the results of simulations performed by CIVA, a computer simulation package. The area of interest is the region with the highest stress between the blade and the web. A welded T-joint coupon made of UNS S41500 was manufactured to represent this high-stress area. During the FCAW welding process, ceramic beads were embedded in the weld to create discontinuities whose size is in the critical range to initiate a crack. Inspection of the material was carried out by various nondestructive testing (NDT) methods namely conventional pulse-echo, phased array, total focusing method (TFM). With these results, detection rates were obtained in order to compare the effectiveness of each method.

KEYWORDS: Nondestructive testing, Defect detection, Ultrasonic testing, Phased-array ultrasonic testing, Detection of rate, Hydroelectric turbine runner.

1. INTRODUCTION

In the province of Quebec, hydraulic turbines produce the vast majority of the electrical power. Hydro-Quebec Research Institute (IREQ) has developed a life estimation model based on the distribution and size of structural discontinuities in turbines to ensure equipment reliability and control production costs. In this model, the probability of a cracking event at any given point in time depends on the joint probability of stress and defect to be above the limit defined by the material properties[1]. Indeed, if discontinuities remain undetected, they might initiate fatigue cracks under dynamic, in-service stresses leading to unplanned failure, which itself results in high repair costs and long downtime [2]. It is desirable to supply the life estimation model with accurate data regarding the distribution and size of discontinuities present in the turbine to reduce unplanned outage costs. This type of data is typically determined using NDT methods to detect, locate, and size flaws. The current study aims at identifying the best ultrasonic inspection methods that will provide reliable flaw data to their life estimation model. Multi-pass flux-cored arc welding (FCAW), used for turbine runner joints, naturally generates certain discontinuities such as slag inclusions, lack of penetration, macro shrinkage, and thermal stress cracking. Welding discontinuities and dynamic stress concentration result in a higher failure probability in Francis turbine runners [2,3]. In the runner, maximum stresses are located along the welds near the trailing edge of the blades. The critical weld region extends to approximately 300 mm from the trailing edge for both blade-to-crown and blade-to-web welds.

NDT is the development and application of technical methods that examine materials or components. With these methods, the pieces are not destroyed, and the future usefulness and serviceability detects, locates, measures, and evaluates flaws' remain. There is a wide range of NDT methods based on physical principles of electromagnetic radiation, sound, and other inherent properties of materials. The techniques selected should consider safety, economic, efficiency, and time considerations [4]. Ultrasonic testing (UT) is a suitable method for detecting and sizing flaws embedded or growing from inaccessible surfaces. Ultrasonic waves can propagate through thick solid parts. Therefore, UT is suitable for flaws far beneath the inspection surface, unlike methods that can only detect defects on, or very close to the inspection surface, e.g., Eddy current testing or methods that detect flaws connected to the inspection surface such as visual methods and penetrant testing. When defect assessment calculations require a value on how deep the defect has grown, ultrasonic testing is the primary desired method. It is used to detect various types of flaws, such as cracks and inclusions and a wide range of materials, compared to magnetic particle testing methods, which require the component to be ferromagnetic. Ultrasonic waves are inherently safe compared to radiography methods, which use ionizing radiation and thus

require multiple protection types [5,6]. The basic NDT methods such as Visual Testing (VT), Ultrasonic testing (UT), Penetrant testing (PT), and Radiography (RT) are usually used to inspect hydraulic turbine runners . However, there are detection difficulties in detecting internal flaws in complex geometry, such as the runner's weld joints. Since hydraulic turbine runners are generally inspected using different ultrasonic inspection methods [2,3,7,8,9,10], this study's principal focus is on comparing capability of advanced ultrasonic inspection for the hydroelectric turbine industry using both simulation and experiments to identify the best practices for both fabrication and in-service inspection of the high-stress regions.

2. EXPERIMENTAL PROCEDURE

2.1. MANUFACTURING PROCESS DESCRIPTION

Inspection of turbine runner welds is an essential aspect of electric-generator units' in-service reliability [1]. In-service inspection data from installed runners show that fabrication flaws are found in the weld joint near the blade's trailing edge. Flaws were discovered by applying a phased array ultrasonic technique using a small wedge to provide suitable contact on a curved surface and good volumetric coverage with an azimuthal focal law type. Typically, flaws are within 30mm of the trailing edge and in the weld reinforcement that smooths the stresses at the blade's end. Some flaws were found isolated, but clusters of up to 7 indications were also observed. The presence of flaws at the edge of the blade in the area of high service stress is considered in the current investigation. This area is where the start and stop of welding occurs, and thus it is not surprising to observe in-situ point-like reflectors in the weld reinforcement. A T-joint sample was manufactured in martensitic stainless steel (UNS S41500) in accordance with the manufacturing requirements of turbine runners. The T-joint geometry often mimics a turbine runner's trailing edge, with both edges being 25mm in thickness. The base plate is 60mm thick and provides the same ultrasonic path for an inspection performed from the turbine web. The weld cap and blade ends are ground to obtain a smooth finish with a curved radius of 25mm. The preparation is a J-shape grove with a 3mm gap between the web and blade. Welding was carried out using a multi-pass FCAW process and EC410NiMo electrodes (same ultrasonic properties as UNS S41500). The study selected the dimensions of the joint to match a typical turbine runner assembly. Typically, 34 passes are required to fill the joint.

2.2. FLAW SIZE AND DISTRIBUTION

For technical manufacturing constraints imposed by the small size of the flaws examined by the current study (e.g., size of flaws between 1 mm and 5 mm), the scope is limited to inclusion flaws. Inclusions designate the incorporation, in the weld bead, of a foreign compound. Besides, the case of metal inclusions is studied to control the size of the flaws and the repeatability that are defined by the imprisonment of a foreign particle in the metal's mass. These flaws were relatively present in welded joints in laboratory samples that made inclusion a representative flaw for the current study. Spherical beads of a specific size are integrated into the weld fusion to simulate an inclusion. The choice of spherical shape is justified by limiting the external error factors that are linked to the defects' positioning and orientation.

To conduct the study, the requirement for precision on the defects' size, the obligation to respect an acceptable level of repeatability, and the flaws spherical shape guided in choosing ball bearings as the defect to be included. The extreme thermal conditions and the electric arc passage, during welding, close to the balls, forced the researchers to choose ceramic balls that were more resistant to extreme temperatures. This is because they interfered less with the heat-welding arc because of their non-conductive electrical properties.

The study considered three types of ceramic balls; alumina oxide balls (Al_2O_3), zirconia balls (ZrO_2), and silicon nitride balls (Si_3N_4). In this regard, all three types of balls were tried to determine the best ones for the study. After a series of tests, the study found that the alumina oxide (Al_2O_3) balls were to be avoided. This is because, despite the fact they offer a higher operating temperature compared to silicon nitride (Si_3N_4), they did not resist the electric arc passage and exploded. Therefore, the study chose the silicon nitride balls because they were stronger and kept their original shape .During welding, holes have been drilled in the weld pass to implement artificial flaws at known locations, as shown in Figure 1.

Ceramic beads are inserted into these holes, and the holes are filled by welding. Thirty ceramic beads are distributed in the weld of the T-joint sample. They were of either 1, 2, 3, 4, or 5 mm in diameter (6 beads of each size). This range of discontinuity sizes reflects the critical range to initiate a fatigue crack. A three-millimeter diameter flaw has the critical size to develop a fatigue crack under cyclic loading from stress calculation. Beads are located within 75mm from the edges of the sample in order to mimic the situation observed on in-service runners.
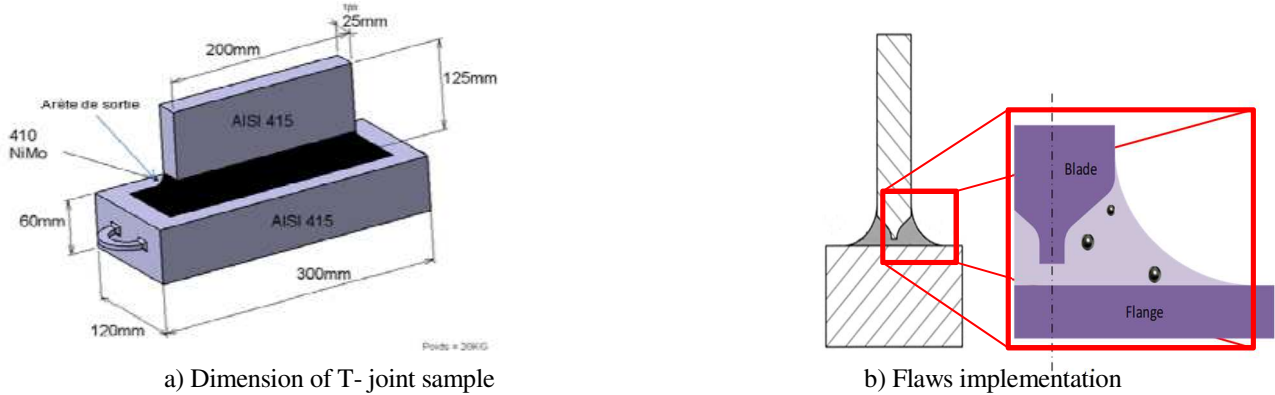
a) Dimension of T- joint sample

b) Flaws implementation

Fig 1 The experiment setup overview

2.3. CONVENTIONAL ULTRASONIC TESTING (UT)

Four experienced UT practitioners with CGSB (Canadian General Standards Board) level 2 or 3 certification in Ultrasonic Testing did inspect the T-joint sample. The study performed inspections as per the Canadian Standards Association (CSA) W59, Welded steel construction [11]. The study used a flat, 2.25 MHz 1/2in round transducer mounted on a refracting wedge to produce a refracted shear wave beam at either 60° or 70° from normal. The conventional ultrasonic testing inspection was carried out using Olympus Epoch 600 and Krautkramer USN 58L Ultrasonic Flaw Detectors, as shown in Figure 2. All indications, rejectable or not, were to be reported.
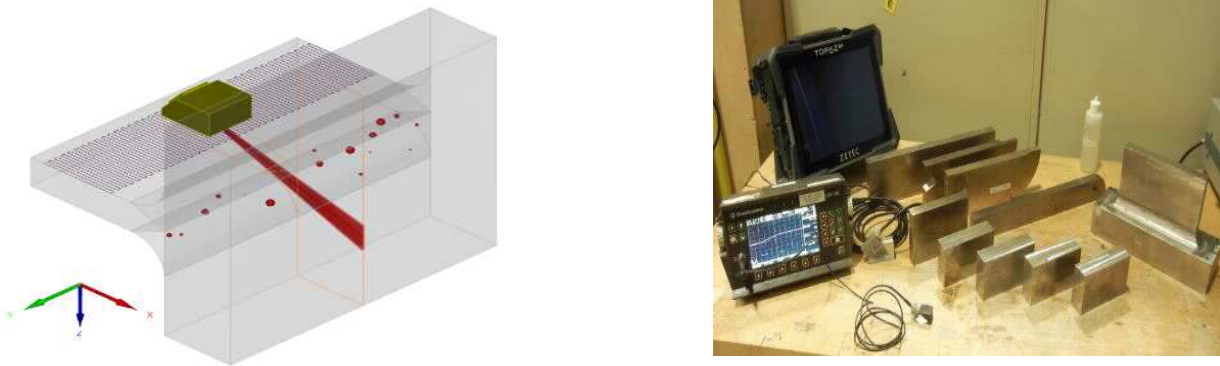

Fig 2 a) Raster scanning from both blade surfaces b) Ultrasonic Testing Equipment

2.4. PHASED ARRAY ULTRASONIC TESTING (PAUT)

The scan plans prepared to inspect the regions of interest were devised according to standards. These scan plans indicate the required refracted beam angle and the probe standoff positions to ensure appropriate volume coverage. Wherever possible, welds shall be inspected from both sides of the blade [12,13,14]. The ultrasonic system was calibrated using standard blocks to ensure the repeatability and reliability of experimental data [11,12].

Phased Array (PA) transducers can be referred to as multiple small conventional transducers (elements) that are housed within a single unit. Each transducer can be pulsed individually; by varying the delay between elements, the individual waves' constructive interference will occur at the desired angle, which enables the focus to be achieved. The phased array technique is a beamforming method that relies on emission delay to shape the beam in terms of refracted angle and position of the near field. A set of delays required to create a specific beam angle and focus point is called a focal law [15,16,17,18]. By electronically changing the delays rapidly, the focal law group can produce an azimuthal scan with a starting angle, a final angle, and an angle step. For example, a focus group can use the following set of angles: starting at 40°, an increment of 1°, and stop at 70°. A phased array probe has limits for beam formation; hence, both wave physics and array limitation must be taken into account. In the experiment, the wedge nominal refracted angle is 55 shear wave and the array of 5MHz, with 0.6 mm element spacing, produces an acceptable beam profile in the range of 40° to 70° shear wave [19,20]. The PAUT inspection was carried out using TOPAZ 64, as shown in Figure 2. The transducers were all linear Phased Array Ultrasonic probes operating at a center frequency of 5 MHz. The three models

used in these inspections differ mainly in terms of the number of elements in the array, namely 12, 16, and 64 (Table 1). They were all used to perform manual or linear-encoded sectorial (Azimuthal) scans ranging from 40° to 70° from normal incidence, as shown in Figure 3. Data acquired along two different scan indexes (probe standoff positions) were combined to cover the whole volume of interest in a single file to analyze.
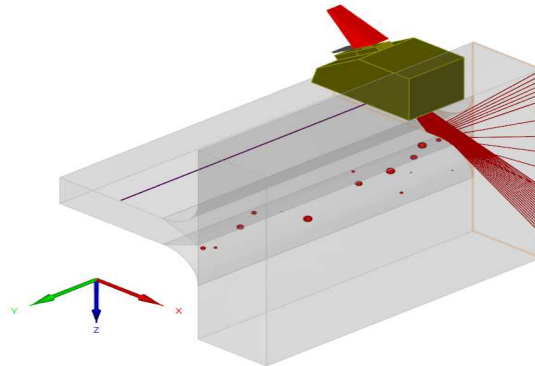

Fig 3 Sectorial scanning from both blade surfaces

Probe	Frequency (MHz)	# Element	Aperture (mm)	Elevation (mm)	Wedge angle (°)
5L12-51S	5	12	7.2	10	51SW
AM5M-55S	5	16	9.6	10	55SW
LM5M-55S	5	64	38.4	10	55SW

Table 1 Used PAUT probes

The study developed an inspection configuration in accordance with the number of transducer elements and the focal group's capability to insonify the whole weld volume on the opposite face. The inspection strategy involves inspecting the direct skip to prevent beam spread and avoid ghost echoes caused by reflection from the weld cap's curved radius. With a direct skip inspection, the ultrasonic configuration is simpler by mainly focusing the beam for a metal path range of 10 to 50 mm. These permit the use of 16 elements per focal law and use small footprint wedges or a 64-element transducer's front elements to minimize the standoff distance. With these configurations, the focal group's high angle can hit the T-joint center where it meets with the web, and the lower angles can probe most of the weld cap radius. Only a small hidden area exists and cannot be covered with angle beam inspection from the blade. The only inspection technique that can provide 100% coverage of the weldment is from the web using a normal incidence wedge. Inspection from the web was not attempted because this surface is not accessible during an in-service inspection. The following conclusions can be drawn from the results obtained;

1) Flaw resolution increases with the number of active elements used in the array;
2) However, the use of 32-element does not improve inspection performance. This finding could be attributed to the impact of a larger active aperture on the generated ultrasonic beam's characteristics. Indeed, the beam's exit point is further away from the weld's edge in this case. Besides, the beam is larger, and its power is spread over a larger cross-section, thus reducing the echo reflected by a given flaw.This is why focusing has been added to this configuration to narrow down the beam size in the range of interest;
3) Linear-encoded PAUT scans can distinguish two closely spaced flaws more easily than manual inspection. You can see example of PAUT results in Figure 4.

2.5. TOTAL FOCUSING METHOD (TFM)

The Total Focusing Method (TFM) is still part of the Ultrasonic Testing (UT). This is because it uses the same basic principles as PAUT as well as the conventional UT [21].In this study, the new phased-array technique called the TFM is included in the test matrix. Unlike the sectorial scan described previously, this technique is not a beamforming method. The TFM is an imaging technique that processes elementary A-scan data to extract the amplitude for a determined path from a firing to a receiving element. After multiplexing all elements as emitter and receiver and delaying and summing all the required amplitude, a data point in the region of interest is assigned an amplitude. The algorithm is simple, but the memory and processing burden increases geometrically with the increase in the number of elements of an array and the size of the area of interest. As a result, it is simple to achieve the configuration of TFM because once the transducer, the wedge, and the mode are defined, the user creates a rectangular area of

interest, which is subdivided into a grid. In this regard, the grid spacing is the critical variable, which is normally smaller than one-fifth of the wavelength [22,23,24]. However, if the spacing is above this value, the measured amplitude fails to be within 2dB of the true amplitude, hence, producing unreliable results. All experiments respected the wavelength criteria and opted for values that had a spacing of at most one-tenth of the wavelength.
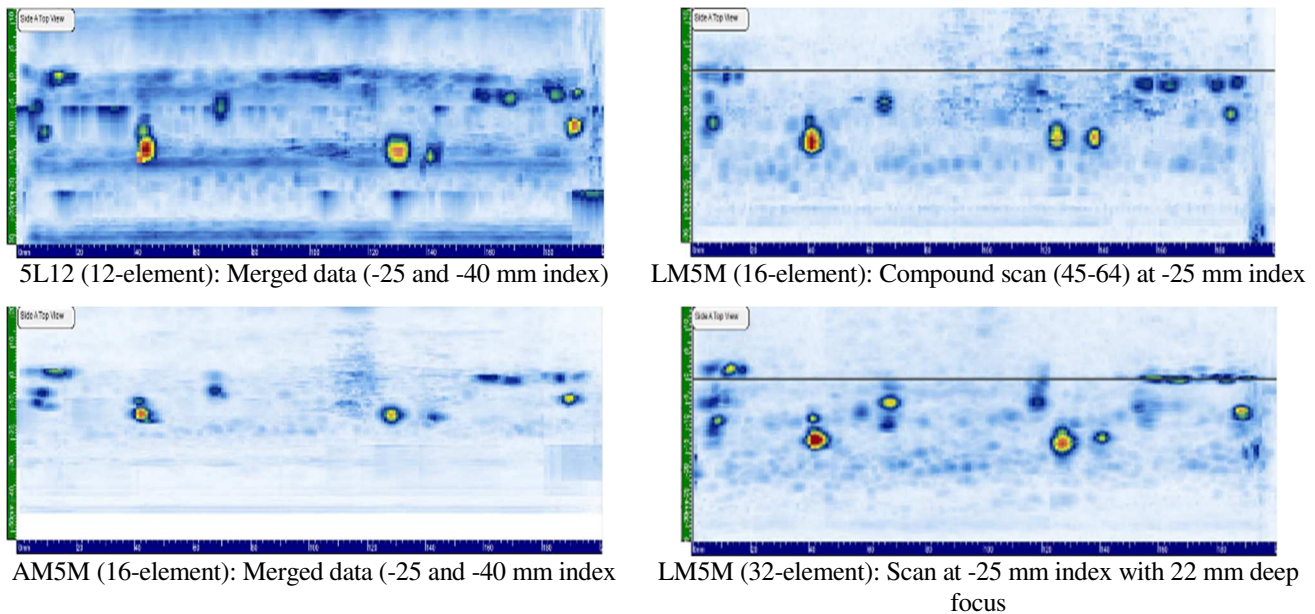

5L12 (12-element): Merged data (-25 and -40 mm index)

LM5M (16-element): Compound scan (45-64) at -25 mm index

AM5M (16-element): Merged data (-25 and -40 mm index

LM5M (32-element): Scan at -25 mm index with 22 mm deep focus

Fig 4 Example of PAUT results (Side A, Side view)

The TOPAZ 64 includes a beam simulation amplitude map function that helps to optimize all the parameters. Therefore, with the use of TFM, the region of interest covered the whole weld on the opposite side of the entry surface. In this regard, the sample was to be tested from both sides of the blade in order to fully cover the weldment. The experimental work used a 64-element linear array probe at a nominal frequency of 5MHz.The study used two wedges, one for generating shear wave and one for generating compression wave, and performed both manual and encoded scans. The linear encoder scan is done with the wedge's front abutting the weld cap, which produces a scan index of -25 mm. For manually delivered inspection, the technician has the freedom to make transversal, lateral, and skewing movements to locate discontinuities and peak them. The T-joint was examined using T-T and L-L direct modes with linear encoded scans and manual inspection. The T-T and L-L modes were used in the experiments because they produce a good amplitude response from a volumetric discontinuity. In this study, before starting the sample's inspection, the 3mm SDH was used on the martensitic sample (same material properties) for TFM model calibration. From these results, we obtained the following conclusions;

1) TFM results appear clearer, with fewer spurious indications and better-defined flaw geometries.
2) The Longitudinal-Longitudinal reconstruction mode seems to give slightly better results than the Transverse-Transverse mode.
3) We obtained a slightly better detection rate with manual TFM as compared to the encoded one. We suspect that this is due to the operator's ability to minutely adjust the probe's position to improve the signal to noise ratio on the testing unit display. An example of TFM results is observed in Figure 5.

2.6. EXPERIMENTAL DETECTION RATE

The performance of the different ultrasonic inspection techniques tested are compared in Figure 6. Obviously, among all these techniques, conventional UT results have the lowest detection rate. This could be because the fixed-angle beam can miss a flaw more easily than with ultrasounds impinging the flaw from different angles. Although the inspection is carried out to a well-defined standard, the detection rate is highly dependent on the operator. The certified practitioners reported between 7 to 16 flaws out of the 30 embedded in the weld, with an average reporting of 11 flaws.
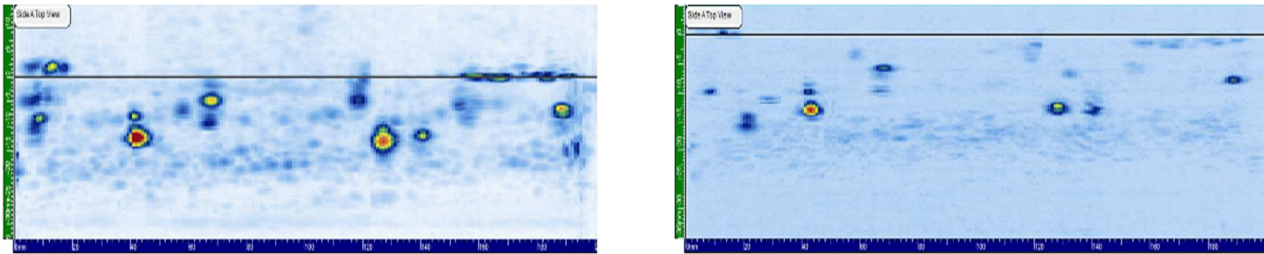
LM5M (32 elements): Sectorial scan at -25 mm index with 22 mm deep focus b) LM5M (64 elements): FMC scan at -25 mm index with encoder, direct TFM T-T
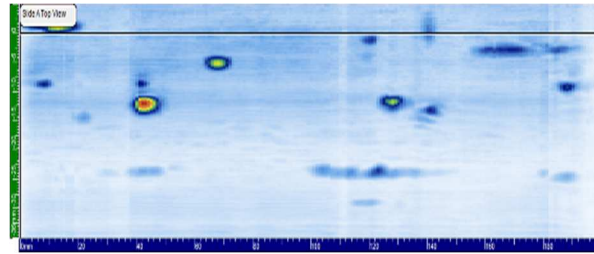
c) LM5M (64 elements): FMC scan at -25 mm index with encoder, direct TFM L-L

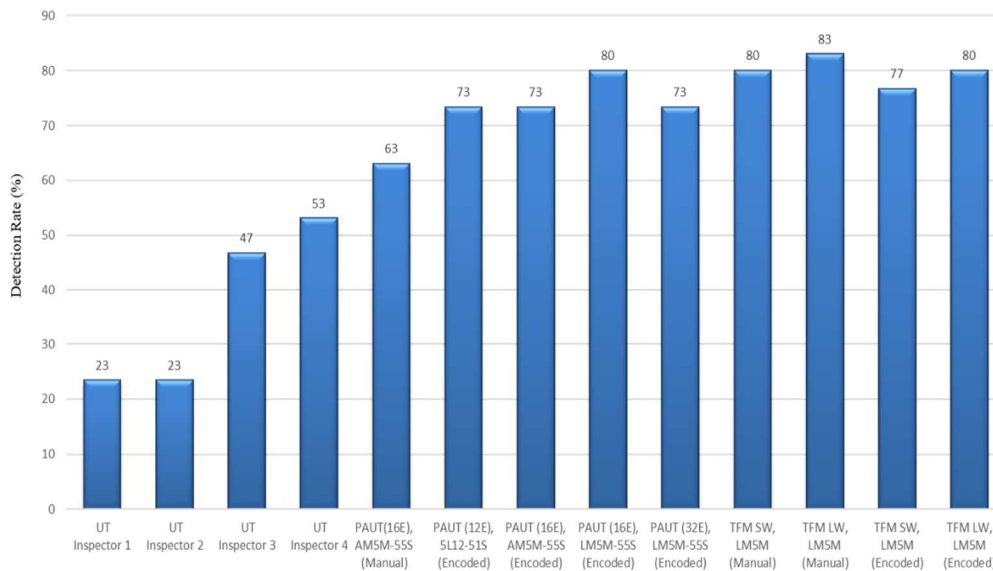**Fig 5** Example of TFM results (Side A, Side view)

Fig 6 Experiment, Different ultrasonic methods

Several difficulties were observed with manual testing; (a) Challenging to report a flaw nearby a larger reflector with all the attention on the large reflector, (b) Manual reporting of flaw position is cumbersome and leads to errors, (c) Low amplitude signal just above the rejection threshold is easily discarded, (d) the report's quality is directly related to the inspector's diligence in taking clear and precise notes. If the report is written several days after the test, the notes' quality is of paramount importance.

Manual phased array inspection suffers some of the limitations observed with a fixed-angle beam probe. The detection is done on the fly, and the flaw's information is written during the inspection. If the sample has several flaws, the technician can get confused when measuring and reporting flaws. However, one of the advantages of manual PAUT inspection is the freedom the operator has to explore a suspected flaw by executing various probe motion; pivoting the transducer or orbital movement to reveal the target's

volumetric features. The manual phased-array inspection provided the highest maximum amplitude measured and revealed flaws hidden in the trailing edge weld reinforcement. However, even if the manual phased-array found flaws hidden in the geometry, on average, it detected fewer flaws than the linear-encoded phased array.

The linear encoded inspection provides repeatable scans, and flaws with low amplitude are detected more readily by comparing the local base noise to check for any localized increase that would reveal a flaw. Close flaws may be separated, and when using the projection views, their location and separation can be measured. Generally, the aperture of 12 and 16 elements produced a reasonably good detection rate, and the small footprint of the 12-element transducer allows it to cover the center of the weld. As the aperture increases, the stand-of distance increases, and the weld's center is no longer covered. This explains why the 32-element tests did not perform better than the 12 or 16 element tests despite having a smaller beam diameter and a more extended working range covering the whole weld path.

The TFM method produced a higher detection rate, slightly better than a sectorial scan. One advantage noticed during the test is the operator can readily size the diameter of the flaw. This helped identify small beads from noise since the shape was maintained while probing the area. The TFM could also probe nearer to the surface and provided good coverage of the whole weldment. There is no dead zone compared to a 32 aperture sectorial scan. In our sample, the material has a low noise level suitable for a TFM inspection, which explains the high detection rate obtained with the study sample. Another advantage of the TFM is flaws could be categorized in apparent size or apparent reflective features. Small ceramic bead produces a specific round-shaped signal area proportional to their size, while larger beads showed either oriented facets or multiple facets surrounding the bead. TFM provided details about the reflective surface's nature, while a sectorial scan did not provide any hints about the flaw's small features.

A multi-element probe is, therefore, a better candidate in terms of detection rate. Although the difference is not huge, TFM seems to perform slightly better than standard PAUT sectorial scanning.

The optimum inspection strategy in order to reveal the most implanted flaws is to perform the inspection in two steps:

Step 1: linear encoded sectorial scan with an aperture of 16 elements or linear encoded TFM scan.

Step 2: manual inspection of the trailing edge and weld reinforcement using either a sectoral scan with an aperture of 16 elements or a 64-element TFM scan. In practice, because a real runner's trailing edge is not a flat surface, a small PAUT probe with a 12 or 16- element aperture is the only practical method for that region.

3. CIVA MODELLING AND ANALYSIS

The current study used the ultrasonic module of CIVA to simulate the welded T-joint sample inspection considered previously. Models for the sample and the inspection system have been defined as accurately as possible. There is a wide range of input parameters available to the model (Figure 7); only to give a few of the different parameters that need to be entered, we can mention:
• a CAD model describing the dimension of the sample.
• ultrasonic properties of the steel used to manufacture the sample.
• the location, the size, and the nature of the flaws distributed in the welded joints of the sample.
• ultrasonic probe geometry including a description of the array settings required for PAUT.
• the firing sequence of the elements as well as a description of the exciting impulse.

However, before embarking on a campaign of numerical simulations, it is necessary to validate the various parameters entered through measurements on real samples. This step was performed with a standard calibration block manufactured from the same steel alloy. The study carried out all the steps under the International Institute of Welding [25,26,27].

3.1. SIMULATION OF CONVENTIONAL ULTRASONIC TESTING (UT)

A rectangular single element crystal assembled to simulate conventional ultrasonic testing to a flat refracting wedge was selected as the probe. Both beams refracting at 60° and 70° were tested, as shown in Figure 8. Two steel alloys with slightly different ultrasonic properties have been used for the T-joint sample model. Spherical voids, whose distribution and size mirror the manufactured T-joint sample, have been inserted into the model, as shown in Figure 9. In the real sample, the flaws were produced by silicon nitride balls whose ultrasonic impedance is very similar to that of steel. However, experimentally, we have noticed that ultrasonic reflection does not come from an impedance mismatch at the steel/ceramic interface but from a lack of wetting between the two. Therefore, for simulation purposes, we prefer to use voids. According to Hydro-Quebec's procedure, the numerical system's sensitivity was calibrated, namely, a side-drilled-hole with a diameter of 1.5 mm at a depth of 20 mm.

The following conclusions were obtained from the simulation results: Sample alloys appear to have little to no impact on the system's detection rate and probably be attributed to the similarity between the two alloys' ultrasonic properties. Further work will consider the impact of steel microstructure on the ultrasonic beam's scattering, increasing its attenuation and producing a higher background noise level. Beam refracted at 70° gave a better detection rate than beam refracted at 60°. This result agrees with our experimental measurements and tends to prove our hypothesis; namely, this performance is due to the beam's larger divergence. However, we observe a significant difference between the simulated detection rate (Figure 10) compared to that obtained

experimentally (Figure 6). The reasons for this difference are that the ceramic beads do not behave exactly like a void, and the simulation does not capture that operator's judgment.
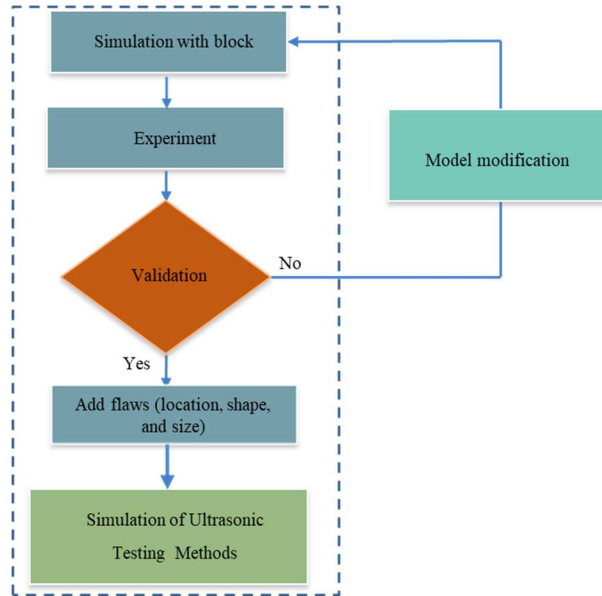
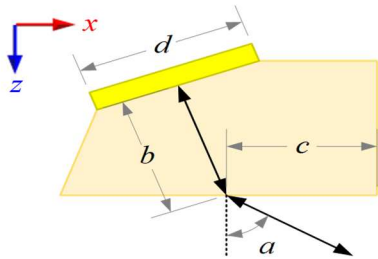

Fig 7 Configuring the CIVA model and input parameters

Fig 8. a) Conventional ultrasonic testing probe

(b) The dimension of the probe

a (°)	b (mm)	c (mm)	d (mm)
60	20	18	16
70	20	15	16
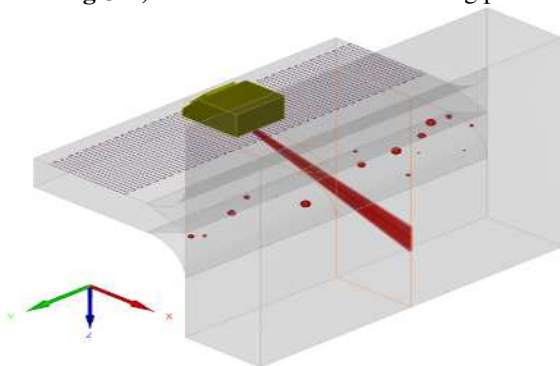
Fig 9. a) Raster scanning with water coupling

b) Material Properties

Velocity	UNS S41500	Alloy steel
Longitudinal wave (m.s^{-1})	5880	5920
Transverse wave (m.s^{-1})	3210	3255
Density (g.cm^{-3})	7.9	7.8

3.2. SIMULATION OF PHASED ARRAY ULTRASONIC TESTING (PAUT)

A linear array of 64 elements assembled to a flat refracting wedge was selected as the probe to simulate phased array ultrasonic testing. In all cases, this probe was used to sectorial scan the sample at angles ranging from 40° to 70°(with & without focusing) as shown in Figure 11. If there was focusing, the focal depth was either 22 or 50 mm.

The electronic focusing enables optimizing the beam shape at the expected defect location and further optimizes the detection probability. Also, focusing at multiple depths improves the ability to size critical flaws for volumetric inspections. Focusing can also significantly improve the signal-to-noise ratio in challenging applications and electronic scanning across many groups of elements, enabling rapid production of the C-Scan images. The T-joint sample model was the same as the one used for conventional UT simulation; same material options, same flaws nature, size, and distribution. According to Hydro-Quebec's procedure, the numerical system's sensitivity was calibrated, namely three side-drilled-holes with a diameter of 1.5 mm at depths of 15, 30, and 45 mm, respectively. The study used the computed time corrected gain (TCG) in this calibration process .The following conclusions were obtained from the simulation results:

Sample alloys appear to have little to no impact on the detection rate of the system; A 16-element configuration has a better detection rate than a 32-element one (Figure 12). The result agrees with the experimental measurements and tends to prove our hypothesis, namely, the impact of the beam exit point and the width of the refracted beam on the sensitivity of these techniques; by phased-array sectorial scanning, we are sweeping the volume with a variety of angles. Even if the targets are not exactly aligned with the center ray as indicated by Civa, there will be components of the wavefront that might hit the targets with a preferred reflection coefficient and directivity. Of course, the S-scan's fixed standoff is a limiting factor that could cause flaws at the extremes of the sectorial sweep to have a weaker response. This will be a factor in the way we set up the 16 element and 32 element apertures; for the same refracted angle, the 32 element aperture has an exit point farther back from the weld. So we are approaching the targets from slightly different angles (and distances).
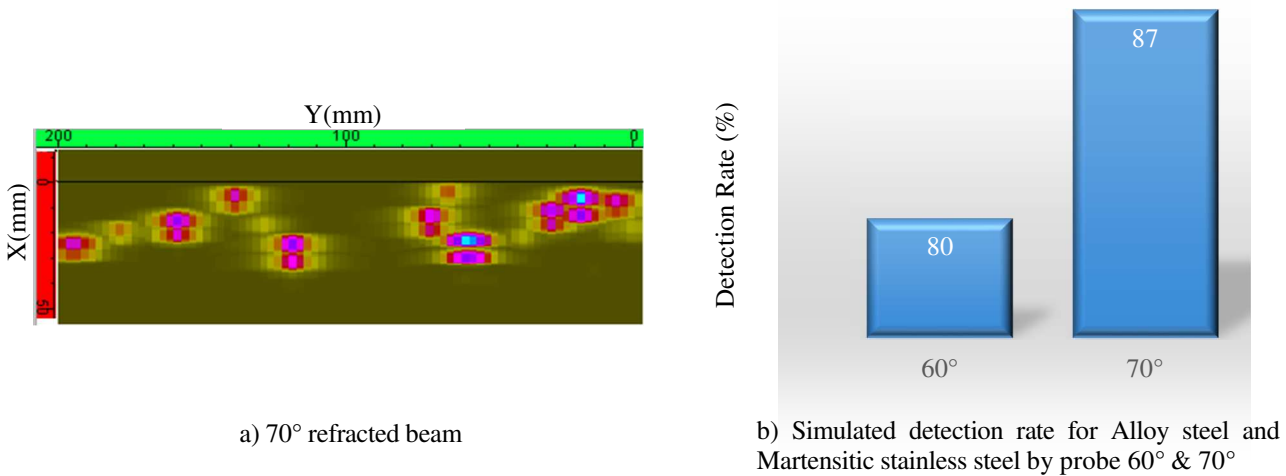

a) 70° refracted beam

b) Simulated detection rate for Alloy steel and Martensitic stainless steel by probe 60° & 70°

Fig 10 Simulation results from Conventional ultrasonic testing probe
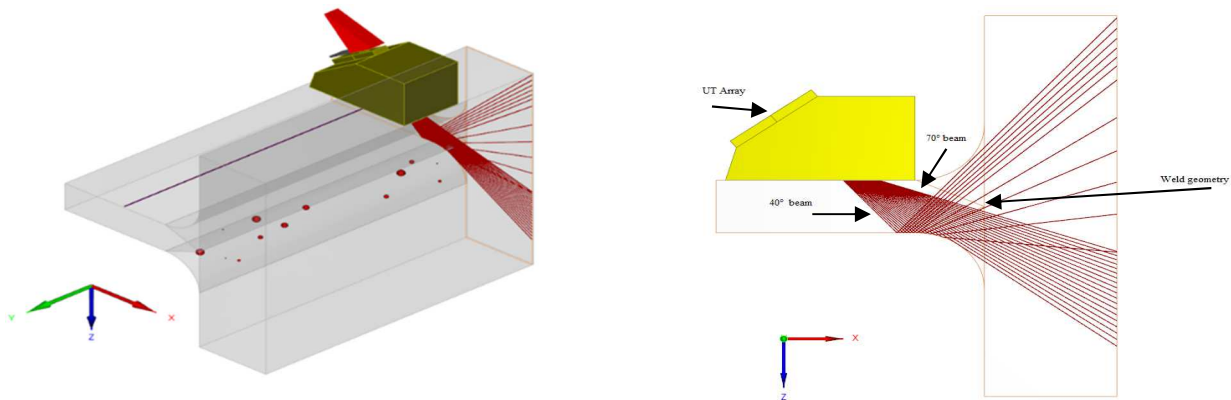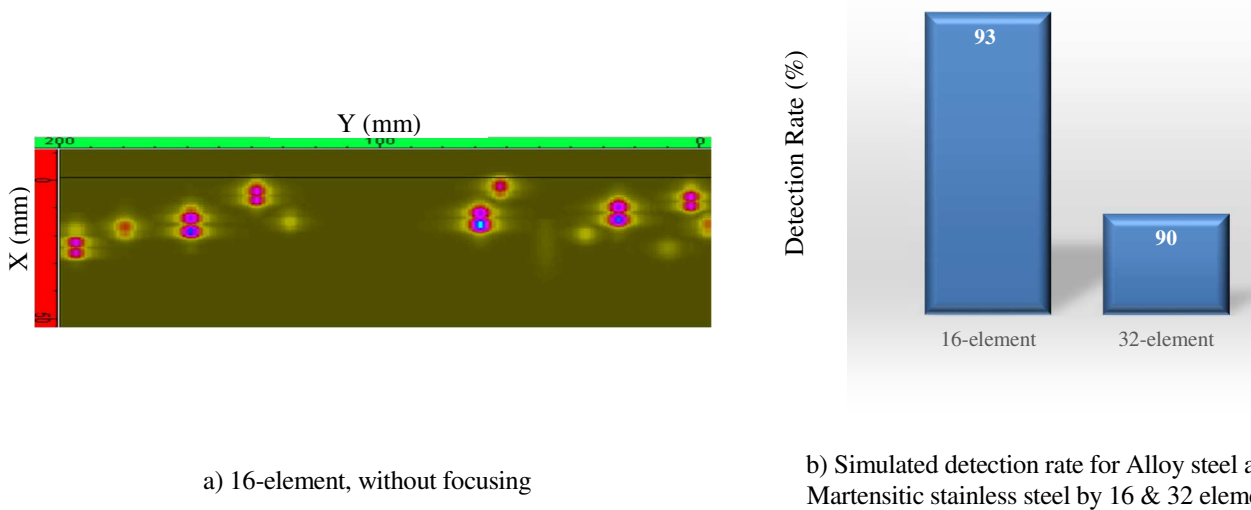

Fig 11. a) Raster scanning with water coupling

b) Setup CIVA ray tracing with the selected sweep angles.

a) 16-element, without focusing

b) Simulated detection rate for Alloy steel and Martensitic stainless steel by 16 & 32 element

Fig 12. Simulation results from PAUT probe

PAUT simulated detection rate is significantly better than the conventional UT one. As mentioned previously, this could be because the fixed-angle beam can miss a flaw more easily than with ultrasounds impinging the flaw from different directions, as is the case with sectorial scans. Also, with a fixed angle and using a raster scan, detection will be a variable that can be a function of the wedge size (limiting the probe's access to the weld) and the beam divergence.

4. FINDING AND DISCUSSION

Our tests showed that conventional Ultrasonic results in the lowest detection rate among the different ultrasonic testing methods evaluated. Although the inspection is carried out to a well-defined standard, the detection rate is highly dependent on the operator. Fixed angle conventional ultrasonic testing (UT) provides less information for accurate assessment of actual flaw conditions. Detection capability increases with the divergence of the beam of a single element probe. Because a beam refracted at 70° is more likely to show greater divergence than one refracted at 60°, the former has a better detection rate. PAUT allows one to use more angles and increases the probability of detection compared to conventional UT.

PAUT sectorial scan is also well adapted to the T-joint sample's geometry. Low angles will be tangent to the weld cap radius, while the high angles will probe the center of the blade to the web region.

The 16-element PAUT probe proves to be a good compromise for detection: Better resolution than the 12-element probe; Compared to the 32-element, a smaller wedge can be used and, for the same refracted angle, the beam exit point is closer to the edge of the weld; The size of the beam is adapted to the range of interest. With 32-element, focusing is needed to narrow down the beam emitted from a larger active aperture but did not lead to a better detection rate.

Linear-encoded PAUT scans can distinguish two closely spaced flaws more easily than manual inspection. Among the different ultrasonic testing methods evaluated, manual TFM resulted in the highest detection rate. It is slightly better than encoded TFM due to the operator's ability to adjust the probe's position to improve the signal to noise ratio on display.

TFM L-L reconstruction mode seems to give slightly better results than the T-T reconstruction mode. The reason for such a result is still under investigation. TFM by nature has better coverage than beam-forming PAUT, and that could explain the slightly higher detection rate. TFM has the advantage of a clear display with appropriate information on the actual distribution and geometry of the flaws (faceted, multi-faceted, sphere-like). However, using the T-T mode did provide more details of the ceramic bead interface and better estimate of the diameter because of the shorter wavelength. TFM requires a transducer with a large number of elements. Thus, a large contact area and good coupling for all the ray paths are needed to produce consistent and repeatable results.

The best inspection strategy to inspect the trailing edge of a runner blade is to perform the inspection in two steps:

Step1: linear encoded scan with either PAUT sectorial scanning or TFM direct mode. PAUT shall use shear wave with the refracted angle from 40° to 70°.TFM could use either L-L or T-T direct mode.

Step 2: manual sectorial scanning with a 12 or 16-element aperture and a small wedge footprint to inspect the trailing edge and the weld reinforcement. The small footprint wedge is essential on a real turbine because of the trailing edge's curvature to maintain good contact while scanning.

5. CONCLUSION AND FUTURE WORK

The preliminary technical approach developed in phase I of this research were tested on a T-weld specimen. When developing the scan plans and the preliminary data analysis, the ray path analysis indicated the need to carry out a minimum of two scans at different index points to enable complete volume coverage of the weld, particularly for thick weld specimens. This study aimed to collect initial data on a simplified mock-up and then compare the experimental ultrasonic data with the results of simulations performed by CIVA. Experimental studies in a laboratory setup showed that, among the different ultrasonic testing methods evaluated, TFM appears to be the best ultrasonic inspection technique to provide reliable flaw data to the IREQ's life estimation model. In addition to this technique's ability to detect flaw distribution, the algorithm allows a better definition of flaw geometry and highlights its different facets. CIVA model could be used to simulate ultrasonic inspection of a weld. However, to obtain reliable data, the sample and the inspection system's models must be defined with a high accuracy level. To do this, we need to adjust model parameters through validation loops based on precise measurements on real calibration samples. While defining accurate numerical models seems like a tedious task, it ultimately drastically reduces the costs of developing a reliable inspection strategy. Our future work uses such models to estimate the probability of detection (POD) of certain ultrasonic techniques applied to hydroelectric turbine runners' inspection.

REFERENCES

[1]   Gagnon, M., Tahan, A., Bocher, P. & Thibault, D. (2012a). « A probabilistic model for the onset of High Cycle Fatigue (HCF) crack propagation: application to hydroelectric turbine runner ». International Journal of Fatigue. doi: 10.1016/j.ijfatigue.2012.09.011

[2]   H. Habibzadeh Boukani, M. Viens, S.-A. Tahan and M. Gagnon, "Case study on the integrity and nondestructive inspection of flux-cored arc welded joints of Francis turbine runners," The International Journal of Advanced Manufacturing Technology, p. 2201–2211, 2018.

[3]   Habibzadeh Boukani H, Viens M, Tahan S, Gagnon M (2014) On the performance of nondestructive testing methods in the hydroelectric turbine industry. https://doi.org/10.1088/1755-1315/22/1/012018

[4]   ASTM E1316-13a, "Non-destructive Examinations " ,2004.

[5]   M. V. Felice et Z. Fan, «Sizing of flaws using ultrasonic bulk wave testing: A review,» Ultrasonics, vol. 88, pp. 26-42, August 2018.

[6]   Revised by Leonard J.Bond, Fundamentals of Ultrasonic Inspection, ASM Handbook, Volume 17, Nondestructive Evaluation of Materials,2018.

[7]   Y. Zhang, X. Li, J. Zhang et H. Ding, «Model-Based Reliability Analysis of P.A. Ultrasonic Testing for Weld of Hydro Turbine Runner» chez International Workshop on Automobile, Power and Energy Engineering (APEE). Procedia Engineering, v 16, College of Power and Mechanical Engineering, Wuhan University, Wuhan, 430072, China, 2011.

[8]   Xiao K, Shi YK, Ma QZ, Zhang J, Li XH , The intelligent ultrasonic system for quality testing of weld connections in turbine runners. In: Advanced materials research, Trans Tech Publ, vol 774, pp 1543–1546,2013. https://doi.org/10.4028/www.scientific.net/AMR.774-776.1543

[9]   Zhang J, Li Xh, Yk S, Ls L , Phased array ultrasonic inspection of embedded defects in hydropower turbine runner welds. Insight-Non-Destructive Testing and Condition Monitoring 56(7),pp390–394,2014. https://doi.org/10.1784/insi.2014.56.7.390

[10] Katchadjian, P."Practical Applications of Ultrasonic Testing in Nuclear and Conventional Industry." Insight: Nondestructive Testing and Condition Monitoring 46 (12): pp754–57,2004. https://doi.org/10.1784/insi.46.12.754.54494.

[11] CSA W59-13 Welded Steel Construction, Metal Arc Welding.

[12] ASTM E2700 –14; Standard Practice for Contact Ultrasonic Testing of Welds Using Phased Arrays.

[13] ISO 17640; Non-Destructive Testing of welds — Ultrasonic testing — Techniques, testing levels, and assessment.

[14] EN 13588; Non-Destructive Testing of welds, Ultrasonic testing, Use of automated phased array technology.

[15] Textbook for Level I&II, Phased array Course, The Welding Institute (TWI) Training.

[16] BS ISO 19675:2017; Non-Destructive Testing, Ultrasonic testing, Specification for a calibration block for phased array testing (PAUT).

[17] Daniel Kass, Michael Moles, Tom Nelligan "Phased Array Testing.", 2014. https://www.olympusims.com/en/books/pa/pa-testing/.

[18] Michael D. C. Moles, Introduction to Phased Array Ultrasonic Technology Applications,2007.

[19] Ginzel, Edward "Phased Array Ultrasonic Technology." https://eclipsescientific.com/Textbooks/Phased Array Ultrasonic Technology 2nd Edition,2013.

[20] Ginzel, E A, and D Johnson, "Phased-Array Resolution Assessment Techniques." NDT.Net – The e-Journal Non-Destructive Testing, no. July 2008. http://www.ndt.net/article/v13n07/ginzel.pdf.

[21] Ditchburn R, Ibrahim M , Ultrasonic phased arrays for the inspection of thick-section welds. Tech. Rep., DTIC Document,2009.

[22] https://www.ndt.net/forum/

[23] Richard, Daniel, Federico Zottig, and Guy Maes "On the Use of Advanced Focusing Techniques for Enhanced PAUT Inspection Capability," no. 1: pp1–8,2018.

[24] Fundamental Principles of FMC and TFM technologies, Zetec training session, June 2017.

[25] Holmes, Caroline, Bruce W. Drinkwater, and Paul D. Wilcox "Post-Processing of the Full Matrix of Ultrasonic Transmit-Receive Array Data for Non-Destructive Evaluation." NDT and E International 38 (8): pp701–11, 2005. https://doi.org/10.1016/j.ndteint.2005.04.002.

[26] E. Iakovleva, S. Chatillon, P. Bredif et S. Mahaut, «Multi-mode TFM imaging with artifacts filtering using CIVA UT forwards models» chez 40th Annual Review of Progress in Quantitative Nondestructive Evaluation - AIP Conference Proceedings, v 1581, p 72-79,2014.

[27] Recommendations for the use and validation of NDT simulation – IIW 2363.

LOCALLY OPTIMAL SUBSAMPLING STRATEGIES FOR FULL MATRIX CAPTURE MEASUREMENTS IN PIPE INSPECTION

Fabian Krieg[*1,2,3]**, Jan Kirchhof**[1,3]**, Eduardo Pérez**[1,3]**, Thomas Schwender**[1]**, Florian Römer**[1]**, Ahmad Osman**[1,2]

[1]Fraunhofer-Institute for Nondestructive Testing IZFP, Campus E3, 66123 Saarbrücken
[2]University of Applied Sciences, htw saar, Goebenstrasse 40, 66117 Saarbruecken, Germany
[3]Technische Universität Ilmenau, Helmholtzplatz 2, 98693 Ilmenau

[*]Corresponding Author: fabian.krieg@izfp.fraunhofer.de

ABSTRACT

In ultrasonic non-destructive testing, array and matrix transducers are being employed for applications that require in-field steerability or which benefit from a higher number of insonification angles. Having many transmit channels on the other hand increases the measurement time and renders the use of array transducers unfeasible for many applications. In the literature, methods for reducing the number of required channels compared to the full matrix capture scheme have been proposed. Conventionally, these are based on using only receive channels close to the transmit channel. Furthermore, Compressive Sensing based approaches have been proposed, which either use random subsampling schemes or optimize the channel configuration based on theoretic bounds derived specifically for the given measurement setup over the full imaging region. In this publication, we investigate a scenario from the field of pipe inspection, where cracks have to be detected in specific areas near the weld. Based on ray-tracing simulations which incorporate a model of the transducer directivity and beam spread at the interface we derive application specific measures of the energy distribution over the array configuration for given regions of interest. These are used to determine feasible subsampling schemes. For the given scenario, the validity/quality of the derived subsampling schemes are compared based on reconstructions using conventional total focusing method as well as sparsity driven reconstructions using the FISTA. The results can be used to effectively improve the measurement time for the given application without notable loss in defect detectability.

KEYWORDS: Total Focusing Method, Compressive Sensing, FISTA, Full Matrix Capture, NDT Methods, Signal Reconstruction, Defects

1. INTRODUCTION

Multi-channel ultrasound measurements allow a high level of flexibility in the data acquisition for imaging and defect recognition. A common acquisition scheme is the full matrix capture (FMC), which denotes consecutively transmitting with one transducer element after another, while all elements receive on each cycle. This acquisition scheme is then commonly paired with the Total Focusing Method (TFM) [1], which is an imaging algorithm applied in post-processing. Reducing the FMC dataset by using fewer transmit or receive channels has been studied in the literature, where using fewer transmit cycles is accounted to reduce the measurement time and fewer receive channels can reduce the hardware cost. In this publication we investigate the former, with the goal of deriving transmit patterns based on a specific region of interest in our imaging region.

The design of sparse ultrasound arrays is extensively being studied in the literature for medical applications, where the most common optimization criteria are side lobe levels and point spread functions over the full aperture. In non-destructive testing transmit subsampling is being investigated in [2], where the authors show that using 2 or 4 elements near the end of the array for excitation is to be favored over transmitting with all elements as one. In [3] and [4] equispaced element choices as well as using only the outer elements are being investigated, concluding that using fewer elements can be an application dependent choice to improve measurement speed. In [5] sparse arrays are designed using a combination of almost different sets and a genetic algorithm using attributes of the point spread function as fitness measure. In [6] using fewer receivers is investigated for near surface defects. In [7] particle swarm optimization is performed to reduce the computation time of FMC by using fewer elements. In [8] a Compressive Sensing (CS) based approach is used for reducing the data both in receive as well as in frequency based on Cramer Rao Bounds. The prioritization of specific areas when designing a sparse array is taken into consideration in [9], though the application is here acoustic source localization using microphones.

In this publication we investigate a scenario where a bowed transducer array is positioned over a moving pipe in production. While the transducer encloses a section of the pipe to ensure recording echoes from a large variety of angles as well as to enable in-field

adjustability, the region where defects are expected is limited to the weld. As a high inspection speed is crucial for the application, resulting in the possibility of investigating the pipe at a higher manufacturing speed, we investigate the reduction of the number of transmit cycles. The transmit elements are chosen based on the a-priori knowledge of the limited area of interest. The reconstruction as well as the array element selection are performed based on a linearized forward model, which, calculated by a raycasting scheme, incorporates effects as transducer directivity and refraction at the pipe boundary. Both the TFM as well as the Fast Iterative Shrinkage-Thresholding Algorithm (FISTA) [10] are evaluated for imaging.

2. METHODS

2.1 FORWARD MODEL

The post-processing algorithms considered in this publication combine data from multiple observation for imaging. The bowed linear array transducer that is used for the measurements is assumed to be stationary during each cycle of transmit and receive events. The data acquisition is performed such that one transducer elements shoots at a time and multiple transducer elements record the echoes [1]. The data from all transmit and receive events at one location is then fused in post-processing.

We consider each observation to be a superposition of multiple time shifted echoes as

$$g_{m_{tx},m_{rx}}(t) = \Re\left\{\sum_d \sum_p \alpha_{m_{tx},m_{rx},p,d}\, h^{(a)}\big(t - \tau_{m_{tx},m_{rx},p,d}\big)\right\} + n(t) \tag{1}$$

where $g(t)$ is an A-scan and m_{tx} and m_{rx} index a transmitter and receiver, respectively. The analytic signal of the transmit pulse is given by $h^{(a)}(t)$, $\Re\{.\}$ takes the real part. Each A-Scan consists of a superposition of echoes from multiple defects d. The ultrasonic wave can have taken different propagation paths and modes from transmitter to defect to receiver, which are indexed by p (see also [11], [12]). The complex factor α models the amplitude and phase change on the path, constructed from the transducer directivity, the interfaces and the interaction with the defect itself. The time-shift τ indicates the propagation time on the path. $n(t)$ indicates zero-mean additive white Gaussian noise.

2.2 TOTAL FOCUSING METHOD

The Total Focusing Method (TFM) allows the estimation of the reflectivity of the specimen at arbitrary points of interest $\mathbf{r} \in \mathbb{R}^2$ with $\mathbf{r} = [x, y]^T$. Starting from the model given in Eq. 1 we assume a perfect point scatterer to be located at $\mathbf{r}$. The reflectivity is then given by correlating the measurement data with the estimated point scatterer response. Repeating this procedure for a set of points of interest yields an image of the reflectivity of the medium.

For the calculation of the reconstruction we limit ourselves to longitudinal propagation, as responses including transversal propagation can be omitted from the data. Furthermore, multi-view data fusion is an open research topic [11] and out of scope of this publication. Amplitude changes due to interfaces have shown to be neglectable for the investigated scenario, furthermore, the influence of attenuation is considered to be small enough to be neglected as well, which is in accordance with the literature [11]. The TFM reconstruction at a point $\mathbf{r}$ is then given by [1]

$$I(\mathbf{r}) = \left| \sum_{m_{tx}} \sum_{m_{rx}} \alpha_{m_{tx},m_{rx}}(\mathbf{r}) g^{(a)}_{m_{tx},m_{rx}}(\tau_{m_{tx},m_{rx}}(\mathbf{r})) \right| \tag{2}$$

where $\alpha_{m_{tx},m_{rx}}(\mathbf{r}) = \alpha_{m_{tx}}(\mathbf{r})\alpha_{m_{rx}}(\mathbf{r})$ is a real weighting factor constructed from the transducer directivities $\alpha_{m_{tx}}(\mathbf{r})$ and $\alpha_{m_{rx}}(\mathbf{r})$ at transmitter and receiver element, respectively. We consider directivities to follow a gaussian shape as $\alpha(\mathbf{r}) = \exp\left(\frac{-\phi(\mathbf{r})}{2\cdot(0.5\phi_{max})^2}\right)$ here, where $\phi(\mathbf{r})$ is the angle of the according propagation path at the transducer element, which can be calculated once the path from the transducer element to $\mathbf{r}$ has been determined.

Matrix Formulation For brevity of notation we now limit ourselves to reconstructions which are performed on an equispaced grid, i.e. to $\mathbf{r} = \mathbf{r}(n_z, n_x) = [n_z d_z + z_0, n_x d_x + x_0]^T$ where n_z and n_x are integers in the range $[0, N_z[$ and $[0, N_x[$, respectively, d_z and d_x denote the sampling intervals and z_0 and x_0 a start point in the according directions. Furthermore, we denote the number of transducer elements as N_{el} and in the case of of using fewer transmit cycles, the number of transmit cycles N_{tx}. The A-scans are considered to be time-discrete equivalents to the continuous definition used before, holding N_t samples acquired at a sampling frequency f_s.

Eq. 2 can be rewritten as matrix-vector product [13], [14], [8]

$$\mathbf{i}_{tfm} = |\mathbf{Mg}| \tag{3}$$

where $\mathbf{g} = \left[\mathbf{g}_{0,0}^{(a)^T}, \mathbf{g}_{0,1}^{(a)^T}, \ldots, \mathbf{g}_{0,N_{el}-1}^{(a)}{}^T, \mathbf{g}_{1,0}^{(a)^T}, \ldots, \mathbf{g}_{N_{tx}-1,N_{el}-1}^{(a)}{}^T\right]^T \in \mathbb{C}^{N_{tx}N_{el}N_t}$ are the stacked analytic representations of the measurement data with $\mathbf{g}_{m_{tx},m_{rx}}^{(a)} \in \mathbb{R}^{N_t}$ being a single A-scan, $\mathbf{i}_{tfm} = [I([z_0, x_0]^T), I([z_0 + d_z, x_0]^T), \ldots, I([z_0 + d_x]^T), \ldots]^T \in \mathbb{R}^{N_z N_x}$ is the vectorized image on the equispaced grid and $\mathbf{M} \in \mathbb{R}^{N_z N_x \times N_{tx}N_{el}N_t}$ is the model matrix and $|.|$ denotes the elementwise absolute value.

The matrix is constructed from blocks $\mathbf{M}_{(n_z,n_x),(m_{tx},m_{rx})} \in \mathbb{R}^{1,N_t}$ as

$$\mathbf{M} = \begin{bmatrix} \mathbf{M}_{(0,0),(0,0)} & \mathbf{M}_{(0,0),(0,1)} & \cdots & \mathbf{M}_{(0,0),(1,0)} & \cdots \mathbf{M}_{(0,0),(N_{tx}-1,N_{el}-1)} \\ \mathbf{M}_{(1,0),(0,0)} & \cdots & & & \\ \cdots & & & & \\ \mathbf{M}_{(0,1),(0,0)} & & & & \\ \cdots & & & & \\ \mathbf{M}_{(N_z-1,N_x-1),(0,0)} & & & & \end{bmatrix} \tag{4}$$

with each block being defined as

$$\left[\mathbf{M}_{(n_z,n_x),(m_{tx},m_{rx})}\right]_{m_t} = \begin{cases} \alpha_{m_{tx},m_{rx}}(\mathbf{r}(n_z,n_x)) & \text{if } \lfloor f_S \tau_{m_{tx},m_{rx}}(\mathbf{r}(n_z,n_x))\rfloor = m_t \\ 0 & \text{otherwise} \end{cases} \tag{5}$$

where $m_t \in [0, N_t[$ denotes an integer index and $[.]_m$ denotes access to the particular element of the column vector and $\lfloor . \rfloor$ is the floor operation. In contrast to the state of the art TFM formulations e.g. in [1], [11] the times of flights are rounded to the temporal sampling grid here. Formulating the problem this way allows for an efficient precalculation of the matrix, reducing the reconstruction to a simple matrix vector multiplication [14] and opening the door for the application of algorithms like FISTA.

The model matrix $\mathbf{M}$ can be calculated for different transmit schemes. In the remainder of the paper we assume that $\mathbf{M}$ was calculated according to the given transmit pattern, furthermore, as a special case, we denote $\mathbf{M}_{fmc}$ with $N_{tx} = N_{el}$ as the matrix that corresponds to the reconstruction of a FMC dataset. Reducing the size of the matrix also consequently reduces the computation time of the reconstruction, which is a simple matrix vector product here.

**Weighting** In the given scenario, the number of A-scans contributing to each reconstruction voxel varies strongly. This is due to the limited insonification angle of each transducer element, the influence of the specimen geometry and refraction as well as the reconstruction being performed on a cartesian grid where as the measurement setup is layed out in a circular pattern. In [15] a weighting to counter the effects of transducer directivity and beamspread has been applied. In a similar spirit we introduce a weighting that corrects for the influence of the refracting boundary in combination with the directivity of our transducer elements. A measure of the visibility of a reconstruction voxel from each active transducer is given by the number of nonzero elements in its corresponding row in $\mathbf{M}$. Summing over these elements further includes the effect of the directivity of the transducers. The vector $\mathbf{e} \in \mathbb{R}^{N_z N_x}$ captures this measure for all voxels and can be computed by:

$$\mathbf{e} = \mathbf{M}_{fmc} \, \mathbf{1} \tag{6}$$

The weight matrix to scale the reconstruction can then be constructed as the inverse of a diagonal matrix constructed from $\mathbf{e}$

$$\mathbf{W} = (\text{diag}(\mathbf{e}))^{-1} \tag{7}$$

yielding the weighted TFM reconstruction as

$$\mathbf{i}_{wtfm} = |\mathbf{W} \, \mathbf{M} \, \mathbf{g}| \tag{8}$$

2.3 FISTA

The task of recovering the point scatterer locations from the measurements using a linear model of the reflectivity of the medium can also be considered as a sparse recovery problem, when the number of point scatterers is small. The reconstruction can therefore also be obtained by approximating a solution to

$$\min_{\mathbf{i}_{FISTA}} ||\mathbf{g} - \mathbf{M}^H \mathbf{W}^H \mathbf{i}_{FISTA}||_2^2 + \lambda ||\mathbf{i}_{FISTA}||_1 \tag{9}$$

where $\mathbf{i}_{FISTA} \in \mathbb{C}^{N_z N_x}$ is the sparse representation, which is equivalent to an image of the reflectivity of the medium, $||.||_n$ denotes the n-norm, λ is a regularization parameter controlling the sparsity of the result and $.^H$ denotes the Hermitian transpose. Such problems can be approximated by the FISTA-algorithm [10], yielding a regularized image of the reflectivity according to $\mathbf{M}$ for our usecase. The matrix $\mathbf{W}$ serves as a normalization to the dictionary $\mathbf{M}$. Note that this is common practice in the Simultaneous Algebraic Reconstruction Technique (SART) [16].

We use the implementation of the algorithm provided in the fastmat-package for python [17]. Following [18], the regularization parameter is chosen as

$$\lambda = \beta ||\mathbf{W}\mathbf{M}\mathbf{g}||_\infty \tag{10}$$

with $0 \le \beta \le 1$.

2.4 RAYCASTING

All the above formulations require the ray paths to be known for the calculation of $\mathbf{M}$. In the literature, two approaches to determine the propagation paths between transmitters, receivers (which are interchangeable due to acoustic reciprocity) and $\mathbf{r}$ are prevalent. In many publications iterative schemes for finding a propagation path that fulfils Fermats principle given one or multiple surfaces are used [12], [11], [19], [20]. On the other hand, e.g. in [21] the Eikonal equations are solved directly to determine the propagation times.

In contrast, we use a scheme where a set of rays is shot for each transmit and receive event. The rays are propagated through the medium and refracted and reflected at each surface on their path. The propagation times and amplitudes are extrapolated to the grid of points of interest on each step using an adaption of the Bresenham line tracing algorithm [22], expanded by a linear interpolation of the amplitudes and propagation times along the line. A sketch that outlines the procedure is given in Fig. 1. The rays are traced on a map that represents the time of flights and amplitudes from which the model is built.
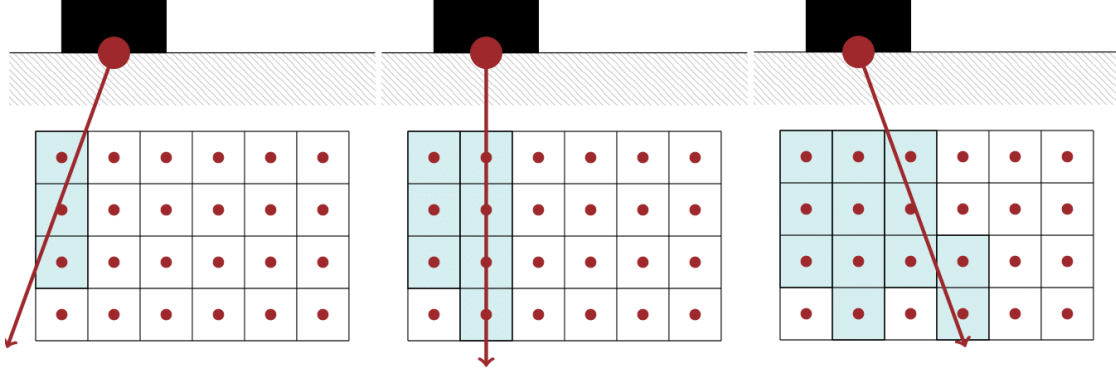

Fig. 1 Sketch illustrating how rays are rasterized and projected to the equispaced voxels used for imaging by a line tracing algorithm

3. TRANSMIT SUBSAMPLING STRATEGY

By using fewer transmit cycles the measurement time can be improved. Our goal is to use the information derived from the raycasting procedure and forward modelling to get an optimal choice of transmit elements for imaging a region of interest. The model in Eq. 3 can be used to derive the linear forward model. The following equation

$$\hat{\mathbf{g}} = \mathbf{M}_{fmc}^H \hat{\mathbf{i}} \tag{11}$$

yields a synthetic dataset $\hat{\mathbf{g}}$ given by a superposition of all point scatterer responses modeled by $\mathbf{M}_{fmc}^H \hat{\mathbf{i}}$. We now choose $\hat{\mathbf{i}}$ such that all entries corresponding to voxels in our region of interest have value 1 and 0 elsewhere. In consequence, $\hat{\mathbf{g}}$ now holds data which, though following a simplified model, reflects a scenario where the full region of interest is reflecting.

We can now sum these theoretical responses to get a measure of how much the excitation of each transducer element contributes to imaging the region of interest as

$$[\mathbf{c}]_{m_{tx}} = \sum_{m_{rx}} \sum_{m_t} |[\hat{\mathbf{g}}_{m_{tx},m_{rx}}]_{m_t}| \tag{12}$$

with $\mathbf{c} \in \mathbb{R}^{N_{el}}$. We assume here that the elements indexed by m_{tx} are ordered such that for adjacent transducer elements the contributions are given by $[\mathbf{c}]_i$ and $[\mathbf{c}]_{i+1}$. In order to get the best trade off between collecting the maximum energy from the region of interest (choosing only the center elements) and using an as wide as possible aperture (using only the outer elements) we use the following heuristic. We divide $\mathbf{c}$ into N_{tx} sections where each section has the same area under curve. We then use the center transducer element corresponding to the center index of each section as transmitter. This can be expressed by the following computation steps. We first compute the cumulative sum $\mathbf{c}^{(c)} \in \mathbb{R}^{N_{el}}$ of the elements of $\mathbf{c}$,

$$\left[\mathbf{c}^{(c)}\right]_{m_{tx}} = \frac{1}{\mathbf{1}^T\mathbf{c}} \sum_{i=0}^{m_{tx}} [\mathbf{c}]_i \tag{13}$$

normalized such that the maximum is 1. We then find our k-th transmitter element index $[\mathbf{p}]_k$ with $\mathbf{p} \in \mathbb{N}^{N_{tx}}$

$$p_k = \min_{\xi} \xi \ \text{ s.t. } \left[\mathbf{c}^{(c)}\right]_{\xi} \geq \frac{1}{N_{tx}}\left(\frac{1}{2} + k\right) \tag{14}$$

which is the smallest index for which $\mathbf{c}^{(c)}$ exceeds the given threshold.
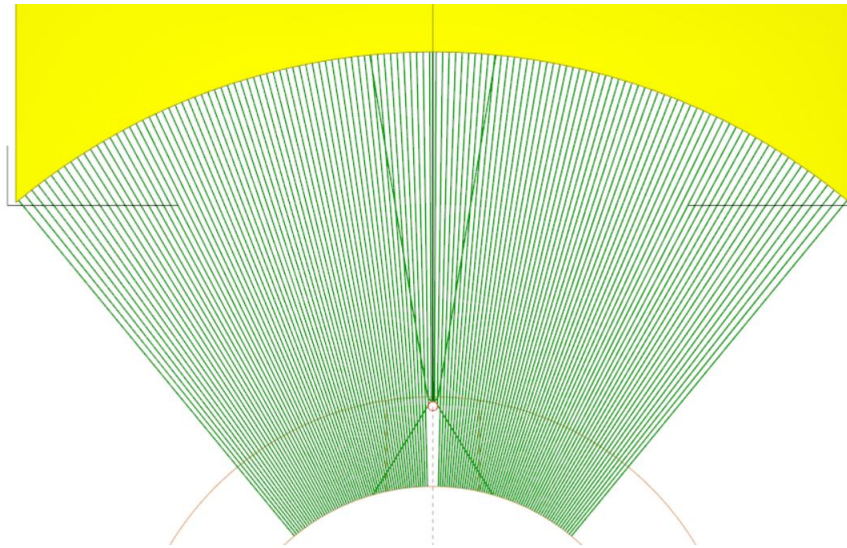
4. RESULTS

4.1 SIMULATION SCENARIO

Fig. 2 Simulation scenario as configured in CIVA

Parameter	Value
transducer radius	35 mm
transducer element count	128
transducer element width	0.3 mm
pitch	0.05 mm
outer pipe radius	16.5 mm
inner pipe radius	11.7 mm
pipe material	steel
coupling material	water

Table 1 Simulation scenario parameters.

Simulations are performed in CIVA 2020 from EXTENDE [23]. The scenario is depicted in Fig. 2. A summary of the simulation parameters is given in Table 1. The simulation mimics an inline inspection application where a circular array is used to monitor a pipe in production. Water is used as an acoustic couplant between transducer and pipe. The weld region is configured to behave like the surrounding material, except for defects being placed in that region, as the main focus of the publication is the investigation of the transmit pattern choice rather than thoroughly modelling a weld.

For each simulation, one inclusion is modelled by a 0.5 mm diameter circular defect. Simulations with the defect being placed at radius 13 mm and 15 mm are performed. The defect is placed centered with respect to the transducer in angular domain.

Furthermore, 0 dB zero-mean white Gaussian noise is added to the simulated measurement data to account for imperfections in the electronics and measurement. The term 0 dB refers here to the noise variance being equal to the energy of the first echo from the defect at the center transducer element in pulse echo mode.

4.2 TRANSMIT SUBSAMPLING

Impact of the region of interest selection In order to optimize our subsampling we choose a region of interest which overlays the weld. The variation of the visibility of the region of interest over the transducer elements is displayed in Fig. 3. When choosing a map that reflects a region near the front wall, as given by (b), only the center transducer elements contribute to the imaging. Vice versa a region near the inner pipe radius (c) can be imaged using a much wider aperture.

Consequently, since imaging with the widest possible aperture is beneficial as defects like cracks can show very direction-specific reflection patterns, the width of the subsampled aperture needs to be chosen carefully. For the remainder of the paper we use the region of interest depicted in (c), which overlays the full weld as our best a-priori guess to the defect positions to be observed in the data. It spans an area of 3.56 mm $\times$ 1.02 mm. From Fig. 3 it is apparent that this region results in an aperture choice that is a mix of (a) and (b).
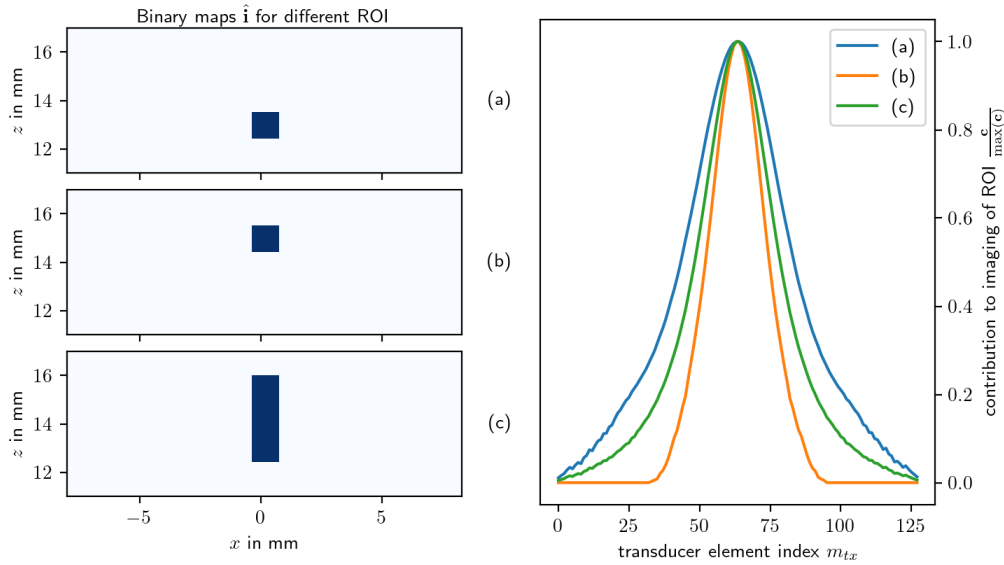
Fig. 3 Impact of different choices for the region of interest (ROI), given by the binary maps $\hat{\imath}$, on the visibility by each transducer element, given by $\boldsymbol{c}$. The ROI correspond to a defect at 13 mm for (a), 15 mm for (b) and the full weld for (c). The ROI (c) is used for selecting the transmit elements in remainder of the paper

The 16, 8 and 4 transmit elements chosen based on the region of interest in our scenario are displayed in Fig. 4. The center of the array is being sampled more densely, as it contributes more energy to our region of interest. Still, a wide aperture is used which can help with the imaging of very specular reflecting defects.

Verification of the transmit element selection scheme To verify the approach to subsampling we perform reconstructions of the simulated measurement data with wider or narrower transmit patterns. To generate these patterns the vector $\boldsymbol{c}$ is linearly interpolated or extrapolated to reflect a wider or narrower energy spread, the patterns are then chosen from that deviated distribution. This is done in order to verify that the chosen approach of taking the distribution from the model matrix is valid.
In Fig. 5 the interpolated distributions $\boldsymbol{c}$ are related to the corresponding scale parameters. For larger values of the scaling factor the curve becomes wider, yielding a more a uniform transmitter distribution over the full aperture. In contrast, a small scale parameter leads to a narrower distribution that results in only picking the center elements of the array as transducers.
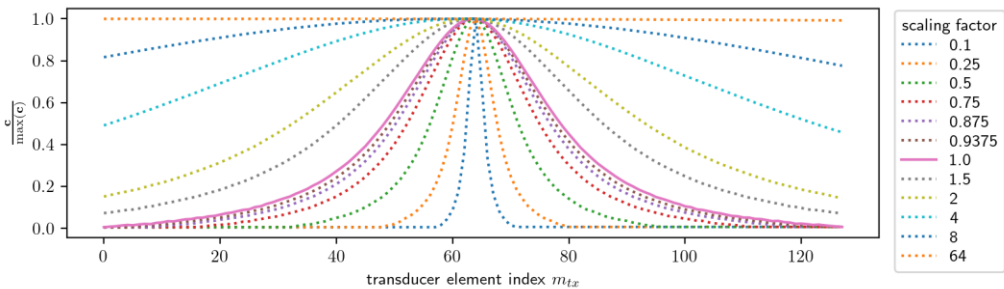

Fig. 5 Plot of the energy distributions over the elements indices gained by linearly interpolating $\boldsymbol{c}$ to a scaled axis. The original distribution, which reflects the $\boldsymbol{c}$ obtained for the region of interest in Fig. 3 (c), is given by the scaling factor 1.0. The distribution is scaled to emulate misalignment of $\boldsymbol{c}$ and investigate the impact on the reconstruction.

We evaluate the transmit element selection scheme in Fig. 6 by choosing the transmit pattern from a scaled $\boldsymbol{c}$ (the scaled $\boldsymbol{c}$ are displayed in Fig. 5) and performing a reconstruction both with FISTA as well as TFM on the given data. The reconstructions are then compared by the ratio of the energy in a square region around the defect to the energy in the whole image. The evaluation has been run both for a defect at $z = 13$ mm in (a) as well as for a defect at $z = 15$ mm averaging over 10 noise realizations for each. All plots have been scaled to maximum 1 for better comparison.

The curves show that the TFM reconstruction performs best for narrow transmit patterns, except for a slight increase for 8 and 16 elements from scaling factor 0.1 to 0.25. The performance decreases for wider aperture choices. The original distribution at scaling factor 1.0 is approximately at half of the peak to minimum performance value. For FISTA the reconstruction of the defect at $z = 13$ mm benefits from using a pattern with scaling factor 0.5 to 1, even failing to reconstruct when picking only the center elements. For the other defect the algorithm performs in a similar fashion as TFM.

The measures indicate that, except for FISTA on the $z = 13$ mm defect, choosing a narrower distribution yields more energy for the defect in the reconstruction, compared to the overall energy. When choosing a wider aperture the performance slowly starts to decrease, as the ultrasonic waves from the outer transmitters that are reflected by the defect have less amplitude due to the transducer directivity and boundary. On the other hand, choosing a wider distribution is beneficial if the defect reflects stronger to the side than back to the center, as it might be the case for a crack. This mismatch is due to the model being derived for perfect point scatterers, which have, unlike the side drilled holes used in the simulations, an omnidirectional reflection pattern.

Consequently, as the measures in Fig. 6 are derived for side drilled holes as reflectors, the results indicate the aperture has been chosen slightly too large. Still, the choice seems suitable, as the algorithm performance is good, and will be more robust to directional reflectors or off-center than a more narrow aperture. The given measures reflect the performance of the algorithms for a side drilled hole that is located perfectly in the center of the aperture. It is also indicated that the aperture choice should not be too narrow by the FISTA reconstruction in Fig. 6 (a) and the slight increase of most curves from scaling factor 0.1 to 0.25. We therefore deem the transmit pattern selection scheme suitable for the application at hand.
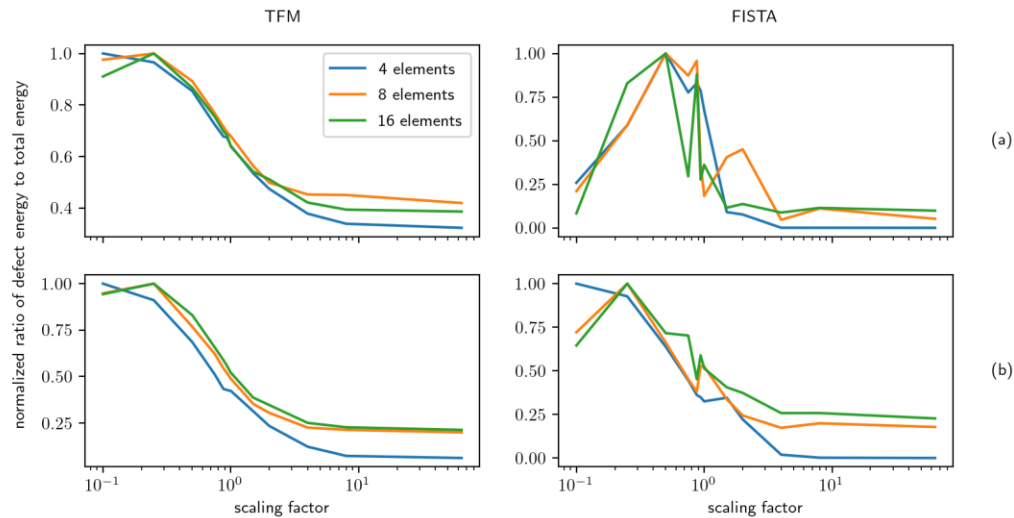

Fig. 6 Performance of the reconstruction for the proposed transmit pattern selection scheme if the underlying model deviates. The deviation is simulated by interpolation of the original c, the scaling factor refers to the distributions shown in Fig. 5. The row (a) displays the results for a circular defect at $z = 13$ mm, the row (b) for a defect at $z = 15$ mm. The proposed scheme yields the measures at scaling factor 1.

Fista and the dictionary normalization FISTA requires tuning the regularization parameter as well as number of steps for the scenario at hand. We empirically determined that $\beta = 0.01$ as well as running 20 steps of FISTA is suitable for our application and kept these values constant for all investigations. To justify the dictionary normalization introduced by the matrix $\mathbf{W}$ in Eq. 9 and eq. 10 the performance of the algorithm is compared with and without the weighting. The comparison is carried out using 4 transmit elements that were determined by the proposed selection scheme. The resulting B-scans are displayed in Fig. 7.

It can be seen that without the weighting, i.e. a uniform $\mathbf{W} = \mathbf{I}$, the level of the noise compared to the maximum amplitude of the defect in Fig. 7 (a) is higher. This is due to the rows of $\mathbf{M}$ corresponding to scatterers in that region having a larger norm, as the region is visible over a wider aperture (compare also to Fig. 3). Consequently, FISTA yields a less sparse solution for scatterers being predominantly in that region, as a slight change to values of $\mathbf{i}_{FISTA}$ associated with that region introduces a large change to the data fidelity term $||.\,||_2^2$ but a small change to the regularization term. For the defect at $z = 15$ mm in Fig. 7 (b), the weighted reconstruction has a better defect to front wall separation. A likely cause for this is the uniformly weighted reconstruction favoring the backwall reflection much more than the weighted reconstruction, leading to a more faint defect image.

Concluding, without the introduction of $\mathbf{W}$ as given in Eq. 7, the FISTA shows more noise, preferably near the inner pipe radius. This is due to the non-uniform effect of the L1-norm regularization term, which is meant to promote sparsity, for non-normalized dictionaries. In praxis, the proposed weighting scheme is capable of countering that effect.
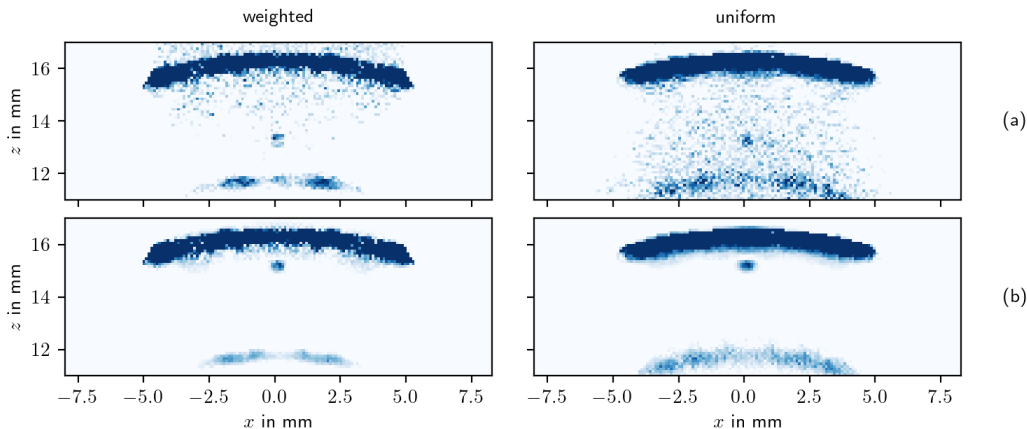
Fig. 7 B-scan views of FISTA reconstructions for four transducer elements comparing the weighting scheme given in Eq. 7 with a uniform weighting, i.e. $W = I$, for (a) a defect at $z = 13$ mm and (b) $z = 15$ mm, respectively. All plots are normalized such that the colormap spans the values from zero to the maximum amplitude of the respective scatterer.

Reconstruction of the simulated data The reconstructions for 4, 8 and 16 transmit elements chosen according to the proposed selection scheme as well as of the full FMC data are given in Fig. 8. For all defect locations, transmit element counts as well as both algorithms the defects are clearly visible. The TFM reconstruction shows more background noise, predominantly for the reconstructions of the defect at $z = 13$ mm. The difference of perceived noise level of the TFM reconstruction for both defects is due to the colormap being adjusted to the maximum amplitude in the region of the defect of the according image. As the defect at $z = 13$ mm has a smaller amplitude the noise is more predominant here.

The FISTA reconstructions show a better separation of defect and frontwall / backwall reflection as well as less noise than the TFM reconstructions, which is due to the algorithm favoring sparser images. Consequently, the algorithm shows a better behavior with regards to the noise in the measurement data. Still, this requires a suitably chosen β as well as number of iterations.

Despite the strong subsampling, imaging the according defect is still possible for all settings. Using fewer transmit cycles increases the noise level, as there is less data to be averaged over. For (a) TFM using 4 transmit cycles the noise floor becomes more pronounced, for FISTA the defect echo is a bit more faint than in the other images. Consequently, when using 4 elements imaging the defects is still possible for the given setup. Using 8 or 16 transmit cycles improves the result so far that no apparent difference to the reconstruction of the FMC data is apparent in the region of interest.
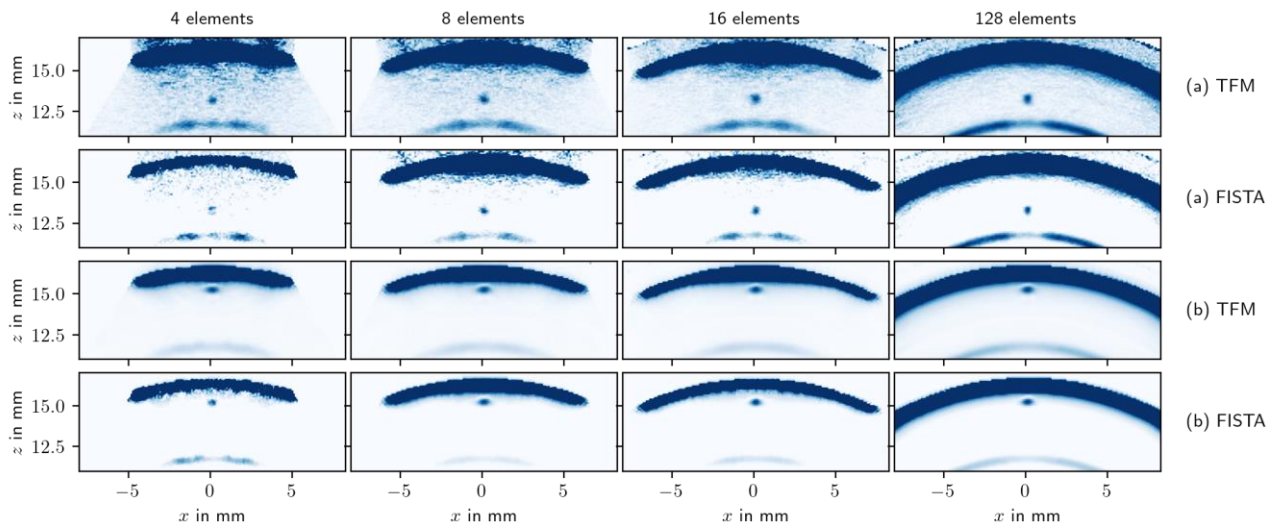
Fig. 8 B-scan views of the reconstructions normalized such that the maximum of the colormap of each image is the maximum value of the defect, where each column shows a different number of transmit elements. The rows indexed by (a) and (b) have been calculated for a defect located at $z = 13$ mm and $z = 15$ mm, respectively..

5. CONCLUSION

We show that a significant reduction of transmit cycles is possible for the simulation scenario at hand. Using only 8 instead of 128 elements in transmit, the TFM and FISTA reconstructions still yield a clear image of the defects. Consequently, the measurement time for the acquisition of one dataset can be reduced by factor 16 with virtually no impairment of the imaging quality for the given region of interest. Furthermore, the computation time of the reconstruction algorithms is scaled down by approximately the same factor.

The transmit elements are chosen according to a deterministic scheme which, for a given region of interest, selects an as wide as suitable aperture while emphasizing those transmit elements that contribute more energy. The scheme is verified by evaluating the performance of the reconstruction algorithms for wider and narrower choices of the aperture. From these observations it becomes apparent that using a slightly narrower aperture would benefit the imaging of the side drilled holes used in the simulations. Still, as less well-behaving and more directional reflections are expected when imaging actual cracks or inclusions, the given aperture choice seems reasonable and in a good performance range over the full region of interest.

Inspired by SART we introduce a normalization of the model matrix, which improves the performance of FISTA in the given scenario. The algorithm does not perform optimally for problems that give varying weight to contributions in the imaging region. Though, this is natural for ultrasound imaging scenarios, as different areas in the imaging region are in most cases being observed by a varying number of transducers. We show empirically that the proposed normalization improves the results in the given scenario.

The reconstructions, normalization for FISTA as well as transmit element selection are based on a linear forward model which is derived using a ray casting scheme. It includes effects like the directivity of the transducer elements as well as the refraction at the pipe boundary. The algorithms are expressed in terms of linear algebra, allowing easy and fast parallel computation and precomputation.

As next step, the findings will be applied and verified on real measurement data. Furthermore, including other propagation modes than only longitudinal propagation seems beneficial, further influencing the aperture choice as well as the possibilities for imaging from a larger aperture. Including multiple propagation modes is inherently possible given the way the algorithms are expressed here, yet the fusion of the multi mode images will require further investigation [11]. Also, in order to reduce the processing time further, including subsampling on the receive side might be beneficial.

ACKNOWLEDGMENT

REFERENCES

[1] C. Holmes, B. W. Drinkwater, and P. D. Wilcox, "Post-processing of the full matrix of ultrasonic transmitreceive array data for non-destructive evaluation," NDT & E International, vol. 38, no. 8, pp. 701–711, Dec. 2005.

[2] L. Moreau, B. W. Drinkwater, and P. D. Wilcox, "Ultrasonic imaging algorithms with limited transmission cycles for rapid nondestructive evaluation," IEEE Transactions on Ultrasonics, Ferroelectrics, and Frequency Control, vol. 56, no. 9, pp. 1932–1944, 2009.

[3] M. Weston, "Advanced ultrasonic digital imaging and signal processing for applications in the field of non-destructive testing," 2012.

[4] L. Moreau, A. J. Hunter, B. W. Drinkwater, P. D. Wilcox, D. O. Thompson, and D. E. Chimenti, "EFFICIENT DATA CAPTURE AND POST-PROCESSING FOR REAL-TIME IMAGING USING AN ULTRASONIC ARRAY," 2010.

[5] H. Hu, J. Du, C. Ye, and X. Li, "Ultrasonic phased array sparse-TFM imaging based on sparse array optimization and new edge-directed interpolation," Sensors, vol. 18, no. 6, p. 1830, Jun. 2018.

[6] H. Zhang, Y. Liu, G. Fan, H. Zhang, W. Zhu, and Q. Zhu, "Sparse-TFM imaging of lamb waves for the near-distance defects in plate-like structures," Metals, vol. 9, no. 5, p. 503, Apr. 2019.

[7] H. Zhang, B. Bai, J. Zheng, and Y. Zhou, "Optimal design of sparse array for ultrasonic total focusing method by binary particle swarm optimization," IEEE Access, vol. 8, pp. 111945–111953, 2020.

[8] E. Pérez, J. Kirchhof, S. Semper, F. Krieg, and F. Römer, "Total focusing method with subsampling in space and frequency domain for ultrasound ndt," in 2019 IEEE International Ultrasonics Symposium (IUS), pp. 2103–2106.

[9] Y. Gershon, Y. Buchris, and I. Cohen, "Greedy sparse array design for optimal localization under spatially prioritized source distribution," in ICASSP 2020 - 2020 IEEE international conference on acoustics, speech and signal processing (ICASSP), 2020.

[10] D. Kim and J. A. Fessler, "Another look at the fast iterative shrinkage/thresholding algorithm (FISTA)," SIAM Journal on Optimization, vol. 28, no. 1, pp. 223–250, Jan. 2018.

[11] N. Budyn, R. L. T. Bevan, J. Zhang, A. J. Croxford, and P. D. Wilcox, "A model for multiview ultrasonic array inspection of small two-dimensional defects," IEEE Transactions on Ultrasonics, Ferroelectrics, and Frequency Control, vol. 66, no. 6, pp. 1129–1139, Jun. 2019.

[12] J. Zhang, B. W. Drinkwater, P. D. Wilcox, and A. J. Hunter, "Defect detection using ultrasonic arrays: The multi-mode total focusing method," NDT & E International, vol. 43, no. 2, pp. 123–133, Mar. 2010.

[13] F. Lingvall, T. Olofsson, and T. Stepinski, "Synthetic aperture imaging using sources with finite aperture: Deconvolution of the spatial impulse response," The Journal of the Acoustical Society of America, vol. 114, no. 1, pp. 225–234, 2003.

[14] F. Krieg, J. Kirchhof, F. Romer, R. Pandey, A. Ihlow, G. del Galdo, and A. Osman, "Progressive online 3-d SAFT processing by matrix structure exploitation," in 2018 IEEE international ultrasonics symposium (IUS), 2018.

[15] P. Wilcox, C. Holmes, and B. Drinkwater, "Advanced reflector characterization with ultrasonic phased arrays in NDE applications," IEEE Transactions on Ultrasonics, Ferroelectrics and Frequency Control, vol. 54, no. 8, pp. 1541–1550, Aug. 2007.

[16] A. H. Andersen and A. C. Kak, "Simultaneous algebraic reconstruction technique (sart): A superior implementation of the art algorithm," Ultrasonic imaging, vol. 6, no. 1, pp. 81–94, 1984.

[17] C. Wagner and S. Semper, "Fast Linear Transformations in Python," arXiv:1710.09578 [cs], Oct. 2017.

[18] E. Carcreff, N. Laroche, D. Braconnier, A. Duclos, and S. Bourguignon, "Improvement of the total focusing method using an inverse problem approach," in 2017 IEEE international ultrasonics symposium (IUS), 2017.

[19] L. Le Jeune, S. Robert, E. L. Villaverde, and C. Prada, "Plane wave imaging for ultrasonic non-destructive testing: Generalization to multimodal imaging," Ultrasonics, vol. 64, pp. 128–138, 2016.

[20] J. A. Ogilvy, "An iterative ray tracing model for ultrasonic nondestructive testing," NDT & E International, vol. 25, no. 1, pp. 3–10, Jan. 1992.

[21] A. J. Brath and F. Simonetti, "Phased array imaging of complex-geometry composite components," IEEE Transactions on Ultrasonics, Ferroelectrics, and Frequency Control, vol. 64, no. 10, pp. 1573–1582, Oct. 2017.

[22] J. E. Bresenham, "Algorithm for computer control of a digital plotter," IBM Systems Journal, vol. 4, no. 1, pp. 25–30, 1965.

[23] EXTENDE, "CIVA." http://www.extende.com.

UAV NDT of aircraft structures

Mr Shakeb Deane

N.P. Avdelidis, A. Tsourdos, X. Maldague, C. Ibarra Castanedo, A.Williamson.

Introduction

This work discusses the importance of composites within the aerospace sector and aims to address the effectiveness and challenges of non-destructive testing (NDT) using an unmanned aerial vehicle (UAV). The study shows how a UAV can be implemented into the aerospace industry for the maintenance of Aircraft. The research focuses on locating damages on a Boeing 737 and some aerospace grade composite samples, the results will be optimised using different signal processing techniques. Operating the UAV autonomously indoors with a localisation system will be explored. A UAV can capture data of hard to reach areas of an aircraft such as the vertical stabiliser, which eliminates the need for scaffolding's, hoping to reduce inspection time and cost.

Objectives

- Develop a UAV to perform active thermography on aircraft composite structures.
- A suitable excitation source, thermal camera and RGB camera are the sensors needing to be equipped onto the UAV.
- An embedded system is used on-board to operate an uncooled thermal camera, an excitation source and real-time abnormality detection.
- Active thermographic data is subject to post-processing using several signal processing techniques and signal-to-noise ratio.
- The UAVs needs adequate localisation which provides good stability. Indoor autonomous flight is being explored.

Methodology

System Architecture

DJI M210 - UAV with a mounted excitation source for active thermography
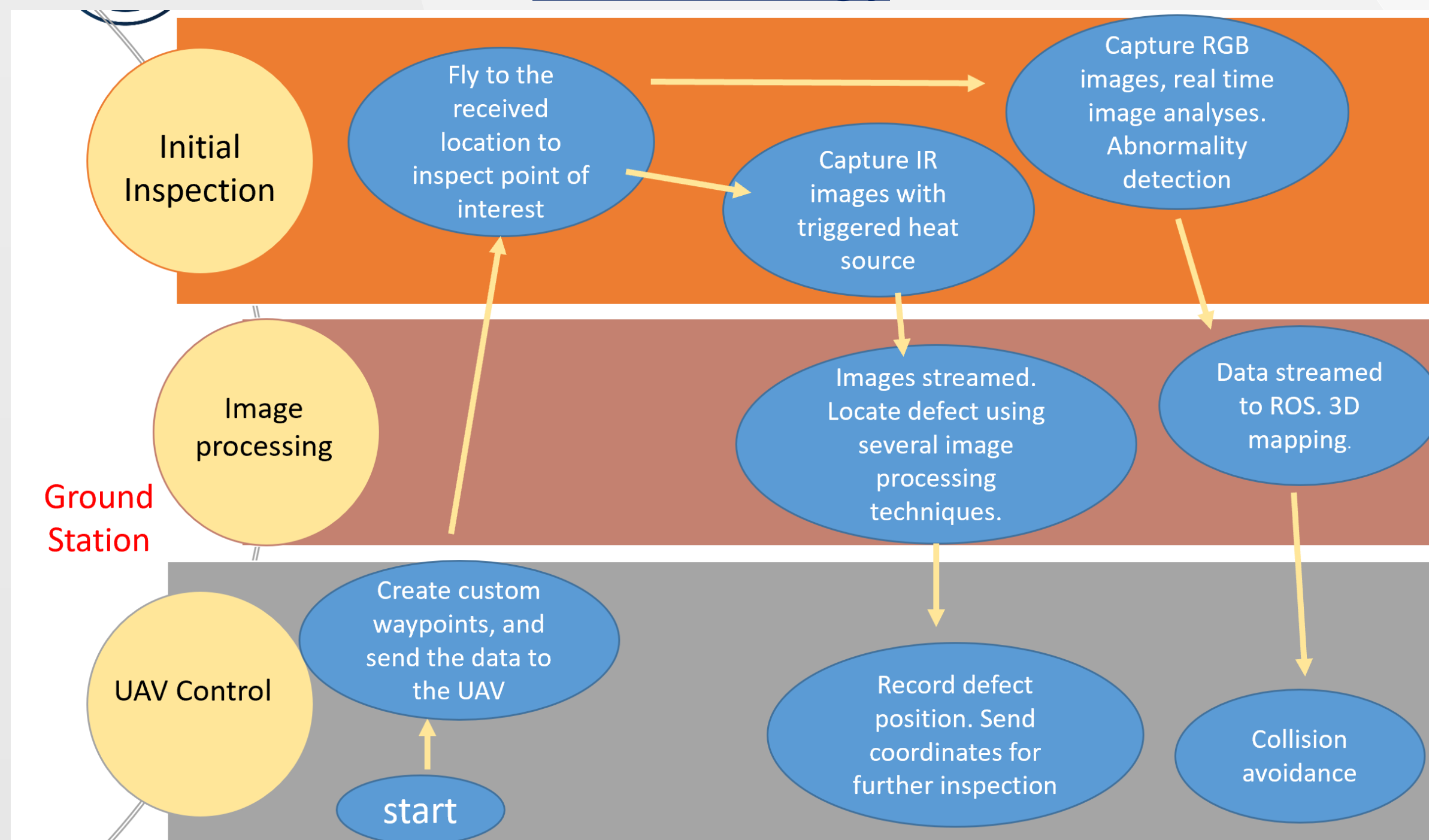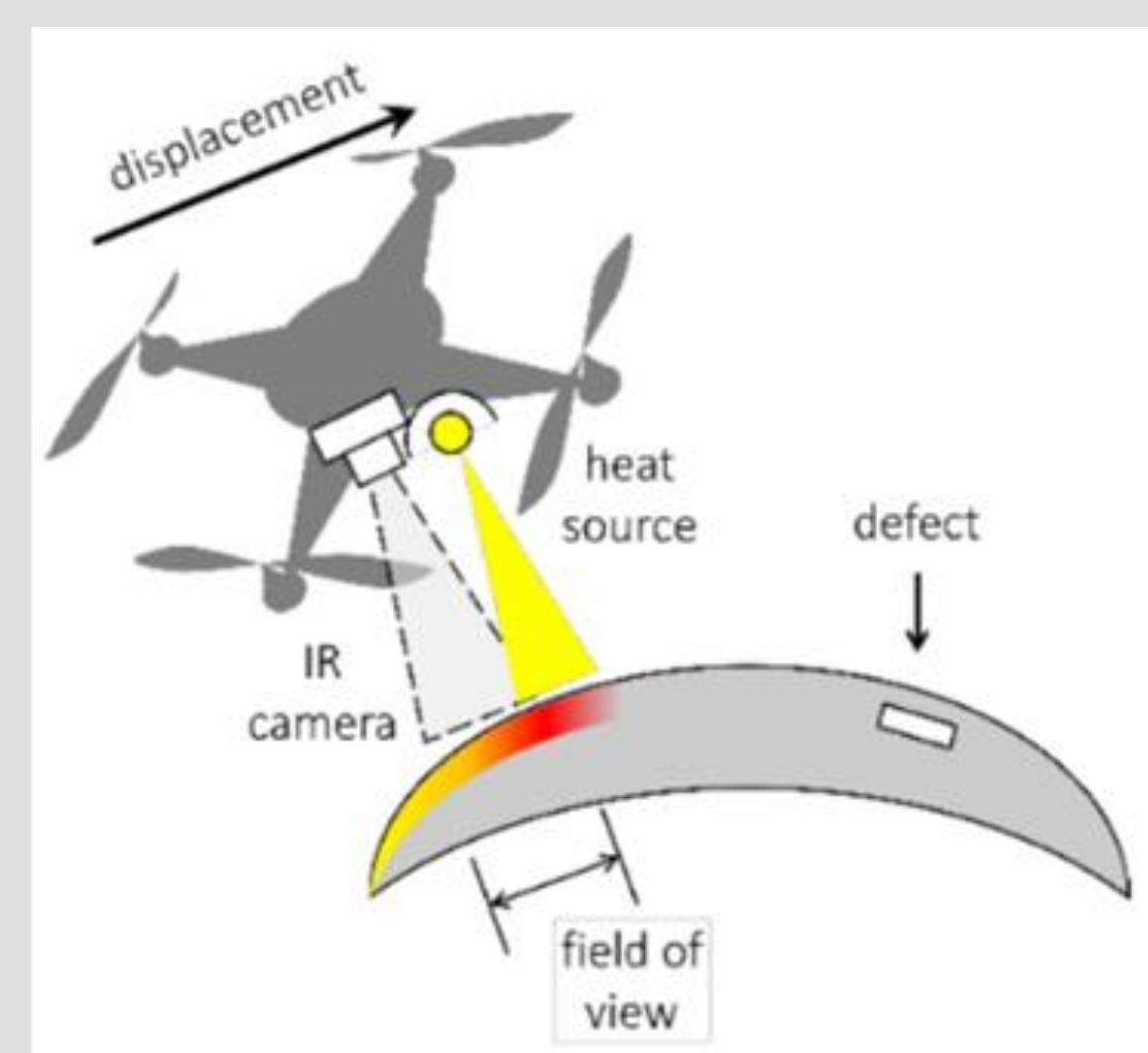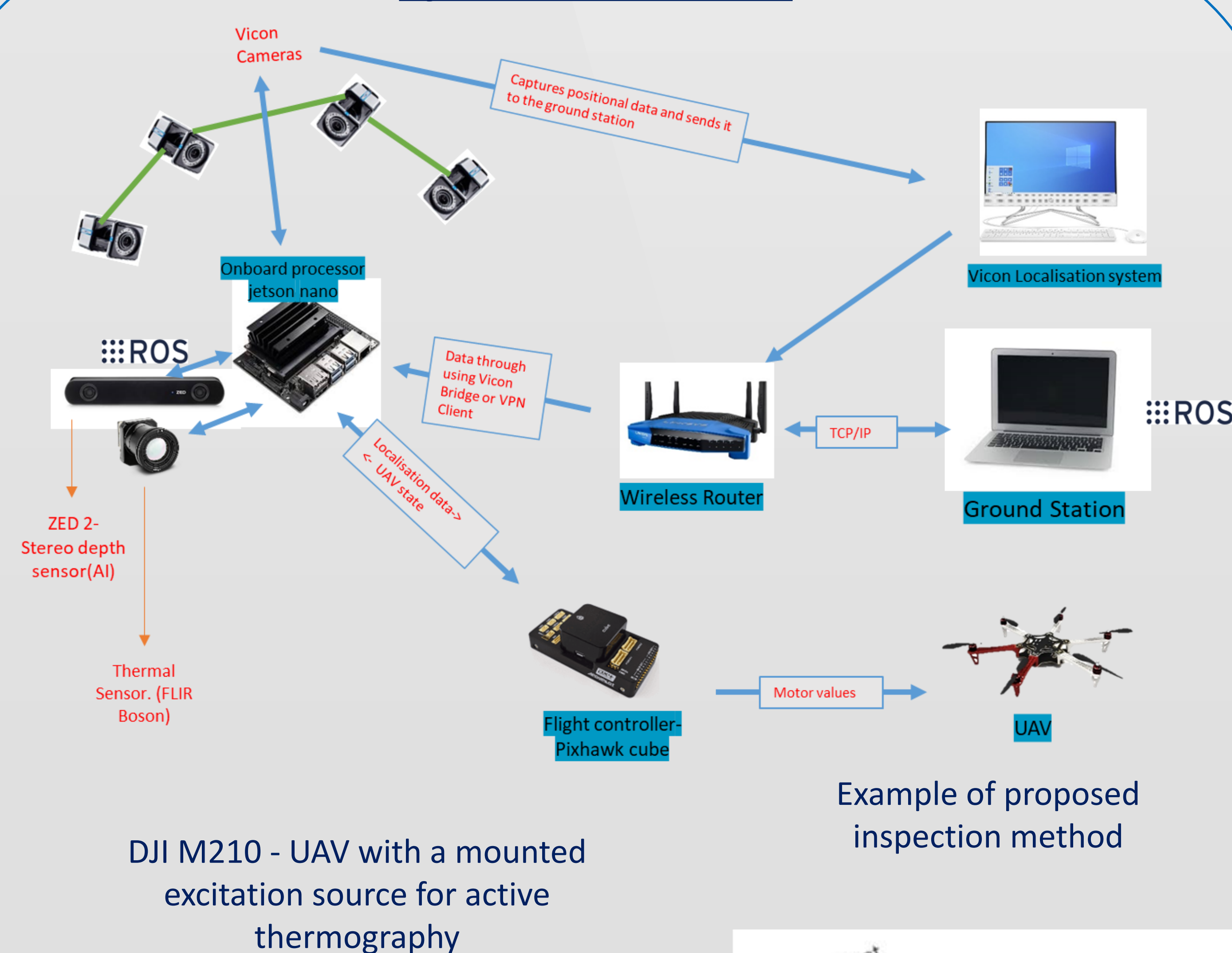

Results

To locate surface defects an image will be taken on-board the UAV and post-processed in real-time using WIFI to transfer the image back to a ground station. The processing of the image looks to find any abnormalities, however this has proven difficult due to the fact some damages are just a few mm big. Inspections of an A320, A319, B737, B787-8 have all been carried out using autonomous UAV inspection and the data is being used to develop an AI model capable of categorising damages after them being located.
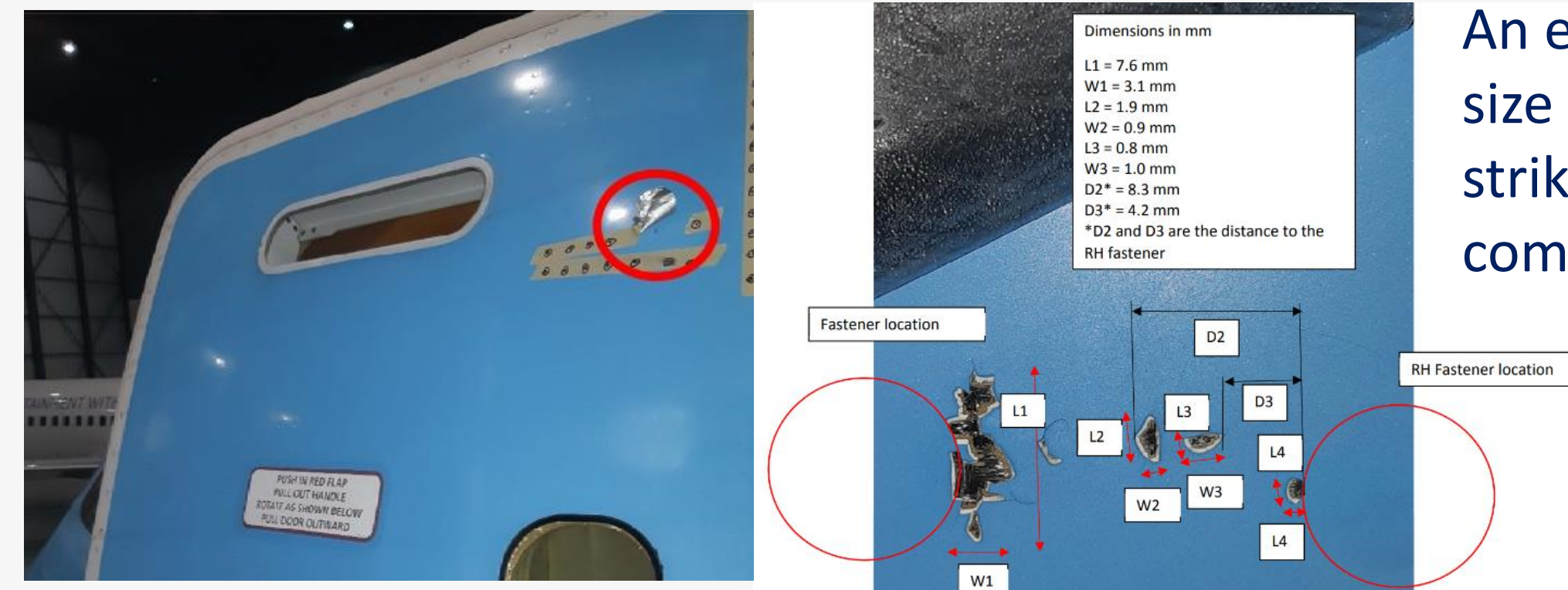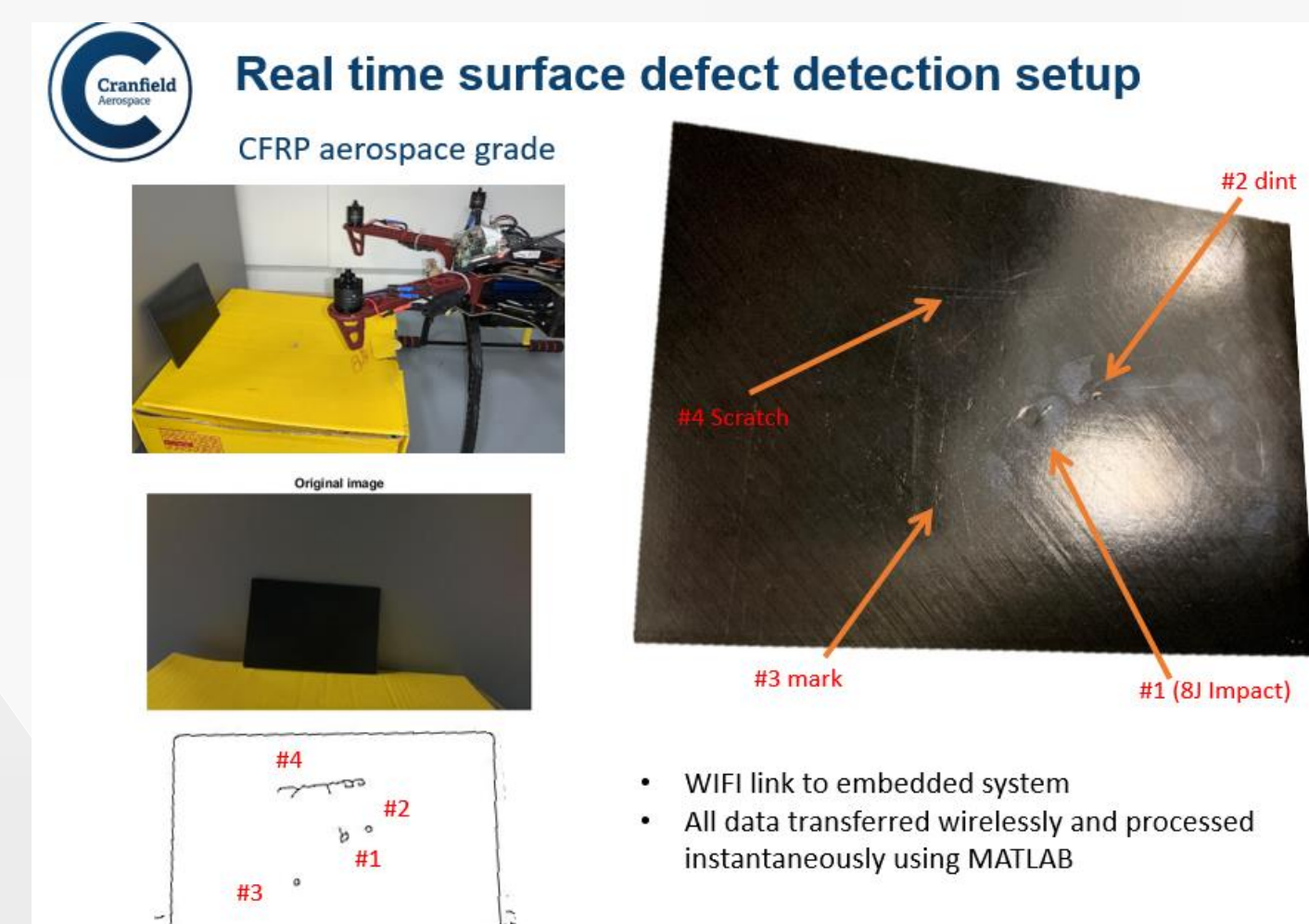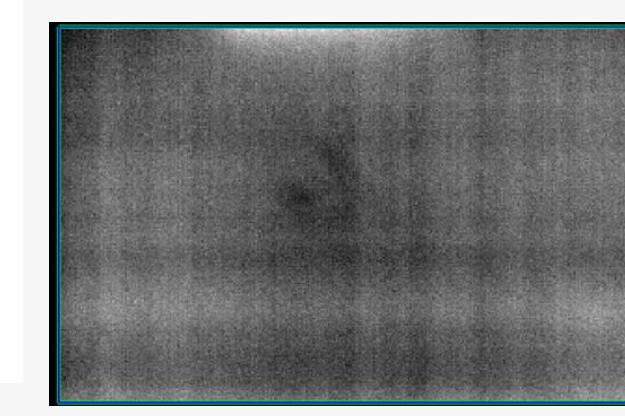

An example of the size of a lightning strike on a composite aircraft.

CFRP does not dint or bend when damaged, which makes it difficult to locate structural damage, especially subsurface i.e barely visible impact damage (BVID). UAV use for active thermography is non-existent, a UAV would allow versatility and would reduce the time and cost of NDT composite inspections.

Static UnCooled camera system with 6KJ of pulse energy per flash.
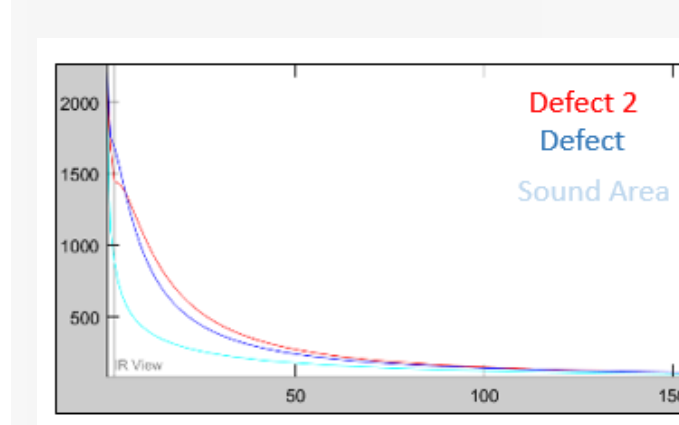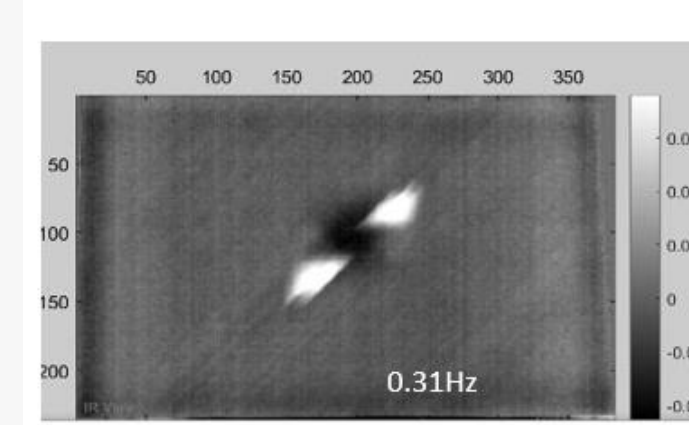
Dynamic UnCooled camera system on a UAV with 1KJ of energy (periodic heating) for 30 seconds.

Real time surface defect detection setup

Real life aircraft inspection of a Boeing 737-400.

Left image: (IR image).   Right image: (corresponding RGB image)

- An abnormality detection algorithm to locate surface damages on a specimen.
- How accurately can AI locate the damage?
- Different lighting and external parameters cause errors. E.g distances, weather, angles ect.
- Find the correct filter by trialling the datasets

- Difficult to reach area (Tail Fin- 36Ft 6In)
- Passive thermography (material excited by the sun)
- Possible water ingress
- **More flights are necessary to reproduce repeatable results**

REF:Composite samples provided by
Hamed Yazdani Nezhad.
Department of Mechanical Engineering and Aeronautics, City University of London, London EC1V 0HB, UK

Conclusions

- The UAV inspection of aerospace structures is a complex process from start to finish. Initially the permissions to fly a UAV around an aircraft at a live airfield can be difficult to obtain. Over the past few years there have been multiple incidents at airports containing UAV's. The UAV disruption forced airports to halt normal operation and restrict take-off and landing, consequently causing a significant loss financial.
- The following documents are required for permissions from airport owners, ATC and the local aviation authority; method statement, risk Assessment, pre-site survey, further Data and insurance.
- Previous research has shown that Active Thermography is an effective NDT inspection method which can be used to evaluate the health of materials and components, without interfering with the serviceability.
- There is a gap in the UAV industry for aircraft NDT especially using active thermography. The research and development seeks to fill this gap by further exploring the active thermographic NDT method and seeking to optimise it by integrating it onto a UAV. This will contain other scientific methods such as autonomous flight, crack detection algorithms, AI and more. The end result aims to provide an all in one time and cost-efficient inspection method.
- UAV inspection could reduce aircraft inspection time from 8hrs to below 1hr, subsequently this is extremely cost efficient.

Acknowledgements

Example of proposed inspection method

Matrix Category Enriched over Semirings for Mathematical Morphology

Hossein Memarzadeh Sharifipour[a,d], Bardia Yousefi[b,c], Xavier P.V Maldague[b]

[a]*Department of Computer Science, Laval University, Quebec city, Canada*
[b]*Department of Electrical and Computer Engineering, Laval University, Quebec city, Canada*
[c]*Address: University of Pennsylvania, Philadelphia PA 19104*
[d]*Corresponding authors: H.M. Sharifipour, Email: Hossein.MemarzadehSharifipour.1@ulaval.ca.*

Abstract

Mathematical morphology contributes many profitable tools to image processing area. Some of these methods considered to be basic but the most important fundamental of data processing in many various applications. In this paper, we modify the fundamental of morphological operations such as dilation and erosion making use of limit and co-limit preserving functors within (*Category Theory*). Adopting the well-known matrix representation of images, the category of matrices, called Mat, can represent an image. With enriching Mat over various semirings such as *Boolean* and $(max, +)$ semirings, one can arrive at classical definition of binary and gray-scale image dilation using the categorical tensor product in Mat. With dilation operation in hand, the erosion can be deduced using the famous *tensor-hom* adjunction. This approach enables us to define new types of dilation and erosion between two images represented by matrices using different semirings other than *Boolean* and $(max, +)$ semirings.

The viewpoint of morphological operations from *category theory* can also shed light to the claimed concept that mathematical morphology is a model for linear logic.

Keywords: Mathematical morphology, Closed monoidal categories, Day convolution, Enriched categories, category of semirings

November 10, 2020

1. Introduction

Mathematical morphology. is a structure-based analysis of images constructed on set theory concepts. Two main induced transformations in mathematical morphology are dilation and erosion established initially by translations, unions and intersections on subsets of euclidean spaces. These transformations were extended to complete lattices later. In a more general form, dilation and erosion are Galois connections over mappings between complete lattices.

According to [1], every operator on a complete lattice which preserves finite supremum($\vee$) is regarded as a dilation and each infimum preserving operator can be nominated as an erosion. This is the most universal definition of dilation and erosion appeared in literature up to our knowledge. Looking toward category theory viewpoint, definition of the dilation and erosion can be generalized to left and right adjoint functors that preserve co-limits and limits respectively.

The first section stares at mathematical morphology and category theory briefly. Most of the consisting material for category theory can be found in [2],[3],[4], [5].

1.1. Matrix representation of images

An image on a computer springs up from quantization of both image space and intensities into discrete values. It is merely a 2D rectangular array of integer values. It is widely accepted to record intensity as an integer number over the interval $[0, 255]$. Conversely, each pixel of a colored image contains three values over the interval $[0, 255]$ corresponding to its RGB values. Roughly speaking, the matrix representation of an image deals closely with a function entitled as a picture function. It is a function f defined on spatial variables x, y. Intuitively, $f(x, y)$ defines the intensity value of the pixel at point (x, y). The following definitions correspond to binary, gray-scaled and color images.

Definition 1 *A binary image is a rectangular matrix with all elements values 0 or 1.*

Definition 2 *A gray-scaled image is a rectangular matrix with values ranging within $[0, 255]$.*

Definition 3 *A color image is a 2D image which has vector of 3 values at each spatial point(pixel).*

1.2. Mathematical morphology

Dilation and erosion constitute the basic operations which construct the backbone for clarifying other widely used operations such as opening, closing, hit-miss and a few others. They have their roots in set theory and boil from a set theoretical view point. These transformations are defined on elements of sets of the source image and the structuring element respectively. The structuring element is generally much smaller in size comparing to the image that it acts on. It functions as a pattern probing the source image, targeting at finding its structure. First we define dilation for binary images as follows [1].

Definition 4 *If A, B are two sets determining the source image and the structuring element respectively, dilation of A and B is defined by [6] and [7] as*

$$A \oplus B = \{a + b | a \in A, b \in B\}, \tag{1}$$

This operation is also called the Minkowski sum. The pertinence of dilation in image analysis area varies from image expanding to filling holes. Erosion is the dual of dilation defined by:

Definition 5 *The erosion of a set A with a structuring element B is: [7, 1]*

$$A \ominus B = \{x \in \mathbb{Z}^2 | \text{ for every } b \in B, \text{ there exists an } a \in A \text{ such that } x = a - b\} \tag{2}$$

Erosion of two sets A, B can also be defined as

$$A \ominus B = \{h \in \mathbb{Z}^2 | B_h \subseteq A\} \tag{3}$$

where $B_h = \{b+h|b \in B\}$ is the translating of B along the vector h and reflection of the set B with respect to origin is defined like

$$\check{B} = \{x \in \mathbb{Z}^2 |\ for\ some\ b \in B, x = -b\} \tag{4}$$

duality of dilation and erosion means that erosion can be written in terms of the dilation:

$$(A \ominus B)^c = A^c \oplus \check{B} \tag{5}$$

where $\check{B}$ has been defined before (3.13). In other words, dilating the foreground is the same as eroding the background, but the structuring element reflects between the two. Likewise, eroding the foreground is the same as dilating the background.

Dilation and erosion are defined for gray scale images in a different way. Dilation and erosion of f where $f : F \rightarrow \mathbb{Z}, F \subseteq \mathbb{Z}^2$ is a function that maps $(x,y) \in \mathbb{Z}^2$ to gray scale value of pixel at (x,y) with structuring element B is denoted as

$$(f \oplus B)(x,y) = \max_{(s,t) \in B}\{f(x-s, y-t)\} \tag{6}$$

$$(f \ominus B)(x,y) = \min_{(s,t) \in B}\{f(x+s, y+t)\} \tag{7}$$

The following more general definition of dilation and erosion can be found in [1].

Definition 6 *Let $\mathscr{L}$ be a complete lattice and $\mathscr{E}_1, \mathscr{E}_2$ be arbitrary sets. The operator $\delta : \mathscr{L}^{\mathscr{E}_1} \longrightarrow \mathscr{L}^{\mathscr{E}_2}$ is a dilation if and only if for every $x \in \mathscr{E}_1$ and $y \in \mathscr{E}_2$ there exists a $\delta_{y,x} : \mathscr{L} \longrightarrow \mathscr{L}$ such that for $F_1 \in \mathscr{L}^{\mathscr{E}_1}$ and $y \in \mathscr{E}_2$,*

$$\delta(F_1)(y) = \bigvee_{x \in \mathscr{E}_1} \delta_{y,x}(F_1(x))$$

The erosion $\epsilon : \mathscr{L}^{\mathscr{E}_1} \longrightarrow \mathscr{L}^{\mathscr{E}_2}$ is given by:

$$\epsilon(F_2)(x) = \bigwedge_{y \in \mathscr{E}_2} \epsilon_{y,x}(F_2(y))$$

Definition 7 *Let $(A, \leq), (B, \leq)$ be two partially ordered sets with two mappings, $F : A \longrightarrow B$ and $U : B \longrightarrow A$. A monotone Galois connection between F, U is for all $x \in A$ and $y \in B$:*

$$F(x) \leq y \Leftrightarrow x \leq U(y)$$

F is referred as the left adjoint and U as an right adjoint. Monotone Galois connections are entitled as adjunctions in literature [8] likewise. The other variety of Galois connections called antitone Galois connections emerges in literature as follows.

Definition 8 *Let $(A, \leq), (B, \leq)$ be two partially ordered sets. Let $F : A \longrightarrow B$ and $U : B \longrightarrow A$. F, U are an antitone Galois connection if for all $x \in A$ and $y \in B$:*

$$y \leq F(x) \Leftrightarrow x \leq U(y)$$

Theorem 1
$$\delta(F_1) \leq F_2 \Leftrightarrow \epsilon(F_2) \leq F_1$$

This theorem confirms that dilation and erosion engage in a monotonic Galois connection.

1.3. Category theory

Category theory is an effort for generalizing and simplifying many properties of mathematical systems by denoting them with objects and arrows. Each arrow $f : A \to B$ represents a function from an object A to another object B. A category is small if its set of objects and arrows are small.

A contravariant functor $F : \mathcal{A}^{OP} \to \mathcal{B}$ maps every object $A \in \mathcal{A}$ to $F(A) \in \mathcal{B}$ and there exist a mapping $\mathcal{A}(A, A') \to \mathcal{B}(FA, FA')$ for each mapping $f : A \to$

$A' \in \mathcal{A}$. Reminding that $\mathcal{A}(A, A')$ is an arrow between the objects, these data are subject to following two conditions:

- any two morphism $f \in \mathcal{A}(A, A')$ and $g \in \mathcal{A}(A', A'')$ can be decomposed by $F(g \circ f) = F(f) \circ F(g)$.

- For any object $A \in \mathscr{A}$, $F(1_A) = 1_{FA}$.

A contravariant functor reverses the direction of arrows. For example $f : A \to B$ gets $F(f) : f(B) \to f(A)$.

Conversely, a covariant functor $F : \mathcal{C} \to \mathcal{D}$ preserves the direction of arrows. Everything is the same as the contravariant functor except : $F(f \circ g) = F(f) \circ F(g)$ for arrows f, g in $\mathcal{C}$.

1.3.1. Natural transformations

Definition 9 *Let $\mathcal{A}$ and $\mathcal{B}$ be categories and F, G two functors $F, G : \mathcal{A} \to \mathcal{B}$. A natural transformation between F, G is an arrow $\alpha_x : F(x) \to G(x)$ for any object $X \in \mathcal{A}$ such that for any arrow $f : X \to Y \in \mathcal{A}$, the diagram depicted in figure 1 commutes,*

$$
\begin{array}{ccc}
F(X) & \xrightarrow{F(f)} & F(Y) \\
\downarrow{\alpha_X} & & \downarrow{\alpha_Y} \\
G(X) & \xrightarrow{G(f)} & G(Y)
\end{array}
$$

Figure 1: Natural transformations

Natural transformations resemble functor isomorphisms.

1.3.2. (Co)-limits

Definition 10 *Given a functor $F : \mathcal{A} \to \mathcal{B}$, a cone of F is an object $O \in \mathcal{B}$ together with a family of arrows $\phi_x : O \to F(x)$ for each $x \in \mathcal{A}$ such that for each arrow $f : x \to y$ in $\mathcal{A}$ we have $Ff \circ \phi_x = \phi_y$ according to figure 2.*
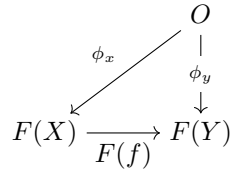
$$O$$

$$\phi_x \qquad \phi_y$$

$$F(X) \xrightarrow[F(f)]{} F(Y)$$

Figure 2: Diagram of a cone

Definition 11 *A limit of a functor $F : \mathcal{A} \to \mathcal{B}$, is a universal cone (L, ϕ_x) such*

that for every other cone (N, ψ_x) of F there is a unique arrow $u : N \to L$ such

that $\psi_x = \phi_x \circ u$ for every X in $\mathcal{B}$.

$$N \qquad\qquad N$$

$$u \qquad\qquad u$$

$$\psi_x \quad L \quad \psi_y \qquad\qquad \psi_x \quad L \quad \psi_y$$

$$\phi_x \qquad \phi_y \qquad\qquad \phi_x \qquad \phi_y$$

$$F(X) \xrightarrow[F(f)]{} F(Y) \qquad F(X) \xrightarrow[F(f)]{} F(Y)$$

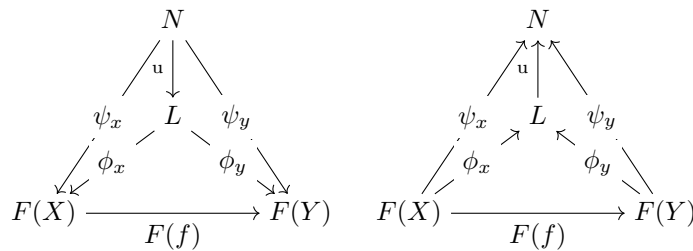Figure 3: a) Diagram of a limit b) Diagram of a co-limit

Definition 12 *Dual to limit, a co-limit of a functor $F : \mathcal{A} \to \mathcal{B}$, is a universal*

co-cone (L, ϕ_x) such that for any other co-cone (N, ψ_x) of F, there exists a

unique arrow $u : L \to N$ such that $\psi_x = u \circ \phi_x$ for every X in $\mathscr{B}$. Figure 3 (b)

illustrates the diagram of a co-limit. A functor $F : \mathcal{A} \to \mathcal{B}$ is called small if $\mathcal{B}$

is a small category. (co)-limits over small functors are called small.

Symbols $\lim_{\longrightarrow}$ and $\lim_{\longleftarrow}$ are used to denote lim and co-limit often in literature.
A category is called (co)-complete if it contains all small (co)-limits. Symbols
$\lim_{\longrightarrow}$ and $\lim_{\longleftarrow}$ are used to denote lim and co-limit often in literature.

1.3.3. (Co)-ends

(co)-ends are useful notions inspired from calculus. Particularly, an end
resembles an infinite product whereas a co-end imitates the idea of an infinite

sum or integral.

100 (co)-ends are special (co)-limits defined on functors of the form $F : \mathcal{C}^{OP} \times$ $\mathcal{C} \rightarrow \mathcal{D}$. Defining (co)-wedge is essential since a (co)-end is a universal (co)-wedge.

A wedge of a functor $F : \mathcal{C}^{OP} \times \mathcal{C} \rightarrow \mathcal{D}$ is an object $O \in \mathcal{D}$ with an arrow $\omega_c : O \rightarrow F(C, C)$ for any object $C \in \mathcal{C}$. The universal property of a wedge

105 enforces that for any arrow $C' \rightarrow C$ for $C, C' \in \mathcal{C}$, the diagram illustrated in (a) commutes.

Conversely, co-ends are defined by natural co-wedges. A co-wedge for a functor $F : \mathcal{C}^{OP} \times \mathcal{C} \rightarrow \mathcal{D}$ is an object O in $\mathcal{D}$ along with an arrow $\omega_c : F(C, C) \rightarrow O$ such that for any arrow $t : C' \rightarrow C$ in $\mathcal{C}$, the diagram illustrated in (a) commutes.

Figure 4: a)Diagram of a wedge b)Diagram of a co-wedge

110

The abusing integral notation for denoting (co)-ends stems from the work of N.Yoneda while he came up with functors $\mathcal{C}^{OP} \times \mathcal{C} \rightarrow \mathsf{Ab}$. The subscripted integral notation $\int_C F(C, C)$ denotes an end of a functor $F : \mathcal{C}^{OP} \times \mathcal{C} \rightarrow \mathcal{D}$ whereas the superscripted integral notation $\int^C F(C, C)$ demonstrates a Co-end

115 for F.

A helpful property of ends which makes them so useful is their capability of representing natural transformations. This can be expressed by the following theorem,

Theorem 2 *Given two functors $F, G : \mathcal{C} \rightarrow \mathcal{D}$, the set of natural transforma-*

120 *tions between F, G denoted by $[C, D](F, G)$ equals to $[C, D](F, G) = \int\limits_{c \in \mathscr{C}} D(F(c), G(c))$.*

Proof 1 *Suppose $\int_{c \in \mathscr{C}} D(F(c), G(c))$ includes morphisms $h(c) : F(c) \to G(c)$ in $\mathscr{D}$. For any other morphism $f : c \to d$ in $\mathscr{C}$, The following diagram commutes as a consequence of an end properties. This is by definition a natural*

$$
\begin{array}{ccc}
F(c) & \xrightarrow{\ F(f)\ } & F(d) \\
{\scriptstyle h(c)}\big\downarrow & & \big\downarrow{\scriptstyle h(d)} \\
G(c) & \xrightarrow{\ G(f)\ } & G(d)
\end{array}
$$

transformation $F \Rightarrow G$.

Some practical properties of ends that will be used later are:

$$\int_{a \in A} \int_{b \in B} F(a, a, b, b) = \int_{b \in B} \int_{a \in A} F(a, a, b, b) = \int_{(a,b) \in A \times B} F(a, a, b, b) \qquad (8)$$

$$\int_A [C, F(A, A)] \simeq [C, \int_A F(A, A)] \qquad (9)$$

$$\int_A [F(A, A), C] \simeq [\int^A F(A, A), C] \qquad (10)$$

125

Definition 13 *A functor $\mathcal{C}, \mathcal{D}$ along with functors $F : \mathcal{D} \to \mathcal{C}$ and $G : \mathcal{C} \to \mathcal{D}$, F is assumed to preserve co-limits, if $\lim_{\longrightarrow i} X_i$ which exists in $\mathcal{C}$ for a functor $X : \mathcal{I} \to \mathcal{C}$, $F(\lim_{\longrightarrow i} X_i) \simeq \lim_{\longrightarrow i} F(X_i)$. Conversely, G is assumed to preserve all small limits if it forces that the limit $\lim_{\longleftarrow i} X_i$ for a functor $X : \mathscr{I} \to \mathscr{C}$ in $\mathscr{C}$ if exists, $G(\lim_{\longleftarrow i} X_i) \simeq \lim_{\longleftarrow i} G(X_i)$.*

130

1.4. Adjunctions

One of the main intentions of mathematics is to compare two models. One way to express that two models or objects are similar is by equality. However,

equality is too much strong in many cases. Another similarity observation in
135 some cases is isomorphism. Isomorphism is a weaker notion comparing with
equality. Two categories $\mathcal{C}, \mathcal{D}$ are isomorphic if there exist two functors $R : \mathcal{C} \rightarrow$
$\mathcal{D}$ and $L : \mathcal{D} \rightarrow \mathcal{L}$ such that $L \circ R = \mathsf{id}_\mathcal{C}$ and $R \circ L = \mathsf{id}_\mathcal{D}$. However, the notion
of isomorphism is also too ambitious to expect in many cases.

Adjunction weakens even the requirements needed by isomorphism for two
140 categories by just asking a one way natural transformation $\eta : \mathsf{id}_\mathcal{D} \Rightarrow R \circ L$ and
another natural transformation expressing $\epsilon : L \circ R \Rightarrow \mathsf{id}_\mathcal{C}$. In the language of
category theory η is called the unit and ϵ is called the co-unit of the adjunction.
Functor L is noted as the left adjoint to functor R and R is called the right
adjoint to L.

145 One can also express the adjunctions in terms of triangular identities [2]
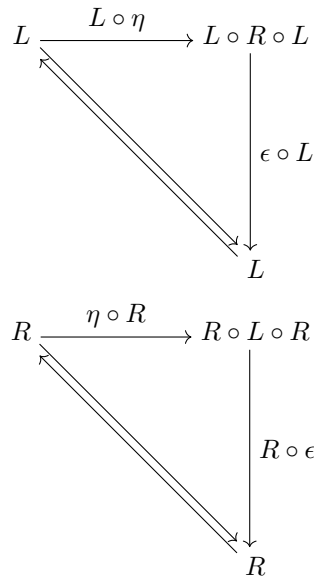depicted by diagrams in figure 5:

Figure 5: Triangle diagrams(Adjunctions)

Example.

Adjunctions in the category of preorders corresponds to functors $F : L_1 \rightarrow L_2^{OP}$,
$G : L_2^{OP} \rightarrow L_1$ between two preorders L_1, L_2. L is the left adjoint of G iff for

any $p \in L_1, q \in L_2$,

$$q \leq F(p) \implies p \leq G(q)$$

The adjunction in category of complete lattices called Galois connections plays a crucial role in mathematical morphology area. To express more, any left adjoint in the category of complete lattices is a dilation and its right adjoint is an erosion consequently.

A major property of adjoints which is widely used in category theory is that they preserve (co)-limits. A left adjoint preserves co-limits whereas a right adjoint preserves limits.

1.5. The Yoneda lemma

The Yoneda lemma is a major and applicative result of category theory. It allows us to embed any category into the category of contravariant functors stemming from that category to the category of sets. The Yoneda lemma makes the life easier by suggesting that one can investigate functors from a small category to the category of sets instead of investigating directly on it. In many cases the former inspection is much more easier.

Definition 14 *Consider a functor $F : \mathcal{A} \to \mathsf{Set}$ from an arbitrary category $\mathcal{A}$ to the category of sets, an object $A \in \mathcal{A}$ and the corresponding functor $\mathcal{A}(A, -) : A \to \mathsf{Set}$. There exists a bijective correlation,*

$$\mathsf{nat}(\mathcal{A}(A, -), F) \simeq FA$$

The main idea inherited in Yoneda lemma is that every information we need about an object $A \in \mathcal{C}$ is encoded in $\mathcal{C}[-, A]$. Yoneda lemma can be expressed by co-ends also. Let $F : \mathcal{C}^{OP} \to \mathsf{Set}$ and $G : \mathcal{C} \to \mathsf{Set}$ be functors. The following formulas express the Yoneda lemma.
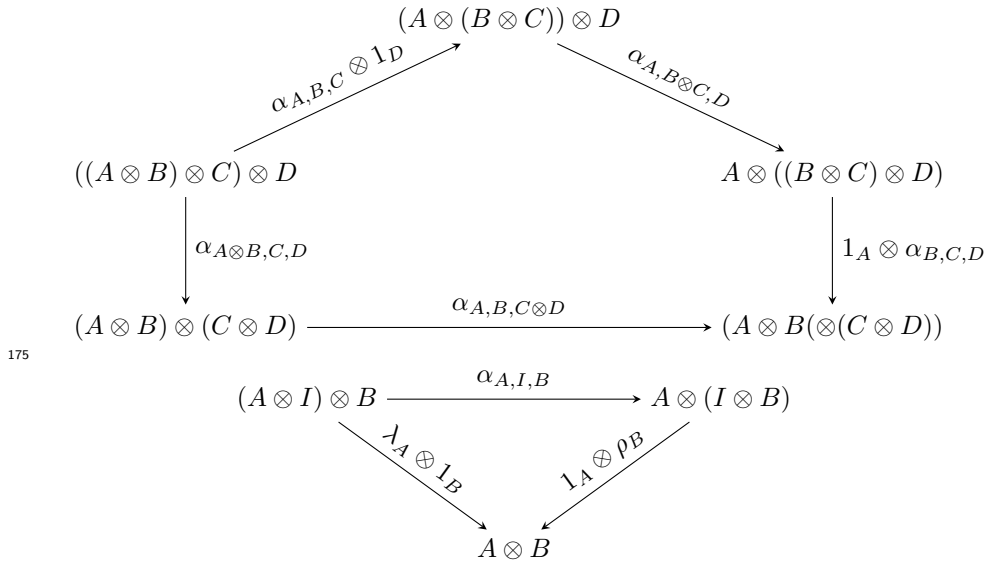
$$F \simeq \int^{A \in \mathcal{C}} FA \times \mathcal{C}[-, A]$$

$$G \simeq \int\limits^{A \in \mathcal{C}} GA \times \mathcal{C}[A, -]$$

1.5.1. Monoidal categories

Definition 15 *A category $\mathcal{C}$ is monoidal if it is equipped with a tensor product $\otimes$ that satisfies some conditions. Roughly speaking $\otimes : \mathcal{C} \times \mathcal{C} \to \mathcal{C}$ is a functor satisfying:*

170

- *$(A \otimes B) \otimes C \to A \otimes (B \otimes C)$ (Associativity isomorphism law)*

- *There exist an identity object I satisfying: $\lambda_A : A \otimes I \to A$ and $\rho_A : I \otimes A \to A$*

- *The following two commutations hold:*

175

A monoidal category is left closed if for each object A the functor $B \longmapsto A \otimes B$ has a right adjoint $B \longmapsto (A \Rightarrow B)$. This means that the bijection $\mathsf{Hom}_{\mathcal{C}}(A \otimes B, C) \cong \mathsf{Hom}_{\mathcal{C}}(A, B \Rightarrow C)$ between the Hom-sets called currying exists.

180   Dually, the monoidal category $\mathcal{C}$ is right closed if the functor $B \longmapsto B \otimes A$ admits a right adjoint. In a symmetric monoidal category the notions of left closed and right closed coincide.

1.6. Enriched categories

Generally, the arrows between two objects A,B in category $\mathcal{C}$ illustrated by $\mathcal{C}[A, B]$ are a set. The notion of enrichment extends that structure from merely a set to more fruitful structures. For instance the set of arrows between two objects may have an abelian structure meaning that it is possible to add the arrows between two objects. A restriction imposed on a category $\mathcal{V}$ on which the arrows are enriched over it is that it should have a monoidal structure. More formally,

Definition 16 *Let $\mathcal{V}$ be a symmetric monoidal category. A category enriched over $\mathcal{V}$ called a $\mathcal{V}$-category consists of:*

- *For all objects $A, B \in \mathcal{C}$, the set of arrows from A to B is an object $O \in \mathcal{V}$.*

- *For all object $A, B, C \in \mathcal{C}$, there exist composition of arrows in $\mathcal{V}$ such that $c_{A,B,C} : \mathcal{C}[A, B] \times \mathcal{C}[A, B] \to \mathcal{C}[A, B]$.*

- *For each object $A \in \mathcal{C}$, an identity arrow exists in $\mathcal{V}$ such that $I \to \mathcal{C}(A, A)$.*

2. Categorical dilation and erosion

Considering the well-known notion of dilation in the category of complete lattices (CompLat), we may generalize it to other categories as follows:

Definition 17 *A dilation is a co-limit preserving functor whereas an erosion is a limit preserving functor.*

We expressed previously that left/right adjoint functors preserve co-limits/limits respectively. Thus, the claim that left/right adjoints are a major source of dilation and erosion functors is pretty precise.

Another concept that we will utilize it for defining morphological operations on matrix representation of images is the Day convolution. Let $\mathcal{V}$ be a complete and co-complete small symmetric monoidal category. Let the enriched Yonedda embedding functor to be $\mathcal{C} \to [\mathcal{C}^{OP}, \mathcal{V}]$. The intuition of Day convolution is that a monoidal structure on $\mathscr{C}$ brings the monoidal structure on $[\mathscr{C}^{OP}, \mathscr{V}]$.

The enriched Yoneda lemma states that any $\mathcal{V}$-enriched functor $[\mathcal{C}^{OP}, \mathcal{V}]$ is canonically isomorphic to a co-end of representables. This means that object can be expressed by $F \simeq \int^{C} F(C) \otimes \mathcal{C}(-, C)$. Taking two functors $F, G : \mathcal{C}^{OP} \to \mathcal{V}$, define their multiplication as:

$$F * G = \int^{C} F(C) \otimes \mathcal{C}(-, C) * \int^{B} G(B) \otimes \mathcal{C}(-, B)$$

Assuming the multiplication operation interchanges properly with the co-end, we get:

$$F * G = \int^{c,b} F(c) \otimes G(b) \otimes (\mathcal{C}(-, c) * \mathcal{C}(-, b))$$

Forcing the Yoneda embedding $\mathcal{C} \to [\mathcal{C}^{OP}, \mathcal{V}]$ be strongly monoidal yields to:

$$F * G \simeq \int^{c,b} F(c) \otimes G(b) \otimes \mathcal{C}(-, c \otimes b). \tag{11}$$

210

Definition 18 *A semiring category $\mathcal{S}$ is a category with two operations of addition and multiplication shown as $(\oplus, \cdot)$ such that $(\mathcal{S}, \oplus, 0)$ is monoidal and symmetric, $(\mathcal{S}, \cdot, 1)$ is monoidal. Left and right distributivity of multiplication over addition is expressed by natural isomorphisms as:*

$$A \cdot (B \oplus C) \to (A \cdot B) \oplus (A \cdot C)$$
$$(B \oplus C) \cdot A \to (B \cdot A) \oplus (C \cdot A)$$

Evidently, a semiring category is a ring in which the elements lack their inverses for addition. The max-plus category may be defined by $a \oplus b = \max\{a, b\}$ and $a \cdot b = a + b$ along with $+\infty$ and 0 acting as unit objects for addition and multiplication.

215 Notions such as group, ring, semirings and many other varieties of algebraic structures are categorized via Lawvere theory [9]. If T is a Lawvere theory and $\mathcal{C}$ is a category with finite products such as set, a functor $F : \mathsf{T}^{OP} \to \mathcal{C}$ creates

a full subcategory called a model of T. The model of Lawvere theories when $\mathcal{C}$ is category of sets is referred as T-algebras. T-algebras built on complete and co-complete category $\mathcal{C}$ which is in most cases category of sets are complete and cocomplete. Literally, the forgetful functors from a T-algebra to set category creates and preserves limits.

Definition 19 *Given two matrices $R_{(m,n)}$ and $S_{(p,q)}$, their tensor product known also as Kronecker product is defined by:*

$$R \otimes S = \begin{bmatrix} r_{1,1}S & \cdots & r_{1,n}S \\ \vdots & & \vdots \\ r_{m,1}S & \cdots & r_{m,n}S \end{bmatrix}$$

Definition 20 *The category of Mat contains the set of integers as objects with arrows between two object m, n as $m \times n$ matrices with the matrix multiplication as composition of arrows. $\mathsf{S} - \mathsf{mat}$ is deducted from enriching Mat on a semiring like S. In other words, $\mathsf{S} - \mathsf{mat}$ has sets as objects and s-valued matrices $m \times n \to \mathsf{S}$ as morphisms. For instance, if $S = (\{0,1\}, \vee, \wedge)$ is the Boolean semiring, then the $\mathsf{S} - \mathsf{mat}$ is exactly the well-known category of Rel.*

The $\mathsf{V} - \mathsf{mat}$ category with the array multiplication, Kronecker product behaving as composition and tensor product respectively with the identity matrix constitute a monoidal category. Let $\mathcal{X}$ be the discrete category containing tuples of integers as objects with arrows $\mathcal{X}((m,n),(m,n)) = \mathbb{Z}$. Let us define F, G as two dimensional matrices over a semiring S. Eventually, $\mathcal{X}$ will act for indexing the two matrices. Day convolution of F, G can be defined by:

$$F * G \simeq \int^{(m,n),(p,q)} F_{(m,n)} \otimes G_{(p,q)} \otimes \mathcal{C}(-, (m,n) \otimes (p,q)). \qquad (12)$$

Defining the tensor product $(m,n) \otimes (p,q)$ on the discrete category $\mathscr{X}$ as $(m,n) \otimes (p,q) = (m+p, n+q)$ brings it a monoidal structure. Thus, 12 can be written

as:

$$(F * G)_{(r,s)} = \bigoplus F_{(m,n)} \cdot G_{(p,q)}. \tag{13}$$

where $m + p = r \wedge n + q = s$.

assuming F, G as the source image and the structuring element, $(F * G)$ can be defined as their dilation. The following example illustrates dilation of two binary images.

Example:

Given $F = \begin{pmatrix} 0 & 1 & 0 \\ 0 & 0 & 1 \\ 1 & 1 & 0 \end{pmatrix}$ and $G = \begin{pmatrix} 0 & 1 & 0 \\ 1 & 0 & 0 \\ 0 & 0 & 0 \end{pmatrix}$, Assuming F, G defined on Boolean semiring, one can derive the formula from 13 using $\vee$ and $\wedge$ as addition and multiplication respectively. So $F * G$ can be calculated like

$$(F * G)[r, s] = \bigvee (F[m, n] \wedge G[p, q]) \tag{14}$$

where $m + p = r \wedge n + q = s$.

Hence, the following matrix will be induced by 14

$$F * G = \begin{pmatrix} 0 & 0 & 1 & 0 & 0 \\ 0 & 1 & 0 & 1 & 0 \\ 0 & 1 & 1 & 0 & 0 \\ 1 & 1 & 0 & 0 & 0 \\ 0 & 0 & 0 & 0 & 0 \end{pmatrix}.$$

It should be noted that this result corresponds exactly to dilating binary image F with the structuring element G using well-known existing formulation. However, by migrating from Boolean to max-plus semiring, formulation of gray-scaled images dilation is calculated by the following Day convolution:

$$(F * G)_{(r,s)} = \max(F_{(m,n)} + G_{(p,q)}). \tag{15}$$

Other known morphological operation than can be derived from 13 is the fuzzy dilation first appeared in [10]. For that intention we need to use the semiring

with $a \oplus b = \max(a, b)$ and $a \cdot b = \min(a, b)$ denoted as the $\mathsf{min} - \mathsf{max}$ to get the formula:

$$(F * G)_{(r,s)} = \max(\min(F_{(m,n)}, G_{(p,q)})). \tag{16}$$

in which $r = m + p \wedge s = n + q$. We can concentrate on celebrated tensor-hom adjunction for extracting the expression of erosion from dilation. Given a closed monoidal category $\mathcal{C}$, tensor-hom adjunction states that for an object $A \in \mathcal{C}$, tensor product $- \otimes A$ is the left adjoint with the internal hom functor $[A, -]$. This can be expressed by:

$$\mathcal{C}[A \otimes B, C] \simeq \mathcal{C}[A, [B, C]] \tag{17}$$

The morphism $\mathcal{C}[A \otimes B, C] \to \mathcal{C}[A, [B, C]]$ is nominated as currying in literature. Intuitively, currying is achieved by $\tau : m \otimes n \to \tau(m)(n)$. The hom-tensor adjunction 17 is used to calculate the right adjoint which is equal to erosion. Suppose $[\mathcal{C}, \mathcal{V}][F * G, E]$ is denoted by M. we have:

M

$\simeq \qquad \langle$ Natural transformations representation by ends $\rangle$

$\int_C [(F * G)C, EC]$

$\simeq \qquad \langle$ Definition of Day convolution $\rangle$

$\int_C [\int^{A,B} (FA \otimes GB \otimes \theta(A \otimes B, C), EC]$

$\simeq \qquad \langle$ Fubini theorem $\rangle$

$\int_C \int_{A,B} [FA \otimes GB \otimes \theta(A \otimes B, C), EC]$

$\simeq \qquad \langle$ Fubini theorem and commutativity of ends $\rangle$

$\int_A [FA, \int_{B,C} [GB \otimes \theta(A \otimes B, C), EC]$

$\simeq \qquad \langle$ Tensor-Hom adjunction $\rangle$

250
$$\int_A [FA, \int_{B,C} [\theta(A \otimes B, C), [GB, EC]]$$

Thus the right adjoint to the tensor product is $[B, C](N) = \int_C [\theta(N \otimes B, C), [GB, EC]]$.

Thus the erosion of two binary matrices F, G depicted by $F *' G$ can be written as:

$$(F *' G)[r, s] = \bigwedge (F[m, n] \wedge G[p, q]) \qquad (18)$$

where $r = m - p$ and $s = n - q$. The erosion of two gray-scaled images can be extracted by using max-plus semiring,

$$(F *' G)[r, s] = \min(F[m, n] - G[p, q]) \qquad (19)$$

where $r = m - p$ and $s = n - q$.

3. conclusion

Category theory provides an abstract unified framework for almost all as-
255 pects of mathematics. This is the first research conducted on creating a unified
definition for two fundamental morphological operations of dilation and erosion.
We have unified morphological operations appeared in contrasting situations like
binary, gray-scaled and fuzzy operators into a uniform definition that can be
extended to some new variations with using different semirings.

260 An interesting horizon for the future research on category theory and math-
ematical morphology can be imagined by *-autonomous categories and mathe-
matical morphology. *-autonomous categories are categorical representation of
linear logic which has been a major research area. Many models for linear logic
such as Petri nets and game semantics has been suggested but none of them is
265 satisfying. Mathematical morphology is claimed to be a model of linear logic
[11]. The authors have shown that every derivable formula in linear logic should
be a model of mathematical morphology but the reverse is an open problem.
Conducting research on *-autonomous which are just symmetric monoidal cate-
gories with an involution object and morphological operations will help to shed

270 the light over relation of linear logic and mathematical morphology.

References

[1] H. J. Heijmans, C. Ronse, The algebraic basis of mathematical morphology i. dilations and erosions, Computer Vision, Graphics, and Image Processing 50 (3) (1990) 245–295.

275 [2] F. Borceux, Handbook of Categorical Algebra: Volume 1, Basic Category Theory, Cambridge Textbooks in Linguistics, Cambridge University Press, 1994.
URL https://books.google.ca/books?id=YfzImoopB-IC

[3] S. Mac Lane, Categories for the working mathematician, Graduate texts in mathematics, Springer-Verlag, New York, 1978.
280

[4] F. Borceux, Handbook of Categorical Algebra: Volume 2, Basic Category Theory, Cambridge Textbooks in Linguis, Cambridge University Press, 1994.
URL https://books.google.ca/books?id=YfzImoopB-IC

285 [5] T. Leinster, Basic category theory, Vol. 143, Cambridge University Press, 2014.

[6] R. M. Haralick, S. R. Sternberg, X. Zhuang, Image analysis using mathematical morphology, IEEE transactions on pattern analysis and machine intelligence (4) (1987) 532–550.

290 [7] J. Serra, Image analysis and mathematical morphology, Academic Press, Inc., 1983.

[8] M. Erné, Adjunctions and galois connections: Origins, history and development, in: Galois connections and Applications, Springer, 2004, pp. 1–138.

[9] F. W. Lawvere, Functorial semantics of algebraic theories, Proceedings of
295 the National Academy of Sciences of the United States of America 50 (5) (1963) 869.

- 125 -

[10] B. De Baets, A fuzzy morphology: a logical approach, in: Uncertainty analysis in engineering and sciences: fuzzy logic, statistics, and neural network approach, Springer, 1998, pp. 53–67.

[11] J. van Benthem, G. Bezhanishvili, Modal logics of space, in: Handbook of spatial logics, Springer, 2007, pp. 217–298.

NON-DESTRUCTIVE INSPECTION OF A DECORATIVE MARQUETRY SAMPLE

Henrique Fernandes[1,2*], Jannik Summa[1,3], Julie Daudre[1,3], Ute Rabe[1,3], Stefano Sfarra[4], Gianfranco Gargiulo[5], Hans-Georg Herrmann[1,3]

[1]Fraunhofer IZFP Institute for Nondestructive Testing, Campus E3 1, 66123 Saarbrucken, Germany
[2]School of Computer Science, Federal University of Uberlandia, Joao Naves de Avila 2121, 38408-100, Uberlandia, Brazil
[3]Chair for Lightweight Systems, Saarland University, Campus E3 1, 66123 Saarbrucken, Germany
[4]Department of Industrial and Information Engineering and Economics, University of L'Aquila, Monteluco di Roio, I-67100, L'Aquila, Italy
[5]Individual Company of Restoration (Gianfranco Gargiulo), Via Tiberio 7b, I-80073, Capri, Italy

[*]Corresponding Author: henrique.fernandes@ufu.br

ABSTRACT

Non-destructive testing of objects and structures is a valuable tool. Specially in cultural heritage where the preservation of the inspected sample is of vital importance. In this paper, a decorative marquetry sample is inspected with three NDT techniques: air-couple ultrasound, computed-tomography scan and infrared thermography. Results from the three techniques were compared.

KEYWORDS: decorative sample, cultural heritage, air-couple ultrasound, computed-tomography scan, infrared thermography

1. INTRODUCTION

The main advantage of a non-destructive technique (NDT) is that the inspected target is not impaired after the inspection. This feature is very important when cultural heritage must be inspected. In this paper, a marquetry decorative sample is inspected with three different NDT techniques. The first technique is air-couple ultrasound (air-UT), the second is x-ray computer-tomography (CT-Scan), and the last one, is the infrared thermography (IRT). In the last one, two different spectral ranges were explored: mid-wave infrared (MWIR) and long-wave infrared (LWIR).

The inspected sample is very ancient, and its origin is unknown. Nevertheless, it is very precious from an historical point of view because the tessellatum layer is unusual. Aesthetically, it seems to be Middle Eastern or North African. The restorer believe that it was a part of a parietal covering or a ceiling.

The size of the sample is 208 x 212 mm, with thickness between 15 and 16 mm where the tessellatum part corresponds to something between 1.5 to 2 mm. The support of the sample is made of wood and the decorative layer is believed to be composed of: mother of pearl (white tesserae), alleged bovine horn, probably cow (amber / gray tesserae), alleged horn or tortoise (some brown tesserae), alleged horn of another ungulate (some brown / black tesserae), and alleged boxwood (at the perimeter). The adhesive used is likely a protein glue, presumed strong glue. The pigment used to dye the stucco seems to be lead-free. Figure 1 shows a picture of the sample.

It is possible that beneath the decorative coating there is the presence of a preparatory drawing made in pencil or more probably engraved with a pointed iron directly on the wood support. The support has been realized with axes obtained from a sub radial section (near to the heart of the plant) as shown in the lateral view of Figure 1. The decorative surface was deliberately applied on the convex part of the support in relation to the known phenomenon of warping.

The geometric marquetry is composed by tesserae of different size and shape. The raw material was first sawed by hand into thin sheets (there are, on the verso, small signs of work related to a hand saw) having a suitable thickness and then cut into small pieces geometrically appropriate to be arranged each other. It seems that the tesserae were then glued directly on the support (which could be confirmed by a probable preparatory drawing realized on the support
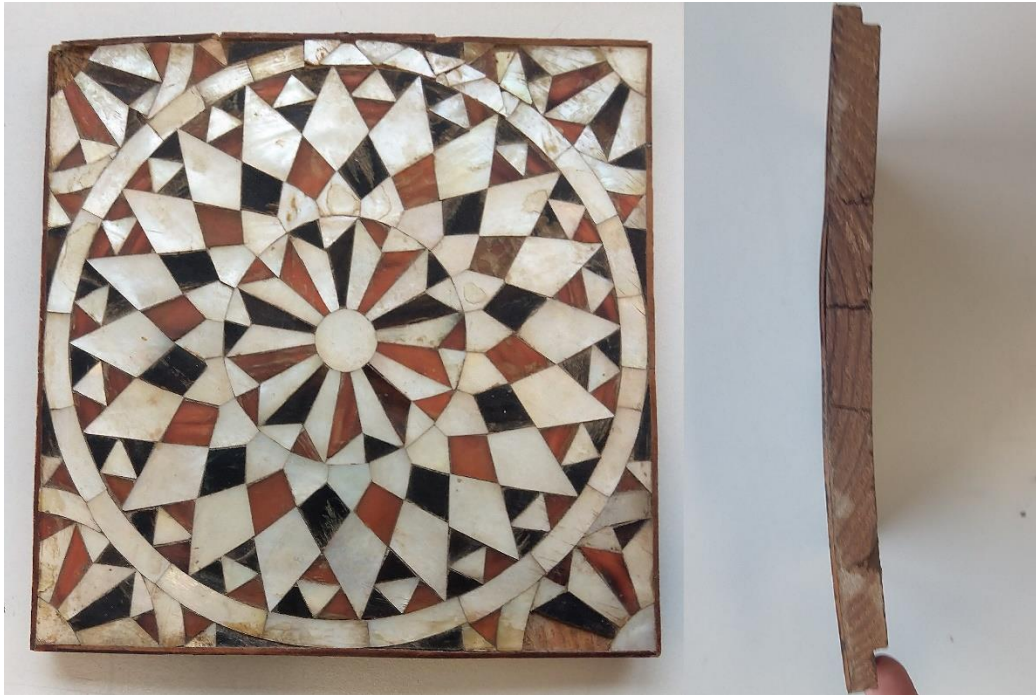
Figure 1 - Decorative marquetry sample - top and lateral views

itself). Once bound to the support, the tesserae were flattened and regularized. This explains why different thicknesses were obtained. Probably, an abrasive was used to fulfill this task, presumably a pumice stone.

The decorative surface appears deformed due to the raise of the support. The deformation is more evident along one of the two sides (adjacent to the tangential section relative to the thickness) due to the resizing of the thickness (concerning the interlocking having a "L" shape). There are some small lacunae in the decorative surface due to the loss of some of the covering's tesserae. It is possible to notice some small lifting mainly caused both by deformation and by simultaneous downsizing of the support. Some tesserae are deformed and tend to lift. Due to the loss of some tesserae, it is possible to see traces of glue on the front support. It seems that a previous restoration work was carried out, limited to an area located near to one of the four corners. On the back of the support, two portions of passing knots are also visible along the cross section.

Five cracks pass through the grain pattern and affect the whole thickness of the support; there are also some traces of old nails, no longer present, and such holes are surrounded by oxide stains. A large chipping work is evident. There are also some very small holes having a quadrangular section. The cracks in the support have been caused, almost certainly, by the loss of moisture (subsequent to the maturing phase) from the support itself after its installation and subsequent downsizing.

2. ACTIVE INFRARED THERMOGRAPHY

In active infrared thermography, an external source is used to disturb the thermal equilibrium in the samples by either heating it up or cooling it down. One of the techniques most used is pulsed thermography (PT) [1,2]. In PT an optical source such as a photographic flash, is used to heat up the sample. A short pulse, usually milliseconds, is fired and a camera captures the thermal response in the sample's surface. In this work, PT was used to inspect, in reflection mode, the marquetry sample. The set-up employed had a 2009 Thermosensorik QWIP Dualband 384, an infrared dual-band camera working simultaneously in the mid-wave (MWIR) and long-wave (LWIR) bands (4.4-5.2 and 7.8-8.8 µm). To heat up the sample, it is used a circular flash device with several lamps which are shown in Figure 2. A short flash
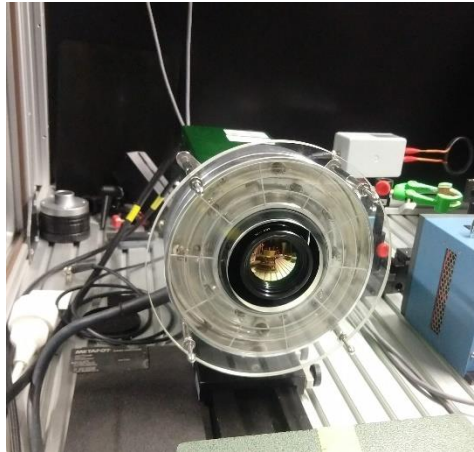
Figure 2 - IR camera and circular flash

was fired for a period of 10 µs and the infrared camera recorded approximately 5 seconds of images at a frame rate of 145fps.

Infrared signal is often very subtle. Thus, an enhancement algorithm must be applied for better visualization of the features of body been inspected. In this paper, principal component thermography (PCT) [3], is used to process the infrared image sets acquired with the PT experiment. PCT involves the application of singular value decomposition to reduce data to a compact statistical representation of the spatial and temporal variations relating the contrasts associated with underlying material defects. In PCT, pixels are transformed into the MxN matrix in which M and N represent the number of pixels and frames, respectively. The transformed matrix is then standardized and reduced by singular value decomposition where the meaningful information in the sequence can be represented in 10 or less empirical orthogonal functions (EOF).

3. AIR-COUPLED ULTRASOUND

Experiments with air-coupled ultrasound were carried out in transmission using two focussing acoustic transducers. Their central resonance frequency being 580 kHz. The focusing length of each transducer is 50 mm. Hence, the sample is placed between the two transducers with a distance of 50 mm on each side.

Since the surface is slightly curved, the measurements are divided into three sections. Thus, each section can be adjusted perpendicular to the transducers. For image acquisition 16 ultrasound pulses are shot (and averaged) every 1 mm in scan (up/down or y-Axis) and index (left/right or x-axis) direction. Figure 3 shows the air-UT set-up.
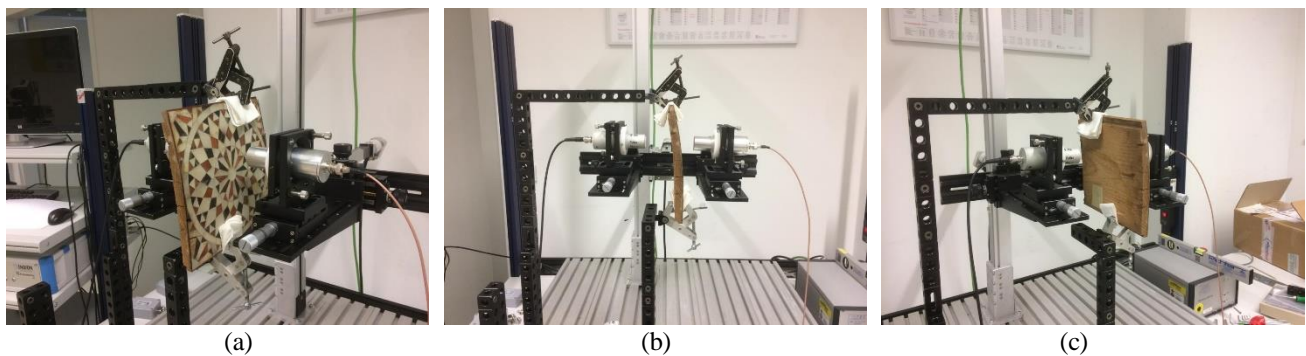

| (a) | (b) | (c) |

Figure 3 - Air-UT set-up. (a) Front view, (b) lateral view, and (c) back view.

4. INSPECTION RESULTS

Three different NDT techniques were applied in the sample: air-couple ultrasound (air-UT), x-ray computer-tomography (CT-Scan), and infrared thermography (IRT). Ultrasound and CT images appear distorted due to curvature present in the sample. In this section, results are presented and discussed.

4.1 AIR-UT RESULTS

To inspect the entire surface of the sample, it had to be divided in three section so that the UT-transducers were perpendicular to the panel surface. One pixel is equals 1 mm in both directions. Figure 4 shows an image where the three sections were fused almost into its original shape. Regions with higher values (red) may indicate delamination.
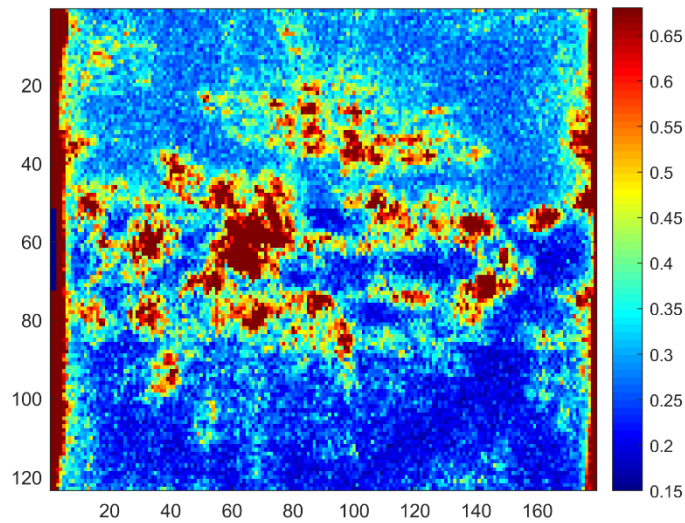

Figure 4 - Air-UT image result

4.2 X-RAY CT-SCAN

Figures 5-8 show some slices obtained with the x-ray ct-scan inspection. The curvature of the sample is clearly seem in the reconstructed slices. The tessellatum part was measured and it has a thickness around 1.86mm. X-ray CT-scan has provided several result images with the greatest number of details. The resolution of each slice of the reconstructed volume is 116.47 microns.
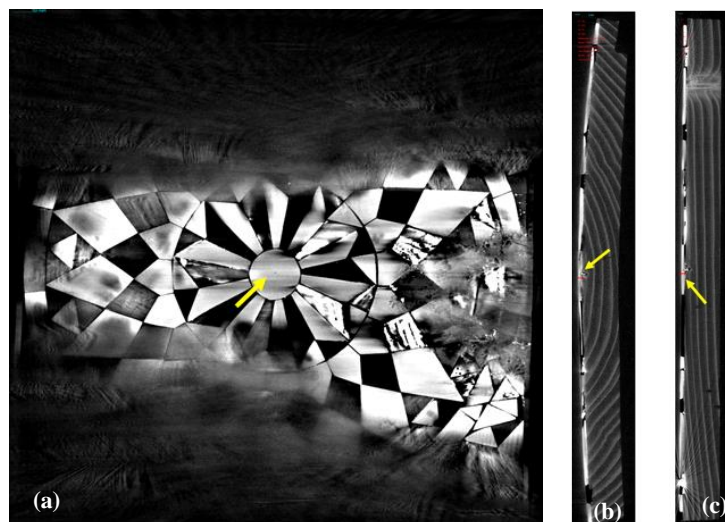

Figure 5 - X-ray ct-scan slice 1. (a) YZ-plan, (b) XZ-plan, and (c) XY-plan
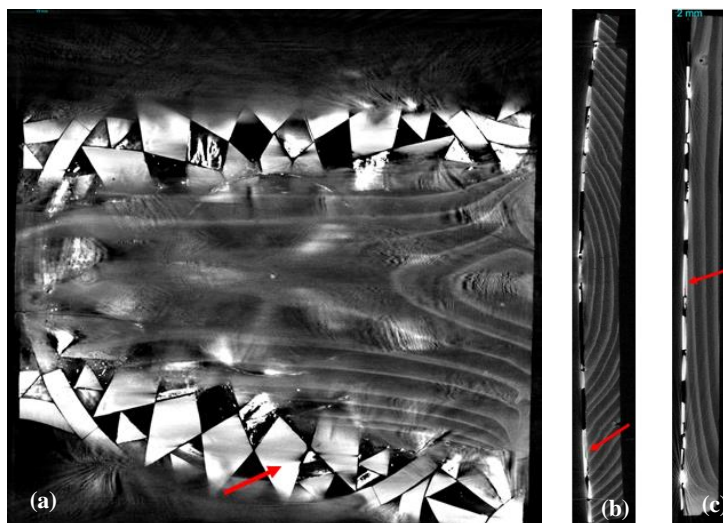
Figure 6 - X-ray ct-scan slice 2. (a) YZ-plan, (b) XZ-plan, and (c) XY-plan
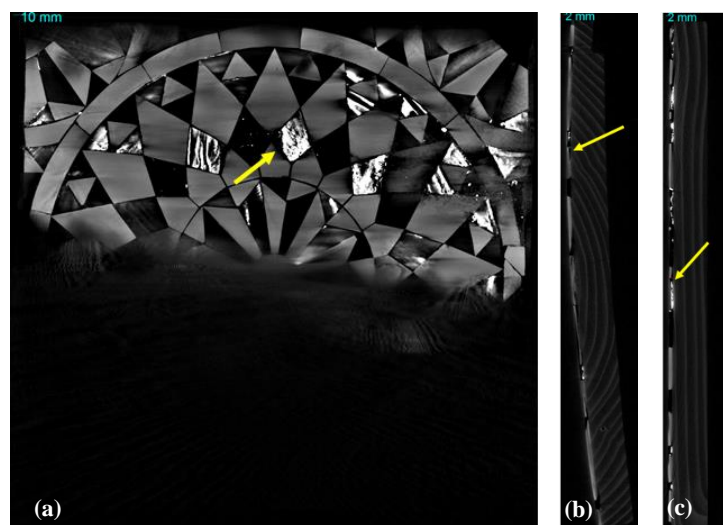

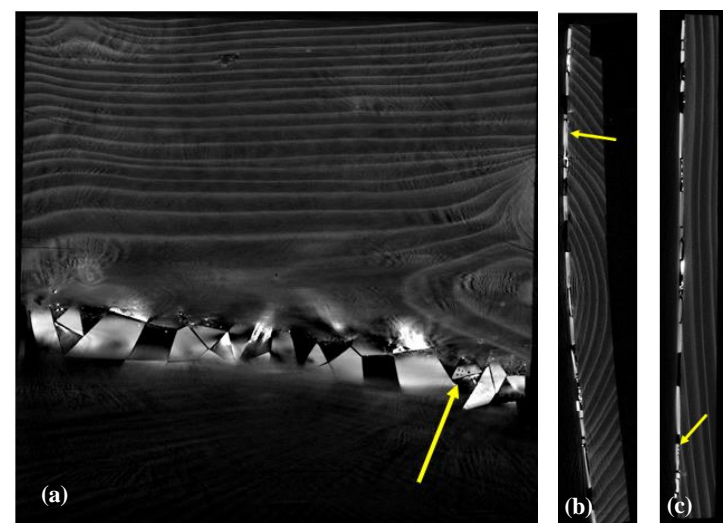**Figure 7** - X-ray ct-scan slice 3. (a) YZ-plan, (b) XZ-plan, and (c) XY-plan

Figure 8 - X-ray ct-scan slice 4. (a) YZ-plan, (b) XZ-plan, and (c) XY-plan

In Figure 5, it is possible to see several tessellatum parts where they are not completely in contact with the wooden sample (delamination). In addition, the yellow arrows indicate the presence of some pours in the three views. In Figure 6, the red arrows indicate a crack in one of the tessellatum part. Other porous parts are also indicated in Figure 7 and Figure 8 by yellow arrows as well.

4.3 INFRARED THERMOGRAPHY

Infrared images are very attenuated by the effect of heat diffusion. Thus, they were processed for quality enhanced and better visualization of the structure of the sample. Images in both mid and long wave spectrums were processed with PCT. Figure 9 shows the first 3 EOFs for each spectrum.
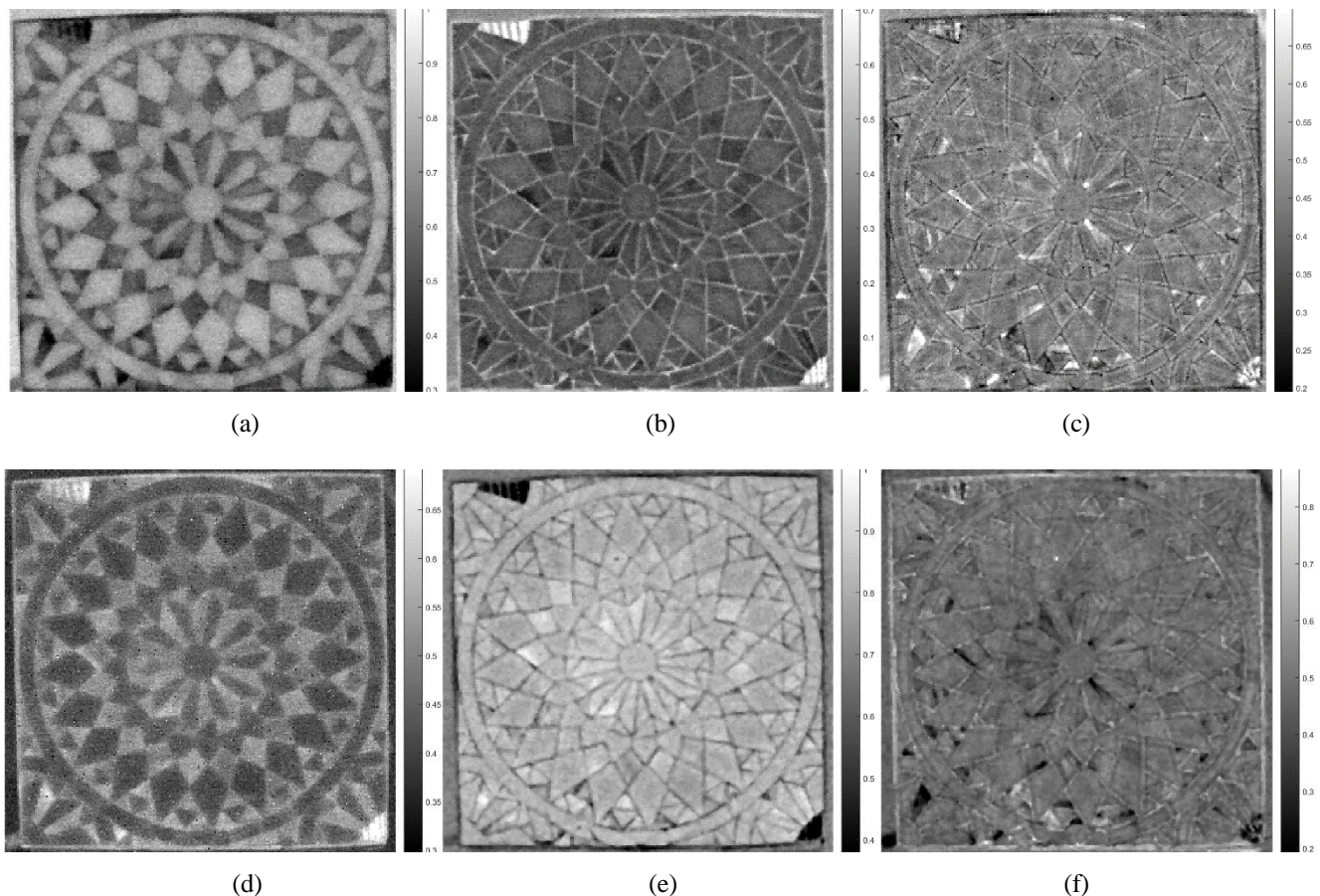

| (a) | (b) | (c) |

| (d) | (e) | (f) |

Figure 9 – PCT results obtained from infrared sequences. (a) First EOF from MWIR, (b) second EOF from MWIR, (c) third EOF from MWIR, (d) First EOF from LWIR, (e) second EOF from LWIR, and (f) third EOF from LWIR

Specially in the second and third EOFs, there are several regions with brighter (darker) values that may indicate some differences in the structure of the tessellatum. Details revealed with mid-wave and long-wave images are the same, the only difference is that they are inverted. Thus, for this sample, either mid or long wave image could be used.

5. CONCLUSION

In this paper, three NDT techniques were applied to inspect a decorative marquetry sample. Results from each technique show different features. Air UT display some red regions that may indicate delamination areas. X-ray CT-scan provided the most detailed images. In the reconstructed slices, it was possible to identify the thickness of the tessellatum parts as well as identify cracks, porous and delamination throughout the sample. Infrared images processed

with PCT revealed several parts with different false colors considering theirs neighbors. This may indicate that tessellatum parts are in different state of conservation.

ACKNOWLEDGMENT

REFERENCES

[1] X. Maldague, Chapter 11 – Techniques of Infrared Thermography: Part 2. Pulse Thermography. In: Maldague X, Moore P O editors, Nondestructive Handbook, Infrared and Thermal Testing, v.3, p.318–327. The American Society for Nondestructive Testing - ASNT Press, Columbus, OH, 3rd edition. (2001).

[2] J. Summa, M. Becker, F. Grossmann, M. Pohl, M. Stommel, H.G. Herrmann. Fracture analysis of a metal to CFRP hybrid with thermoplastic interlayers for interfacial stress relaxation using in situ thermography. Composite Structures, v.193, p.19–28, 2018.

[3] N. Rajic, Principal component thermography for flaw contrast enhancement and flaw depth characterisation in composite structures. Composite Structures, v.58(4), p.521–528, 2002.

CONDITION ASSESSMENT OF PRESTRESSED CONCRETE GIRDERS OF A HIGHWAY BRIDGE IN CANADA

Faraz Masoumi[*], Afshin Sadri[1], Winnie Ying [1], Claudio Pasqualino[1]

[1]Hatch Ltd., 2800 Speakman Drive, Mississauga, Canada L5K 2R7

[*]Corresponding Author: faraz.masoumi@hatch.com

ABSTRACT

Highway and bridge networks are important for economy growth of a country. It is essential to maintain, repair and rehabilitate existing bridges, and/or expand the existing highway. Concrete is the most widely used construction material for bridges in the world, and there are approximately 47,000 number of bridges in Canada, which most of these brides are concrete bridges. About 80% of existing bridges in Canada were built between 1940 and 1999, so the assessment and detection of damage of the existing bridges can allow prompt remedial works to be carried out for campaign life extension and to ensure safety. One of the main damages in concrete is cracks, and if the crack depth extends through the concrete cover of the reinforcement, it can potentially expose the reinforcement to corrosive elements. In this research, four NDT methods were used to determine the condition of a concrete bridge of 47 years old. Namely: visual inspection, crack monitoring, ultrasonic pulse velocity and ground penetrating radar (GPR). Among these methods, ultrasonic pulse velocity was used to measure the depth of longitudinal and inclined cracks on the flanges and webs of prestressed concrete girders in a highway bridge in Ontario, Canada. GPR was used to detect any delamination or debonding between strands/rebars and the concrete. This paper discusses the details of these NDT evaluation.

KEYWORDS: NDT, Ultrasonic Pulse Velocity, Ground Penetrating Radar, Prestressed concrete, Debonding

1. INTRODUCTION

The highway bridge was constructed in 1983. It is a two-span precast prestressed concrete bridge. The total span length of the bridge is 38.4 m (19.2 m, 19.2 m) and the width is 10 m. The structure spans along the east-west direction. The outer limits of the structure have concrete parapets. Figure 1 shows the north side view of the bridge.

Exterior girders have longitudinal cracks on the top surface of the bottom flange along the entire length of the bridge and all girders have inclined cracks on both sides of the webs. This paper investigates the bonding condition between concrete and pre-stressed reinforcement/strands of the girders. The depth of longitudinal cracks was measured on the bottom flange of the two exterior girders and the depth of inclined cracks was measured on the webs of all four girders.

Figure 1: North Elevation of the bridge

2. NDT METHODS TO DETECT DEBONDING AND MEASURE CRACK DEPTH IN CONCRETE

Visual inspection was performed on the entire bridge and areas of concern were selected for further investigations. Ultrasonic Pulse Velocity (UPV) and Ground Penetrating Radar (GPR) were then performed to detect crack depth and debonding, respectively. The technical details about these two NDT methodologies are described in following subsections.

2.1 ULTRASONIC PULSE VELOCITY METHOD

To determine ultrasonic pulse velocity measurements, an ultrasonic pulse analyzer is used (Figure 2). The test methodology is briefly summarized here. Three types of propagating mechanical waves (also called stress waves) are created when the surface of a large solid elastic medium is disturbed by a dynamic or vibratory load: (1) compressional waves (also called the longitudinal or P-waves), (2) shear waves (also called transverse or S-waves), (3) and surface waves (also called the Rayleigh waves). The compressional waves propagate through the solid medium in a fashion analogous to sound waves propagating through air. Each wave type propagates with its characteristic velocity, for a given solid, compressional waves have the highest velocity and surface waves the lowest. In concrete, the velocities of the shear and surface waves are typically 60% and 55% of the compressional wave velocity, respectively. The wave velocities depend on the elastic properties and density of the medium. For a homogenous solid media, the compressional wave velocity is given by the following:

$$V = \sqrt{\frac{KE}{\rho}} \qquad (1)$$

Where
V = compressional wave velocity,
$K = (1-\mu)/((1+\mu)\,(1-2\mu))$
E = dynamic modulus of elasticity
ρ = density
μ = dynamic Poisson's ratio

Figure 2: PULSONIC - Ultrasonic Pulse Analyzer Unit

The coefficient K varies within a narrow range. For example, as μ increases from 0.15 to 0.25 (67% increase), the associated K value increases from 1.06 to 1.20 (12% increase). Thus, variations in E and ρ have a more significant effect on V than variations in μ. For concrete, V typically ranges from 3000 to 5000 m/s.

In the ultrasonic pulse velocity test method, an ultrasonic wave pulse through concrete is created at a point on the surface of the test object, and the pulse travels from that point is reflected by boundaries and interfaces along the travelled path. Knowing the thickness of the bridge webs, the compressive wave velocity of the concrete can be determined.

The test instrument consists of sensors that can pulse and receive. The sensor is connected to an oscilloscope to observe the nature of the received pulse.

The equipment is portable and has a rechargeable battery and charging unit. Typically, pulse times of up to 6500 μs can be measured with 0.1 - μs resolution. The measured travel time is prominently displayed, the instrument comes with a set of two transducers, one each for transmitting and receiving the ultrasonic pulse. Transducers with frequencies of 25 to 100 kHz are usually used for testing of concrete. For this investigation, transducers with frequency of 50 kHz were used. These transducers primarily generate compressional waves at predominantly one frequency, with most of the wave energy directed along the axis normal to the transducer face.

The basic idea on which the pulse velocity method is established that the velocity of a pulse of compressional waves through a medium depends on the elastic properties and density of the medium as shown in Equation (1).

The transmitting transducer of the pulse velocity instrument transmits a wave into the concrete and the receiving transducer, at a distance L, receives the pulse through the concrete at another point. The pulse velocity instrument display indicates the transit time, Δt, it takes for the compressional wave pulse to travel through the concrete. The compressional wave pulse velocity V, therefore, is

$$V = \frac{L}{\Delta t} \qquad (2)$$

To transmit or receive the pulse, the transducers must be in full contact with the test object; otherwise an air pocket between the test object and transducer may introduce an error in the indicated transit time. This error is introduced because only a negligible amount of wave energy can be transmitted through air. Many couplants available in the market can be used to eliminate air pockets and to assure good contact; petroleum jelly has approved to be one of the superior couplants. Other couplants are grease, liquid soap, and kaolin-glycerol paste. The couplants layer should be as thin as possible. While applying constant pressure on the transducers, repeated readings at a particular location should be taken until a minimum value of transit time is obtained. If the concrete surface is very rough, thick grease should be used as a couplants. In some cases, the rough surface may have to be ground smooth, or a smooth surface may have to be established with the use of plaster of Paris or suitable quick-setting cement paste or quick setting epoxy mortar.

There are three possible configurations in which the transducers may be arranged, as shown in Figure 3. These are (1) direct transmission; (2) semidirect transmission; and (3) indirect or surface transmission. The direct transmission method is the most desirable and the most satisfactory arrangement because maximum energy of the pulse is transmitted and received with this arrangement. The semidirect transmission method can also be used quite satisfactorily. However, care should be exercised that the transducers are not too far apart; otherwise the transmitted pulse might attenuate, and a pulse signal might not be detected. The indirect or surface transmission method, is least satisfactory because the amplitude of the received signal is significantly lower than that received by the direct transmission method. This method is very useful for measuring the depth of surface cracks.

The pulse velocity method provides a means of estimating the strength of both in situ and precast concrete although there is no physical relation between the strength and velocity. The strength can be estimated from the pulse velocity by a pre-established graphical correlation between the two parameters. The relationship between strength and pulse velocity is not unique, and is affected by many factors, e.g., aggregates size, type, and content; cement type and content; water-cement ratio; and moisture content.

The pulse velocity method is suitable for the study of homogeneity of concrete, and, therefore, for relative assessment of quality of concrete. Heterogeneities is defined as interior cracking, deterioration, honeycombing, and variations in mixture proportions. Heterogeneities in a concrete member will cause variations in the pulse velocity, for example, the diffraction of a wave pulse around an internal air void will cause an increase in the time of propagation for an assumed path through the void center. Thus, the apparent velocity will decrease, However, only large voids, generally larger than the transducer contact face, will cause measurable reduction in velocity. Also, in situ concrete strength varies in a structure because of the variations in source and proportions of materials, uniformity of mixing, and due to inadequate or variable consolidation. The pulse velocity method is highly effective in establishing comparative data and for qualitative evaluation of concrete. For obtaining these qualitative data, a system of measuring points, i.e., a grid pattern, may be established. Depending on the quantity of the concrete to be evaluated, the size of the structure, the variability expected, and accuracy required, a grid spacing should be established.
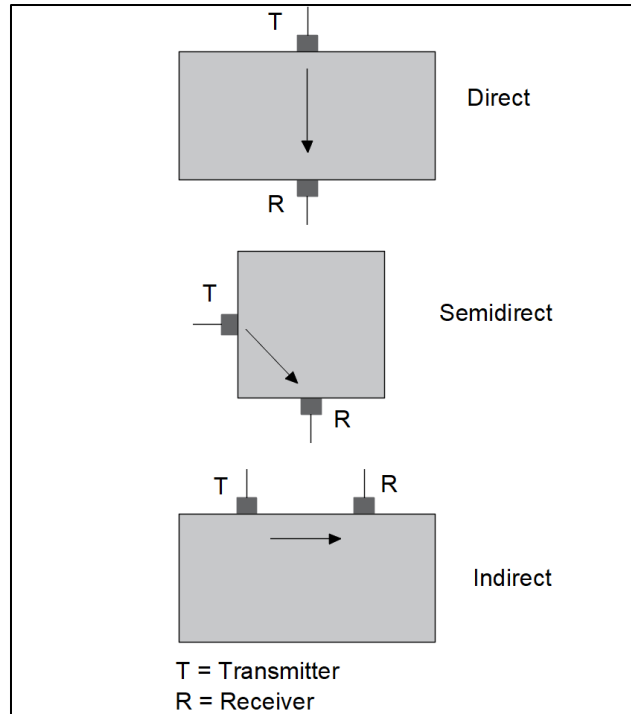
Figure 3: Pulse velocity measurement configurations.

The ultrasonic pulse transmits a very small amount of energy through air, therefore if a pulse traveling through the concrete come upon an air-filled crack or void whose projected area perpendicular to the path length is larger than the area of the transmitting transducer, the pulse will diffract around the defect. Thus, the pulse travel time will be greater than that through similar concrete without any defect. The pulse velocity method, therefore, is an effective in characterizing surface cracks. The depth of crack can be estimated by the pulse velocity method as shown in
. The depth, h is given by Equation (3) as below:

$$h = \frac{X}{T_2}\sqrt{T_1^2 - T_2^2} \qquad (3)$$

where
X= Distance to the transducer from the crack
T_1= transit time around the crack
T_2= transit time along the surface of the concrete without any crack
The scheme for UPV on the bottom flange of the bridge girder is shown in Figure .
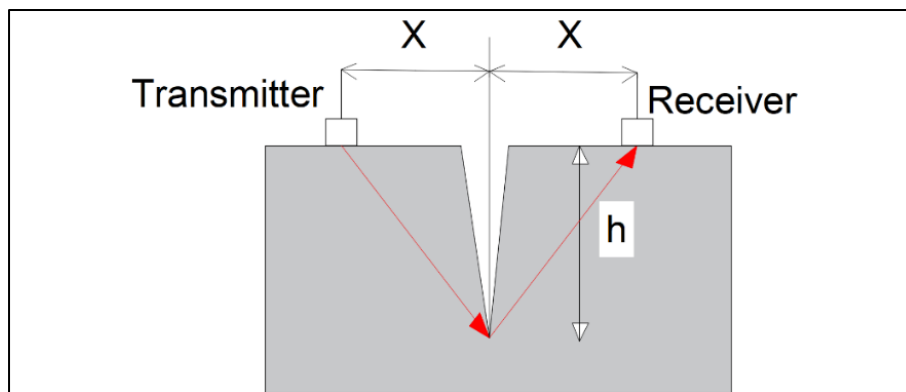

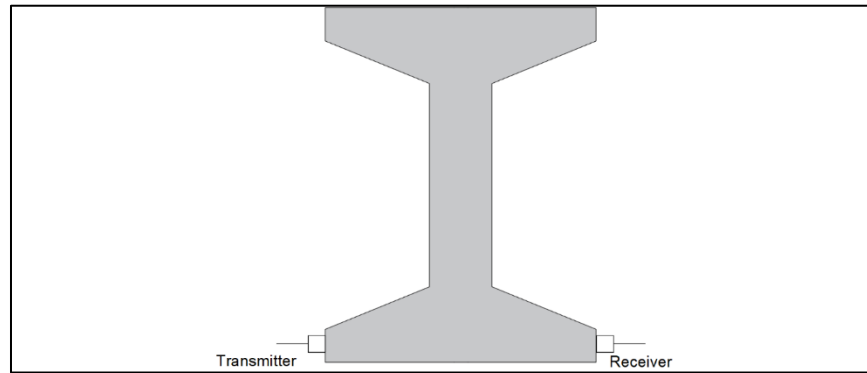Figure 4: Scheme for measurement of surface crack depth, h

Figure 5: Scheme for UPV of Bottom flange

2.2 GROUND PENETRATING RADAR METHOD

Short-pulse radar is a powerful scientific tool with a wide range of applications in the testing of concrete. It is gaining acceptance as a useful and rapid technique for non-destructive detection of delaminations and other types of defects in bare or overlaid reinforced concrete decks. It also shows potential for other applications such as monitoring of cement hydration or strength development in concrete, study of the effect of various admixtures on curing of concrete members. Since development of this method, it is proved the feasibility of transmitting electromagnetic (EM) waves through space as abeam and receiving the reflected signal from an airborne object in the path of the beam. Subsequent refinement in microwave sources and detection circuits made it possible to accurately locate planes. These applications were made possible by the realization that different objects have their own characteristic scattering and reflection properties toward EM waves and that EM waves travel through free space with a constant speed, equivalent to that of light. Such detection systems were eventually called radar, which is an acronym for radio detection and ranging. The speed of microwave and its amplitude as a function of distance traveled in a solid could vary significantly from one material to another, and that these properties can be used to identify and profile subsurface geological features. This led to the development of ground penetrating radar (GPR). Since development of GPR, it have been put to a variety of uses, including determining of the thickness and structure of glaciers, locating ice in permafrost, finding sewer lines and buried cables, measuring the thickness of sea ice, profiling the bottom of lakes and rivers, examining the subsurface of the moon, and measuring scouring around bridge foundations.

In this investigation, a 1.0 GHz GPR system was used to produce images of the embedded reinforcement and strands of the precast girders. The system is an integrated ground penetrating radar (GPR) system specifically designed to meet the needs of concrete inspections. The test unit and its grid lines are shown in Figure 4.

The GPR unit transmits electro-magnetic pulses into the concrete, which are then reflected and detected by the receiver. When there is any disturbance within the scan such as voids, delamination, or changes in moisture content the resultant change in dielectric properties of the scanned object will emit a different frequency wave pattern that will be projected on the scanned image. Details of the GPR technique and its limitations are discussed in ASTM D6087 - 08(2015) e1, ASTM D 4748-87 (1995), ASTM D 6432-99.

Two-dimensional grid scans were performed at the web locations and line scans were performed at the bottom flange on both vertical and longitudinal directions at selected locations.
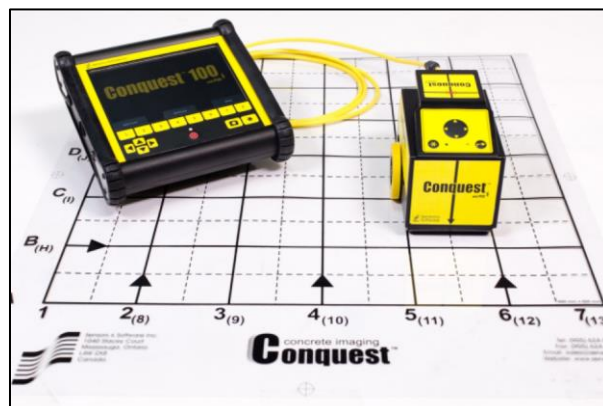
Figure 4: A GPR System

3. RESULTS

The UPV method was used to estimate the depth of cracks at different locations of the girders. This test was performed at 24 locations on the girders and, for each location, various NDT measurements were taken. The layout for UPV measurements is shown in Figure 5.
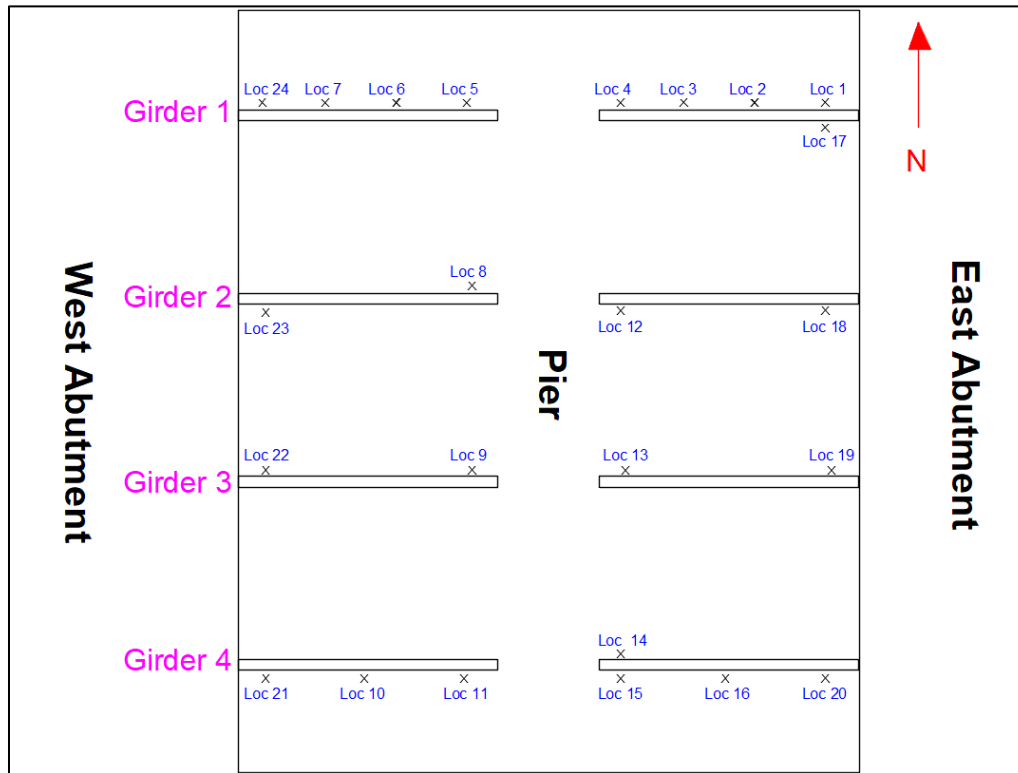

Figure 5: UPV Inspection Layout Plan (not to scale)

The depths of longitudinal cracks were measured at 10 points on the two exterior girder lines. The longitudinal crack depths varied from 12 to 34 mm, which is less than the concrete cover and the cracks did not reach the strands. The depths of inclined cracks were measured at 17 different locations of the four girders. The depths of the inclined cracks varied from 13 mm to 82 mm. The depths of inclined cracks were more than 50 mm in some locations, which is greater than the depth of concrete cover for stirrups and strands. The measurement of crack depth for 6 locations of 4, 8, 9, 12, 17 and 22 were 67, 82, 62, 58, 61 and 71 mm, respectively. The depth of longitudinal and inclined cracks is shown graphically on Figure 7 and Figure 8, respectively.

UPV testing was performed at 3 locations on the bottom flange of the girders (12 locations in total). The layout plan for UPV on bottom flange is shown in Figure 6. The UPV results show the time-of-flight of the pulse from one side of the girder to the other side. The average travel time based on 12 measurements was 146.40 µs and coefficient of variance of 0.139. The width of the bottom flange is 660 mm which shows the velocity of signal is 4508 m/s. This is greater than the typical pulse velocity for ordinary concrete (3700 to 4200m/s) [1]. In this paper, equations 4 [1] is used for the estimation of compressive strength of concrete. The compressive strength of concrete for girders is estimated as 39 MPa.

$$f_c' = -109.6 + 0.033V \qquad (4)$$

Where

V: Velocity of pulse (m/s)

The layout of the GPR scans is shown in Figure 9. Some examples of line GPR and grid GPR scans are shown in Figure 10 and Figure 11. GPR scans could be used for determining reinforcement geometry inside concrete, and line scans could be used for detecting delamination and debonding between concrete and rebars/strands. All line and grid GPR scans were assessed in detail and no delamination or debonding were detected in prestressed concrete girders.
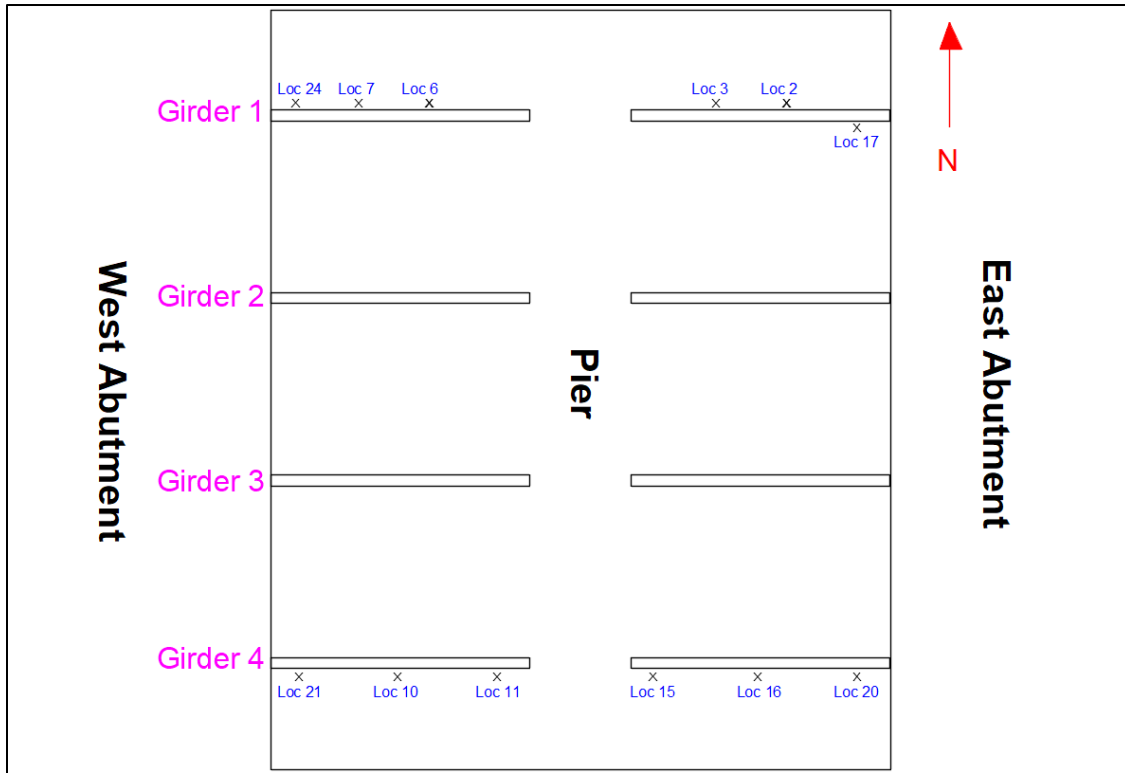
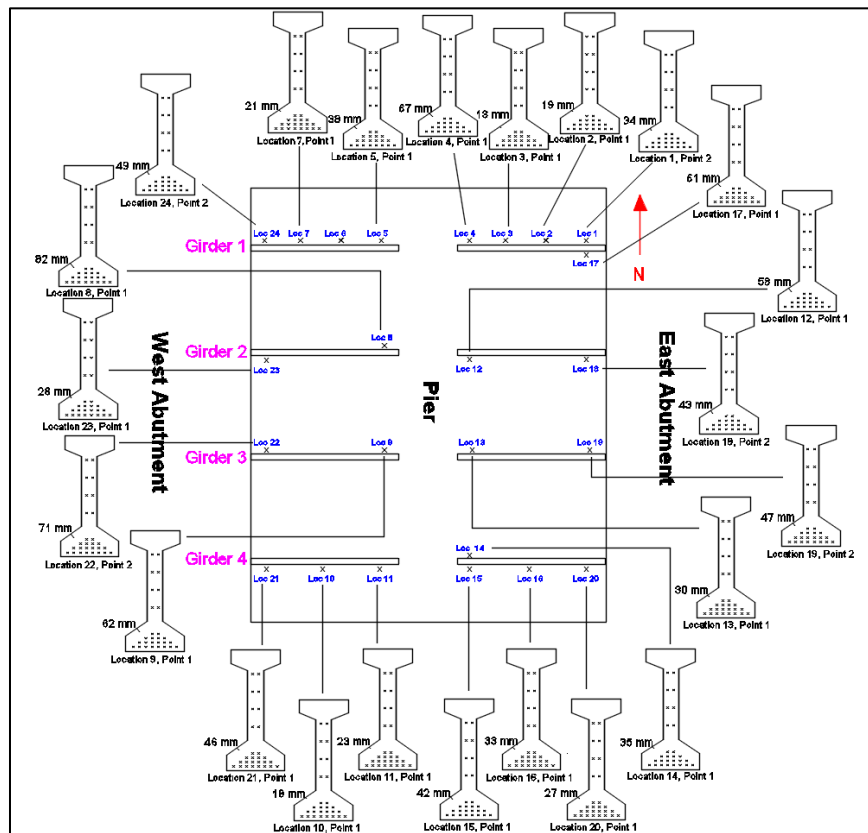Figure 6: Layout plan of UPV tests of the bottom flange indicated by X

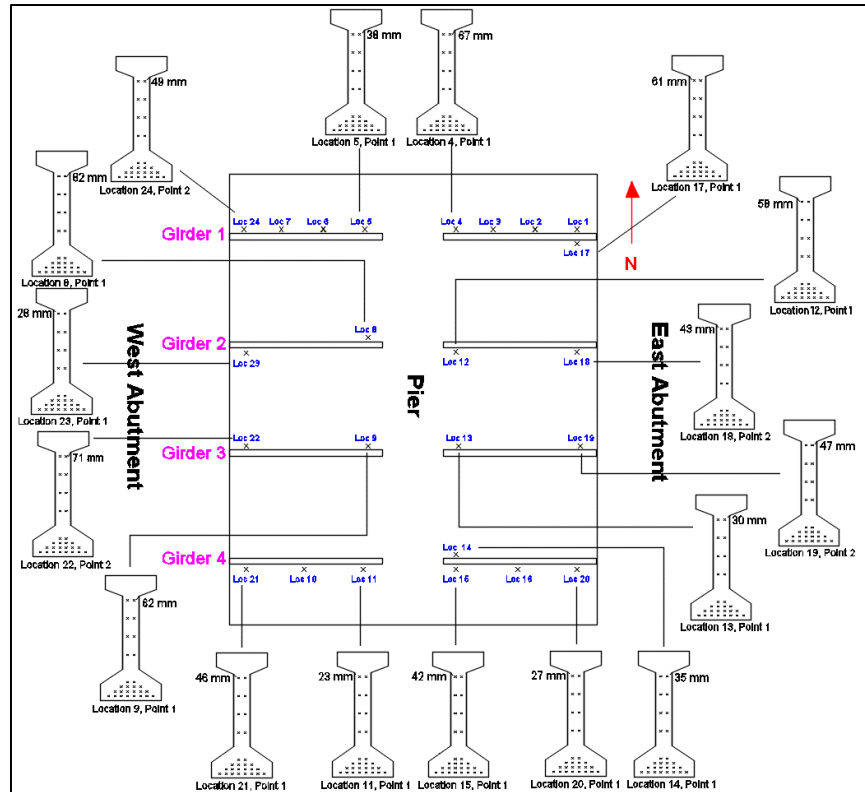Figure 7: Depth of longitudinal cracks on the bottom flange of girders (max. = 82 mm)

Figure 8: Depth of top inclined cracks on web of girders (max. = 82 mm)
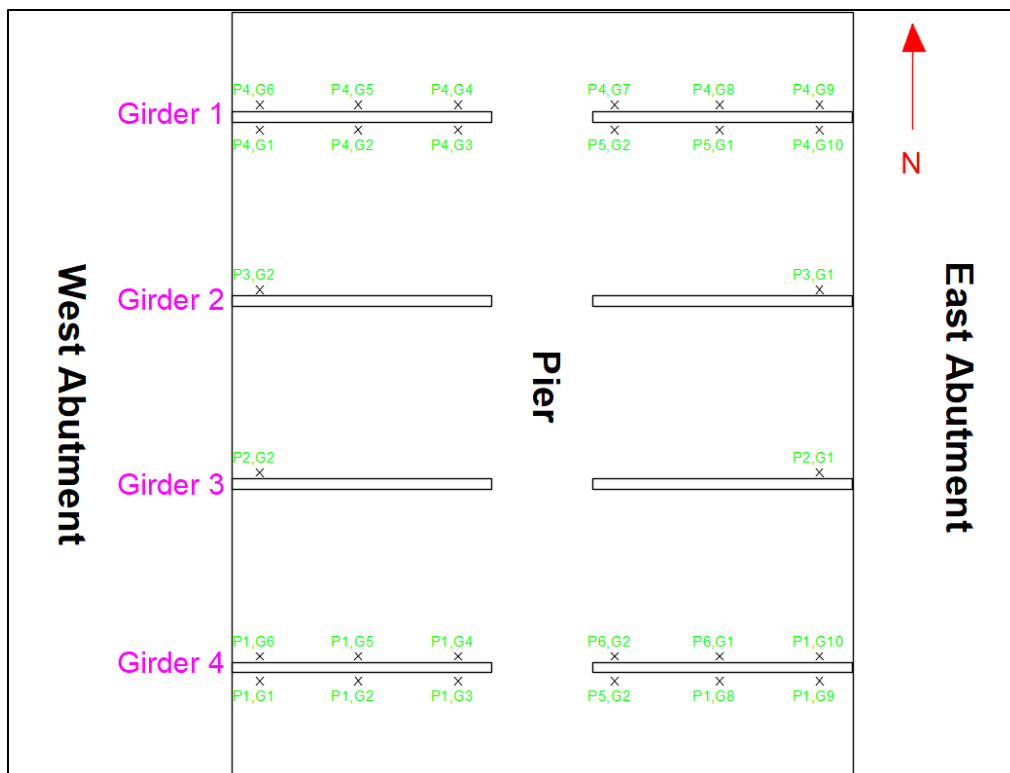

Figure 9: Layout showing the locations of GPR tests indicated by X at the webs of girders
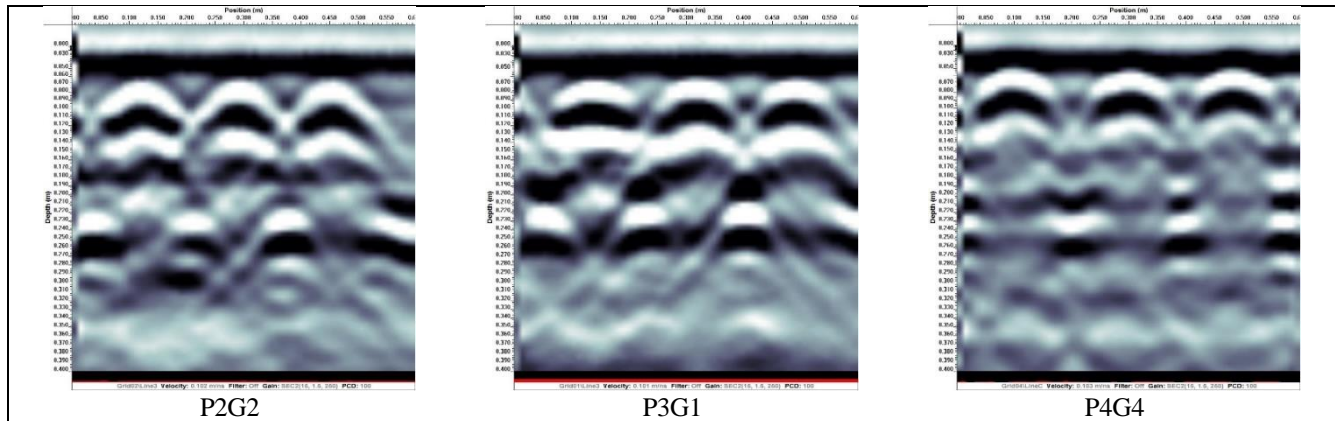
| P2G2 | P3G1 | P4G4 |

Figure 10: Examples of GPR line scans show no delamination or debonding in concrete
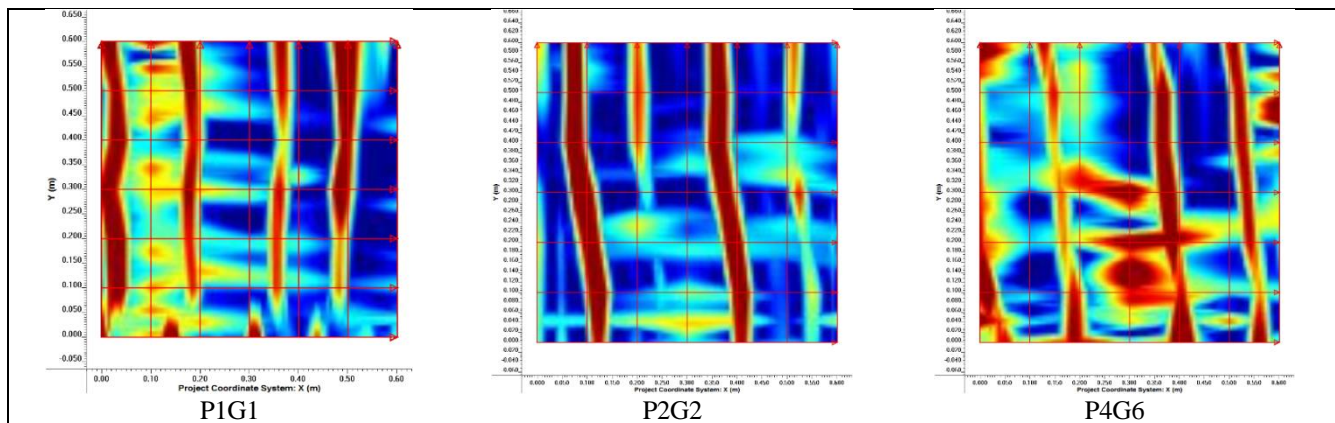

| P1G1 | P2G2 | P4G6 |

Figure 11: Examples of GPR gird scans show the reinforcement and strands in concrete

4. CONCLUSION

The aged bridge was assessed by a thorough NDT investigation. The crack monitoring gauges which were installed in 2019 showed stabilized shear cracks at the outer girders at the piers. The ultrasonic pulse velocity method is used to estimate depth of longitudinal and inclined cracks on the webs and bottom flanges of the prestressed concrete girders. The test results show that depths of cracks are less than reinforcement covers, which indicated that the cracks were initiated from the concrete surface and were not initiated from the prestressed strands. The prestressed strands and reinforcements are protected by the concrete from corrosion. In addition to that, ultrasonic pulse velocity measurements were done on the bottom flange of the girders. For fix and steady thicknesses, having the same concrete material, the first arrival time should be the same in all measurements. This includes the condition where the concrete member includes reinforcement or not. In the case of the presence of reinforcement, the ultrasonic waves go through the concrete and the reinforcement as the acoustic impedance between concrete and reinforcement allow it. Slight change in delay time for the ultrasonic wave's first arrival is expected, as the concrete is a heterogeneous material and the material properties vary in short distances within the same concrete member. However, if there is any delamination between the reinforcement and concrete, the ultrasonic waveform travels around the reinforcement as the delamination will not allow the ultrasonic wave to go through the concrete member and the reinforcement. In this case, the first arrival time will increase notably and can be identified based on the ultrasonic measurements of the area. The test results show that time-of-flight of ultrasound waves were close to each other and that there is no delamination or debonding between concrete and strands/rebars in bottom flange of the girders. GPR scans on webs of the girders show no delamination or debonding. This also confirmed the ultrasonic pulse velocity testing results.

REFERENCES

[1] Malhotra, V.M., and Carino, N.J., Eds. Handbook of Nondestructive Testing of Concrete, 2nd Ed, West Conshohocken: CRC Press, 2004.

PASSIVE GUIDED WAVES TOMOGRAPHY FOR STRUCTURAL HEALTH MONITORING OF PIPES

Valentin Serey[1, *], Huu Tinh Hoang[1], Tom Druet[1], Bastien Chapuis[1]

[1]CEA LIST, 91191 Gif-sur-Yvette, France

[*]Corresponding Author: valentin.serey@cea.fr

ABSTRACT

Corrosion in pipes is a problem faced in several domains, like the oil and gas or nuclear industries, due to the risk of rupture or leakage. Non-Destructive Testing (NDT) techniques using elastic guided waves have proven useful to detect such defects due to their ability to interrogate large structures and their sensitivity to defects. More recently, Structural Health Monitoring (SHM) approach seeks to implement permanently attached sensors over the structure lifetime. Elastic guided waves tomography can reconstruct a thickness map of the structure over a large zone with a reduced number of transducers, and thus localize and characterize corroded areas. Tomographic algorithms are well suited for a passive approach, without wave excitation. In that case, sensors only measure the ambient elastic noise present in the operating structure (due to flow, vibrations…). The cross-correlation of these signals allows getting the same information as with measurements from active sources. Passive process has been demonstrated in plate-like structures. This paper shows experimental results of corrosion imaging in pipes using passive tomography. The passive approach is a path forward for using optic fibers with Fiber Bragg Grating (FBG) instead of piezoelectric transducers, offering a lighter, less intrusive and more permanent solution.

KEYWORDS: Guided Waves, Tomography Imaging, Piezoelectric sensors, Fiber Bragg Grating (FBG), Pipe-like Structures, Corrosion

1. INTRODUCTION

Many industries have to face erosion and corrosion problems in pipes. The SHM process aims at interrogating the state of health of a structure during its lifetime with an attached instrumentation.

Tomography techniques using elastic guided waves have proven useful to detect and locate damages [1]. Most of the time the SHM system implies the use of piezoelectric elements. Unfortunately, this type of sensors does not resist extreme conditions (*e.g.* high temperature), adds weight to the structure and their use as actuators necessitates heavy cabling. Optical fibers with FBG are a good alternative [2], but can only be used as receivers and not transmitters. Passive methods seeks to achieve the same results as with active sources, but without them. They rely on extracting information from the ambient noise of the structure, which also carries waves. For instance, a structure, during its service, can undergo several vibrations: air turbulence for a plane, turbulent fluid in a pipe, vibrations caused by engines…

This abstract quickly reminds the passive tomography imaging principle, shows experimental results on a pipe using two arrays of PZT, then compare the active and passive approaches to detect a corrosion defect. It then discusses on the use of FBG.

2. PASSIVE TOMOGRAPHY

Guided wave tomography imaging process consists in surrounding the monitored area with a distribution of sensor and measuring the responses between all the different possible couples of sensors. The collected data are then inverted to produce a thickness map of the area. Several assumptions are necessary to choose a propagation model for tomography.

Assuming that the wall thickness is small regarding the pipe radius, the propagation of guided waves can be modeled by a phase velocity field that depends only on the wall thickness and not the direction, thus the acoustic model can be used in this case. The tomography can then be implemented by unwrapping the pipe and treating it as a flat plate [3].

The passive method uses cross-correlation on the random field (ambient noise) measured simultaneously at two points, to reconstruct the information of propagation between them. Passive method exploits the presence of ambient noise in the structure, *e.g.* the flow of fluids inside pipes or the structure vibrations. The idea comes from the geophysics domain [4]. The relationship between the cross-correlation and the Green's function has been established in several articles such as [5]. The passive measurement between two points A and B consists in simultaneously measuring the ambient elastic noise in A and in B. Under certain conditions, the cross-correlation of these signals allows obtaining Green's function between A and B. The tomography can

then be applied using signals correlated from ambient noise at different measuring points and the resulting passive signals are then used as an input data for tomography algorithm as described in [6] in order to reconstruct thickness map.

3. RESULTS

The considered configuration consists in a 2.15 mm thin, 254 mm outer diameter steel pipe instrumented with two arrays of 15 PZT sensors. An area is artificially corroded, and an optical scan was done to know the exact thickness. The results of the tomography are displayed in Figure 1. The reference thickness map is presented in Fig.1(a), and imaging using either active or passive methods are respectively in Fig.1(b) and Fig.1(c). Both methods are able to correctly locate and estimate the global shape of the corrosion defect. Minimal remaining wall thickness is correctly captured, which is the most important information for safety.
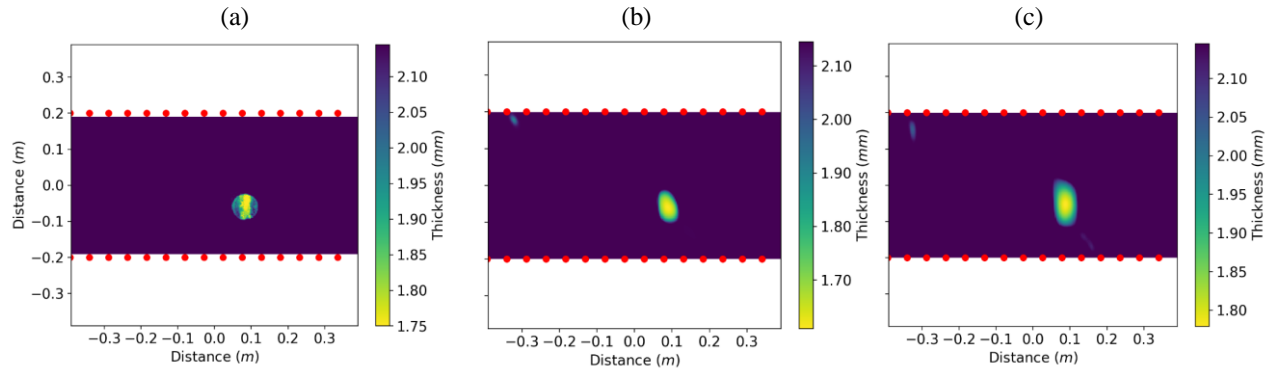

Fig. 1 (a) real thickness map, (b) active imaging and (c) passive imaging of a corrosion defect in a pipe.

4. TOWARDS THE USE OF FBG

Passive wave measurements with FBG sensors is also possible with noise cross-correlation [2]. The next step is to obtain the same results as with piezoelectric elements using arrays of FBGs and obtain maps similar to results of Fig. 1. Some challenges need to be faced, such as the FBG directivity. So far, first results have been obtained using active hybrid tomography with one ring of piezoelectric transducers and one ring of FBG [7].

5. CONCLUSION

This paper have briefly presented the active and passive tomography for corrosion or erosion detection. The obtained results for both active and passive cases are in agreement with the defect real location and size. Future works will specifically focus on the implementation of optical fiber Bragg grating sensors to reduce the intrusiveness of sensors in the SHM system. Encouraging results let envision the use of such an SHM system in harsh environment (radiations, high temperatures, explosive atmosphere).

REFERENCES

[1] Huthwaite, P. Improving accuracy through density correction in guided wave tomography. *Proc. Roy. Soc. A* (2016), 472(2186), 20150832.
[2] Druet, T. *et al*. Passive guided waves measurements using fiber Bragg gratings sensors. *JASA* (2018), 144(3), 1198-1202.
[3] Willey, C. L. *et al*. G. Guided wave tomography of pipes with high-order helical modes. *NDT & E International* (2014), 65, 8-21.
[4] Campillo, M. & Paul, A. Long-Range Correlations in the Diffuse Seismic Coda. *Science* (2003), 299, 547-549.
[5] Sabra, K. G. *et al*.. Extracting time-domain Green's function estimates from ambient seismic noise. *Geophys. Res. Lett.* (2005), 32(3).
[6] Druet, T. *et al*.. Passive guided wave tomography for structural health monitoring. *JASA* (2019), 146(4), 2395-2403.
[7] Druet, T. *et al*. Effect of Fiber Bragg gratings receiver's directivity on guided wave tomography of pipe. *Proc. 12th IWSHM* (2019), Stanford.

NUMERICAL SIMULATION AND EXPERIMENTAL STUDY OF CAPACITIVE IMAGING TECHNINQUE AS A NON-DESTRUCTIVE TESTING METHODN

Farima Abdollahi-Mamoudan[1*], Sebastien Savard[2], Tobin Filleter[3], Clemente Ibarra-Castanedo[1], and Xavier P. V. Maldague[1*]

[1]Department of Electrical and Computer Engineering, Universite Laval, 1065 Avenue de la Medecine, Quebec, QC G1V 0A6, Canada ; farima.abdollahi-mamoudan.1@ulaval.ca (F.A.M.), clemente.ibarra-castanedo@gel.ulaval.ca (C.I.C), xavier.maldague@gel.ulaval.ca (X.P.V.M.)
[2]Eddyfi Technologies, 3425, av. Pierre-Ardouin, Quebec, QC, G1P 0B3, Canada; ssavard@eddyfi.com (S.S.)
[3]Department of Mechanical and Industrial Engineering, University of Toronto, 5 King's College, Toronto, ON, M5S 3G8, Canada; filleter@mie.utoronto.ca (T.F.)

[*]Corresponding Author: xavier.maldague@gel.ulaval.ca, farima.abdollahi-mamoudan.1@ulaval.ca

ABSTRACT

It was recently demonstrated that a co-planar capacitive sensor could be applied to the evaluation of materials without the disadvantages associated with the other techniques. This technique effectively detects changes in the dielectric properties of the materials due to, for instance, imperfections or variations in the internal structure, by moving a set of simple electrodes on the surface of the specimen. An AC voltage is applied to one or more electrodes and signals are detected by others. This is a promising inspection method for imaging the interior structure of the numerous materials, without the necessity to be in contact with the surface of the sample. In this paper, Finite Element (FE) modelling was employed to simulate the electric field distribution from a co-planar capacitive sensor and the way it interacts with a non-conducting sample. Physical experiments with a prototype capacitive sensor were also performed on a Plexiglas sample with sub-surface defects, to assess the imaging performance of the sensor. A good qualitative agreement was observed between the numerical simulation and experimental result.

KEYWORDS: co-planar sensor; capacitive sensing; NDT techniques; FE modelling; defects

1. INTRODUCTION

There are several methods for evaluating the integrity of materials, and an important category of them is Non-Destructive Evaluation (NDE) or Non-Destructive Testing (NDT) methods. This field includes identifying and characterization the flaw on the surface and under the surface of materials without cutting apart or altering the material [1]. It means NDT refers to the process of evaluating and inspecting materials to identify or detect defects in comparison with some standards without changing the main features or damage to the tested object. NDT techniques supply affordable ways of assessing a specimen individually or may be applied to the whole material for testing in a manufacturing system for quality control purposes [2].

There are some advantages and disadvantages inherent to all NDT methods that made them more or less suitable for a particular application in relation to the coverage area, the penetration depth and the problems associated with the interpretation of the results [3]. For instance, ultrasound testing is a mature technique allowing the identification and characterization of deep defects, but requires contact with the object being inspected and the use of water-based couplants (liquid or gel); radiography testing provides high-resolution images and deep penetration, but requires access to both sides of the object and employs ionizing radiation, which constitutes a risk of radiation exposure; infrared thermography testing allows the inspection of large areas in a fast and contactless manner, but is limited to relatively shallow defects and requires advanced signal/image processing for defect characterization; Eddy current testing (ECT) is very effective for certain types of defects (cracks, corrosion, etc.) under several layers of materials, but is limited to conductive materials and is not well suited for the detection of delaminations in composites; etc. It has recently been shown that an alternative electromagnetic method based on a capacitive sensor can be used as an NDT method [2].

For non-conducting materials, NDT methods are not as well developed as compared to those for metallic materials. One approach to evaluate non-conducting materials is to characterize their dielectric properties. The dielectric strength and the dielectric constant are the dielectric properties of non-conducting or low conductivity materials. The voltage a material can withstand before an electrical breakdown happens is called "dielectric strength" and a measure of the material's capability of storing electric energy is called "dielectric constant" or "permittivity". There exist alternative approaches that are based on the characterization of materials permittivity such as microwave techniques and resonant testing. However, these techniques require expensive equipment and/or complex operating procedures. Capacitive sensing on the contrary is a straightforward and inexpensive approach [2].
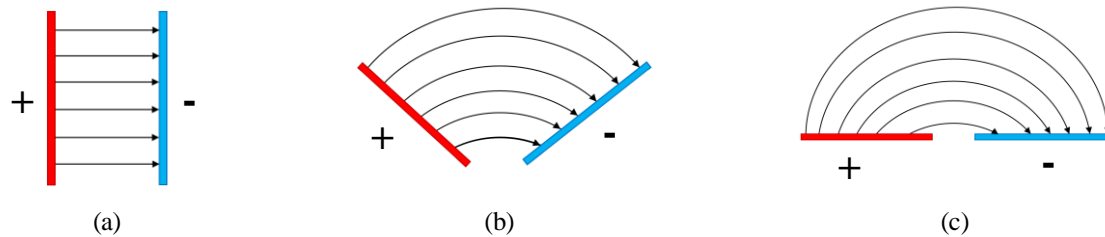
(a)   (b)   (c)

Fig. 1 Schematic of the electric field distribution as electrodes turns from a parallel geometry of the capacitor (left) to co-planar (right): (a) Parallel-plate capacitor whose, (b) Electrodes open up to provide, and (c) One-sided access to the specimen.

The co-planar capacitive technique was first introduced in 2006 [4]. This novel approach, usually referred to as Capacitive Imaging (CI), is an electromagnetic NDT method that uses arrays of electrodes to generate an electric field distribution within the specimen. The electric field distribution can penetrate within dielectric materials and changes in response to the structure of the material under test leading to a variation in the output voltage [5, 6]. The capacitive technique has shown great potential to inspect a wide range of materials and structures from insulators to conductors [5].

CI technique offers a possible way to overcome some of the restrictions imposed by existing NDT methods. For instance, the technique works in a volume averaging manner and therefore the scattering issue with the ultrasonic method is absent [7]. The low cost, fast response, non-intrusive, non-invasive, no ionizing radiation involved and flexibility in the design of the electrodes provide CI with a great potential to be applied in a wide range of applications. Furthermore, the co-planar structure allows one-sided inspection [8], which is especially useful when access to both sides of the specimen is limited [9]. Moreover, this is a non-contact technique [5] and the lift-off (the air gap between the surface of the electrodes and specimen) can be optimized, leading to an applicable method in the detection of corrosion under insulation (CUI), including the detection of large surface features in metals and therefore the presence of even small amounts of rust [10]. This technique is especially useful in defence where composites are extensively used for both equipment and strengthening structures [11]. These features of co-planar capacitive sensor make it an attractive option for applications in NDT [6], material characterization [8], and imaging [12].

The principle of this technique involves placing two (or more) electrodes over the surface of the sample and then applying an AC voltage between them. This system acts as a capacitor whose altering in capacitance indicates variations in the internal structure (such as the presence of a defect) [13]. Normally, in a regular capacitor, the plates are parallel. When a voltage is applied between these plates, they produce a uniform electric field distribution. This electric field does not restrict itself to the area between the electrodes when the electrodes are gradually open, but extends to a wider space and forms a fringing field [9]. This fringing field expands into the sample for NDT purposes. Scanning a pair of electrodes over the surface of the specimen and measuring changes in stored charges for a given voltage makes a map of the changes in the electrical properties within the sample [7]. The fringing field between the driving and sensing electrodes becomes predominant when the electrodes open to a co-planar plane. This kind of sensor is named a co-planar sensor in literature [9]. Figure 1 shows a schematic diagram showing how the electric field distribution changes when the two capacitor electrodes change from a parallel-plate to a co-planar so that the final part produces a fringing field [7]. The sensor electrodes can be scanned over the surface of a large mechanical structure to inspect the intrinsic properties of the sample and obtain information.

Such as some other NDT methods, the capacitive technique is sensitive to lift-off, which refers to the air gap between the surface of the co-planar electrodes and specimen which causes a decrease in the capacitance between the electrodes and hence a reduction in output voltage. In addition, it reduces the extent of penetration of the electric field into the sample which leads to a decrease in the depth of penetration [9]. The lift-off should therefore be as small as possible to achieve greater signal strength and sensing depth (especially for investigating dielectric material) [14] with no need to use couplant materials.

The sensor manufacturing steps include material selection for electrodes, the insulation layer of the surface of the electrodes, the sensor substrate, and the choice of a production method. The electrodes are made of materials with high electrical conductance, such as copper. A very thin insulation layer (with a few micrometres in thickness) is usually placed on the surface of the electrode to prevent direct contact of the electrodes with the specimen and to protect the electrode surface from scratches. The thickness of the insulation layer and the sensor substrate can affect the electric field strength and depth of penetration, hence, need to be optimized. Several manufacturing techniques of the capacitive sensor, including microelectromechanical systems (MEMS) [15], printed circuit boards (PCB) and manual production can be selected depending on sensor dimensions and costs [9].

To evaluate the sensor performance, it is required to explain the general design parameters. Therefore, in this paper, firstly the design factors such as the geometry of the electrodes, the number of electrodes and their arrangement, shielding plate and guard electrode of the capacitive sensor are presented. The electric field distribution from a co-planar capacitive sensor in the different condition of a specimen was considered by 3D Finite Element (FE) modelling, and finally, the imaging performance of the method was evaluated using a pair of triangular co-planar electrodes with physical experiments.

2. SENSOR DESIGN

There are several parameters in sensor design for assessing the performance of a sensor. One design parameter may influence several aspects of sensor performance. On the other hand, more than one design factor should be considered in order to achieve the desired sensor performance. Therefore, knowing how design parameters affect sensor performance leads to sensor optimization for a specific application. Additionally, instrumentation-related issues should be considered in order to achieve the right measurements of a sensor [9]. The important design parameters for a co-planar capacitive sensor include the electrode geometry, the number of electrodes and their arrangement, shielding and guarding.

2.1 ELECTRODE GEOMETRY

The performance of a co-planar capacitive sensor is primarily determined by its geometry, which includes the size, shape, and separation distance between the electrodes [16]. They are the most important parameters which affect the electric field strength and the penetration depth of the probe [17]. A bigger electrode size provides a deeper penetration depth; however, it reduces the image resolution in imaging applications since it samples a bigger area of the specimen. The shape of electrodes can be a simple form such as square, rectangular, triangular shape, or complex shape, like a comb or spiral shape. Free space width between adjacent electrodes refers to the separation distance between the electrodes and has a significant impact on the measured output. Therefore, the geometry of the electrode influences the sensor performance in signal strength, depth of penetration and sensitivity of the measurement and need to be optimized and selected with care [9, 18].

2.2 NUMBER OF ELECTRODE AND THEIR ARRANGEMENT

The number of electrodes proper to a given application depends on the geometry of the sample and its physical parameter. For some applications, such as proximity or displacement measurement, in which there is a direct relationship between capacitance measurements and the distance of a specimen, a single sensing element, like an annular sensor is often enough to infer the proximity of the specimen from capacitance measurement. For more complex situations, such as imaging or NDT applications, an array of electrodes would be more adequate. In addition, the arrangement of the electrodes and the available space in the system to place the electrodes must be considered [9, 16].

2.3 SHIELDING AND GUARDING

Generally, a shielding plate and a guard electrode are employed to shape the electric field, and more importantly to eliminate stray capacitance and noise [17]. Indeed, a shielding plate, which is placed on top of the main electrodes, is needed to attenuate the undesirable electric field, to eliminate parasitic capacitance and noise in the sensing electrodes; and a guard electrode, which surrounds the main electrodes and between them, will be used to prevent the electric field lines to go directly to the sensing electrode. In this way, they have to travel further into the specimen to reach the sensing electrode, thus, the penetration depth will increase as shown in Figure 2. Usually, the shielding plate and guard electrode are held at ground potential and different types of them can be used depending on the capacitor measurement circuit [18].

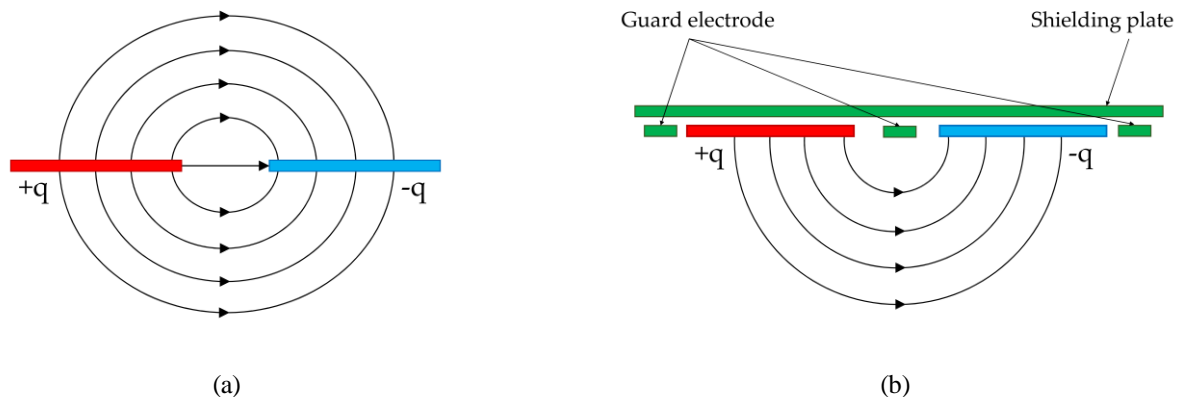(a)   (b)

Fig. 2 Schematic diagrams for capacitive probe with and without shielding plate and guard electrodes: (a) Cross-section of the capacitive probe without shielding plate and guard electrodes and (b) Cross-section of the capacitive probe with shielding plate and guard electrodes.

3. THE PENETRATION DEPTH OF THE CAPACITIVE TECHNIQUE

For a planar capacitance sensor, the penetration depth can be defined as the maximum distance in the vertical direction to the electrodes that produces a detectable change in the sensor output. It is an important parameter to assess the sensor performance because it indicates how far the sensor can sense [19]. The penetration depth is determined by the material properties (such as permittivity), the noise level of the equipment, and the electrode geometry (shape, size, and arrangement) [9, 18]. The material permittivity has certainly an important impact on the penetration depth, the higher the permittivity the faster the decay of the electric field. However, the primary factor having an influence on the penetration depth of a given material is the geometry of the driving and sensing electrodes. In the case of co-planar capacitive sensors, penetration depth determination is difficult due to the complexity of the fringing electric field and the variety of the probe geometry. A practical and straightforward manner to determine the effective penetration depth of the capacitive sensor is to place the probe over the inspected specimen and gradually move it away from its surface while measuring the capacitance between driving and sensing electrodes [9]. This technique is different from those used for eddy currents, where the depth of penetration can be controlled by varying the frequency while the penetration depth of capacitive probes mainly depends on the probe geometry and properties of the specimen [18].

4. NUMERICAL SIMULATION AND EXPERIMENTAL WORK

The capacitive probe is the key part of the instrumentation and requires to be designed carefully. For sensors with a constant overall electrode area, the penetration depth increases with the distance between the electrodes. A larger distance between electrodes will however decrease the signal strength (the measured output) as the coupling between the driving and sensing electrodes would be weaker and would reduce the image resolution as they are sampling a larger area of the sample and more importantly it is physically disallowed if the overall probe size is constant. Triangular electrodes can be applied to balance these trade-offs [20]. This electrode geometry is an interesting choice for many situations as it would likely allow deep penetration into the material being tested, with a symmetrical electric field distribution. As stated in the previous section, the electric field distribution is a function of the electrode geometry and so this aspect has to be designed with care [5]. The co-planar electrodes with the same overall sensing areas are used in this work, as shown in Figure 3, namely capacitive probes with back-to-back triangular electrodes. Generally, this pair of triangular electrodes could be specified by the overall size, the base (b), the height (h) of each triangle and the separation distance between the closest points of the two triangles (s). In this work, the triangular electrodes have the same overall size with b = 15.0 mm, h = 15.0 mm and s = 4.0 mm. In addition, a shielding plate and guard electrode are employed for this co-planar capacitive sensor. Note that the field distribution predicted by the Finite Element (FE) model, as discussed below, is determined primarily by these geometric factors in the model.

4.1 NUMERICAL SIMULATION

Conceptually, the capacitive method is straightforward. The electrodes provide an electric field distribution when an AC voltage is applied between the driving and sensing electrodes. The presence of the specimen and any variation in its properties (such as the presence of a defect) within the area covered by the electric field will change the field pattern distribution. A distortion in the electric field causes a change in the charge induced in the sensing electrode, and this change in the charge can be used for defect detection purposes [7]. The resulting signal is sent to standard instruments such as charge amplifiers that increase the signal-to-noise ratio (SNR) and allow small changes in the signal to be recorded, processed and outputted as a DC voltage. Since the presence of delaminations, cracks and other imperfections changes the electric field distribution in various distinctive ways, a basis for detecting defects can be established [5].

(a)   (b)

Fig. 3 (a) Photograph of the pair of triangular electrodes and (b) Diagram of the capacitive sensor as viewed from the top surface.
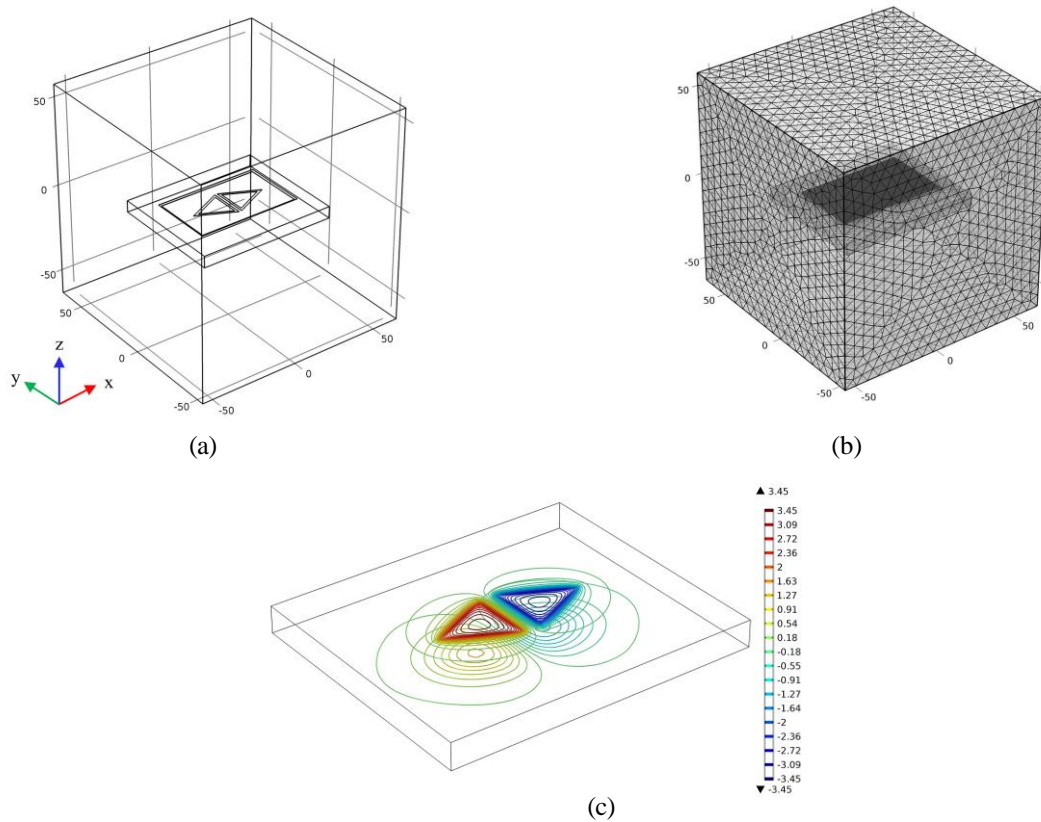
(a)

(b)

(c)

Fig. 4 3D model of the finite element modelling: (a) the computational domain (120 mm × 120 mm × 120 mm) with a co-planar capacitive probe, (b) model after finite element mesh generation, and (c) The electric potential contour lines on the surface of the sound specimen.

In order to understand the way electric field distributions are produced by the electrodes, and to identify how they may interact with the materials of interest, it was felt important to model the expected behavior. In this paper, we want to demonstrate the distribution of the electric field and how changes in the specimen might affect the output. Finite Element (FE) modelling enables valuable information (such as visualization of the results) to towards analyzing the performance of the capacitive sensor more easily. Although finite element methods are well established in engineering calculation, care must be taken to secure suitable mesh densities in critical regions, in particular near to the source of field singularities [21]. The major source of errors is the discretization processes of the conductor segments bordering different dielectrics and of the dielectric interfaces. However, there is no need to do the complicated mathematical process in order to simulate the defects in the samples in the finite element method. This is a useful tool for predicting the fields from capacitive electrodes and how these fields are likely to interact with different materials and defects [5, 22]. Therefore, Finite Element (FE) modelling has been employed to predict the distribution of the electric field from capacitive electrodes and signal changes that are likely to be generated under experimental conditions.

Theoretical simulation models were constructed using COMSOL™ Multiphysics FE package, which can be used to model the predictions of the electric field distribution in different situations. The purpose of this analysis is to observe the field distribution and the variation of electric field strength as a function of the sample properties such as existing defects and depths of a defect. The electric field distribution for all situations has been analyzed using a three-dimensional (3D) finite element method.

In this model, the driving and sensing electrode were driven by a 5.0 V and − 5.0 V, respectively, with a 100 kHz sinusoidal signal. The shielding plate and guard electrode were set to ground potential. Based on this, there is an electric field between the positive and negative electrodes and the electric field distribution is formed in the local region in the specimen under the electrode pair and the lift-off between the sample and probe. A pair of a co-planar triangular electrode is placed above the surface of a specimen, and the setup is enclosed in a 120 mm × 120 mm × 120 mm block centred at the point ($x = 0$, $y = 0$, $z = 0$). This block was defined to be the computational domain, as shown in Figure 4 (a). A physics-controlled mesh was used and the mesh generation density is set to "Finer". Providing the environment and necessary system parameters the mesh is generated in the model as shown in Figure 4 (b). Figure 4 (c) shows the solved back-to-back triangular capacitive sensor model for a sound specimen. The contour lines on top of the specimen represent electric potential values.
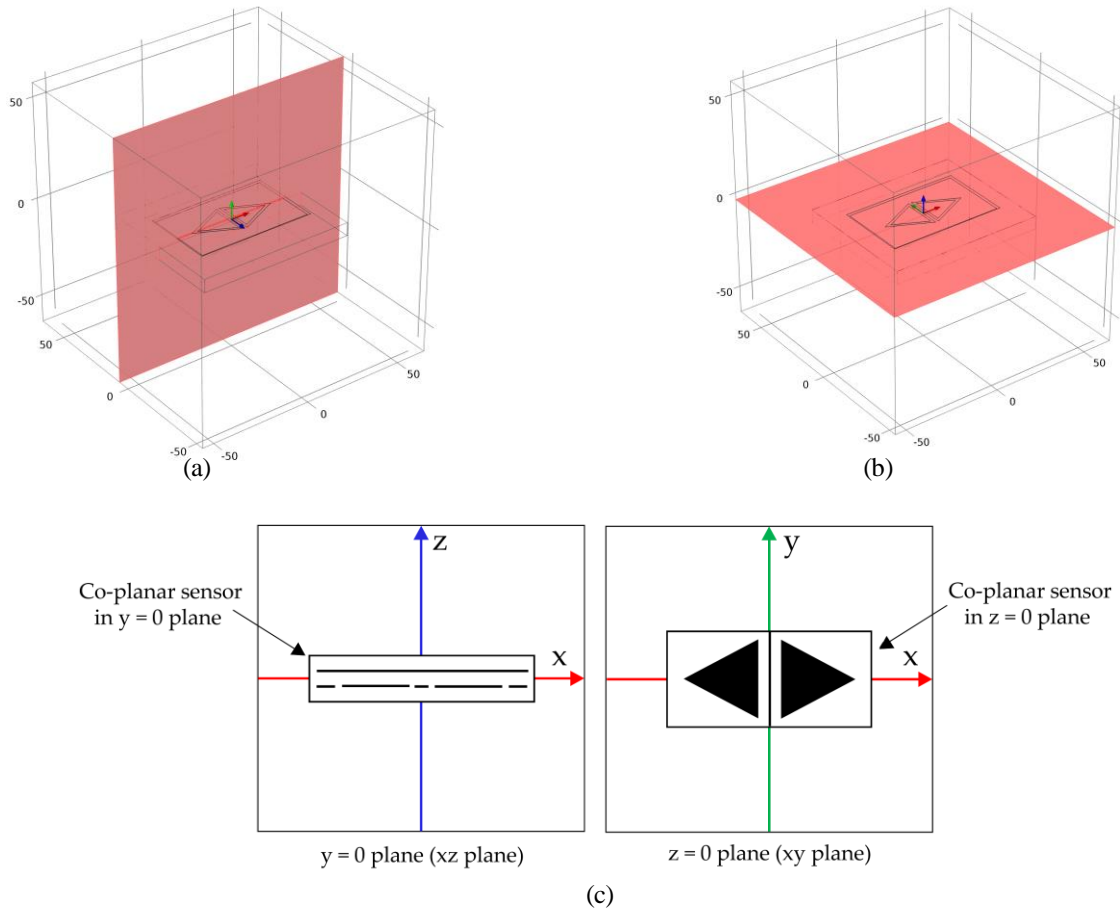
Fig. 5 The cross-sectional plane along the long axis of symmetry of the capacitive probe: (a) $y = 0$ plane (xz plane), (b) $z = 0$ plane (xy plane), and (c) plane coordinate systems for the two kinds of cross sections.

In the coordinate system illustrated in Figure 5, based on which the results will be presented hereafter, the probe surface is centred at ($y = 0$ or $z = 0$). $Y = 0$ plane (or xz plane) is the cross-sectional plane along the long axis of symmetry of the capacitive probe, as shown in Figure 5 (a), and $z = 0$ plane (or xy plane) is the parallel plane under the probe surface at the sample surface, as shown in Figure b. To clarify the results, the plane coordinate systems for the two kinds of cross-sections are shown in Figure c.

Figure 6 shows a sample of the electric field distribution prediction of the 3D finite element models for the co-planar capacitive electrodes and how these fields behave under different conditions. This figure is a contour plot of the electric field in the $y = 0$ plane. Figure 6 (a) shows this example for a sound zone of a specimen, Figure 6 (b) shows a sample of output for a defective zone filled with air, and Figure 6 (c) shows the electric field distribution for a specimen with a narrow crack on the surface. It can be seen that the presence of defects distorts the electric field within and around the regions of discontinuity in the sample and this leads to a variation in the detectable signal on the sensing electrode. This is because of the different dielectric properties such as permittivity (or dielectric constant) presumed for the sample and defects. Therefore, the model shows how the capacitive sensor detects the defects due to the different dielectric properties between the sample and defect.

Simulations were conducted to determine the effect of various depths of sub-surface defects on the electric field strength. The real non-conducting sample, a Plexiglas plate containing three sub-surface air-filled cylindrical voids at different depths, was simulated. Figure 7 shows a surface plot of the electric field of the back-to-back triangular electrodes for the different defect depth in the $z = 0$ planes, including Figure 7 (a) a sound sample, (b) a defect in 0.5 mm depth, (c) a defect in 1.0 mm depth, and (d) a defect in 1.5 mm depth. By comparing the results, it can be inferred the presence of the air-filled defect at different depths causes a different distortion of the electric field and this would lead to a detectable change in the output. This is caused by the different values of permittivity (or dielectric constant) assumed for the solid sample (Plexiglas, permittivity = 3.4) and air (permittivity = 1.0). Thus, the model shows how the capacitive probe detects sub-surface defects due to a permittivity difference between the sample and defect.

It is obvious from these results that the electric field strength decreases as the depth of the defect increases. In other words, the penetration depth and strength of the electric field vary for different depths of the defect. This is confirmed by the experimental
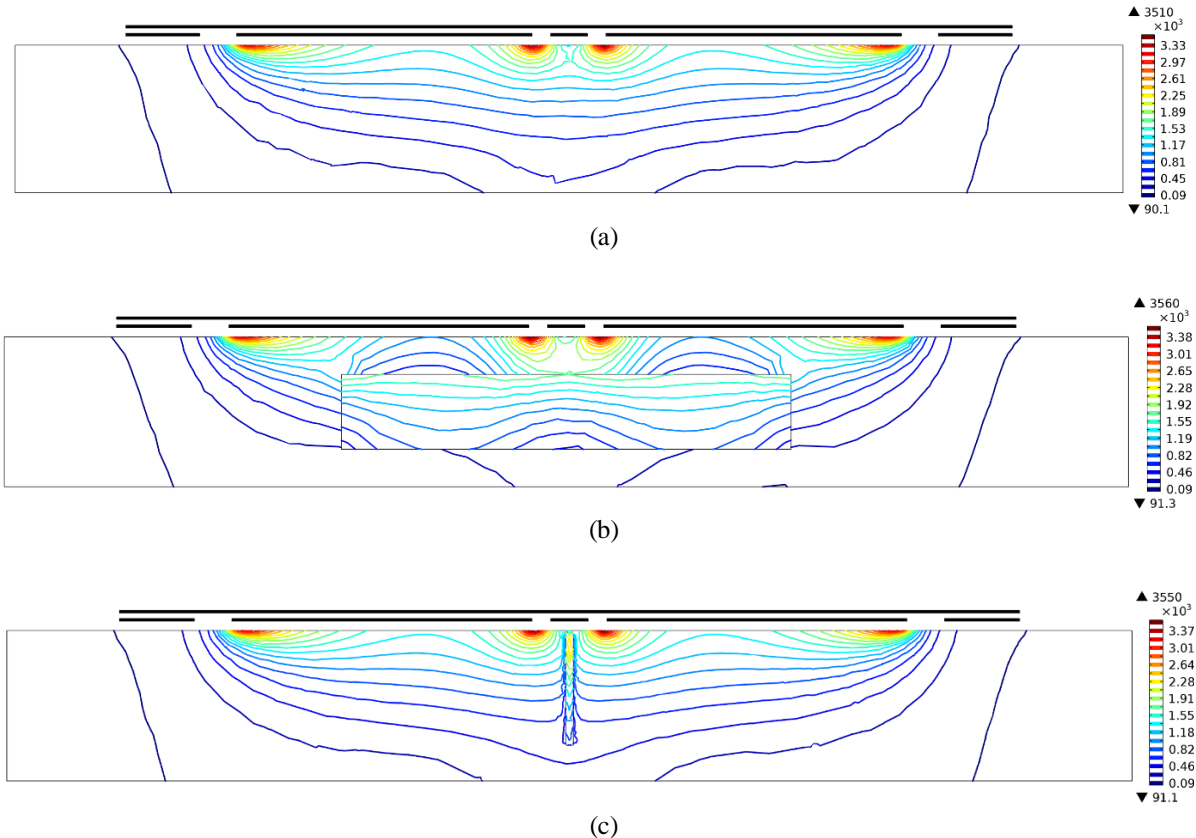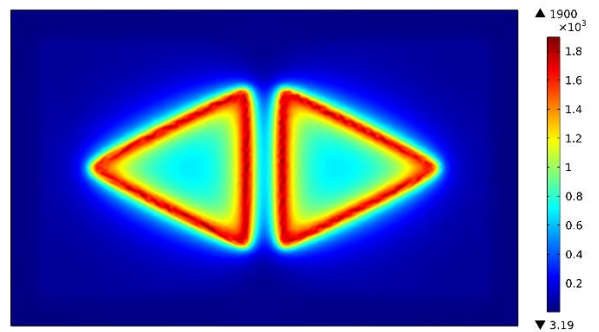
(a)

(b)

(c)

Fig. 6 Simulations of the electric field distribution (V/m) for a sample in \emph{y} = 0 plane: (a) no defect, (b) void under the surface, and (c) a sample with a narrow crack on the surface.

result to be shown later in this work. Moreover, these figures show that different depths of a defect create a different electric field pattern which can be used to estimate the defect depth.

4.2 EXPERIMENTAL RESULTS

Figure 8 illustrates the experimental arrangement used for the capacitive technique experiments presented in this work. The experiments use a capacitance set-up that is composed of a single pair of back-to-back triangular electrodes made of copper plates as shown in Figure 3. A shielding plate is placed on its top side to ensure that the radiated electric field emanates predominantly in the direction towards the specimen and to provide protection against the effect of the ambient stray fields on the output results. In addition, a guard electrode is applied to increase the penetration depth of the sensor. One of the electrodes is used as a driver electrode and the other one as a receiver. To generate an electric field, one of the plates is employed as a transmitter and connected to Ectane. Ectane is a multi-technology, powerful and compact instrument for generating and analyzing signals. The frequency range of this instrument is 5 Hz up to 10 MHz and the generator output is up to 20 V, peak to peak. A differential amplifier is placed inside Ectane to process the received signal successively. The output signal from the Ectane is a simple DC voltage level that is proportional to the instantaneous value of the dielectric property of the material averaged over the field distribution within the material.

The hidden depth of the defect is also a factor affecting the co-planar capacitive sensor performance. To investigate the effects of it in non-conducting specimens, a set of experiments were carried out on a 6.5 mm thick Plexiglas plate. The plate contains three sub-surface defects of 12 mm diameter located at different depths (0.5 mm, 1.0 mm, and 1.5 mm). Figure 9 (a) illustrates the schematic diagram of the sample. The co-planar CI probe was scanned over the Face (A) (the face without the defects) using a two-axis scanning system (*x-y* table). In this scan, the co-planar capacitive sensor was held 1.0 mm off the surface of the specimen

(a)
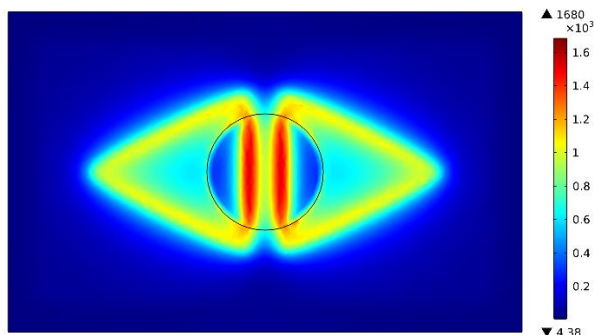
(b)
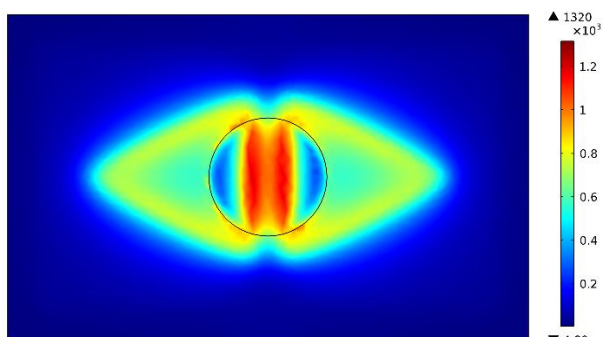
(c)

(d)

Fig. 7 Simulations of the electric field distribution (V/m) for a sample in \emph{z} = 0 plane: (a) no defect, (b) a defect at 0.5 mm depth, (c) a defect at 1.0 mm depth, and (d) a defect at 1.5 mm depth.

(a constant lift-off = 1.0 mm) and scanned over a 40 mm × 160 mm area with a 0.2 mm step in the *x*-axis and 1.0 mm in the *y*-axis. The speed of the probe was set to 10 mm/s.

Figure 9 (b) is the image obtained by scanning the co-planar capacitive sensor over the surface of the Plexiglas sample. The technique easily detected these defects,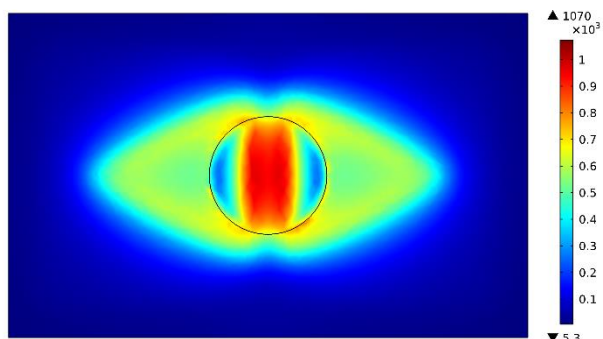 and this is due to the different dielectric properties between the material of the specimen (Plexiglas) and the defect (air). It can be seen from the result, the defect at 0.5 mm depth, which is the shallowest defect in the Plexiglas specimen, appeared as a darker colour, especially a darker red colour which is representing the highest output voltage in this result. Likewise, the other two defects appeared as a lighter area, depending on their depth representing lower output voltage values. This result is in good qualitative agreement with the result of the simulations as seen in Figure 7.
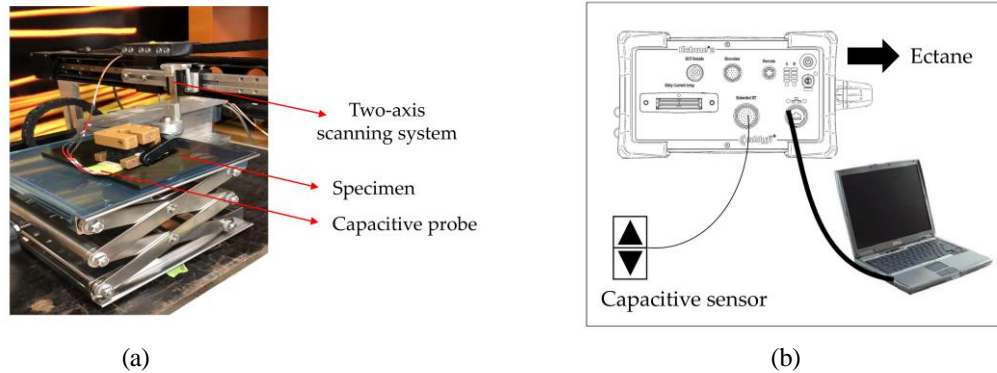

(a)

(b)

Fig. 8 (a) The experimental arrangement used for the capacitive imaging and (b) typical configuration: Ectane with the capacitive sensor.
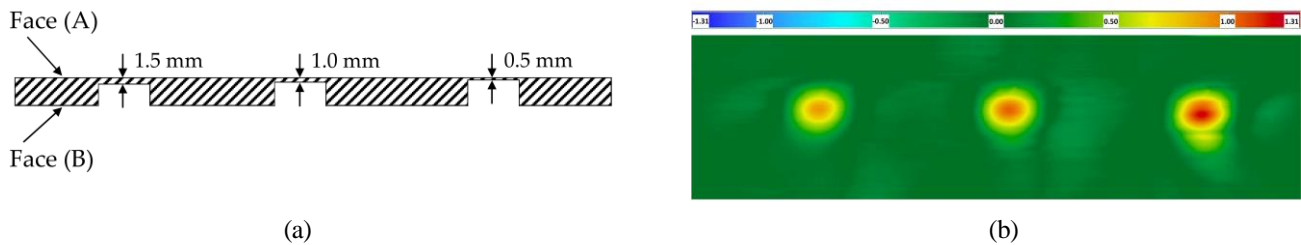

(a)

(b)

Fig. 8 (a) Diagram of the Plexiglas specimen with three holes of different depths and (b) the capacitive image based on voltage values. In this image obtained from the scanning of the probe on the specimen, the striking feature is the red and yellow area, which suggests the successful detection of the defects. It can be seen that the colour of the defect-free area is green. (The reflection on the third right-most defect is because of the mechanical adjustment.)

It can be inferred that when a specimen is placed under the co-planar capacitive electrodes, most of the electric field from the sensor penetrates into the specimen and then ends on the sensing electrode. The dielectric properties of the specimen and defects influence the electric field distribution and, hence, on the electric potential of the sensing electrode. Therefore, an existing defect in the specimen will change the electric field pattern, which leads to the changing in the detectable signal of the sensing electrode. It is worth mentioning the penetration depth is determined mainly by the probe geometry, the electric properties of the specimen and the lift-off.

5. CONCLUSION

A feasibility study of the co-planar capacitive sensing technique which has certain advantages for NDT applications was explored through a numerical simulation and experimental tests. Numerical Finite Element (FE) analysis was conducted to demonstrate the validity of the proposed defect detection technique. The 3D FE modelling has indicated that the electric field distribution of a selected electrode pair can penetrate into dielectric materials and can be used to detect the presence of defects in the form of air voids and crack. The preliminary investigation into the appliance of capacitive sensing for the detection of hidden holes within the specimen has been successfully shown. Experimental results on the Plexiglas plate containing sub-surface holes of various depths gave a sign of the response of the technique. A good qualitative agreement was observed between the experimental and simulations

result. The results obtained by the co-planar capacitive method illustrate that the technique is non-contact, non-invasive, and only requires single-sided access to the specimen. The couplant such as gel or water is not required, and there is no need for specific surface preparation. In addition, there are no radiation exposure problems. Therefore, this technique has the potential to be used in many NDT application areas where traditional methods may have difficulty.

In practice, the condition is typically more complicated compared to the sample inspected during this work. Defect specifications will be unknown, and voids could also be poorly defined. Further development of the capacitive probe is needed to meet different practical requirements and provide enhanced diagnostic information, e.g. systematic identification and characterization of defects. It should be emphasized that the depth of the penetration is mainly determined by the probe geometry, the electric properties of the specimen and the lift-off distance between the surface of the probe and the specimen, this will be further studied in future work.

AUTHOR CONTRIBUTION

FUNDING

ACKNOWLEDGMENT

REFERENCES

[1] S. Gholizadeh, "A review of non-destructive testing methods of composite materials," *Procedia Structural Integrity,* vol. 1, p. 50–57, 2016.

[2] T. Chen, "Capacitive sensors for measuring complex permittivity of planar and cylindrical structures," 2012.

[3] A. A. Nassr, W. H. Ahmed and W. W. El-Dakhakhni, "Coplanar capacitance sensors for detecting water intrusion in composite structures," *Measurement science and technology,* vol. 19, p. 075702, 2008.

[4] Z. Liu and H. Liu, "Experimenting capacitive sensing technique for structural integrity assessment," in *2017 IEEE International Conference on Industrial Technology (ICIT)*, 2017.

[5] X. Yin, G. G. Diamond and D. A. Hutchins, "Further investigations into capacitive imaging for NDE," *Insight-Non-Destructive Testing and Condition Monitoring,* vol. 51, p. 484–490, 2009.

[6] G. G. Diamond and D. A. Hutchins, "A new capacitive imaging technique for NDT," in *Proceedings of European Conference on NDT*, 2006.

[7] X. Yin and D. A. Hutchins, "Non-destructive evaluation of composite materials using a capacitive imaging technique," *Composites Part B: Engineering,* vol. 43, p. 1282–1292, 2012.

[8] A. V. Mamishev, K. Sundara-Rajan, F. Yang, Y. Du and M. Zahn, "Interdigital sensors and transducers," *Proceedings of the IEEE,* vol. 92, p. 808–845, 2004.

[9] X. Hu and W. Yang, "Planar capacitive sensors–designs and applications," *Sensor Review,* 2010.

[10] X. Yin, D. A. Hutchins, G. Chen and W. Li, "Detecting surface features on conducting specimens through an insulation layer using a capacitive imaging technique," *NDT & E International,* vol. 52, p. 157–166, 2012.

[11] D. Sharma, S. Goyal, R. Khanna and A. Mukherjee, "Non-destructive testing of materials using capacitive sensing technique," *MIT International Journal of Electronics and Communication Engineering,* vol. 1, p. 73–77, 2011.

[12] B. Cheng, "Security imaging devices with planar capacitance sensor arrays," 2008.

[13] X. Dérobert, J. Iaquinta, G. Klysz and J.-P. Balayssac, "Use of capacitive and GPR techniques for the non-destructive evaluation of cover concrete," *Ndt & E International,* vol. 41, p. 44–52, 2008.

[14] X. Yin, C. Li, Z. Li, W. Li and G. Chen, "Lift-off effect for capacitive imaging sensors," *Sensors,* vol. 18, p. 4286, 2018.

[15] Z. Chen and R. C. Luo, "Design and implementation of capacitive proximity sensor using microelectromechanical systems technology," *IEEE Transactions on Industrial Electronics,* vol. 45, p. 886–894, 1998.

[16] X. Yin, G. Chen, W. Li and D. A. Huthchins, "Design and characterization of planar capacitive imaging probe based on the measurement sensitivity distribution," in *AIP Conference Proceedings*, 2013.

[17] X. B. Li, S. D. Larson, A. S. Zyuzin and A. V. Mamishev, "Design principles for multichannel fringing electric field sensors," *IEEE Sensors Journal,* vol. 6, p. 434–440, 2006.

[18] X. Yin, D. A. Hutchins, G. Chen and W. Li, "Preliminary studies on the design principles of capacitive imaging probes for non-destructive evaluation," *International Journal of Applied Electromagnetics and Mechanics,* vol. 42, p. 447–470, 2013.

[19] D. Chen, X. Hu and W. Yang, "Design of a security screening system with a capacitance sensor matrix operating in single-electrode mode," *Measurement Science and Technology,* vol. 22, p. 114026, 2011.

[20] X. Yin, D. A. Hutchins, G. Chen, W. Li and Z. Xu, "Studies of the factors influencing the imaging performance of the capacitive imaging technique," *Ndt & E International,* vol. 60, p. 1–10, 2013.

[21] E. Costamagna and P. Di Barba, "Inhomogeneous dielectrics: conformal mapping and finite-element models," *Open Physics,* vol. 15, p. 839–844, 2017.

[22] G. Meng, A. J. Jaworski and J. C. S. Kimber, "A multi-electrode capacitance probe for phase detection in oil–water separation processes: design, modelling and validation," *Measurement Science and Technology,* vol. 17, p. 881, 2006.

CNN FOR RIPENESS CLASSFICATION OF WATERMELON FRUITS BASED ON ACOUSTIC TESTING

Dominique Albert-Weiß[1*], Egla Hajdini[1], Matthias Heinrich[2], Ahmad Osman[2]

[1]University of Applied Sciences, htw saar, Goebenstrasse 40, 66117 Saarbruecken, Germany
[2]Fraunhofer Institute for Nondestructive Testing IZFP, Campus E3 1, 66123 Saarbrücken, Germany

[*]Corresponding Author: d.albert-weiss@htwsaar.de

ABSTRACT

A pivotal topic in food science and monitoring is the assessment of the quality and ripeness of agricultural products by using nondestructive testing techniques. However, these statistical methods do not provide a sufficient method as they do not reflect the complexity when working with natural products. While deep learning has earned high acknowledgement by surpassing state-of-the-art benchmarks, it has only gained interest in the application of nondestructive testing within the recent years. For this, the rise in popularity of deep learning can largely been drawn back to learning the representation of the data by extracting features within the latent space which cannot be determined in a direct manner. In this paper, we study the change in ripeness and shelf life of watermelon fruits by applying deep learning to acoustic data based on acoustic resonance testing. We describe the architecture of a deep convolutional neural network that classifies between ripe and overripe watermelon fruits. The neural network was trained based on acoustic information of the spectral domain as well as on morphologic and experiment-based features.

KEYWORDS: Convolutional Neural Networks, acoustic resonance testing, food monitoring

1. INTRODUCTION

With increasing need for sustainability in food monitoring and quality inspection, the assessment of agricultural commodities by non-destructive testing has gained in valuable interest. The examination of the fruit ripeness is specifically a concern in regard to fruits with thick rind where the state of the fruit is not directly discernible by visual inspection [1]. While technologies such as visible (VIS) and near infrared (NIR) spectroscopy have been related to biochemical traits [2] [3] [4], acoustic resonance testing is used as a reference for determining the material stiffness by studying the natural resonance frequencies based on vibrational properties [5]. For this the object is excited by a short hammer impact, providing a spectrum of frequencies reflecting its resonance behavior. While it classically has been used to detect voids and cracks within the specimen tested, an adaption to fruits may be reasonable when taking into regard that the microstructure and density change within the life span of a fruit. The acoustic response can, thus, be treated as an acoustic fingerprint of the fruit whose resonance frequency is changing within the shelf life of the agricultural good [6].

While acoustic resonance testing is sensitive to morphological changes, deep learning methods have proven to compensate this problem when trying to detect the ripeness of agricultural products by providing the neural network with a large amount of data allowing for better generalization [7]. With this in mind, deep neural networks are ideally suited for the inspection of agricultural goods where numerous parameter change within a fruit's life cycle while simultaneously showing a wide range of product heterogeneity. We thus provide a CNN architecture that allows for binary classifying the fruit ripeness of watermelon. For this, the acoustic data is transferred into the frequency domain. After learning low-level features in the spectral domain these are concatenated with morphological and measurement-specific parameters. To get a better understanding of the neural architecture, we refer to Fig. 1.
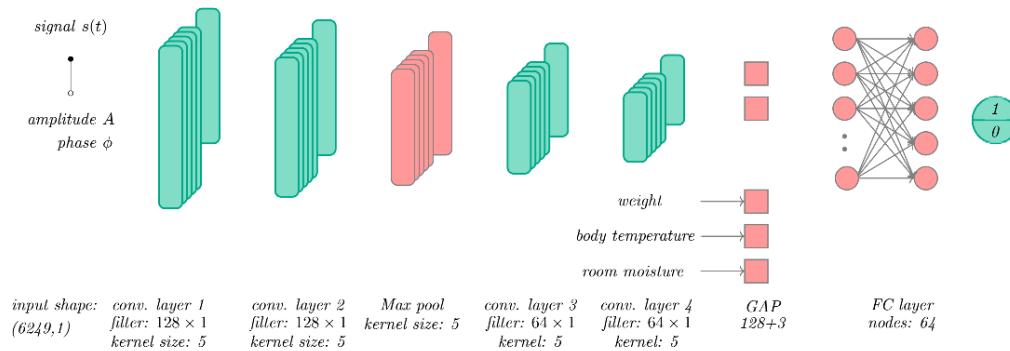
signal $s(t)$

amplitude A
phase ϕ

weight
body temperature
room moisture

input shape:	conv. layer 1	conv. layer 2	Max pool	conv. layer 3	conv. layer 4	GAP	FC layer
(6249,1)	filter: 128 × 1	filter: 128 × 1	kernel size: 5	filter: 64 × 1	filter: 64 × 1	128+3	nodes: 64
	kernel size: 5	kernel size: 5		kernel: 5	kernel: 5		

Fig. 1 Architecture of the Convolutional Neural Network

2. RESULTS ON NEURAL ARCHITECTURE

Deep Learning revolutionized data processing by allowing to validate and discover entangled structures based on their raw data inputs. One hallmark of deep learning is its ability to operate as function approximator based on a cascade of multiple nonlinear differentiable transforms. Furthermore, the success can be allocated to its data-driven approach where additional feature engineering avoided, specifically of interest when it is not clear what to search for. The most common approach in deep learning for classification is based on supervised learning, where the training process builds upon a known mapping between input and label output [8]. During training an objective function is optimized by computing the error measure between the predictive score and the ground truth. This is achieved based on backpropagating through the neural network by adjusting the training weights.

Convolutional neural networks (CNN), originally inspired by the experiments of the visual cortex of cats, has recently experienced a rise of interest due to the efficiency in image-related tasks. CNNs are specifically designed for processing data that happened to have a discrete topology. While the feed-forward network does not consider the structural properties of the input, convolutional neural network (CNN) allow to further constrain the architecture by a convolutional operation. This leads to a reduced number of parameters required which derives by the sparsity constrains wrapped upon on the weight matrix [40] [41].

The training process of the neural network is based on the acoustic information in the frequency domain containing both amplitude and phase information as input. Furthermore, the weight of the fruit as well as the body temperature and the room moisture where considered by passing it into the GAP layer with the compressed features of the amplitude and phase signal. The training was executed at a learning rate of 0.001. The activation function used throughout the network was the rectified linear function (ReLu). The binary classification was obtained based on binary cross-entropy at the dense layer. The model was trained with a 70-30 split at a batch size of 128 for 100 epochs while the learning rate was chosen to be 0.001. A visualization of the learning curves of the loss and accuracy evolving with each epoch can be found within the Fig. 2.
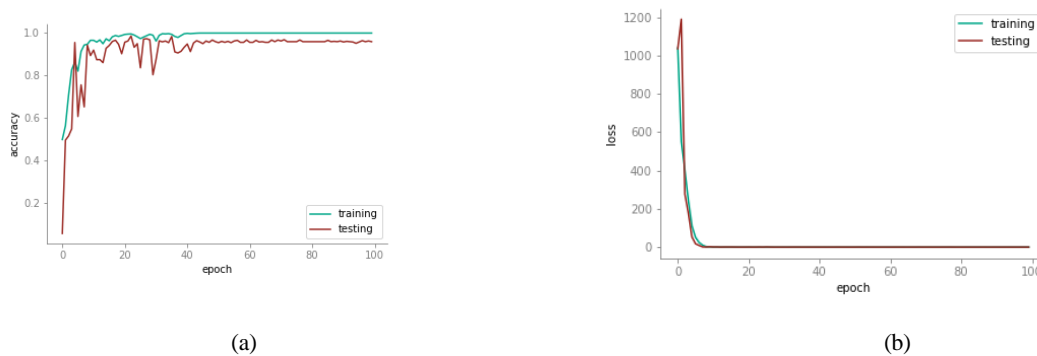

(a)

(b)

Fig. 2 Training curves of the CNN for the (a) accuracy and (b) loss over 100 epochs

REFERENCES

[1] E. Arendse, O. A. Fawole, L. S. Magwaza and U. L. Opara, "Non-destructive prediction of internal and external quality attributes of fruit with thick rind: A review," *Journal of Food Engineering,* vol. 217, p. 11–23, 2018.

[2] L. E. Rodriguez-Saona, F. S. Fry, M. A. McLaughlin and E. M. Calvey, "Rapid analysis of sugars in fruit juices by FT-NIR spectroscopy," *Carbohydrate Research,* vol. 336, no. 1, p. 63–74, 2001.

[3] B. M. Nicolaï, K. Beullens, E. Bobelyn, A. Peirs, W. Saeys, K. I. Theron and J. Lammertyn, "Nondestructive measurement of fruit and vegetable quality by means of NIR spectroscopy: A review," *Postharvest Biology and Technology,* vol. 46, no. 2, p. 99–118, 2007.

[4] L. S. O. U. L. N. H. C. P. J. R. Magwaza, S. Wouter and B. Nicolaï, "NIR Spectroscopy Applications for Internal and External Quality Analysis of Citrus Fruit - A Review," *Food Bioprocess Technol,* vol. 5, p. 425–444, 2012.

[5] W. Zhang, Z. Lv and S. Xiong, "Nondestructive quality evaluation of agro-products using acoustic vibration methods - A review," *Critical reviews in food science and nutrition ,* vol. 58, no. 14, pp. 2386-2397, 2014.

[6] E. Coffey, "Acoustic Resonance Testing," *2012 Future of Instrumentation International 08.10.2012 - 09.10.2012,* pp. 1-2, 2012.

[7] Y. LeCun, Y. Begio and G. Hinton, "Deep Learning," *Nature,* pp. 436-444, 2015.

[8] A. Krizhevsky, I. Sutskever and G. Hinton, "ImageNet Classification with Deep ConvolutionalNeural Networks," *Neural Information Processing Systems (NIPS),* 2012.

[9] A. Krizhevsky, I. Sutskever and G. E. Hinton, "ImageNet Classification with Deep Convolutional Neural Networks," *Conference on Neural Information Processing Systems (NIPS),* 2012.

[10] K. He, X. Zhang, S. Ren and J. Sun, "Deep residual learning for image recognition," *arXiv preprint arXiv:1512.03385,* 2015.

[11] D. K. H. Han and J. Kim, "Deep Pyramidal Residual Networks," *arXiv preprints arXiv:1610.02915,* 2017.

[12] X. Zhang, Z. Li, C. C. Loy and D. Lin, "PolyNet: A Pursuit of Structural Diversity in Very Deep Networks," *arXiv preprints arXiv: 1611.05725,* 2017.

[13] R. Moscetti, R. P. Haff, E. Stella, M. Contini, D. Monarca, M. Cecchini and R. Massantini, "Feasibility of NIR spectroscopy to detect olive fruit infested by Bactrocera oleae," *Postharvest Biology and Technology,* vol. 99, pp. 58-62, 2015.

[14] P. Fito, M. Ortolá, R. d. los Reyes, P. Fito and E. d. los Reyes, "Control of citrus surface drying by image analysis of infrared thermography," *Journal of Food Engineering,* vol. 61, no. 3, pp. 287-290, 2004.

[15] E. G. Barcelon, S. Tojo and K. Watanabe, "X-ray Computed Tomography for Internal Quality Evaluation of Peaches," *Journal of Agricultural Engineering Research,* vol. 73, no. 4, p. 323–330, 1999.

[16] P. Verboven, G. Kerckhofs, H. K. Mebatsion, Q. T. Ho, K. Temst, M. Wevers, P. Cloetens and B. M. Nicolaï, "Three-dimensional gas exchange pathways in pome fruit characterized by synchrotron x-ray computed tomography," *Plant physiology,* vol. 147, pp. 518-527, 2008.

[17] H. Kinjo, N. Oshiro and S. C. Duong, "Fruit maturity detection using neural network and an odor sensor: Toward a quick detection," *2015 10th Asian Control Conference (ASCC),* pp. 1-4, 2015.

[18] J. A. Abbott, "Quality measurement of fruits and vegetables," *Postharvest Biology and Technology,* vol. 15, pp. 207-225, 1999.

[19] P. Baranowski, W. Mazurek, B. Witkowska-Walczak and C. Sławiński, "Detection of early apple bruises using pulsed-phase thermography," *Postharvest Biology and Technology,* vol. 53, no. 3, p. 91–100, 2009.

[20] J. Wang, K. Nakano, S. Ohashi, K. Takizawa and J. G. He, "Comparison of different modes of visible and near-infrared spectroscopy for detecting internal insect infestation in jujubes," *Journal of Food Engineering,* vol. 101, no. 1, pp. 78-84, 2019.

[21] J. Hongwiangjan, A. Terdwongworakul and K. Krisanapook, "Evaluation of pomelo maturity based on acoustic response and peel properties," *Int. J. Food Sci, Tech.,* vol. 50, pp. 782-789, 2015.

[22] K. K. Vursavus, Y. B. Yurtlu, B. Diezma-Iglesias, L. Lleo-Garcia and M. Ruiz-Altisen, "Classification of the firmness of peaches by sensor fusion," *Int. J. Agr. Biol. Eng.,* vol. 8, pp. 104-115, 2015.

[23] J. Blahovec, S. Kuroki and N. Sakurai, "Cooking kinetics of potato tubers determined by vibration techniques," *Food Res. Int.,* vol. 40, pp. 576-584, 2007.

[24] S. Terasaki, N. S. N. M. N. Y. R. Wada and D. J. Nevins, "Nondestructive measurement of kiwifruit ripeness using a laser Doppler vibrometer," *T. ASAE,* vol. 44, pp. 81-87, 2001.

[25] R. Abbaszadeh and A. Y. Y. D. Rajabipour, "Nondestructive determination of watermelon flesh firmness by frequency response," *LWT-Food Sci. Technol.,* vol. 60, pp. 637-640.

[26] S. Terasaki, N. Sakurai, J. Zebrowski, H. Murayama, R. Yamamoto and D. J. Nevins, "Laser Doppler vibrometer analysis of changes in elastic properties of ripening 'La France' pears after postharvest storage," *Postharvest Biology and Technology,* vol. 42, no. 2, pp. 198-207, 2006.

[27] Z. Gao, Y. Shao, G. Xuan, Y. Wang, Y. Liu and X. Han, "Real-time hyperspectral imaging for the in-field estimation of strawberry ripeness with deep learning," *Artificial Intelligence in Agriculture,* vol. 4, pp. 31-38, 2020.

[28] L. Hou, Q. Wu, Q. Sun, H. Yang and P. Li, "Fruit recognition based on convolution neural network," *2016 12th International Conference on Natural Computation, Fuzzy Systems and Knowledge Discovery (ICNC-FSKD),* pp. 18-22, 2016.

[29] Y. Zhang, S. Wang, G. Ji and P. Phillips, "Fruit classification using computer vision and feedforward neural network," *Journal of Food Engineering,* p. 167–177, 2014.

[30] M. S. Hossain, M. Al-Hammadi and G. Muhammad, "Automatic Fruit Classification Using Deep Learning for Industrial Applications," *IEEE Trans. Ind. Inf. (IEEE Transactions on Industrial Informatics),* vol. 15, no. 2, pp. 1027-1034, 2019.

[31] G. Zeng, "Fruit and vegetables classification system using image saliency and convolutional neural network," *IEEE 3rd Information Technology and Mechatronics Engineering Conference (ITOEC),* 2017.

[32] J. Steinbrener, K. Posch and R. Leitner, "Hyperspectral fruit and vegetable classification using convolutional neural networks," *Comput. Electron. Agric.,* vol. 162, pp. 364-372, 2019.

[33] K.-J. Langenberg, R. Marklein and K. Mayer, Ultrasonic Nondestructive Testing of Materials, CRC Press, 2012.

[34] M. Taniwaki, M. Tohro and N. Sakurai, "Measurement of ripening speed and determination of the optimum ripeness of melons by a nondestructive acoustic vibration method," *Postharvest Biol. Tec.,* vol. 56, pp. 101-103, 2010.

[35] J. Ortiz-Viedma, A. Rodriguez, C. Vega, F. Osorio, B. Defillipi, R. Ferreira and J. Saavedra, "Textural, flow and viscoelastic properties of Hass avocado (Persea americana Mill.) during ripening under refrigeration conditions," *Journal of Food Engineering,* vol. 219, p. 62–70, 2018.

[36] K. O. I. J. C. Falade and F. A. Ayanwuyi, "Kinetics of mass transfer, and colour changes during osmotic dehydration of watermelon," *Journal of Food Engineering,* vol. 80, pp. 979-985, 2007.

[37] E. M. Yahia, Postharvest Biology and Technology of Tropical and Subtropical Fruits: Mangosteen to White Sapote, Kent: Elsevier Science, 2011.

[38] V. P. R. S. G. C. Paul, "The fading distinctions between classical patterns of ripening in climacteric and non-climacteric fruit and the ubiquity of ethylene-An overview," *Journal of food science and technology,* vol. 49, no. 1, pp. 1-21, 2012.

[39] M. Gipperich, M. Heinrich, U. W. T. Rabe and S. Nyga, "Untersuchung und Vergleich verschiedener berphrender und berührungsloser Methoden zur Schwingungsanregung bei der akustischen Resonanzanalyse," *Deutsche Gesellschaft für Akustik (DEGA),* pp. 964-967, 2019.

[40] Q. Nugyen, *Optimization Landscape of Deep Neural Networks, Dissertation,* Saarbrücken, 2019.

[41] I. Goodfellow, Y. Bengio and A. Courville, Deep Learning, MIT Press, 2016.

[42] Y. LeCun, L. Bottou, Y. Bengio and P. Haffner, "Gradient-based learning applied to document recognition," *Proceedings of the IEEE,* 1998.

[43] X. Glorot and Y. Bengio, "Understanding the difficulty of training deep feedforward neural networks," *AISTATS,* 2010.

[44] J. Steinbrene, K. Posch and R. Leitner, "Hyperspectral fruit and vegetable classification using convolutional neural networks," *Computers and Electronics in Agriculture,* vol. 162, pp. 364-372, 2019.

[45] Z. M. Khaing, Y. Naung and P. H. Htut, ""Development of control system for fruit classification based on convolutional neural network," 2018.

[46] M. S. A.-H. M. Hossain and G. Muhammad, "Automatic Fruit Classification Using Deep Learning for Industrial Applications," *IEEE Transactions on Industrial Informatics,* vol. 15, pp. 1027-1034, 2019.

[47] L. Hou.

[48] S. Nordiyana, M. Y. A. Salim, M. Shakaff, M. N. Ahmad and A. H. Adom, "Development of electronic nose for fruit ripeness determination".

OUTPUT-ONLY BRIDGE SCOUR MONITORING USING MEASURED VIBRATION

Esmaeil Ghorbani,[1] Dr. Dagmar Svecova,[1] Evangeline Murison,[2] Dr. Young-Jin Cha[1*]

[1] University of Manitoba, 15 Gillson St, Winnipeg, MB R3T 5V6, Canada
[2] Manitoba Infrastructure, 600-215 Garry Street, Winnipeg, MB R3C 3P3, Canada

[*]Corresponding Author: young.cha@umanitoba.ca

1. MOTIVATION AND DESCRIPTION

The excavation and removal of sediment around a bridge pier by the flowing water's erosive action are called bridge scour. Several studies have shown that the causes of more than 50% of bridge failures in the U.S. were due to flooding and scour. In addition to the loss of human life, economic losses and disruption in transportation systems are other significant issues that may arise because of bridge scour.

Visual inspection seems to be one intuitive method of monitoring scour at a bridge pier. However, accessibility to the pier foundation during the flood season and the backfilling of holes could prevent visual inspection and thus cause the scour monitoring process to be ineffective. Mounting different types of underwater sensors around the pier foundation could be another solution. These sensors can detect scour, but they are typically designed for one-time use only and must be replaced after each flood season; therefore, this method could be costly. Industrial companies are seeking techniques to account for these drawbacks and thus develop a more reliable scour monitoring technique.

Removal of sediments around a bridge pier affects the level of bridge pier vibration as a consequence of changes in the global stiffness of the bridge pier. Taking advantage of this fact, principles of vibration-based scour monitoring technique can be defined. Many studies have shown that scour decreases the natural frequency of a bridge pier. However, the majority of these studies have only been conducted on a laboratory scale. Also, such studies have typically only detected the occurrence of scour without presenting any information regarding the scour level.

Damage identification techniques are generally classified into three groups: data-driven, physics-model-based, and hybrid techniques. In data-driven approaches, data is used solely to infer the desired feature of the data as a damage indicator. These techniques can usually detect damage, but they are rarely able to localize or quantify the level of the damage. Model-based approaches are able to detect, localize, and quantify the detected damage using a physics-based computational model that is updated in a recursive process until the computational model response converges with the real system behavior. However, it is quite challenging to develop a fine-tuned model. Therefore, hybrid techniques were developed as a trade-off between model complexity and convergence of the model response with the real response. Hybrid techniques have the advantages of both model-based and data-based approaches for damage identification, which could be used for damage quantification as well. Damage quantification plays an essential role in reliability analyses of structures.

In the present study, a nonlinear Kalman filter was applied to the recorded vibration data from the top of a bridge pier. Kalman filtering is a model-based approach that requires a computational model to identify damage. River water, vehicular traffic, pedestrians, and wind are the main excitations that vibrate a bridge pier. Hence, including an excitation variable in the computation model would increase the uncertainty of the model, resulting in incorrect predictions. To avoid this issue, an output-only scour monitoring technique is proposed in the present study.

2. RELEVANT RESULTS

The present study included two parts. First, a simulation study was conducted in MATLAB. Then, an experimental test was conducted on an instrumented, in-service bridge in Manitoba. In the simulation study, an Euler beam model was developed considering river water and sediments around the pier as external effects (Fig. 1-a). This model showed how the sediments around the bridge pier would affect its global stiffness and vibration level. For scour monitoring, the system response was examined in a nonlinear Kalman filter benchmark to extract the stiffness (i.e., soil behavior) of the sediments around the pier. The robustness of the proposed approach was examined for different types of excitations and soils (i.e., soil behaviors). To evaluate the robustness of the proposed approach under different loading conditions and soil profiles, three different frequent occurrence loadings (white noise, ambient, and periodic excitations) were applied to the model simultaneously with three different profiles representing the soil behavior around the pier.
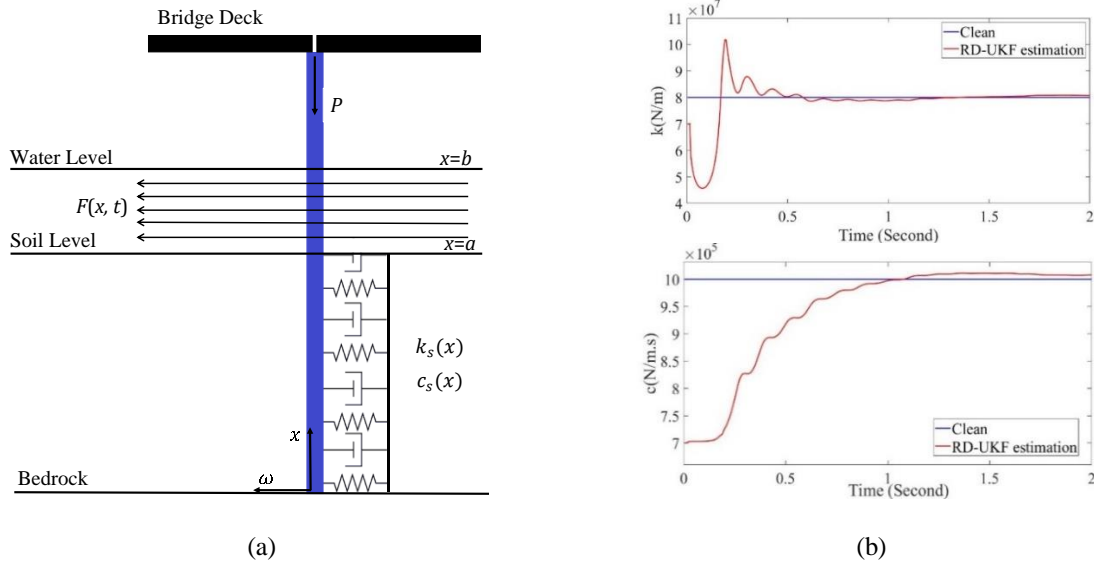
(a)   (b)

Fig. 1: (a) a simple schematic of the bridge pier, (b) the predicted stiffness and damping values of the soil around the bridge pier

Fig. 1-b shows the predicted stiffness value assuming a constant profile of soil stiffness. The stiffness profiles of other soil types are presented in the full paper context. In the next step of the study, a concrete pier of an existing in-service bridge in Manitoba was evaluated, taking the effects of the river water, vehicular traffic, and pedestrians into consideration. This bridge was instrumented in 2019 to record the acceleration of vibration at the top of two piers close to one of the girders (Fig. 2). Data is recorded on a bi-monthly schedule to track changes in the bridge pier's dynamic specification due to the scour of the soil around the pier foundation. The bridge was rehabilitated in 2015; there is a low probability of change or damage to other parameters.

(a) data accqusition   (b) the installed sensor   (c) the bridge view   (d)Pier 5 at Feburary

Fig. 2: A bridge instrumented in Manitoba

3. CONCLUSION

An output-only, model-based scour monitoring technique is presented in this study. A continuous Euler beam was developed as a bridge pier and used in the scour monitoring process with a nonlinear Kalman filter. The present study results showed that this technique is robust for different types of excitations and soil behaviors around the pier foundation. The results also confirmed that this technique is a viable method for predicting soil removal levels around the pier. Two sensors mounted on two piers of an in-service bridge in Manitoba prone to scour validated the simulation findings.

ADVANCED SIGNAL PROCESSING TECHNIQUES TO IMPROVE THE DETECTION OF DEFECTS IN PRESSURE VESSELS BY ACOUSTIC EMISSION TESTING

Konstantin Polyakov[1*], Fernando López[2], Martin Viens[1]

[1]École de technologie supérieure, 1100 Rue Notre-Dame Ouest, Montréal, QC, Canada ;
[2]TORNGATS Technical Services 5635 Rue Rideau, Québec, QC, Canada

*Corresponding Author: konstantin.polyakov.1@ens.etsmtl.ca

Acoustic emission testing is a well-known and versatile inspection method for structural health monitoring and non-destructive evaluation of several components found in the petrochemical industry, such as pressure vessels, pipelines and storage tanks. The sensitivity and reliability of the method is affected by spurious signals (background noise) from technological process or the environment. This paper presents current investigations aimed at developing and implementing an algorithm based on adaptive filtering with the purpose of minimizing the background noise impact. An experimental setup has been developed to simulate an acoustic emission testing of a component under stress. Adaptive filter algorithms have been implemented and tested for detecting and de-noising the AE signals obtained when the reference tests are subjected to mechanically-induced stress.

KEYWORDS: acoustic emission, signal processing, noise filtering

1. INTRODUCTION

Acoustic emission (AE) is a passive diagnostic method in which AE sensors detect the transient elastic waves radiated by a structure under operational stresses, allowing this way to localise and evaluate active defects such as cracks, leaks and other mechanical damages. Existing practices and instruments of AE require to use threshold data recordings aimed at minimizing the impact of the background noise in the final results, however is most cases this approach can not be implemented to the diagnostic of operating pressure vessels if the signal-to-noise ratio (SNR) is less than 1. Current advances in digital signal processing such as adaptive filtering hasn't been yet implemented in AE systems, but the interpretation and analysis of data under the presence of high amplitude noise have been widely studied in other fields that are related to the AE diagnostics of industrial components. This paper study the concepts found in seismic-acoustic emissions [1], and digital filtering noisy speech signals [2] in order to develop a robust methodology of signal processing when inspecting in-service pressure vessels.

2. PROPOSED APPROACH TO INVESTIGATE THE IMPLEMENTATION OF ADVANCED SIGNAL PROCESSING ON AE DATA

2.1 EXPERIMENTAL SETUP

An experimental setup (Fig.1, a) has been developed to simulate an acoustic emission testing on carbon steel plates subjected to mechanical stress. The specimens under investigations are made of grade 44W steel and thickness of 6.35, 12.7 and 15.875 mm. Furthermore, the plates present circular shape (420 mm diameter) in order to provide a more homogeneous stress distribution. The samples tests have defect irradiators such a notch aimed at simulating the growth of crack-like flaws.

The stress is been applied to the samples using a hydraulic cylinder with force capacity up to 117kN and powered by a manual pump. The force applied to the specimens is monitored and controlled by using a high accuracy load cell connected to a data acquisition card and digital meter and also by the readings of the manometer installed in the hydraulic system.

The rate of defect growth that takes place during the application of the stress is monitored by an eddy current probe connected to a data acquisition card. This approach allows the monitoring of the defect growth synchronized with other experimental parameters aimed at precisely selecting the acoustic emission signals inherent to the defect growth. The detection and registration of acoustic emission waves is made using wide band AE sensors and high-resolution data acquisition card. Raw data obtained from the experiments is recorded and analyzed via LabVIEW [3] while further signal processing is carried out using the Simulink toolbox of MATLAB.

2.2 PRINCIPES OF SIGNAL FILTERING

Adaptive filters (AF) are widely used in different fields of NDT&E mainly for the suppression of acoustic and electric noises. A usual scheme of the AF (Fig.1, b) has two inputs: a reference noise signal $n1$, not correlated with the desired/useful signal, s but directly correlated with the noise $n0$; and the combination of signals $s+n0$. The task of AF is to transform the input signal to maximally approximate it to the reference signal. Once the filtering process is carried out, an estimate of signal noise is obtained since the only noise component of the input signal is correlated with the reference signal. The subtraction of the error signal e from the input signal will yield the useful signal [4].

For the case of the non-destructive evaluation of pressure vessels, the AF uses single input scheme with blind adaptation algorithm. This input receives a mixture of noise and potential useful signal from the flaws present in the tested object. The principle of this filtration algorithm is that it uses a delayed input signal as a virtual reference of noise non-correlated with potential useful signal. The minimization of the error in determining the error signal is performed the least square algorithm. During the implementation of this approach firstly AE signals without applied noise have been obtained by the experimental setup and the signals are artificially contaminated by noised. To approximate the study to real conditions, the filtering process is the implemented to the AE signals from stressed test samples.

3. CONCLUSION

The present work will demonstrate that the acoustic emission testing of in-service equipment in highly noised environments can be possible without losing the useful signals. The results show the potential applicability of this approach for detecting acoustic emission signals from defects in pressure vessels with high level of background noise.

ACKNOWLEDGMENT

REFERENCES

1. Chebotareva, I.Ya., Structure and dynamics of a geomedium in noise seismic fields, the methods and experimental results, Yearbook of Russian Academy of Science, 12th edition, pp. 147–156, Moscow, Russia, 2011.
2. Borisagar, K.R., Thanki, R.M., Sedani, B.S., Speech Enhancement Techniques for Digital Hearing Aids. Cham: Springer International Publishing, 2019.
3. Martaj, N.; Mokhtari, M. Apprendre et maîtriser LabVIEW par ses applications; Springer Berlin Heidelberg: Berlin, Heidelberg, 2014.
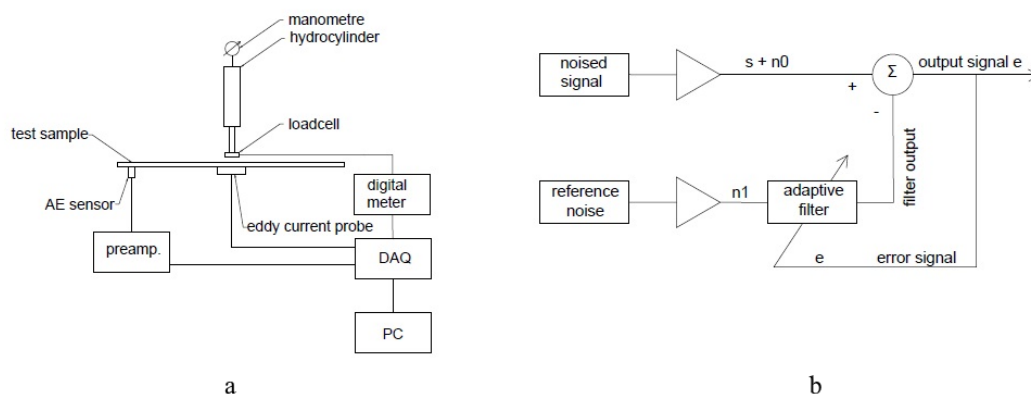4. Simon Haykin Adaptive filter theory; Upper Saddle River, New Jersey: Pearson; 2014.

Fig. 1 a) schema of experimental setup; b) schema of adaptive filter

A NOVEL DRONE-ENABLED APPROACH FOR GAS LEAK DETECTION USING THERMAL IMAGE FLOW ANALYSIS

Parham Nooralishahi[1*], Fernando Lopez[2], Xavier Maldague[1]

[1]Department of Electrical and Computer Engineering, Université Laval Quebec QC Canada
[2]TORNGATS Quebec QC Canada

*Corresponding Author: parham.nooralishahi.1@ulaval.ca

ABSTRACT

The recent development of gas imaging technologies has raised a growing interest for various applications. Gas imaging can significantly enhance functional safety by early detection of hazardous gas leaks. Moreover, optical gas imaging technologies can be used to identify possible gas leakages and to investigate the amount of gas emission in industrial sites, which is essential, primarily based on current efforts to decrease greenhouse gas emissions all around the world. Therefore, exploring the solutions for automating the inspection process can persuade industries for more regular tests and monitoring. One of the main challenges in gas imaging is the proximity condition required for data to be more reliable for analysis. Therefore, the use of unmanned aerial vehicles can be very advantageous as they can provide significant access due to their maneuver capabilities. Despite the advantages of using drones, their movements, and sudden motions during hovering can diminish data usability. In this paper, we propose a novel approach to localize the possible gas leak from an image stream collected by an aerial platform. The introduced solution localizes the areas that demonstrate a gas flow-like motion as well as the origin of gas emission using thermal image flow analysis. Moreover, we investigate the use of the phase correlation technique for the reduction of the effect of drone movement during the hovering. The significance of the results presented in this paper demonstrates the possible use of this approach in the industry.

KEYWORDS: Unmanned Aerial Vehicle, Optical Gas Imaging, Non-Destructive Test, Aerial Inspection, Thermography

1. INTRODUCTION

Thermal imaging cameras have already been used for decades for various applications in the petrochemical and oil and gas industries; the typical applications partly include thickness loss detection and the examination of pipe integrity. Despite all the development in non-destructive thermal inspection solutions, many challenges need to be addressed. Gas imaging is a relatively new area that investigates the use of thermal imaging technologies to observe gas emission, leakages, and even flows. The new Optical Gas Imaging technologies are developed to observe various types of gases, such as hydrocarbon gases and volatile organic compounds (VOCs). The analysis of gas emission can be very beneficial in many industries, such as chemical manufacturing or oil and gas. The early detection of many hazardous gases, for instance, VOCs or Methane, can increase the functional safety of the system and prevent any health risk for the personnel. Moreover, gas imaging can assist industries in reducing product loss as well as to meet regulatory emission reduction requirements by monitoring and detecting possible leakages in real-time.

Conventional inspection approaches for gas leak detection requires direct contact of inspectors with the environment. Due to the hazardous nature of these gases, an inspection of these sites can put the personnel at considerable health risk. Also, likely access constraints imposed by the conditions like height or temperature of an operating facility can make the inspection very challenging or even impossible. Therefore, using unmanned aerial vehicles for the inspections can decrease the risk as well as the cost and time of the operation. The maneuver capabilities provided by drones can assist inspectors better access to the facilities and reduce the inspection time, which can motivate the companies to perform them more regularly. Moreover, this approach minimizes the number of required staff on-site, which can also lead to cost- and time-saving.

In order to decrease the risks and potential product loss, industries rely on accurate and reliable reports and analyses prepared by experts for detecting the issues and maintain the systems. Therefore, providing the tools and automation processes can assist inspectors in providing more reliable analysis and reports with less human error in a more satisfying time frame.

In this paper, we introduced a drone-enabled solution for localizing the gas leak using thermal image flow analysis. One of the issues in the analysis of aerial thermal image streams is the rigid motion of UAVs even while hovering, which can diminish the usability of the recorded image streams. In this paper, we investigate the use of the phase correlation algorithm for minimizing the effect of the motions.

2. BRIEF SUMMARY OF THE PROPOSED METHOD

As discussed earlier, this study investigates a novel approach in the detection of gas leaks using unmanned aerial vehicles based on the analysis of thermal image flow; therefore, first, we begin by explaining the introduced scenario for the designed approach. In this scenario, the thermal image streams are collected while the drone is hovering, and the thermal camera is aiming at the targeted environment. In an uncontrolled environment, the thermal radiation variation and dynamic background can raise many challenges in the analysis of gas flow; therefore, in this study, it is assumed that there are no or limited motions in the background. One of the common issues in thermal image streams is the thermal radiation variation between different views due to different exposure levels, angle of views, and the automatic determination of radiation range applied by advanced thermal cameras. So, an intensity-based histogram adjustment method based on a reference image explained in [1] is applied on consecutive frames. Then the thermal images are aligned using phase correlation schema introduced in [2]. The phase correlation uses the frequency-domain representation of an image to estimate the relative translative offset between two images. It demonstrates significant performance for rigid motions, and the time complexity is comparably acceptable. Finally, the frames are cropped to contain the consistent areas of the images.

The proposed gas leak detection is based on the analysis of thermal image flow; therefore, the removal of static pixel values can enhance the detection of optical flow in consecutive images. Consequently, the background pixel values of each frame are subtracted by considering the first frame as ground truth. Also, an integral image-based adaptive thresholding technique explained in [3] is utilized. Then, a dense optical flow proposed in [4] is employed to measure the magnitude of motions and variations. Although dense optical flow techniques are computationally more expensive, the non-rigidness and inconsistency of the gas flow make the feature-based approaches are unreliable.

The measured motion magnitude calculated by optical flow is then filtered by a pre-determined threshold, as shown in Figure 1-c. The result is a 3-dimensional matrix containing the magnitude of local motions across all the processed frames. Afterward, a probabilistic map is calculated to specify the probability of the occurrence of possible gas flows, as illustrated in Figure 1-b. The map is used to remove sudden motions and inconsistent local motions. Then, a histogram-based segmentation technique is employed to eliminate outliers and insignificant local motions. Finally, based on the probabilistic map, two regions are determined: (a) hotspot areas (origin of the gas leak) and (b) areas with the highest flow intensity (gas emission), as shown in Figure 1-a.
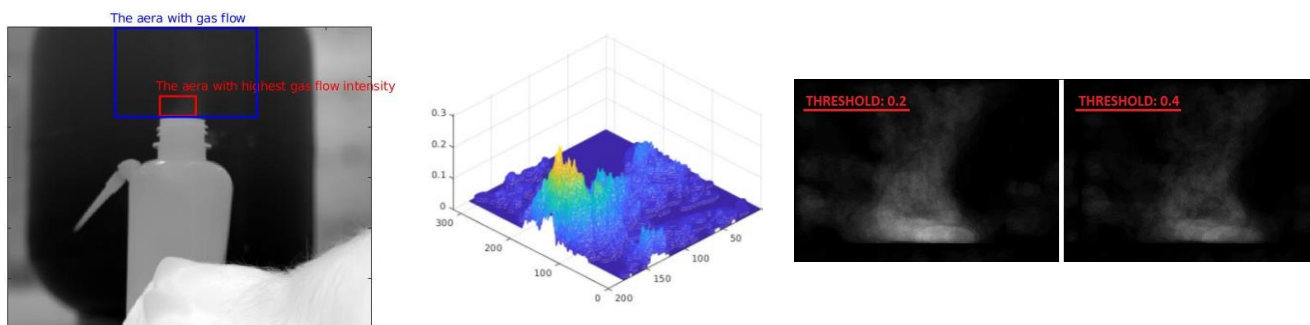

Fig. 1 The result of gas leak detection: (a) LEFT: the detection of the origin of gas leak and the region of gas flow, (b) CENTER: probabilistic map, and (c) RIGHT: the thresholding result of magnitude correlation matrix.

3. CONCLUSION

In this paper, we investigated the employment of drones for gas leak detection. We addressed the challenges of thermal inspection for this specific application and tackled them using a novel approach. The currently conducted experiments show promising results in an isolated environment, which can be considered as a motivation to further explore the application of drone-based gas imaging techniques in various applications. Future works will mainly focus on two areas. First, we will work on a new approach to estimate the origin of gas leaks based on flow patterns. Furthermore, we will investigate new techniques to deal with dynamic background and thermal radiation variations.

REFERENCES

[1] H. Niu, Q. Lu and C. Wang, "Color Correction Based on Histogram Matching and Polynomial Regression for Image Stitching," in 2018 IEEE 3rd International Conference on Image, Vision and Computing (ICIVC), 2018.

[2] R. B. Srinivasa and B. N. Chatterji, "An FFT-based technique for translation, rotation, and scale-invariant image registration," IEEE transactions on image processing, vol. 5, no. 8, pp. 1266--1271, 1996.

[3] D. Bradley and G. Roth, "Adaptive thresholding using the integral image," Journal of graphics tools, vol. 12, no. 2, pp. 13-21, 2007.

[4] G. Farneback, "Two-frame motion estimation based on polynomial expansion," Scandinavian conference on Image analysis, pp. 363-370, 2003.

NONDESTRUCTIVE EVALUATION OF REPAIRED REINFORCED CONCRETE BEAM BY UNPRECEDENTED POLYMER CEMENT MORTAR MIXED WITH STEEL FIBER

Rahimullah Habibzai

Ph.D. Student, Graduate School of Science and Technology, Kumamoto University, Japan
Lecturer at Engineering Faculty, Shiekh Zayed University, Khost, Afghanistan

ABSTRACT

The damage and deterioration in the existing concrete structures cause poor performance under service loading. This getting worse state is due to increment in service loading, ageing, corrosion as well fatigue, environmental hazards and environmental effects. It is very significant to understand phenomenon associated with cracking in order to maintain the structure subject to safety and economic considerations. This study investigates the acoustic emission of repaired defective reinforced concrete beams by unprecedented polymer cement mortar mixed with steel fiber. The compressive strength, split tensile strength and flexural strength tests were performed on repaired, stiffened and reference reinforced concrete beams, cylinders and small mortar prisms. During the flexural test of specimens, a sensor was installed to detect the acoustic emission of specimens under cyclic four-point loading. The cumulative acoustic emission hits were hardly detected, particularly just before the yield point in the loading process of the mortar prisms. Such behavior is a characteristic of brittle materials. Meanwhile, the Kaiser effects were not observed during application of cyclic loads on repaired specimens, while it was seen in under cyclic loaded reference beams. Based on the results of acoustic emissions, stainless steel fiber had a promising effects on the mechanical properties of mortar and potential durability applications. Acoustic Emission result indicates that the ultimate peak load and moment carrying capacity were improved in preloaded stiffened beams. The mechanical properties were improved in preloaded re-strengthened beams and deflection was reduced. The results of the present investigation can be utilized in health monitoring of repaired and stiffened concrete structures subjected to flexural load.

KEYWORDS: Acoustic Emission Testing, Kaiser Effect, Steel Fiber Polymer, Repair and Strengthening RCC beams

1. INTRODUCTION

The damage and deterioration in the existing concrete structures cause poor performance under service loading. This getting worse state is due to increment in service loading, ageing, corrosion as well fatigue, environmental hazards and environmental effects [1]. It is very significant to understand phenomenon associated with cracking in order to maintain the structure subject to safety and economic considerations [2].

At present monitoring of concrete structure is carried by destructive testing or non-destructive testing (NDT). Recently, around the globe, structural health monitoring is substantial to evaluate the retrofitting and repair of structures. Structures experience man-made and natural disasters that need more specific and accurate assessment in preparation of an event or beyond the event. The most commonly used material in structures is concrete which can be assessed in many ways. The factors to be considered in the test are cost, time, and the idle period during assessment. In order to achieve a better and more economical test, one of the procedures is utilization of a non-destructive test (NDT). The NDT in concrete is complex due to its nonhomogeneous ingredients and design mix.

From research, there are two common tests that are available in the literature. The NDT test can be classified as insensitive or sensitive to internal damage. The techniques, which are not sensitive to internal damage, do not correlate well with mechanical load or any damage. This test includes a sudden change in the measurement of a parameter which indicates the unexpected failure of concrete. Examples of these NDT tests are the Ultrasonic Pulse Velocity (UPV) test, SONREB (ultrasonic pulse velocity test and rebound hammer) test, and the chain drag method. On the other hand, NDT tests that are sensitive to internal damage involve parameters that correlate well with internal load. Examples of sensitive NDT tests are the non-linear ultrasonic test [3–5] and the Acoustic Emission (AE) test [6].

Acoustic emission (AE), monitoring is a distinctive, non-invasive and submissive NDT which is now extensively accepted and is being used in the field of civil engineering for structural health monitoring. AE signals are diminishing elastic waves formed due to release of the energy in the material by propagating micro-damages. The damages are caused due to micro-crack growth, movement of voids, crack initiation as well grain boundary sliding and development, phase changes in the crystalline structure [7]. AE signals accompany only active damages that are initiated or developed during subjected loading conditions [8]. The advantages of AE technique are that the position of developing cracks can be determined and also the

whole structure can be tested at once without intruding into any process associated with the structure [9]. AE testing characteristics can be used for both global and localized monitoring of damage portion. However one major drawback of using AE testing is unavailability of a standard procedure to use it in all types of the structures or bridges [10].

In the recent time AE technique has been applied to evaluate and classify the cracks as well as damages of reinforced concrete beams considering with diverse thickness. However in concrete structures it is difficult to classify the cracks due to the parameters such as response data, material properties as well sensor location and member geometry [11, 12].

In general, classical or parameter-based technique or signal based AE technique is employed for monitoring structures [13]. To identify damages and classify the crack mode, a probabilistic approach based procedures, particularly Gaussian mixture modelling [14-16] has been applied so that to get better of the shortages related to crack classification suggested by [17,18].

The introduction of fibers was brought in as a solution to develop concrete due to enhancing its flexural and tensile strength. Fibers are generally discontinuous, randomly distributed throughout the cement matrices [19]. The inclusive properties of steel fiber reinforced polymer cement composite mortar (SFRPCM) that is used in this research are, containing enough workability, higher level of stiffness, modulus of elasticity, shear, and flexural strength. It has advantages on bondage with an original layer of concrete and easy applying to deteriorated area. The optimum size of the steel fibers recommended acting on the elastic zone (strength and cracking) or plastic zone (ductility and deformation) are different. In the elastic zone, the fibers must be numerous and small, while in the plastic zone, the fiber length must be large enough to ensure their proper anchorage in the matrix [20].

The main purpose of this study is to perform a nondestructive evaluation of repaired defective reinforced concrete beam by utilization of a unique mortar consist of steel fiber polymer cement mortar. Additionally, to analyze the integrity and robustness of specimens during cyclic loading.

The importance of this study stems from the fact that a large number of reinforced concrete buildings have been damaged, defective and vulnerable to damage. It is well known that during the service period of concrete structures are not only maintenance-free, but face to aggressive environment and natural disasters as well. Additionally, faults in design, poor workmanship, as well as overloading, affects the long-term service and quality of concrete structures. This research work proposes a proper repair technique to guarantees the safety of residents, serviceability and recoverability of defective concrete structures. Moreover, this chosen repairing method protects reinforcing steel bars from exterior effects, and finally improves the structure's durability. We used a unique repairing and strengthening material, reinforced polymer cement mortar included with steel fiber to repair and strengthen the defective reinforced concrete beam. Also, we compared three repairing and strengthening techniques result along with reference beams. Furthermore, Acoustic Emission of specimens was performed during three and four-point cyclic loading to analyze the integrity, soundness and Kaiser effects of specimens repaired with SFRPCM. To investigate and compare the load-bearing capacity improvement, we applied three and four point loading on all repaired and reference specimens.

2. ACOUSTIC EMISSION

A wide variety of damage techniques has been explored for structural health monitoring (SHM) so far, namely fiber optics, ultrasonic, sonic infra-red and vibration-based damage detection eddy-current methods, radiography and acoustic emission (AE) [21, 22]. Among them, AE has been used in the SHM field for over five decades and has been shown to be a very convenient and reliable monitoring tool over the other techniques. AE is a phenomenon that occurs when an elastic wave generates from rapidly released energy inside a material, for instance, at the initiation of a crack [23]. Acoustic emission techniques can monitor the overall structural integrity continuously during the normal operation of structures, to detect automated cracks. Thus it becomes a well-fitted method for SHM. High sensitivity to minute damage and the ability to detect sophisticated areas make AE an appealing monitoring tool for structural health monitoring of large civil infrastructures [24, 25]. The diagrammatic presentation of the AE phenomenon can be seen in Figure 1.1, where the structure is subjected to stress and cracks occur. The cracks act here as a source of AE waves, which propagate through the structure and can be detected by AE sensor. The sensor turns the AE waves into electrical signals and sends them to the AE acquisition system for further analysis.

Recent research in AE includes the testing of RC beams with high initial loading cycles that produced fewer acoustic emission signals [26]. A recent overview of AE on fatigue damage assessment summarized that the damage in RC beams subjected to increasing load in conjunction with this technique is still limited [27]. The combination of NDT to assess damage in RC concrete proved to be effective. The latest development includes "infradock", where inspection techniques for on-site measurements should be synthesized as a prognosis procedure [28]. This test includes ultrasonic, impact-echo, and acoustic emission tests [29]. In addition, the AE test was used in detecting cracks in concrete damaged under Alkali-Silica Reaction [30]. Results showed that the high frequency range of AE events between 300 kHz and 400 kHz can be an indication of aggregate cracking, while the low frequency range of AE events between 100 kHz and 300 kHz can be an indication of matrix cracking between the paste and interfacial transition zone (ITZ). Weighted peak frequencies were also used to characterize

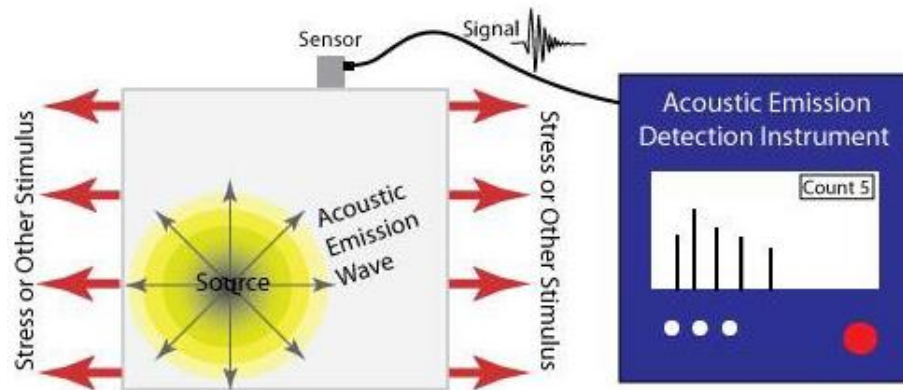damage in different stages of stress-strain diagram [31].

Fig. 1.1 Acoustic emission technique [32]

3. EXPERIMENTAL PROCEDURE

In this experimental work, 8 reinforced concrete beams with dimensions of 550 mm by 150 mm by 150 mm, 24 concrete cylinders (200 mm height and 100 mm diameter), 24 SFRPCM cylinders (100 mm height and 50 mm diameter) and 3 SFRPCM prisms (160 mm by 40 mm by 40 mm) were prepared.

Two beams (BN-1), shown in Fig. 3.1, were normal RC beams that were reference in comparison with the performance of other repaired beams. The other two beams (BRP-1), had a gap that is a pseudo removed area due to the replacement of damaged concrete in the middle of the span (140 mm wide by 75mm height by 150 mm depth). These beams were kept wet by wrapping with wet clothes for 7 days and repaired by using SFRPCM as filling the pseudo gap after the surface of the target area treated by primer coat. The specimens were tested under three-point and four-point loading.

The other two beams (BRP-2) were made exactly like BRP-1. After curing, however, both side surfaces and the lower surface were cleaned and primer undercoat was applied. Additionally, the surfaces were dried for tight bonding of the extra SFRPCM layer. The total thickness of SFRPCM layer was 25 mm. After curing, they were tested under three-point and four-point loading.

The remaining two beams (BRP-3) were prepared with pseudo crack by insertion a 5mm thick resin plate (106 mm length and 150mm depth) in the middle of the beam span. After 7 days of curing, the crack was filled out by injecting solidifying material. The surface of the beams was cleaned and treated well so that SFRPCM extra layer containing 25 mm thickness, easily and effectively bond with the original surface. All the units in Fig 3.1 are in cm, otherwise noted.
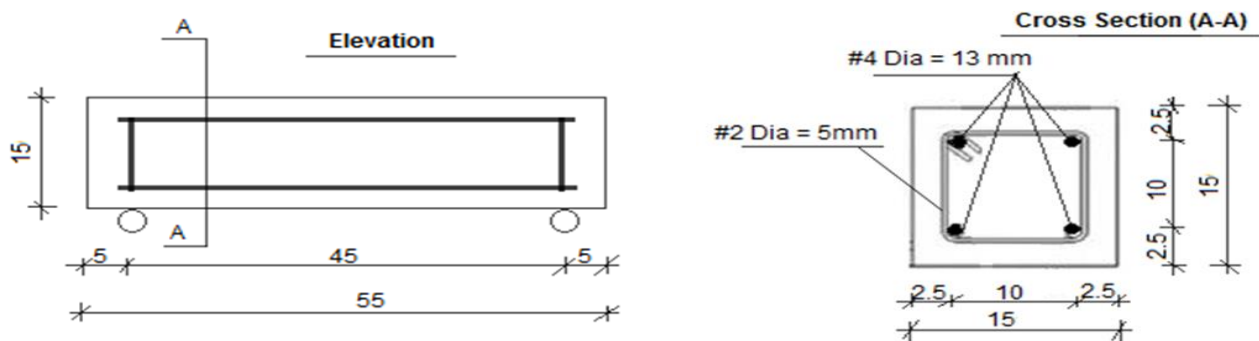

Fig.3.1 Beam Design, elevation and cross-section of the reference beam

3.1 Materials

3.1.1 Concrete

The characteristic grade of concrete used in this research was 27 N/mm2. It consisted of cement, aggregates, water, and admixture. Four batches of concrete mix with the volume of 210 lit were produced and the specimens (beams and cylinders) were casted. The average value of slump was 11.3 cm and the average value of air content was 3.975%. The mix design of concrete is indicated in Table 3.1.

Table 3.1 Mix proportion of concrete mixture

Maximum Aggregate Size	Range of Slump	Amount of Air	W/C	s/a	Water	Cement	Fine Aggregate	Coarse Aggregate	Water reducer
20 mm	18 cm	4.5%	57%	42.8%	183 Kg/m^3	321 Kg/m^3	740 Kg/m^3	1164Kg/m^3	1.5%

3.1.2 SFRPCM

The repairing and re-strengthening material, SFRPCM had consisted of premixed cement-based mortar and mixture liquid. The polymer cement premixed mortar consisted of Portland cement and silica-fume (silica-fume cement) as the binder so that the mortar gets high strength. The fine aggregate was silica sand which its granular size was less than 2.4 mm. A little of poly (ethylene-vinyl) = acetate powder has been added as premixing. The mass ratio of binder to fine aggregate was nearly 1:1. Besides, the contents of polymer powder was less than 10 % of the complete mass. Regularly the water/cement ratio was 32%. To improve and strengthen the mortar ductility, we applied steel fiber instead of carbon, glass or resin fiber. The mix proportion of SFRPCM is shown in Table 3.2.

Table 3.2 Mix proportion of steel fiber reinforced polymer cement mortar

Material	Weight (Kg)	Density (gr/cm^3)	Volume (lit)
Steel Fiber	0.14	7.85	0.018
Powder (Cement+ sand + Polymer)	3	2.4	1.25
Water	0.48	1	0.48

We grouted a solidifying injection material into imitating crack of the specimens. The product is comprised of premixed ultrafine powder and mixture liquid. The injection material is ultra-micro-fine cement-based infusion materials. Because the slurry is very low in viscosity and superior in fluidity, it penetrates for minute crazing and forms a minute hardening body. The mixture liquid is a water solution of styrene-butadiene copolymer emulsion containing a little lithium sulphite. The styrene-butadiene copolymer functions as adhesive and elastomer. Nitrite lithium is concrete repair materials having both reinforcing rod antirust effects and ASR expansion suppressant effects. In addition, Nitrite lithium is more effective in regenerating a passivity capsule of the reinforcing rod surface. The nitrite ion among other ingredients of nitrite lithium is suitable materials for repairing of deteriorated parts of concrete. The deleterious factors for this deterioration could be addressed reinforcing rod corrosion such as salt attack damage the neutralization (carbonation) of concrete.
On the other hand, the lithium-ion is suitable as repair materials for the ASR deterioration because it is effective in making alkali-silica gel non-expansible. The nominal strength for bonding, bending and compression are 5.1 N/mm2, 5.3 N/mm2 and 37.9 N/mm2 respectively.

3.1.3 Primer coating material

We have applied the primer treatment material on the surface of the concrete in advance of applying repair by the SFRPCM.
The primer treatment material is the water solutions of acrylic copolymer emulsion and poly (ox ethylene) = alkyl ether. We have applied the material adjusting the set coating amount of 200 g/m^2 so that the bonding strength of the SFRPCM with the object concrete body is improved. After a curing time of 3 hours for drying the primer treatment, we have applied the steel fiber reinforced polymer cement mortar on the concrete beam specimen.

3.1.4 Reinforcement of concrete

We used four main re-bars with a diameter of 13mm per concrete specimen. The grade is SD345. Re-bar yield strength and tensile strength are 348.59 N/mm^2, 546.57 N/mm^2 respectively. Additionally two stirrups with a diameter of 5mm are used to tie the main rebars. The tensile strength of stirrups is given 686.07 N/mm^2 accordingly.

3.2 Testing

The average compressive strength of the concrete cylinder is 54.31 MPa after 7 days and 65.73 MPa after 28 days respectively. For compressive and split tensile strength tests, cylinders specimens of dimensions with 200 mm height and 100 mm diameter were cast. The top surface of the specimens were leveled and finished homogeneously. 6 cylinders in each batch cured for 7 days and the remaining 6 for 28 days. These cylinders were tested after 7 and 28 days on the digital compression testing machine. The failure load was noted. To investigate and compare the load-bearing capacity of concrete beam specimens, they were tested under three and four-point loading test machine. The effective span was 450 mm as shown in Fig. 3.1. Furthermore, two acoustic emission sensors were installed on the surface of beams to detect initial fractures and Kaiser Effect during cyclic loads. Fig 3.2 shows the concrete beam specimens under four-point loading. Load and corresponding deflections were noted up to failure. In each category two beams were tested and their average value is reported. Totally eight beams were tested with different cyclic loads.

Fig 3.2 Concrete prism under three and four point loading and installed AE sensors on its surface

4. RESULT AND DISCUSSION

There are several non-destructive evaluation/testing (NDE/NDT) techniques for local structural health monitoring Most of them are based on the use of mechanical waves (such as ultrasonic and acoustic emission techniques), electromagnetic waves (for example, Magnetic particle testing, Eddy current testing and radiographic techniques) and fiber optics (though they can be used for global monitoring). Further details on these methods can be found in [33, 34]. Acoustic Emission (AE) refers to the generation of transient elastic waves produced by a sudden redistribution of stress in a material. When a structure is subjected to an external stimulus, localized sources trigger the release of energy, in the form of stress waves, which propagate to the surface and are recorded by sensors. Sources of AE vary from natural events like earthquakes and rock bursts to the initiation and growth of cracks, slip and dislocation movements, melting, twinning, and phase transformations in metals. In composites, matrix cracking and fiber breakage and debonding contribute to acoustic emissions. Hence, it can be concluded that passive AE technique can efficiently serve to monitor flexural performance of RC structures subjected to loading induced damage. Further, it also works effectively to monitor and evaluate the performance of SFRPCM repaired beams. AE technique can facilitate nondestructive evaluation of RC structures subjected to loading much before the damage reaches to a catastrophic level. AE can result from the initiation and growth of cracks, slip and dislocation movements, twinning, or phase transformations in metals. In any case, AE's originate with stress. When a stress is exerted on a material, a strain is induced in the material as well. If discontinuities created in a material do not expand or move until that former
stress is exceeded, this phenomenon known as the Kaiser Effect, which can be seen in the load versus AE plot in BN-1. However, in BRP-2 test, the Kaiser Effect could not be seen in contrast with BN-1. The AE activities are shown in Fig. 4.1. Fig. 4.2 and Fig.4.3. Particularly, acoustic emission were hardly detected remarkably just before the yield point in loading tests of the SFRPCM mortar bars. Such behavior is a characteristic of brittle materials.
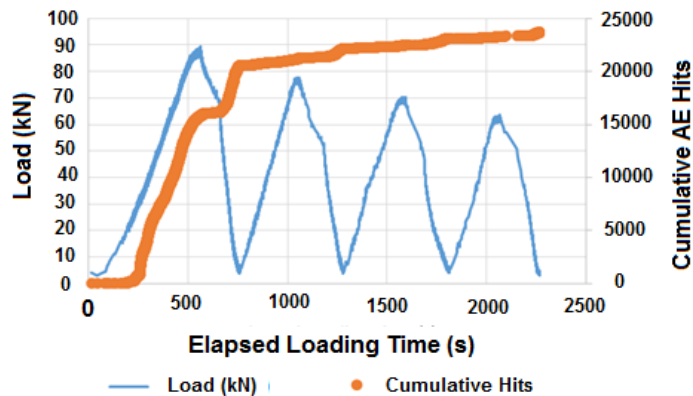
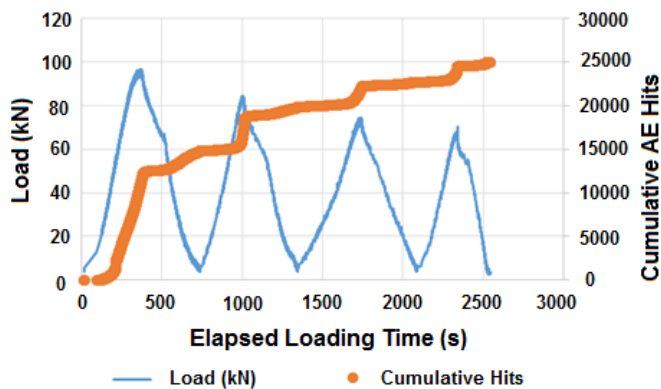Fig. 4.1 Load and AE plot in BN-1 under three-point loading test.

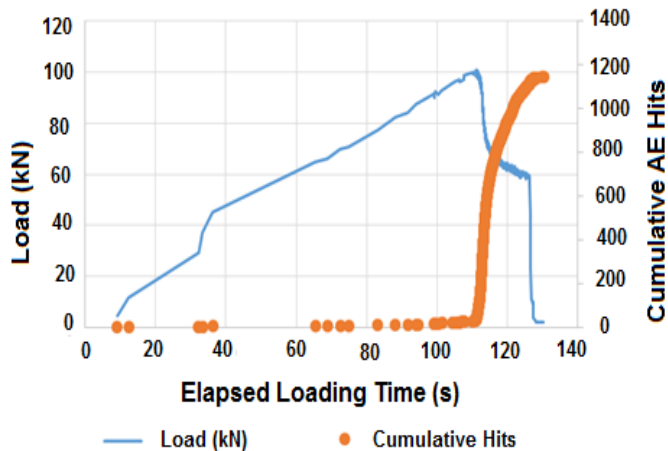Fig. 4.2 Load and AE plot in BRP-2 under three- point loading test

Fig. 4.3 Load and AE plot in SFRPCM prism under four-point loading test.

Fig 4.4 shows the maximum peak load of specimens during application of three-point loading. It shows that BRP-2 repaired and Stiffened beams had the highest peak value among other specimens. According to AE test result, BRP-2 specimens showed integrity during three and four point loading compared to other specimens. Finally, it is concluded that the repairing and stiffening technique described as BRP-2, seems effective and strong in comparison to the other methods.
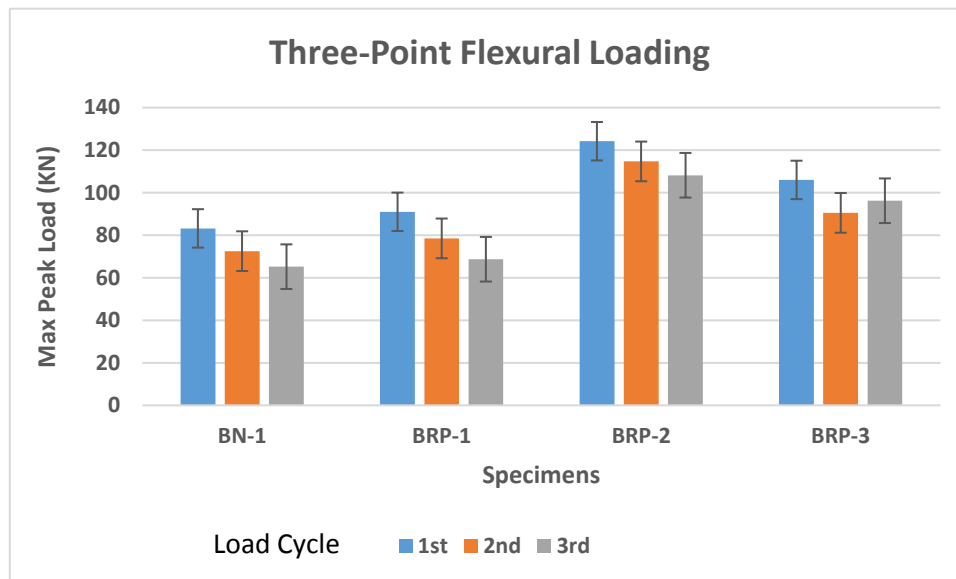
Fig. 4.4. The maximum peak load of specimens during application three-point loading.

The following Fig.4.5 and Fig.4.6 show different crack pattern of repaired and reference beams. After de-loading the specimens were examined and they are clearly shown in below pictures. In retrofitted defective beams, the cracks occurred near repaired area and no shear cracks were seen. Moreover the SFRPCM was not separated from patch area, which indicates its strong bond with adjacent layer of concrete and re-bars.

Fig. 4.5 Crack pattern in BN-1 beam after applying maximum cyclic three-point loading.

Fig. 4.6 Crack pattern in BRP-2 beam after peak application of peak load in three-point loading.

4. CONCLUSION

The deterioration progress of a repaired reinforced concrete beam under loading at laboratory test scale is monitored by the application of AE analysis with good results but there is not much published evidence of the technique being used successfully on full scale reinforced concrete structures. This tests will establish the potential for AE monitoring as a NDT technique in reinforced concrete structures.

The repair of defective RC beams using SFRPCM causes reappearance of the AE phases with an increase in the number of cumulative AE hits pointing towards improved integrity of the beams after repair with SFRPCM. Successful AE monitoring of reference and further SFRPCM repaired defective beams establish it as a good potential real time NDT candidate for RC beams subjected to simultaneous defective, repair and loading.

During cyclic loading on repaired beam (BRP-2), the Kaiser Effect could not be seen. However, it could be seen the load versus AE plot during cyclic loading on reference (normal) beams.

It could be suggested that, the AEs with restriction releasing such as the friction was seen during the reloading process because resistance for the transformation revived by the relocation in the material was accomplished again in unloading process. The cumulative acoustic emission hits were hardly detected, particularly just before the yield point in the loading process of the mortar prisms. Based on the results of Acoustic Emissions, stainless steel fiber had a promising effects on the mechanical properties of mortar and potential durability applications. All the repairing techniques had a promising results compare to the reference beam. The second repairing and stiffing technique (BRP-2), presented the best result among all specimen. SFRPCM had a unique bonding with the original surface of concrete and steel re-bar.

ACKNOWLEDGMENT

REFERENCES

[1] Prem PR, Murthy AR, Ramesh G, Bharatkumar BH, Iyer NR. Flexural behaviour of damaged RC beams strengthened with ultra high performance concrete. In: Advances in structural engineering. India: Springer; 2015. p. 2057–69.

[2] Aggelis DG. Classification of cracking mode in concrete by acoustic emission parameters. Mech Res Commun 2011; 38(3):153–7.

[3] Ongpeng, J.M.C.; Oreta, A.W.C.; Hirose, S. Effect of Load Pattern in the Generation of Higher Harmonic Amplitude in Concrete Using Nonlinear Ultrasonic Test. J. Adv. Concrete Technol. 2016, 14, 205–214.

[4] Ongpeng, J.M.C.; Oreta, A.W.C.; Hirose, S.; Nakahata, K. Nonlinear Ultrasonic Investigation of Concrete with Varying Aggregate Size under Uniaxial Compression Loading and Unloading. J. Mater. Civ. Eng. 2017, 29.

[5] Ongpeng, J.M.C.; Soberano, M.; Oreta, A.W.C.; Hirose, S. Artificial Neural Network Model using Ultrasonic Test Results to Predict Compressive Stress in Concrete. Comput. Concrete 2017, 19, 59–68.

[6] Ongpeng, J.M.C.; Oreta, A.W.C.; Hirose, S. Damage progression in concrete using acoustic emission test through convex hull visualization. ACI Mater. 2016, 113, 737–744.

[7] Shiotani T. Application of the AE improved b-value to quantitative evaluation of fracture process in concrete-materials. J Acoust Emiss 2001;19:118–33

[8] Goszczyn´ ska B, S´ wit G, Tra̧ mpczyn´ ski W, Krampikowska A, Tworzewska J, Tworzewski P. Experimental validation of concrete crack identification and location with acoustic emission method. Arch Civ Mech Eng 2012;12(1):23–8.

[9] Vidya Sagar R, Raghu Prasad BK, Sharma R. Evaluation of damage in reinforced concrete bridge beams using acoustic emission technique. Nondestruct Test Eval 2012;27(2):95–108.

[10] Rehman SKU, Ibrahim Z, Memon SA, Jameel M. Nondestructive test methods for concrete bridges: a review. Constr Build Mater 2016;107:58–86.

[11] Aldahdooh MAA, Bunnori NM. Crack classification in reinforced concrete beams with varying thicknesses by mean of acoustic emission signal features. Constr Build Mater 2013;45:282–8.

[12] Shahidan S, Pulin R, Bunnori NM, Holford KM. Damage classification in reinforced concrete beam by acoustic emission signal analysis. Constr Build Mater 2013;45:78–86.

[13] RILEM Technical Committee. Recommendation of RILEM TC 212-ACD: acoustic emission and related NDE techniques for crack detection and damage evaluation in concrete. Mater Struct 2010;43(9):1183–6.

[14] Reynolds DA, Rose RC. Robust text-independent speaker identification using Gaussian mixture speaker models. Speech Audio Process IEEE Trans 1995;3 (1):72–83.

[15] Reynolds D. Gaussian mixture models. Encycl Biometrics 2015:827–32.

[16] Reynolds DA, Quatieri TF, Dunn RB. Speaker verification using adapted Gaussian mixture models. Digital Signal Process 2000;10(1):19–41.

[17] RILEM Technical Committee. Recommendation of RILEM TC 212-ACD: acoustic emission and related NDE techniques for crack detection and damage evaluation in concrete. Mater Struct 2010;43(9):1183–6.

[18] Farhidzadeh A, Salamone S, Singla P. A probabilistic approach for damage identification and crack mode classification in reinforced concrete structures. J Intell Mater Syst Struct 2013;24(14):1722–35.

[19] Kishor S. Sable, Madhuri K. Rathi, Effect of Different Type of Steel Fibre and Aspect Ratio on Mechanical Properties of Self Compacted Concrete, Volume 2, Issue 1, July 2012. (IJEIT).

[20] A. Ellouze, M. Ben Ouezdou, and M. A. Karray, "Experimental Study of Concrete Steel Fibers Slabs. Part I: Behavior under uniformly distributed loads", International Journal of Concrete Structures and Materials, Vol. 4, No. 2, (2010), pp.113-118

[21] Willcox, M. and G. Downes, A brief description of NDT techniques. Toronto: NDT Equipment Limited, 2003.

[22] Holford, K.M., Acoustic Emission In Structural Health Monitoring. Key Engineering Materials, 2009. 413: p. 15-28.

[23] Scruby, C., An introduction to acoustic emission. Journal of Physics E: Scientific Instruments, 1987. 20(8): p. 946.

[24] Kaphle, M.R., Analysis of acoustic emission data for accurate damage assessment for structural health monitoring applications. 2012.

[25] Corporation, P.A. Acoustic Emission. [cited 2015]; Available from: www.physicalacoustics.com.

[26] Xiangqian, F.; Shaowei, H.; Jun, L.; Congjie, W. Acoustic emission properties of concrete on dynamic tensile test. Constr. Build. Mater. **2016**, 114, 66–75.

[27] Noorsuhada, M.N. An overview on fatigue damage assessment of reinforced concrete structures with the aid of acoustic emission technique. Constr. Build. Mater. **2016**, 112, 424–439.

[28] Ohtsu, M. AE and Related NDT for Damage Evaluation of Civil Structures: Prospective Applications of AE measurements to infra-dock of concrete structures. Constr. Build. Mater. **2018**, 158, 1134–1142.

[29] Ohtsu, M. Elastic wave methods for NDE in concrete based generalized theory of acoustic emission. Constr. Build. Mater. **2016**, 122, 845–854.

[30] Farnam, Y.; Geiker, M.R.; Bentz, D.;Weiss, J. Acoustic emission waveform characterization of crack origin and mode in fractured and ASR damaged concrete. Cem. Concrete Compos. **2015**, 60, 135–145. [CrossRef]

[31] Paul, S.C.; Pirskawetz, S.; Van Zijl, G.P.A.G.; Schmidt, W. Acoustic emission for characterising the crack propagation in strain-hardening cement-based composites (SHCC). Cem. Concrete Res. **2015**, 69, 19–24

[32] Center, N.R. Introduction to Acoustic Emission Testing. Avilable from: [cited 2015]; Available from: https://www.nde-ed.org/EducationResources/CommunityCollege/Other%20Methods/AE/AE_Intro.htm.

[33] P.C. Chang, S.C. Liu. Recent research in non destructive evaluation of civil infrastructure. Journal of materials in civil engineering. 2003 May/June 2003; 15(3) :298-304

[34] A.Mccrea, D. Chamberlain, R. Navon. Automated inspection and restoration of steel bridges- a critical review of methods and enabling technologies. Automation in construciton. 2002; 11:351-73

LONG-TERM NUMERICAL ANALYSIS OF SUBSURFACE DELAMINATION DETECTION IN CONCRETE SLABS VIA INFRARED THERMOGRAPHY

Sandra Pozzer[1*], Francisco Dalla Rosa[2], Zacarias Martin Chamberlain Pravia[2], Ehsan Rezazadeh Azar[3], Xavier Maldague[1]

[1]Department of Electrical and Computer Eng., Laval University, 1065, av. de la Médecine, Quebec (Quebec), G1V 0A6, Canada
[2]Department of Civil Engineering, University of Passo Fundo, BR 285, Passo Fundo (Rio Grande do Sul), 99052-900, Brazil
[3]Department of Civil Engineering, Lakehead University, 955, Oliver Road, Thunder Bay (Ontario), P7B 5E1, Canada

[*]Corresponding Author: sandra.pozzer.1 @ulaval.ca

ABSTRACT

One of the concerns about the use of passive Infrared Thermography (IRT) for structural health monitoring (SHM) is the determination of the favorable period to conduct the inspections. This paper investigates the use of numerical simulations to find appropriate periods for IRT-based detection of subsurface damages in concrete bridge slabs under passive heating along one year of time-span. A model was built using the Finite Element Method (FEM) and calibrated using the results of a set of thermographic field inspections on a concrete slab sample. The results showed that the numerical simulation properly reproduced the experimental thermographic measurements of the concrete structure under passive heating, allowing the results to be extended for a longer testing period. The long-term FEM results demonstrated that the months of spring and summer are the most suitable for passive IRT inspections in this study, with around 17% more detections compared to the autumn and winter periods in Brazil. The goal of this research was to enhance the possibility of using FEM beyond the design stage because this computation tool can provide support to SHM.

KEYWORDS: Infrared Thermography, Concrete Bridges, Non-Destructive Test, Delamination, Finite Element Method

1. INTRODUCTION

The aging of the transportation infrastructure raises questions about the safety and serviceability of the existing bridges worldwide, which requires pertinent planning for the maintenance of these infrastructure assets[1]–[4]. Inspections have a fundamental role in bridge management, allowing diagnoses and prognoses based on the existing state of the structural elements [5]. As the performance of a structure depends on the integrity of the elements that compose it, the number of interventions in an operating structure must be set to a minimum. Therefore, the use of non-destructive tests (NDT) has become attractive, representing a fast, harmless, and accurate approach to examine the structure without interrupting or impairing its operation [6].

Infrared vision (IR) has gained interest as NDT due to its capability of examination beyond the visible spectrum [7]. The inspection is based on the thermal contrast between different materials, given a heat flux variation [8]. Undamaged elements normally present uniform heat distribution on theirs surface, while internal or surface defects change the heat dissipation by providing resistance or increasing the heat dissipation through the element. As a result, the inspection reveals defected areas with high or low temperature patterns in the surface thermograms [9]. Moreover, the IRT approach is being constantly improved by the combination with other NDT methods and the use of computational techniques to advance the collection, storage, visualization, and analysis of the thermographic data [10]–[17].

Finite Element Method (FEM) constitutes one method of numerical simulation, where the domain of a complex problem is divided into sub-regions of simple geometry, i.e., finite elements [18]. This method could provide similar outputs to the realistic infrared thermography inspection, including the information about the temperature over time and the thermal map of the inspected surfaces [19]–[22]. Thus, this tool offers the possibility of reducing the time and cost required to make test samples and the need for numerous tests in the target structures.

Numerical analysis and IRT have been integrated to detect or examine damages in concrete structures [23]–[28]. However, only a few researchers have investigated the combination of IRT and FEM for the inspection of concrete bridges [22], [29]–[34]. Therefore, this study proposes the use of FEM to support long-term inspection plans in concrete bridges using the solar loading thermography. A thermal camera was used to inspect a sample of concrete bridge slab with artificial subsurface delamination during different seasons and weather conditions. A numerical model was developed to simulate the experimental concrete specimen, radiation source, and IRT inspection. To validate the model, a comparison between the experimental and numerical surface temperatures and thermal gradients was performed. Then, the calibrated model was used to predict the most favorable periods to detect the subsurface delamination during one year of inspection.

2. EXPERIMENT

2.1 CONCRETE SAMPLE

A set of IRT experiments were previously performed by Pozzer et al. [35] to collect thermographic data, which were used to develop the numerical model in this research. Three samples of bridge slabs were built with subsurface delamination simulated with Styrofoam, which has a thermal conductivity (0.027 W/m°C) close to the air (0.024 W/m°C) and can represent a real subsurface delamination [22]. These thermographic inspections were conducted once a month in November 2018, February, April, June, and July 2019, in an hourly interval from 7:00 am to 9:00 pm. One of these concrete samples was destructed after the end of the IRT experiments to obtain the exact position of the subsurface damages, which allowed to improve the numerical modelling of the present study. Each specimen had nine Styrofoam square defects of different lateral sizes (5.0, 10.0, and 15.0 cm) and located at different depths ($2.0 \leq z \leq 5.0$ cm). Fig. 1 shows the details of the inspected concrete sample with delamination.
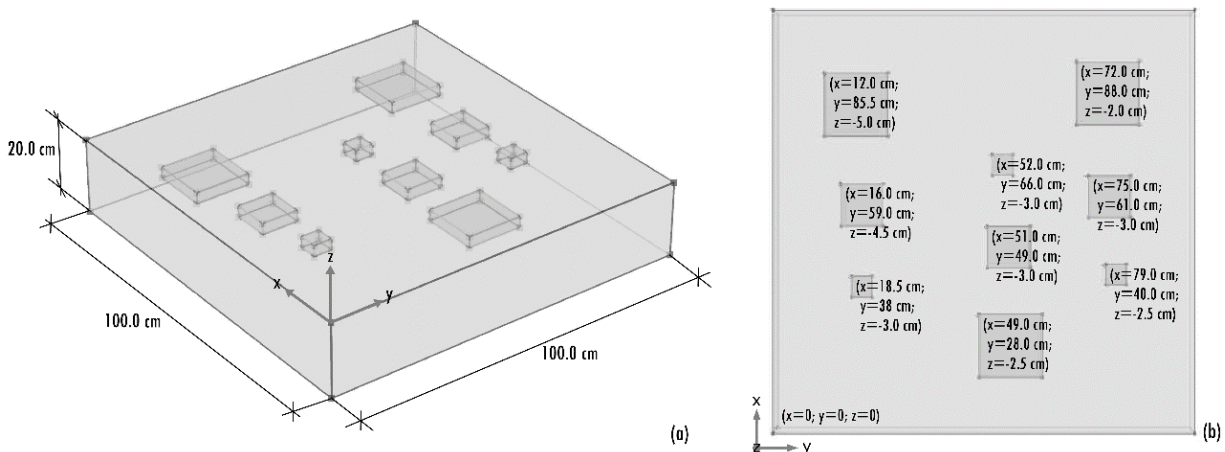

Fig. 1 Concrete sample with artificial delamination (a) 3D view (b) Coordinates of the fabricated damages

2.2 INFRARED THERMOGRAPHY MEASUREMENTS

The experiment was conducted outside of the Infrastructure Laboratory at the University of Passo Fundo, located in Passo Fundo, Rio Grande do Sul, Brazil (Lat. 28°13'36.28"S, Long. 52°23'10.92"W). Fig. 2 shows a concrete sample after construction and the location of inspections.

Fig. 2 (a) A concrete sample after curing; (b) Location of the samples in the university site

Several studies demonstrated that the sensitivity of passive IRT inspections is associated with the variation of the environmental conditions [22], [30], [35]–[38]. This research study carried out the thermographic imagery in different times of the day and months to capture the effects of different seasons on the outcomes of inspections. All the experimental tests were performed under passive heating using a TESTO 881-1 (160x120 FPA, 50 mK, 8-14μm, 33Hz) infrared camera. The inspections were performed in the reflection mode, with the camera positioned in a vertical support at 2.5 meters from the inspected sample, considering a 90° angle from the concrete top surface. The variables of ambient temperature, wind speed, and solar radiation were monitored during the test periods. A digital J Prolab Thermometer was used to register the air temperature and a portable DAVIS Turbo Meter

Anemometer was used to measure the wind speed. The solar radiation values were obtained from the meteorological station existing near the study site, which is linked with the Brazilian Meteorology Institute [39] database. The detection of the damage was measured by the thermal gradients, which represent the temperature difference between the concrete surface on top of the delaminated area and the concrete surface without delamination.

3. FINITE ELEMENT METHOD (FEM)

Heat transfer problems that include solar radiation are difficult to solve analytically, as they require transient solutions of complex nonlinear partial differential equations [18]. Thereby, FEM has become attractive for these iterative processes. This numerical modelling method includes reproducing the tested geometry, dividing it into finite elements (mesh), and exposing the sample to the heat source and boundary conditions through the time of interest. Then, the governing differential equation of the heat transfer problem is replaced by finite algebraic equations at the finite points created in the element at the given time. The COMSOL Multiphysics software, Version 5.2 from COMSOL Inc., was used for the finite element simulation. The Heat Transfer with the Surface-to-Surface Radiation module was used due to its ability to model solar radiation, which varies with the location and orientation of the samples.

3.1 MODEL GEOMETRY AND MESH

The thermal numerical simulation was modelled as a three-dimensional, non-linear, and transient analysis. The model represented the concrete sample and its damages at the identical position and dimensions as the experimental sample. The solar orientation was configured according to the experimental program as well, where the x-axis represents the North/South direction, and the y-axis represents the East/West direction. The slab sample was divided into a mesh of 22593 tetrahedral elements, in an adaptive refinement, i.e. changing according to the size and position of each solid. It used an element size named "Finer", the third thinnest level among nine options available in COMSOL software. The dimensions of the mesh elements varied between 4.0 millimeters and 5.5 centimeters, with minimum element quality of 0.137. The quality of the elements can vary between 0 and 1, where 1 represents an optimal element and 0 indicates a degenerated component. There is no predetermined value for what the element's quality should be since it depends on the analyst judgement and the required precision of the model. For the most applications, however, elements with a quality below 0.1 are considered limited [40]. In this case, the "Finer" option represented a balance between the element's quality and the computational time. The model geometry and mesh definition are shown in Fig. 3.
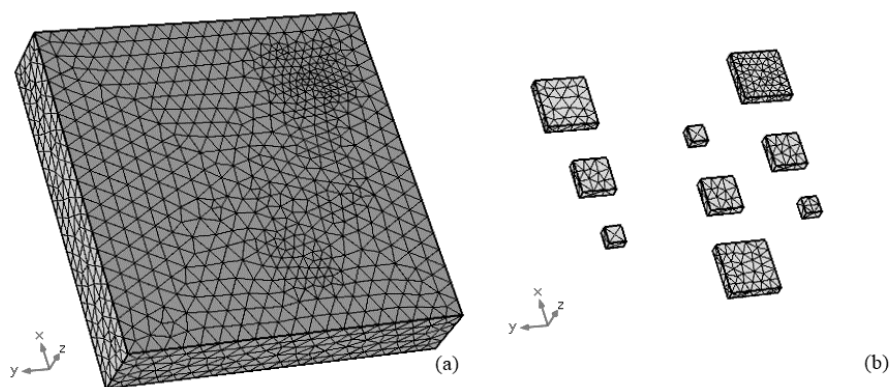
Fig. 3 Geometry and mesh for the concrete sample (a) and simulated delaminations (b)

3.2 MATERIAL PROPRIETIES

The thermal properties of the materials were determined according to the concrete and Styrofoam used in the experimental program, complemented by technical references presented in previous studies [17], [22]. The values are presented in Table 1.

Material properties	Unit of measure	Concrete	Styrofoam
Density	kg/m³	2400	25
Specific Heat	J/ (kg. K)	1008	1130
Thermal conductivity	W (m.K)	Temperature dependent	0.027
Emissivity	-	0.9	-

Table 1 Materials properties for the numerical simulation

3.3 BOUNDARY CONDITIONS

Solar radiation, convection, and ambient temperature were set as boundary conditions for the simulated model. The main heat source was the incident solar radiation over time, which varies according to the geographic location of the sample and the Sun orientation (zenith angle and solar elevation). This parameter was included using the External Radiation Source feature in the software, which was configured based on the latitude (28°13'36.28"S), longitude (52°23'10.92"W), and time zone (-3) of the test location.

The second boundary condition was the heat transfer by convection. Since Sharples and Charlesworth [41] established an approximate correlation between the wind speed (V) and convective heat transfer coefficient (h_w), their study was used to determine a daily wind-induced convective heat transfer in the present study, using the following equation:

$$h_w = 6.5 + 3.3V \ (W/m^2.K) \qquad V \le 6 \ m/s \tag{1}$$

Hiasa et al. [22], [32], [33] used a similar approach to calculate the convection coefficient for their numerical thermographic simulation. However, they performed a one-day test and stipulate a constant heat transfer coefficient based on the maximum wind speed data. In this study, the daily average of wind speed was used to find the daily convective heat transfer coefficients.

The third boundary condition was the ambient temperature. The diurnal variation of the ambient temperature (T_{amb}) follows a simple sinusoidal periodic distribution of 24 hours, depending on the average daily temperature $\left(T_{avg}\right)$ [42]:

$$T_{amb}(t) = T_{avg} + \Delta T cos\left(2\pi \frac{t-14}{24}\right) \tag{2}$$

Where T_{avg} and ΔT are parameters corresponding to the average daily temperature and half of the daytime temperature variation, respectively. The variable t represents the time and is expressed in hours. Table 2 shows the information about the environmental conditions measured during the field test days. The solar radiation value in each day was set according to the average of the positive irradiation values registered by the database. The FEM analysis was carried out in an hourly basis.

Month	Day of inspection	Solar Radiation (W/m². s)	Wind speed (m/s)	Average Temperature (°C)	Half diurnal Temperature Variation(°C)
November	22/11/2018	574.02	3.21	23.95	6.90
February	23/02/2019	524.14	1.30	27.00	8.85
April	18/04/2019	464.19	1.71	17.55	5.80
June	14/06/2019	276.48	2.85	20.28	5.60
July	06/07/2019	408.58	1.38	3.81	6.35

Table 2 Meteorological data used in the numerical simulation

4. RESULTS AND DISCUSSION

The results of one of the inserted delamination are presented to perform the comparison between the experimental and numerical surface temperatures and thermal gradients. Other studies showed that different internal defect characteristics (size, thickness, and depth) have distinct thermal responses through the day [32], [33], [35], [38] affecting the favorable period to detect the damages using IRT. In the present study, both experimental and simulated results for the upper-right (2 centimeters deep) delamination will be shown next, followed by the yearly analysis performed using the finite element method.

4.1 COMPARISON OF EXPERIMENTAL AND SIMULATED RESULTS

Fig. 4 shows four pairs of thermograms obtained from the experiment and FEM simulation. The temperature range of the thermograms was unified to facilitate the surface temperature comparison and the color pallet was adjusted to improve the visualization of the damages in each experiment. The chosen palette has one scale where the red color represents the highest surface temperatures, and the blue color is associated with the lowest surface temperatures. The presented thermograms are from 12:00 (noon) and 9:00 pm, representing heating up and cooling down phases registered in the passive IRT inspection, respectively.
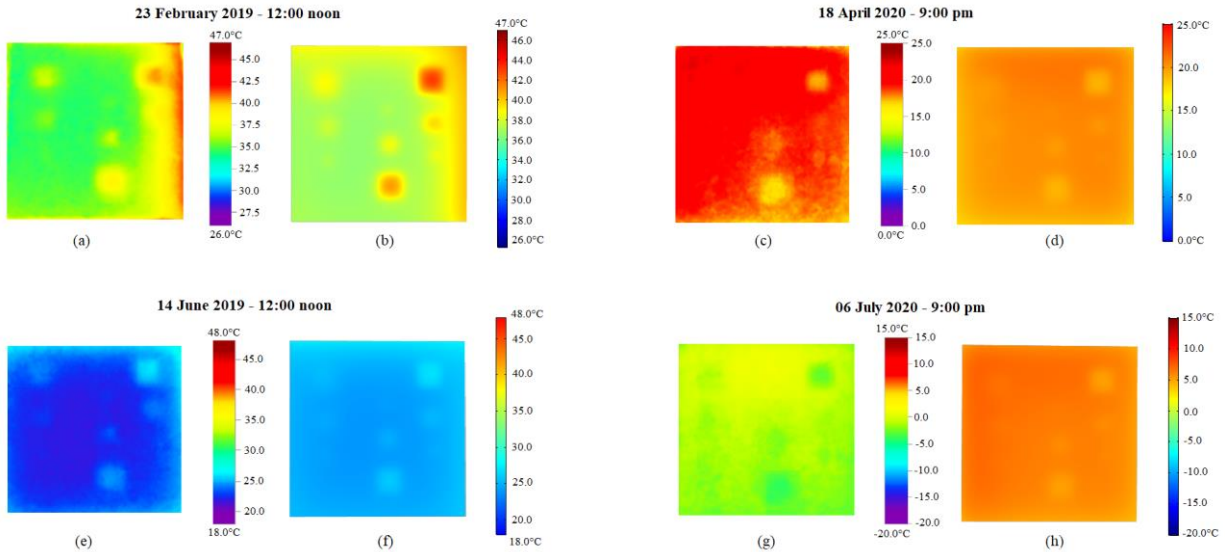
Fig. 4 Comparison between thermograms obtained from the IRT experiments (a, c, e, and g) and simulated by FEM numerical model (b, d, f, and h)

In Fig. 4 it is possible to observe a non-uniform heating in the experiment, where the heating and cooling processes follow the solar movement, which varies through the day and the months. Fig. 4(b) confirms the work of Hiasa et al. [22] by showing that the numerical model can reproduce the heating of the sample edge according to the solar orientation. In general, the surface temperatures are convergent. However, the experimental thermograms present a high level of non-uniform heating when compared to the FEM simulations, which were caused by the environmental conditions on the field. Relative humidity, presence of clouds, and surroundings elements were not considered in the numerical simulation which could have led to the inconsistencies observed between the actual temperature measurements and simulation [22]. A higher discrepancy exists between Fig. 4(g) and Fig. 4(h), where the difference in the surface temperature reached 7° C. One possible explanation for this difference could be the presence of humidity and fog in the experiment environment, which is a common situation during the winter mornings and nights, causing a lower temperature in the concrete surface in the experimental sample. A complete quantitative temperature comparison for the delamination is provided in Fig. 5.
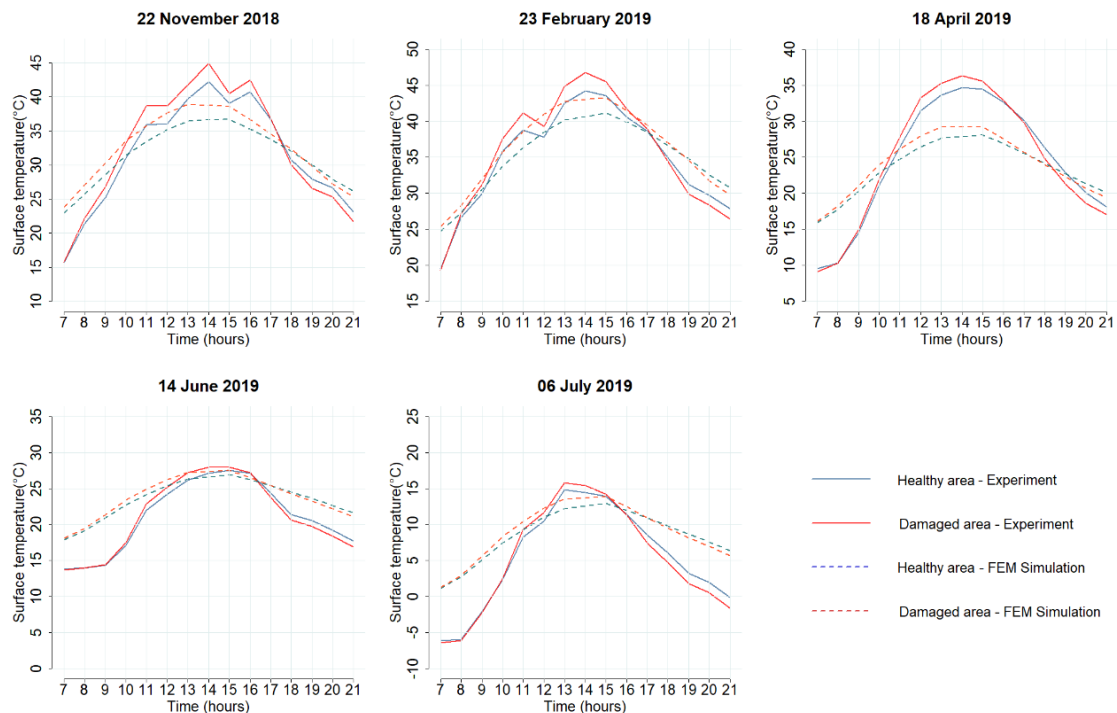

Fig. 5 Comparison of surface temperatures measured in the IRT experiment and simulated by the FEM

The differences between simulated and experimental surface temperatures were observed mainly during the morning and evening. As reported in the thermograms analysis, these differences are probably due to the boundary conditions assumed in the model, which only considered the sample orientation related to the Sun, solar radiation, coefficient of convection based on the wind speed, and ambient temperature at the study site. Also, several susceptible errors in the technique could have contributed to the observed difference, including errors in the accuracy of the thermal camera, in the instrumentation used to measure the environmental conditions or by the local weather station. Also, the modelling errors relating to the temperature differences between the equation used for calculating the ambient temperature in the software, and the estimated material properties. However, the purpose of this study was to verify the competence of the computer-based technique to detect subsurface damages and identify a convergence with the thermal gradients' detections in the IRT practical application, under different boundary conditions. Further works will address the FEM updating to optimize the parameters used in the proposed model.

The thermal gradient between the healthy and damaged surface temperatures is the main parameter for detecting damages in infrared thermographic inspections. In this context, Fig. 6 shows the difference between the measured and simulated contrast values during the days of experimentation.
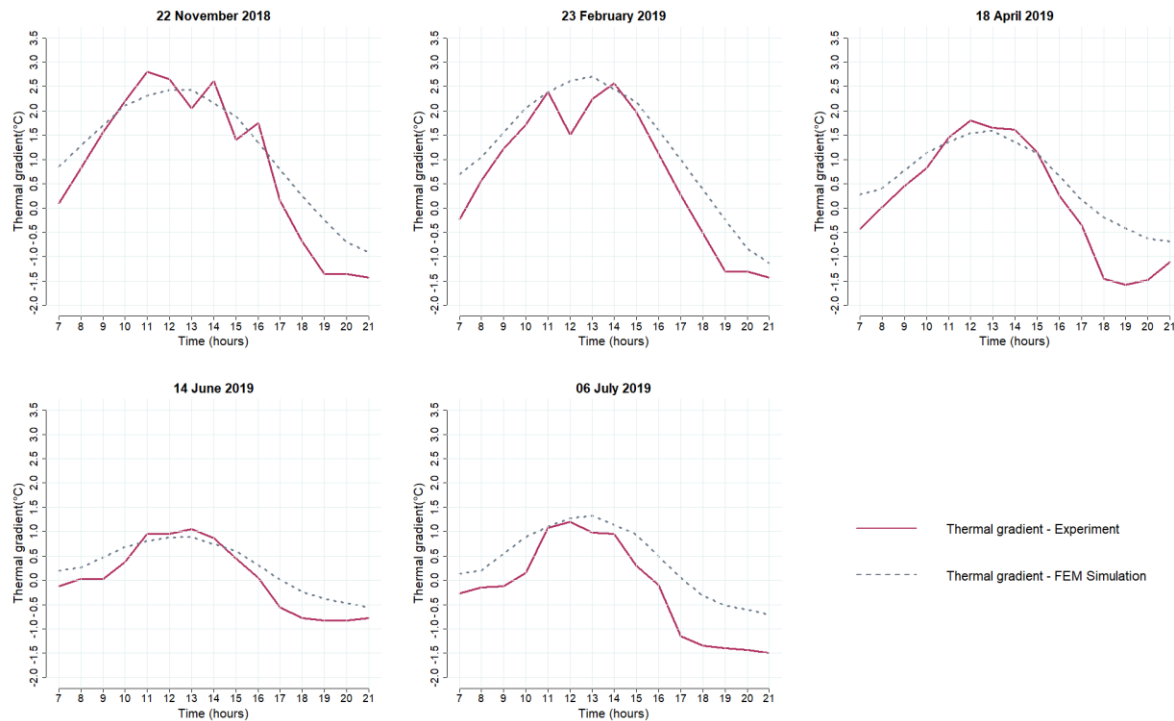

Fig. 6 Comparison between the thermal gradients obtained from the IRT experiment and simulated by the FEM

Fig. 6 shows that the contrast values obtained by the numerical simulation are aligned to those calculated from the measurements performed by the IRT thermal camera, even with the temperature differences reported in the previous figures. The amplitude of the simulated contrast followed the periodic variation of the gradients through the days that the experiments were carried out, where gradients were small for the autumn and winter months (April, June, and July) compared to spring and summer months (November and February). The Pearson Correlation (R), the Mean Bias Error (MBE), and the Mean Absolute Error (MAE) were calculated to assess the covariability and the deviation among the simulated results from the FEM model and the observed results from the IRT experiments (Table 3).

Experiment	Healthy Area			Damaged Area			Thermal Gradient		
	R	MBE(°C)	MAE(°C)	R	MBE(°C)	MAE(°C)	R	MBE(°C)	MAE(°C)
22 Nov. 2018	0.98	0.02	3.07	0.98	0.31	3.37	0.97	0.29	0.51
23 Feb. 2019	0.97	0.20	2.17	0.97	0.63	2.46	0.97	0.48	0.51
18 Apr. 2019	0.99	-0.93	4.21	0.99	-0.55	4.36	0.98	0.38	0.47
14 Jun. 2019	0.96	2.51	2.78	0.97	2.73	2.96	0.97	0.22	0.29
06 Jul. 2019	0.98	3.24	3.95	0.98	3.82	4.38	0.97	0.58	0.58

Table 3 R, MBE, and MAE for the surface temperatures and thermal gradients measured and simulated in the daily experiments

The MBE measures the overall bias of the model and MAE measures the absolute extent of the errors without considering their directions [43]. Table 3 shows that in most cases the MBE produced positive values for the surface temperatures and thermal gradient, indicating that the model has a trend to overestimate the experimental results. An exception is seen in April, where MBE showed that the model underestimates the surface temperatures. However, thermal gradients were constantly overestimated. These trends can be confirmed by looking at the curves in Fig. 5 and Fig. 6. The MAE is greater for the surface temperatures simulations, with averages differences ranging from 2.17 °C to 4.38 °C. However, the absolute error is under 0.6°C in all thermal gradient tests, which indicates that the contrast between healthy and damaged area is convergent, despite the surface temperature differences. Therefore, these results are aligned with previous studies findings[22], [29]–[34], where the numerical simulation presented the capability of reproducing the thermal gradients measured in the thermographic inspections using passive heating. Rumbayan and Washer [29] reported the deviation measurements for the thermal contrast between their model and the experimental results. The correlation indices (R) were between 0.70 and 0.92 and the contrast differences (MBE) and absolute error (MAE) were below 1 °C. In this sense, we confirm the authors' conclusion that the FEM can represent a tool to support practical IRT inspections.

The computational modelling showed the possibility of identifying subsurface damage in reinforced concrete bridge slabs at different times of the year, under different environmental conditions of temperature, wind speed and solar radiation Although the simulated thermal gradient results present an average difference of 0.39°C compared to the experimental inspection, the correlation between the model results and the experimental study was equal or above 0.97 in all the thermographic tests. Consequently, the reasonable accuracy of the simulation supports the extrapolation of the model analyses to a large period.

4.2 DISCUSSION ON APPROPRIATE PERIODS FOR IRT INSPECTION OF CONCRETE BRIDGE SLABS BASED ON LONG-TERM FEM ANALYSIS

Numerical simulation of one year of the inspection was performed using the FEM model and the weather conditions data available in the meteorological database [39] near the study site. The period of simulations started on November 1st, 2018, the same month that the experimental program started, and ended on 31 October 2019, with hourly time steps. Each daily simulation took an average time of 152 seconds, which reduced an entire year analysis to approximately 16 hours. The simulations were performed using a desktop computer with 16 GB RAM, 2.3 GHz Intel Core i7 CPU, and an NVIDIA GeForce MX250 GPU. The varying input parameters of the model are presented in Table 2. Conventionally, the year was divided into the local seasons: autumn (March, April, and May), winter (June, July, and August), spring (September, October, and November) and summer (December, January, and February). The results are separated by the seasons and are presented in Fig. 7.
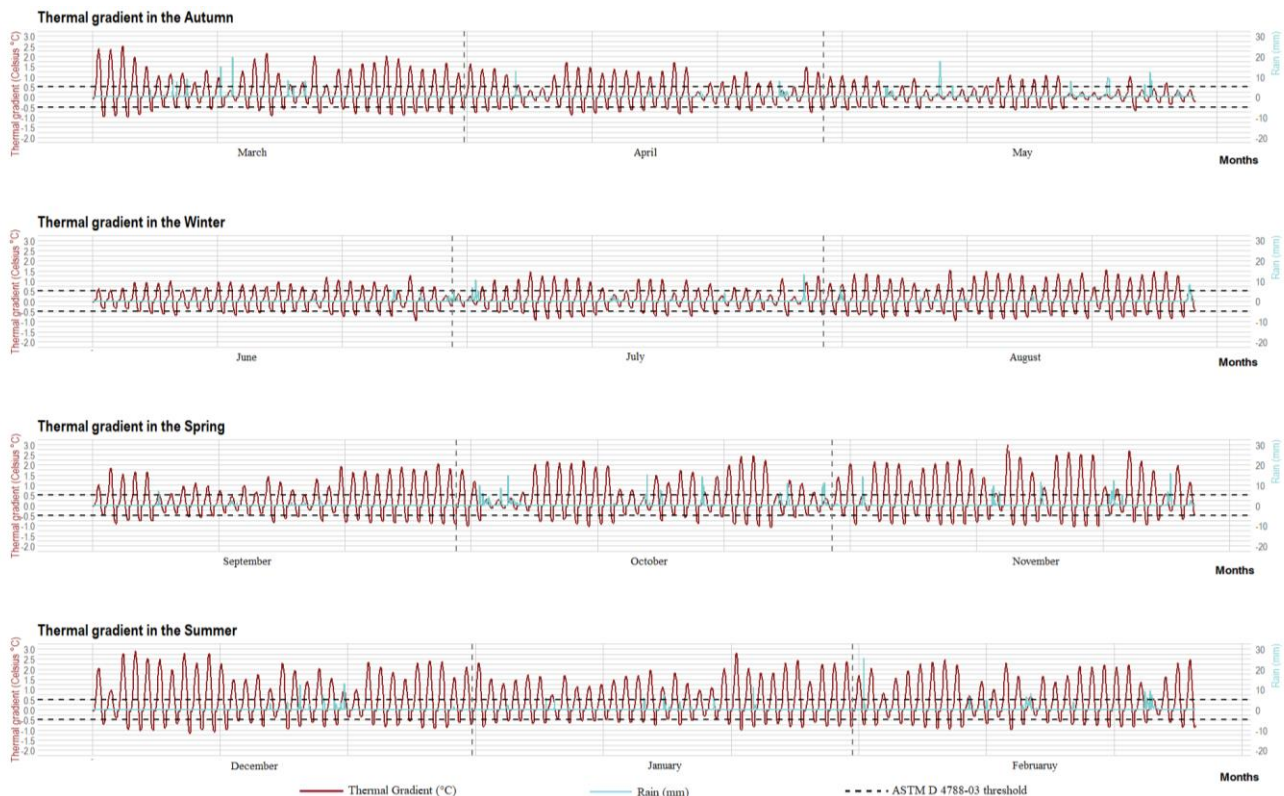

Fig. 7 Thermal gradient results from the FEM simulation of one year of IRT inspection

The incidence of the rain was plotted in Fig. 7 and the numerical model correctly simulated the low thermal gradients values in these events, mainly between the ±0.5°C thresholds. The solar radiation parameter allows this prediction, as rainy days usually have low solar radiation levels, generating a model outcome that correctly shows these days as not favorable for inspections. ASTM D 4788-03 [44] recommends that the bridge deck remain dry for at least 24h hours before an IRT inspection. Also, the regulation prescribes a minimum thermal gradient of 0.5 °C between healthy areas and areas with suspected delamination. A dashed line was inserted in Fig. 7 to highlight the detection threshold stipulated by the ASTM D 4788-03 [44].

The direct observation from Fig. 7 allows us the perception of difference in the thermal gradient behavior along the seasons, where months with warmer weather have greater thermal gradient values and a larger number of simulations with reliable thermal gradients (out of the ASTM D4788-03 boundaries). The greater thermal gradient between damaged and undamaged areas facilitates subsurface damage identification [8], [9], [32], [36], because the contrast in the thermograms colors becomes more noticeable with the increase of the temperature difference. Table 4 presents the number and percentage of IRT simulations that exceed the ASTM D4788-03 recommendation of a minimum thermal gradient, according to the different seasons considered in the simulation.

Season	Month	N° of detections	N° of simulations	Monthly Detection Percentage (%)	Season Detection Percentage (%)	6-Months Detection Percentage (%)
Autumn	March	367	744	49.33	35.46	
	April	275	720	38.19		
	May	141	744	18.95		35.87
Winter	June	227	720	31.53	36.28	
	July	216	744	29.03		
	August	358	744	48.18		
Spring	September	326	720	45.28	48.08	
	October	325	744	43.68		
	November	399	720	55.42		53.29
Summer	December	456	744	61.29	58.56	
	January	428	744	57.53		
	February	381	672	56.70		

Table 4 Quantitative results of thermal gradient observations above the threshold recommended by ASTM D4788-03 [44]

In a monthly analysis, December presented a larger percentage of contrast results exceeding the 0.5 °C threshold. This month represents the beginning of the summer in Brazil and together with January and February, compose the summer season in the southern hemisphere. This season had a higher quantity of simulations of thermal gradient values exceeding the ASTM D 4788-03 recommendation. The warmer weather in the summer facilitates the heating propagation by solar radiation, the main heating source for passive IRT inspection, which increases the heating of the concrete sample and therefore, the identification of the damages [32], [35]–[38]. Winter and autumn months also present a high incidence of solar radiation; however, the air temperatures usually are lower than summer and spring, and the presence of humidity and fog are more frequent, which make the heat propagation difficult. In general, it can be observed that the summer and spring represent favorable periods to perform infrared thermographic inspections under passive heating in the location of study, with 17.42% more reliable detections than the autumn and winter period. These findings challenge the observation of Hiasa et al. [32], which reported no significant effect of seasonal environment on the simulated thermal gradient in Orlando, Florida. One explanation could be the extent of the simulation, where they simulated one sunny day in each season, while this study performed an extended simulation of the entire seasons. Moreover, the study location probably has a different weather condition, which naturally produces different results. On the other hand, our data support the Al Gharawi et al. [45] work by showing that the thermograms captured in warmer months tend to have higher contrast results compared to colder months.

The results of this research imply that having the geographic information of the location (coordinates and global zone), a reliable meteorological database and the characteristics of the damaged structure, the inspector may simulate the daily thermal oscillation at the inspected structure. Thus, by evaluating the results of the finite element simulation, the inspector would be able to assess the most favorable time window to carry out the thermographic inspection of subsurface defects in reinforced concrete bridge slabs, avoiding excessive visits to the bridge field and/or experimental tests, as was previously stated by previous studies [22], [30], [32]. The use of numerical simulation to support the IRT-based bridge inspections highlights an application for the finite element method in infrastructure health monitoring. The proposed simulation approach also meets the premises of sustainability since it intends to help the maintenance of the structures to allow their use by the next generations.

To the best knowledge of the authors, the studies present in the literature did not simulate a passive IRT numerical analysis for an entire year. The complete simulation of a long period allows us to assess the effects of the seasonal variations in the IRT inspections

without excessive tests, showing that spring and summer seasons are favorable periods to use the IRT technique. Although the presented results depend on the characteristics of the sample and the study location, the general concept of the model can be considered for further analysis of other concrete structures, and in other locations, and environmental conditions. Moreover, the model can be improved by adding a greater number of experimental tests and more precise physical parameters. In addition, an agenda of the practical tests must be maintained since the thermal proprieties of the structural materials may change along the lifetime of structures and the FEM model requires calibration [46].

5. CONCLUSION

We proposed a numerical simulation for supporting long-term inspection plans using a passive IRT method for the detection of subsurface damages in concrete bridge decks. The model was developed using FEM which showed promising agreement with surface temperatures and thermal gradients measured in the experimental tests, supporting the extrapolation to long-term analysis to find favorable windows for inspections. A major advantage of numerical models to simulate IRT inspections is the thrift of time, effort, and resources spent in the construction of the samples or in the visits to the structure to find the best times to perform the measurements. The number of factors that influence passive IRT inspections is a limitation of this approach and can lead to discrepancies in the surface temperatures simulations. Further research efforts could use the finite element model updating technique to improve the accuracy of the results and also to provide a table with validity periods for inspection related to latitude of interest.

ACKNOWLEDGMENT

REFERENCES

[1] American Road and Transportation Builders Association (ARTBA), "Bridge Report. 2020", 2020. https://artbabridgereport.org/ (Assessed oct. 14, 2020).

[2] M. van Balen *et al.*, *Research and innovation in bridge maintenance, inspection and monitoring: a European perspective based on the Transport Research and Innovation Monitoring and Information System (TRIMIS).* 2019.

[3] C. B. L. Oliveira, M. Greco, e T. N. Bittencourt, "Analysis of the brazilian federal bridge inventory", *Rev. IBRACON Estrut. E Mater.*, vol. 12, nº 1, p. 1–3, 2019.

[4] European Commission, "Discussion Paper - State of infrastructure maintenance", 2019. https://ec.europa.eu/growth/sectors/construction/observatory (Assessed oct. 04, 2020).

[5] I. Garrido, S. Lagüela, R. Otero, e P. Arias, "Thermographic methodologies used in infrastructure inspection: A review—data acquisition procedures", *Infrared Phys. Technol.*, vol. 111, p. 103481. 2020.

[6] P. C. Chang e S. C. Liu, "Recent Research in Nondestructive Evaluation of Civil Infrastructures", *J. Mater. Civ. Eng.*, vol. 15, nº 3, p. 298–304, 2003.

[7] Ibarra-Castanedo C., Sfarra S., Genest M., e Maldague X, "Infrared Vision: Visual Inspection Beyond the Visible Spectrum", in *Integrated Imaging and Vision Techniques for Industrial Inspection: Advances and Applications*, ISBN 978-1-4471-6741-9, pp. 42-57, Liu, Z., Ukida, H., Ramuhalli, P., Niel, K. (Eds.), Springer. 2015.

[8] X. Maldague, *Theory and practice of infrared technology for nondestructive testing.* Wiley, 2001.

[9] X. Maldague, *Nondestructive Evaluation of Materials by Infrared Thermography*, 1º ed. Springer-Verlag London, 1993.

[10] N. Gucunski, R. Romero, S. Kruschwitz, R. Feldmann, e H. Parvardeh, "Comprehensive bridge deck deterioration mapping of nine bridges by nondestructive evaluation technologies", Iowa Department of Transportation, Final Report, 2011.

[11] D. G. Aggelis, E. Z. Kordatos, D. V. Soulioti, e T. E. Matikas, "Combined use of thermography and ultrasound for the characterization of subsurface cracks in concrete", *Constr. Build. Mater.*, vol. 24, nº 10, p. 1888–1897, 2010.

[12] F. Khan e I. Bartoli, "Detection of delamination in concrete slabs combining infrared thermography and impact echo techniques: a comparative experimental study", San Diego, California, United States, 2015, p. 94370I.

[13] T. Omar e M. L. Nehdi, "Remote sensing of concrete bridge decks using unmanned aerial vehicle infrared thermography", *Autom. Constr.*, vol. 83, p. 360–371. 2017.

[14] K. Vaghefi, T. (Tess) M. Ahlborn, D. K. Harris, e C. N. Brooks, "Combined Imaging Technologies for Concrete Bridge Deck Condition Assessment", *J. Perform. Constr. Facil.*, vol. 29, nº 4, p. 04014102, 2015.

[15] S. Pozzer, E. Rezazadeh Azar, F. Dalla Rosa, e Z. M. Chamberlain Pravia, "Semantic Segmentation of Defects in Infrared Thermographic Images of Highly Damaged Concrete Structures", *J. Perform. Constr. Facil.*, vol. 35, nº 1, p. 04020131, 2021.

[16] E. McLaughlin, N. Charron, e S. Narasimhan, "Automated Defect Quantification in Concrete Bridges Using Robotics and Deep Learning", *J. Comput. Civ. Eng.*, vol. 34, nº 5, p. 04020029, 2020.

[17] C. Ibarra-Castanedo, S. Sfarra, M. Klein, e X. Maldague, "Solar loading thermography: Time-lapsed thermographic survey and advanced thermographic signal processing for the inspection of civil engineering and cultural heritage structures", *Infrared Phys. Technol.*, vol. 82, p. 56–74, 2017.

[18] Y. A. Çengel e A. J. Ghajar, *Heat and mass transfer: fundamentals & applications*, Fifth edition. New York, NY: McGraw Hill Education, 2015.

[19] J. M. Kleinfeld, "Applying FEA to Perform Heat Transfer Calculations to Increase the Utility of IR Thermography", p. 30, 2002.

[20] F. L. Rodríguez e V. de Paulo Nicolau, "Inverse heat transfer approach for IR image reconstruction: Application to thermal non-destructive evaluation", *Appl. Therm. Eng.*, vol. 33–34, p. 109–118, 2012.

[21] R. Chowdhury, "Heat Transfer Fundamentals Applicable to Infrared Thermography of Concrete Structures", in *AIP Conference Proceedings*, Green Bay, Wisconsin (USA), 2004, vol. 700, p. 1042–1049.

[22] S. Hiasa, R. Birgul, M. Matsumoto, e F. Necati Catbas, "Experimental and numerical studies for suitable infrared thermography implementation on concrete bridge decks", *Measurement*, vol. 121, p. 144–159, jun. 2018, doi: 10.1016/j.measurement.2018.02.019.

[23] S. Belattar, J. Rhazi, e A. E. Ballouti, "Non-destructive testing by infrared thermography of the void and honeycomb type defect in the concrete", *Int. J. Microstruct. Mater. Prop.*, vol. 7, nº 2/3, p. 235, 2012.

[24] F. Khan, M. Bolhassani, A. Kontsos, A. Hamid, e I. Bartoli, "Modeling and experimental implementation of infrared thermography on concrete masonry structures", *Infrared Phys. Technol.*, vol. 69, p. 228–237, 2015.

[25] Ch. Maierhofer, A. Brink, M. Röllig, e H. Wiggenhauser, "Quantitative impulse-thermography as non-destructive testing method in civil engineering – Experimental results and numerical simulations", *Constr. Build. Mater.*, vol. 19, nº 10, p. 731–737, 2005.

[26] S. Belattar, "The Finite Element Method and Infrared Thermography Applied to the Characterization of Defects in a Chimney Structure", apresentado em Quantitative InfraRed Thermography Asia 2015, 2015.

[27] Cheng, T. Sakagami, e S. Kubo, "Determination of delamination depth in concrete structure based on inverse analysis of thermography data", Orlando, Florida, 2010, p. 76610E.

[28] R. G. Dragan, I. C. Rosca, D. Cazangiu, e A. S. Leonte, "Thermal Response for a Reinforced Concrete Slab Analyzed with Active Infrared Thermography and Comsol Multiphysics", *Appl. Mech. Mater.*, vol. 760, p. 627–632, 2015.

[29] R. Rumbayan e G. A. Washer, "Modeling of Environmental Effects on Thermal Detection of Subsurface Damage in Concrete", *Res. Nondestruct. Eval.*, vol. 25, nº 4, p. 235–252, 2014.

[30] E. Güray e R. Birgül, "Determination of Favorable Time Window for Infrared Inspection by Numerical Simulation of Heat Propagation in Concrete", in *Proceedings of 3rd International Sustainable Buildings Symposium (ISBS 2017)*, vol. 7, S. Fırat, J. Kinuthia, e A. Abu-Tair, Orgs. Cham: Springer International Publishing, 2018, p. 577–591.

[31] S. Hiasa, "A data processing methodology for infrared thermography images of concrete bridges", *Comput. Struct.*, p. 14, 2017.

[32] S. Hiasa, R. Birgul, e F. N. Catbas, "Investigation of effective utilization of infrared thermography (IRT) through advanced finite element modeling", *Constr. Build. Mater.*, vol. 150, p. 295–309, 2017.

[33] S. Hiasa, R. Birgul, e F. N. Catbas, "Effect of Defect Size on Subsurface Defect Detectability and Defect Depth Estimation for Concrete Structures by Infrared Thermography", *J. Nondestruct. Eval.*, vol. 36, nº 3, p. 57, 2017.

[34] L. Różański e K. Ziopaja, "Applicability analysis of IR thermography and discrete wavelet transform for technical conditions assessment of bridge elements", *Quant. InfraRed Thermogr. J.*, vol. 16, nº 1, p. 87–110, 2019.

[35] S. Pozzer, Z. M. C. Pravia, E. Rezazadeh Azar, e F. Dalla Rosa, "Statistical analysis of favorable conditions for thermographic inspection of concrete slabs", *J. Civ. Struct. Health Monit.*, vol. 10, nº 4, p. 609–626, 2020.

[36] A. Watase, R. Birgul, S. Hiasa, M. Matsumoto, K. Mitani, e F. N. Catbas, "Practical identification of favorable time windows for infrared thermography for concrete bridge evaluation", *Constr. Build. Mater.*, vol. 101, p. 1016–1030, 2015.

[37] B. N. K. Raja, S. Miramini, C. Duffield, M. Sofi, P. Mendis, e L. Zhang, "The influence of ambient environmental conditions in detecting bridge concrete deck delamination using infrared thermography (IRT)", *Struct. Control Health Monit.*, vol. 27, nº 4, 2020.

[38] G. Washer, R. Fenwick, e N. Bolleni, "Effects of Solar Loading on Infrared Imaging of Subsurface Features in Concrete", *J. Bridge Eng.*, vol. 15, nº 4, p. 384–390, 2010.

[39] INMET, "Estação meteorológica de observação de superfície automática". http://www.inmet.gov.br/portal/index.php?r=estacoes/estacoesautomaticas (Assessed aug. 14, 2020).

[40] H. Gothäll, "How to Inspect Your Mesh in COMSOL Multiphysics", *COMSOL*, 2017. https://www.comsol.com/blogs/how-to-inspect-your-mesh-in-comsol-multiphysics/ (Acessed sep. 21, 2020).

[41] S. Sharples e P. S. Charlesworth, "Full-scale measurements of wind-induced convective heat transfer from a roof-mounted flat plate solar collector", *Sol. Energy*, vol. 62, nº 2, p. 69–77, 1998.

[42] COMSOL, "Parasol and Solar Irradiation", *COMSOL*, 2019. https://www.comsol.com/model/sun-s-radiation-effect-on-two-coolers-placed-under-a-parasol-12825 (Assessed oct. 10, 2020).

[43] B. Urquhart, M. Ghonima, D. (Andu) Nguyen, B. Kurtz, C. W. Chow, e J. Kleissl, "Chapter 9 - Sky-Imaging Systems for Short-Term Forecasting", in *Solar Energy Forecasting and Resource Assessment*, J. Kleissl, Org. Boston: Academic Press, 2013, p. 195–232.

[44] American Society for Testing and Materials, "ASTM D4788 – 03: Standard Test Method for Detecting Delaminations in Bridge Decks Using Infrared Thermography". 2013.

[45] M. Al Gharawi, Y. Adu-Gyamfi, e G. Washer, "A framework for automated time-lapse thermography data processing", *Constr. Build. Mater.*, vol. 227, p. 116507,. 2019.

[46] T. Omar e M. Nehdi, "Condition Assessment of Reinforced Concrete Bridges: Current Practice and Research Challenges", *Infrastructures*, vol. 3, nº 3, p. 36, 2018.

Infrared-terahertz fusion inspection for jute/kenaf-glass hybrid composites

Jue Hu, Hai Zhang, Stefano Sfarra, Carlo Santulli, Guiyun Tian and Xavier Maldague

Abstract: Natural fiber composites have received growing attention for investigation owing to the potential of serving as candidate for artificial fiber composites. However, the complexity in structure requests more effective imaging technique for the inspection. In this work, a novel multi-modality spatial-spectral data fusion technique is proposed to merge data from terahertz wave transmission imaging and infrared thermography. An unsupervised deep residual fusion algorithm is adapted for merging information. Furthermore, the fusion results are 3D reconstructed to exhibit an overall view of the composites, and validated to be accurate by X-ray CT.
Keywords: Natural fiber composite, non-destructive testing, data fusion, unsupervised learning

1 Introduction

Natural fiber composites have many advantages such as environment friendly, lightweight and low cost. Several investigations of natural fiber composites such as coir, hemp, jute and bamboo have been already presented to reveal the mechanical properties of these composites. However, composites with internal quality issue may results in serious accident and huge loss in real industrial applications.

An effective non-destructive testing method needs to be developed to guarantee the safety. Advances in NDT inspection on composite structures have been reviewed by many papers such as in [2], [3]. As is known, defect information from a single sensor is usually incomplete and ambiguous.

In this work, in order to provide comprehensive defect information for non-destructive evaluation and reduce the uncertainty of measurement, a novel IRT and THz-TDS data fusion technique is proposed for natural fiber composites inspection.
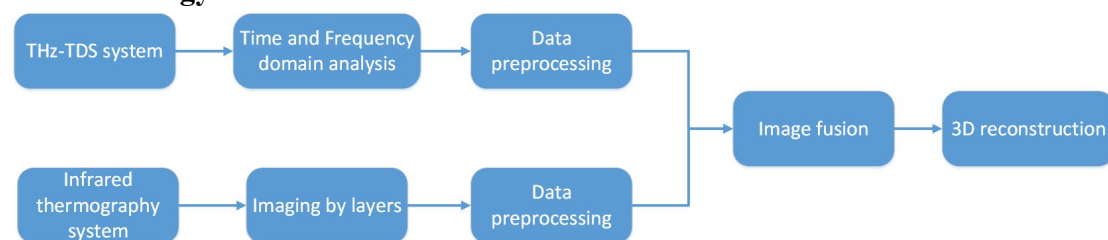
2 Methodology

Fig. 1. Schematic diagram of proposed multi-modality spatial-spectral data fusion technique

In this study, a novel multi-modality spatial-spectral data fusion technique is proposed. The complete schematic diagram of the proposed technique is shown in Fig. 1. Raw data collected from THz-TDS system is analyzed in both time and frequency domain to get images based on different time domain representation and spectral characteristics of the materials. The thermal sequence from IRT system is also analyzed for imaging

from different depth. After that, the analytical results from THz-TDS and IRT are preprocessed to ensure that images from different modalities are in strict geometrical alignment and intensity matching. An unsupervised deep residual fusion network is proposed to fuse the images from different modality and the fusion results are reconstructed in 3D formula to exhibit overall view of the composites.

3 Results

The specimens involved in this study include jute and kenaf fiber laminates [4]. One sample was manufactured with jute/glass hybrid fiber. The composite was laminated by the sequence of surface veil, chopped strand matrix and jute fiber. Another sample was conducted with kenaf/glass hybrid fiber. A sandwich structure is adapted to construct the laminate. The core was fabricated with continuous kenaf/glass hybrid fiber yarns whereas the two skins were made of chopped strand matrix with surface veil.
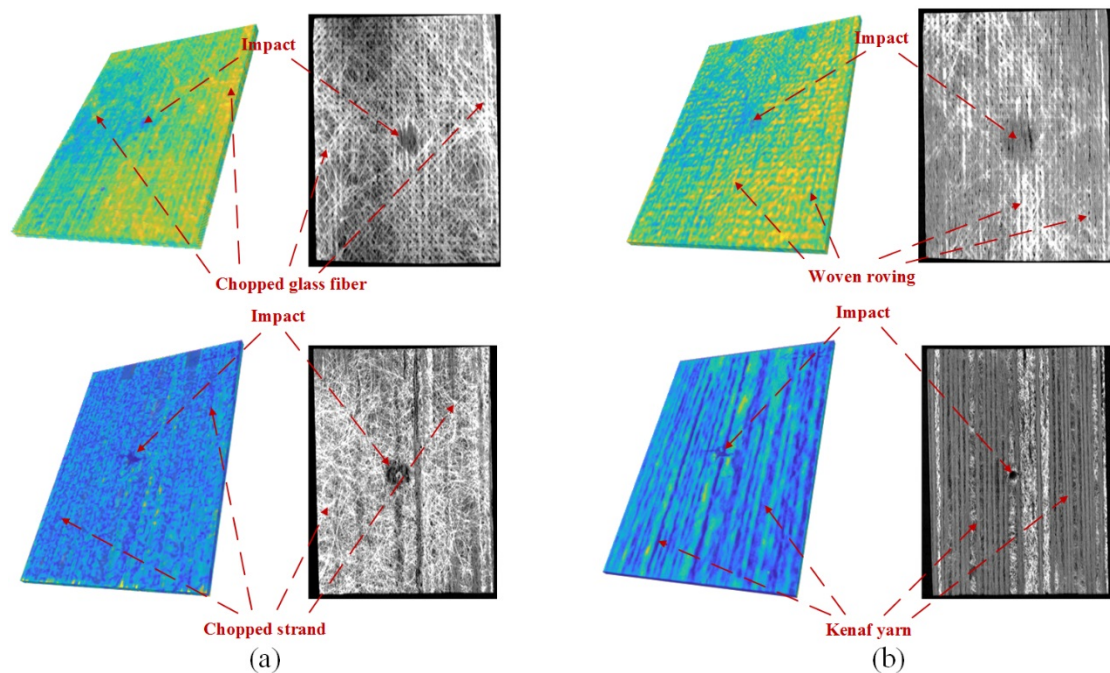

Fig. 2: 3D reconstruction on the fusion results and comparison with X-ray computed tomography inspection: (a) Jute composite sample; (b) Kenaf composite sample.

In Fig. 2, the 3D reconstruction on the fusion results has been shown. 3D reconstruction models are cut to present the horizontal-section. In the jute composite illustrated in Fig. 2(a), the content distribution of chopped glass fiber provided by THz-TDS modality could be mapped to the X-ray computed tomography inspection. In addition, the low velocity impact induced damage and air holes inspected by IRT are observed in the fusion result. In the horizontal-section on the woven roving layer, interlaced low intensity strips provided by THz-TDS reveal the woven roving which are fused with the low velocity impact induced damage appeared in IRT results.

In the kenaf composite illustrated in Fig. 2(b), chopped strand matrix appeared high absorption in THz-TDS amplitude imaging is fused with impact induced damage provided by IRT. It is worth noting that, the fiber content distribution and orientation

could be viewed in the fusion results. In the horizontal-section on the kenaf yarn layer, kenaf fiber yarn is clearly observed by THz time-domain imaging which could be mapped to the X-ray computed tomography inspection. Moreover, low velocity impact induced damage inspected in IRT is merged into fusion result.

In Fig. 3, the 3D reconstruction model on fusion result of kenaf fiber composite is compared with X-ray computed tomography inspection in details. Comparisons are conducted on both horizontal-section and cross-section. Horizontal-section is extracted on the depth of 0.16 mm and the cross-section is cropped at the line 48.4 mm above the lower edge.

On the horizontal-section, total 25 kenaf fiber yarns could be mapped into the X-ray computed tomography inspection. Furthermore, several clusters of yarns could be mapped into CT inspection one-by-one due to the especially high contrast provided near the area in the fusion results, e.g., a cluster of six yarns on the left of impact induced damage, a cluster of four yarns and a single yarn on the right edge of this laminate.

On the cross-section, kenaf yarns in the fusion results could match these yarns to CT inspection. Clusters of four and six kenaf fiber yarns on the left part is clearly observed while the cluster of four yarns near the right edge is not shown as high resolution as the horizontal-section.
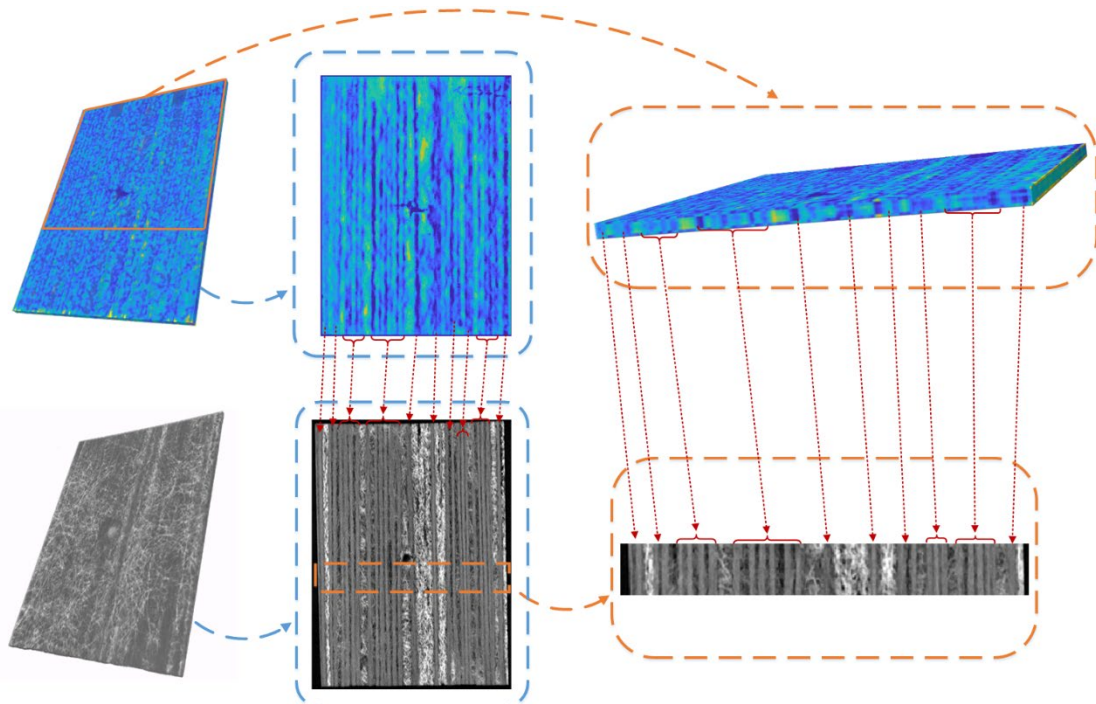

Figure 3: Cross-section and horizontal-section imaging on fusion results of kenaf fiber composite compared with X-ray computed tomography inspection

References

[1]   I. M. De Rosa, C. Santulli, and F. Sarasini, "Acoustic emission for monitoring the mechanical behaviour of natural fibre composites: A literature review," *Compos. part a Appl. Sci. Manuf.*, vol. 40, no. 9, pp. 1456–1469, 2009.

[2]   S. Gholizadeh, "A review of non-destructive testing methods of composite materials," *Procedia Struct. Integr.*, vol. 1, pp. 50–57, 2016.

[3]   P. Duchene, S. Chaki, A. Ayadi, and P. Krawczak, "A review of non-destructive techniques used for mechanical damage assessment in polymer composites," *J. Mater. Sci.*, vol. 53, no. 11, pp. 7915–7938, 2018.

[4]   H. M. Akil, I. M. De Rosa, C. Santulli, and F. Sarasini, "Flexural behaviour of pultruded jute/glass and kenaf/glass hybrid composites monitored using acoustic emission," *Mater. Sci. Eng. A*, vol. 527, no. 12, pp. 2942–2950, 2010.

É. du CAO

à la frontière des connaissances
at the cutting edge of knowledge